Transitioning of Spent Advanced Gas Reactor Fuel from Wet to Dry Storage

James Bruce Goode

School of Chemical and Process Engineering

University of Leeds

Submitted in accordance with the requirements for the degree of Doctor of Philosophy

December 2017

The candidate confirms that the work submitted is their own, except where work which has formed part of jointly authored publications has been included. The contribution of the candidate and the other authors to this work has been explicitly indicated below. The candidate confirms that appropriate credit has been given within the thesis where reference has been made to the work of others.

The work in section 3.3-5, 3.8 and 9.3 of the thesis has appeared in publication as follows:

Drying Simulated Advanced Gas Reactor Fuel: Proving the Concept by James B. Goode, David Harbottle and Bruce C. Hanson in the Proceedings of Waste Management 2017.

Parts of chapters 6-10 have, at the time of thesis submission, have been accepted for publication pending revisions as follows;

Vacuum Drying of Advanced Gas Reactor Fuel by James B. Goode, David Harbottle and Bruce C. Hanson in Annals of Nuclear Energy.

I was responsible for all work in both cases.

In both cases the contribution of the other authors was supervisory.

Acknowledgements

Firstly I would like to thank my supervisors Professor Bruce Hanson and Doctor David Harbottle for their assistance and guidance throughout the course of my PhD studies.

Next I would like to thank a number of the technical staff throughout the university. All of the staff within the School of Chemical and Process Engineering have been of assistance but special mention should be given to Diane Cochrane, Susanne Patel, Ben Douglas and Adrian Cunliffe.

From other departments I would like to thank Dr Ben Johnson of School of Physics and Astronomy and Dr Steven Brookes of the School of Dentistry for carrying out XPS and CT analysis respectively. Also Anna Clough who provided assistance when I was struggling with some of the many graphing issues I had.

I have also clearly had the assistance of various other students at oen time or another and would like to thank Wei Ding and Matthieu Lasfargues and also May Chan Choen of the University of Manchester who provided guidance in sample preparation.

I would also like to thank all of the staff of the Faculty of Engineering mechanical workshop and even greater thanks to the staff of the electrical workshop.

From outside the university I would like to thank Steve Walters of the National nuclear Laboratory for providing me with a length of unused AGR cladding for my experiments as well as David Hambley also of NNL who was instrumental in providing funding for the drying rig along with the NDA.

I would like to thank the EPSRC and the University of Leeds for funding my research.

Finally I would like to thank my former History tutor at Keele University. He was the one person at Keele who saw any potential in me and it is only due to his reference that I was able to return to university at the age of 27.

Abstract

Upon removal from a reactor spent nuclear fuel is placed into water storage for a period of time since water provides both a decay heat sink and radiation shielding. In the UK this fuel has traditionally been reprocessed however the decision has been made that this will cease in 2018 in favour of an open fuel cycle and direct disposal to a degological disposal facility, although this is not expected to be available until 2075. Current experience with pond storage has found that fuel can be safely stored in caustic dosed ponds for at least 25 years and therefore the current plan is to extend water storage until around 2040, however how the fuel will be stored for the remaining 35 years is yet to be decided.

One option that is being considered is the use of dry storage which is being used successfully in the USA for the storage of fuel from Light Water Reactors. One of the most important factors when utilising dry stores is an effective drying step and this PhD is aiming to look at this area in particular.

Commercial drying methods have been developed for use with Zircaloy and aluminium clad fuels however this PhD intends to develop a method that can be used to dry Stainless Steel clad fuels such as those used in the UK's Advanced Gas Reactors (AGR).

Since intact AGR fuel has yet to be examined following storage the first part if this thesis looked at preparing samples for later macro scale testing. Samples were treated to induce defects known to be of concern and analysed with the conclusion being that bound water is of no concern for drying operations and can be disregarded when preparing samples. Since AGR is known to have failed by stress corrosion cracking water trapped within microcracked pins is a likely issue. A section of

tube was prepared by compression and boiling in magnesium chloride which micro CT imaging found to have images of a similar size to known failures. This tube was prepared into a test piece for later testing.

The second part of the thesis looks at macro scale testing using the test piece described above and a similar test piece with a 300μm pinhole. A multipurpose drying rig capable of vacuum drying and flowed gas drying was constructed. In the first phase of drying tests vacuum drying and flowed gas drying were compared using a test piece with a 300 μm pinhole and the impact of different cover gas was assessed. vacuum drying was found to be significantly more effective than flowed gas drying with the type of cover gas having little impact. Most importantly this work guided further improvements to the rig.

The second phase of this work carried out more detailed drying tests on vacuum drying and flowed gas drying and utilised the pinholed and cracked test piece. The greatest influencing factor on the drying rate (the rate at which water could be removed from inside the test piece) was found to be the water level inside the test piece with broadly similar rates being found in all conditions and with both test piece when the test piece was full. As the water level within the test piece dropped, vacuum drying quickly became more effective. This was not helped by considering energy usage. There was however a feeling that flowed gas drying was limited due to the pipework size.

In the final phase of testing the ability to detect the point which all water was removed (the end point) from the test piece using online instrumentation was assessed. Currently a vacuum rebound test is used which is both time consuming and if flowed gas drying is being used requires additional plant equipment. It was found that dew point measurements appeared to give a relatively clear indication of the end point when for both vacuum drying and flowed gas drying. For vacuum drying only the measurement of mass flow and pressure also gave a reasonable indication of end point.

Contents

List of Tables

List of Figures

Abbreviations

AGR	Advanced Gas Reactor
bcc	body centred cubic structure
CT	Computed Tomography
DoE	United States Department of Energy
DSC	Direct Scanning Calorimtry
EDX/EDS	Energy Dispersive X-Ray Spectroscopy
fcc	face centred cubic structure
FHD	Forced Helium Dehydration
FM	Flow Meter
$FWHM$	Full Width Half Maximum
ID	Internal/Inside Diameter
IGA	Intergranular Attack
IGC	Intergranular Corrosion
$IGSCC$	Intergranular Stress Corrosion Cracking
INL	Idaho National Laboratory
LWR	Light Water Reactor

MCO	Multi Canister Overpack
MS	Mass Spectrometer/spectrometry
NDA	Nuclear Decommissioning Authority
NNL	National Nuclear Laboratory
OD	Outside Diameter
OPV	Over Pressure Valve
$P\&ID$	Process and Instrumentation Drawing
PA	Pinholed Acrylic
$PPMm$	Parts per million by mass
RH	Relative humidity
SCC	Stress Corrosion Cracking
SEM	Scanning Electron Microscopy
$STEM$	Scanning Transmission Electron Microscopy
TEM	Transmission Electron Microscopy
TGA	Thermogravimetric Analysis
$UNGG$	Uranium Naturel Graphite Gaz
XPS	X-ray Photoelectron Spectroscopy
XRF	X-Ray Fluorescence

Chapter 1

Introduction and PhD Aims and Objectives

Since the building of the Chicago Pile in 1942 nuclear fission reactors have been used by man to produce material for weapons, electricity and medical isotopes. The by-product of this process has been the production of spent nuclear fuel as a waste product. This highly toxic waste poses a unique set of problems as the toxicity comes from radiation, types of which can be highly penetrating making containment difficult, is reduced only by time (allowing the atoms to decay naturally) and can not be destroyed by chemical means[1]. These issues are further complicated by the decay heat produced by the fuels themselves even decades after irradiation and the fact that the half-lives of the wastes produced range from a matter of seconds to millions of years, meaning that waste treatment options must consider what will happen with wastes not only in the short term but also for generations to come and thousands of years into the future.

Upon removal from a reactor spent nuclear fuel is generally placed into water to provide both a decay heat sink and radiation shielding, however for permanent disposal two viable options have been identified; direct or geological disposal as part of an open fuel cycle and reprocessing as part of a closed fuel cycle. In simple terms geological disposal is burying spent nuclear fuel in its entirety (i.e. entire fuel bundles including cladding and structural components) in rock formations

[1]Neutron bombardment can be used to accelerate decay and reduce activity although this is not generally regarded as being viable for the large quantities of fuel produced.

from which radionuclides can not escape. While in theory this sounds relatively easy, the toxicity of the wastes and the time frames involved mean that site selection must be made very carefully. Sites must be chosen such that any escape of radioactive materials from the containment during storage does not enter the water table and such that the site is of no danger to future peoples. The discovery of the natural reactors that formed in Gabon 1800 million years ago and the elevated levels of fission products in the area suggest that such a disposal route is viable. Reprocessing involves subjecting fuel to numerous chemical treatments each of which separates out a different group of elements. These processes were initially developed to allow the extraction of plutonium for defence purposes however cladding, uranium and other transuranic elements can also be isolated. With a fully closed fuel cycle it is theoretically possible to reuse 96% of the initial heavy metal. While the remaining 4% must be placed into storage, the volumes of waste have been reduced dramatically as has the time until waste has reached what is regarded as an acceptable level[1].

1.1 UK spent nuclear fuel Storage and Disposal

Since the primary purpose of early reactors was the production of plutonium for weapons, reprocessing was the favoured method and in the UK this has continued up until the present day at Sellafield's Thermal Oxide Reprocessing Plant (Thorp). It has now been decided that in future the UK will adopt an open fuel cycle. The adoption of an open fuel cycle requires the building of a geological disposal facility which is not currently expected to be available until 2075. Experience to date has shown that UK Advanced Gas Reactor (AGR) spent nuclear fuel can be safely stored in caustic dosed ponds for at least 25 years and hence it is intended to caustic dose the Thorp Receipt and Storage Pond to pH 11.4 and hold fuel there until at least 2038. This leaves a gap of 35 years for which an interim storage solution must be found.[2]

[1] The long lived isotopes are the minor actinides which can be retrieved and used as fuel in fast reactors hence the waste consists of shorter lived isotopes only.

[2] Disposal and storage are different activities. Disposal is a permanent last step for radioactive wastes and a geological disposal facility is not designed to allow fuel to be retrieved. Storage

In 2012 the Nuclear Decommissioning Authority (NDA) published a report into the credible options for treatment of uranium oxide fuel[1]. One option that was considered was the use of interim dry storage. The decision to stop reprocessing in the United States was made in 1977 but a geological disposal facility is still to be completed. This led to a major capacity issue at US spent fuel ponds and the use of dry storage has been adopted successfully and is now used around the world. The basic principle of dry storage is to remove the fuel from a pond and place it into a steel and/or concrete container or vault. Such systems have much lower maintenance costs so long term costs are reduced.

When fuel is reprocessed it is initially dissolved in nitric acid. This can be done by transferring the fuel directly from the storage pond to the dissolver, however in a dry store any water present is likely to cause major corrosion issues and as such fuel must be dried prior to emplacement. For zircaloy clad fuels from Light Water Reactors (LWR) considerable research has been carried out into the degree of dryness required and the most effective method of achieving this, however AGR fuel utilises stainless steel cladding and consequently existing methods of dry storage can not be used directly in the UK.

1.2 Thesis Structure, Aims and Objectives

The intention of this PhD is to begin to investigate the drying behaviour of spent nuclear fuel with the aim being to develop a method by which AGR fuel can be effectively dried. It is hoped that this will provide evidence that can be used to support a safety case for the use of interim dry storage as an alternative to pond storage for AGR spent nuclear fuel[1]. The structure of this thesis comes about as a result of two distinct phases of research that have taken place.

When the project was first discussed the first question to be asked was "what is the fuel like when it comes out of a pond"? At the time a post storage examination programme had not yet been commenced and even at the time of writing the

on the other hand is a temporary measure, albeit one that may potentially last centuries, and further treatments may be required.

[1]Even if fuel is not placed into dry storage there is likely to be a need for a drying step prior to direct disposal.

initial results from this programme are yet to be released. As such it was clear that before any experiments relating to the drying of spent fuel could take place it would be necessary to try and establish the condition that fuel would be in upon removal from a pond to allow any samples used in drying tests to be representative. Consequently the first aim, and part one of this thesis looks at sample preparation, beginning with a literature review which covers the lifecycle of a fuel pin and how that will have affected its structure and composition, followed by the results of a number of tests that have been carried out in an attempt to reproduce any changes that may have taken place and also to characterise these samples. To this end the literature review section also includes a brief introduction to some of the techniques that have been used. The overall results of these chapters are used in the drying tests that are carried out in part two.

Having developed a set of samples that are believed to be suitably representative of long stored spent nuclear fuel the second part of this work aims to carry out the drying tests that are considered to be the primary purpose of this project and it is these drying tests that are covered in part two. Once again this part begins with a literature review which covers the basic science of drying and then dry storage of spent nuclear fuel, the types of drying methods that have been used and other related work. Two distinct types of spent fuel drying are identified and the following chapters cover the experiments that are undertaken using these two methods. Comparisons of these results is then carried out. There is also an investigation into end point determination to ascertain whether it is possible to mark the end point of a drying process using online instrumentation and measurement.

Part I

Sample Preparation and Characterisation

Chapter 2

Literature Review

This literature review section is intended to provide a background to the experimental work carried out in Part 1. It begins with a brief introduction to nuclear reactors and the life cycle of nuclear fuel. The impact of radiation on the degradation of fuel and the reactor core is discussed as are details of different corrosion mechanisms. The final section gives a description of the various techniques used in the experimental work in part 1.

2.1 Introduction

From the late 1940's until 1979 the nuclear industry within the UK was based upon graphite moderated gas cooled reactors. The Windscale Piles, the first of which began operation in 1950, were designed purely for the production of plutonium for atomic weapons and consisted of a graphite core containing horizontal channels into which fuel elements of natural uranium clad in aluminium were inserted. Since the production of plutonium was the only requirement the reactors were air cooled with the 150°C air being released to the atmosphere. This design was developed to become the worlds first commercial power reactor. While plutonium production was still the priority it had been realised that the waste heat could be utilised. Carbon dioxide replaced air as the coolant gas due to its reduced corrosivity and a closed cycle was utilised to minimise the release of radioactivity. Natural uranium was still used for fuel and due to its low neutron cross section magnesium was

used for cladding with small amounts of aluminium to prevent oxidation (hence the name MAGnesium Non-OXidising).

A similar design was used in France for their first generation reactors known as Natural Uranium Graphite Gas reactors (in French Uranium Naturel Graphite Gaz or UNGG), however while France now followed America in the development of Light Water Reactors, in the UK the second generation nuclear reactor fleet saw an evolution of the gas cooled reactor with the Advanced Gas-cooled Reactor or AGR.

One of the key changes made to the AGR's was the increase in thermal efficiency to around 40% (compared to around 32% in LWR's) with the use of higher temperature and pressure coolant gas. In order to accommodate the increase in temperature natural uranium was replaced with uranium dioxide pellets and magnesium cladding with stainless steel. To overcome the higher neutron cross section of steel compared to magnesium, fuel was enriched to 2.5-3.5% U-235, which also allowed higher burnup of fuel thus reducing refuelling requirements.

Upon removal from a reactor spent nuclear fuel, whether from an AGR or LWR is generally placed into water for at least five years. The water acts as a heat sink to remove decay heat and provides shielding. After five years spent nuclear fuel has generally cooled sufficiently to allow reprocessing to take place. In the United States reprocessing ceased in 1977 with the intention that cooled fuel would be transferred to a geological disposal facility. Over 35 years later that geological disposal facility is yet to be completed and this has lead to a chronic shortage of storage space in cooling ponds, despite re-racking of fuel to increase packing efficiency. This shortage led to the adoption of dry storage. The key requirements for the dry storage of spent nuclear fuel are the maintenance of the integrity of the fuel to prevent the release of fission products, ensuring that the fuel can be safely retrieved at a later date and the prevention of criticality during storage[2, 3]. Corrosion can have a significant detrimental impact on all of these factors and since this is promoted by the presence of water the drying of fuel is a critical step.

2.2 ASTM C-1553

While dry storage of wetted spent nuclear fuel has not been used in the United Kingdom it has been used overseas particularly in America to the point where ASTM standard C-1553 (Standard Guide for Drying Behavior of Spent Nuclear Fuel)[4] has been developed. Since it is written for the US market it primarily concerns aluminium and Zircaloy clad fuels rather than the stainless steel clad fuels found in the UK, however many of the key concepts and basic principles apply equally to all cladding types. Consequently it is an excellent introductory document to the field. One of the key issues that it discusses is the "types" of water that may be present and while it is a relatively simple concept it is vital to the whole concept of drying. The document discusses five types of water (table 2.1).

Bound water	Bound water includes adsorbed surface layers of water, and nearly all chemisorbed water.
Chemisorbed water	Water that is bound to other species by forces whose energy levels approximate those of a chemical bond.
Physisorbed water	Water that is physically bound (as an adsorbate, by weak forces) to internal or external surfaces of a material.
Unbound water	Water in the solid, liquid or vapour state that is not physically or chemically bound to another species
Trapped water	Unbound water that is physically trapped or contained by a surrounding matrix , blocked vent pores, cavities or by the nearby formations of solids that prevent or slow escape.

Table 2.1: Definitions of water related to nuclear fuel drying used in ASTM C-1553[4].

Within this document the following definitions will be used wherever possible; The definitions for physisorbed and chemisorbed water will be used from table 2.1 with the term bound water being used to cover these two forms collectively. The definition for trapped water will be used from table 2.1 and the term free water will

be used to describe untrapped water (i.e. a drop sitting on an open surface). The term unbound water will be used to describe free and trapped water collectively.

ASTM C-1553 also presents information on how to confirm dryness. For aluminium and Zircaloy clad fuels this is achieved by way of a vacuum rebound test. After drying has been completed the fuel canister is evacuated to below 3 Torr (∼4 mBarA) and the vessel is isolated. If water is present then the pressure will rise as that water vaporises. The canister is assumed to be dry if the pressure remains below 3 Torr for 30 minutes.

2.3 Fuel Life Cycle

The life cycle of a fuel pin begins with the production process. The fuel cladding arrives at the AGR fuel manufacturing plant where stainless steel tubes are machined to form helical ribs on the surface which create turbulence as the coolant passes and increases heat transfer. Following machining an end cap is welded into one end of the fuel pin and and the uranium dioxide fuel pellets are then inserted. The pins are then filled with helium before having the second end cap welded into place. The pins are then exposed to an increased pressure compressing the anti stacking grooves against the pellets and the pins are checked for leaks. Finally the pins are annealed at 930 °C in hydrogen for one hour. Each pin is approximately 1 m in length and 15.5 mm in diameter with a 400 μm wall thickness. The fuel pellets are annular with an outside diameter of around 14.5 mm and an inner diameter 6.4 mm

A fuel element used in AGR reactors is shown in fig. 2.1a. Each element consists of thirty six pins held together by stainless steel grids and surrounded by a graphite sleeve. A stainless steel tie bar is threaded through the guide tube of eight elements (seven in the case of Dungeness B) to produce what is known as a stringer and these are in turn lowered into one of 308 channels in the graphite core [5]. Coolant gas is flowed through the core entering at the base at ∼290°C and leaving at the top at ∼650°C [6]. The cladding temperatures are normally in the region of 350°C to 825°C [7].

After irradiation for up to five years in a reactor the elements are removed and initially cooled in carbon dioxide until a predetermined temperature is reached.

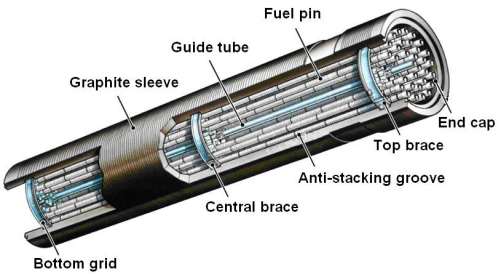

(a) AGR fuel element.

(b) Slotted can

Figure 2.1: An AGR fuel element and slotted can (taken from [8]).

The elements are then transferred to a cooling pond at the reactor where they are held in demineralised water until they are moved to Sellafield. Here they are transferred to the caustic dosed Thorp receipt and storage pond where they will remain for a period expected to be at least 25 years. From this lifecycle it can be seen that the key factors in the fuels life are the five years spent in the reactor and the time spent in the caustic dosed pond.

2.4 Reactor Materials

The following section discusses the key materials used within the core of an AGR, why they are used, the problems introduced and how these are overcome.

2.4.1 The Graphite Core and CO_2 Based Coolants

Graphite moderated, CO_2 cooled reactors such as Magnox and AGR's rely upon their core of graphite blocks to provide moderation for the fission reactions as well as mechanical strength, and consequently maintenance of core integrity is of paramount importance for reactor performance and life. For a long while it has been known that a major cause of degradation is the radiation induced oxidation

of graphite. Equation 2.1 gives the overall equation for the oxidation of graphite in CO_2. The exact details of this process are somewhat complex and have been thoroughly reviewed by Best et al[5] however the process is summarised below.

$$C + CO_2 \rightarrow 2CO \tag{2.1}$$

The reaction occurs due to the production of reactive oxidising species by ionising radiation which are able to react with the graphite walls when they come into contact. The likelihood of this happening can be reduced with the addition of a gaseous inhibitor which can in effect mop up the reactive species before they can reach the walls. Fortunately CO, which is also a product of reaction 2.1 is such an inhibitor and at low powers as found in the early Magnox reactors the addition of just a few ppm additional CO is sufficient to prevent core degradation[5].

For higher power reactors experimental work was carried out to find the best combination of materials to prevent core oxidation[9, 10]. While graphite corrosion inhibition by the presence of CO is due to gas phase reactions, inhibition by hydrogenous impurities is due to the changes in surface chemistry. In the later Magnox reactors (Oldbury and Wylfa) hydrogen was added to the core which formed an equilibrium of H_2, CH_4, and H_2O. Water and hydrogen were then found to be able to bind to the surface oxide of the graphite producing a protective surface complex[10]. At the higher radiation levels found in AGR's inhibition is achieved by the addition of small quantities of additional methane which form a sacrificial carbonaceous layer on the graphite surface[5]. While these treatments reduce core corrosion to negligible levels the carbonaceous deposits from methane inhibition were also found to form on metal surface such as fuel cladding leading to problems of reduced heat transfer.

Work into the mechanism of formation of these deposits was carried out by Cairns et al[11] using radio frequency plasma discharge apparatus. The process operated at a low pressure (4.7 mbar) with a 1:1 mixture of CO_2 and CH_4 and was able to ascertain that the process was surface catalysed with a silica coating being sufficient to prevent deposition. Later work by Horsley and Cairns[12] with the same apparatus established that catalytic activity was driven more specifically

by the presence of Ni and/or Fe since annealing and oxidation treatments that formed outer layers rich in Cr and/or Mn would also prevent deposition.

Sykes et al[13] developed an apparatus which was used to test the effect of nickel and iron carbonyls on the formation of carbon deposits. Two gas mixes, which simulated the gas expected to be found in an AGR due to radiolysis, were flowed through a furnace at conditions (temperature and pressure) similar to those within an AGR. This found that the carbon deposition was promoted by nickel carbonyls while iron carbonyls had no impact on deposition. This work compared by SEM the deposits found by experiment with real deposits found on elements removed from an AGR. While differences were found, both simulated and real deposits consisted of agglomerations of spherical carbon particles and contained electron rich regions believed to be nickel particles, however for the real AGR deposits these agglomerations had formed into what were described as tree like structures.

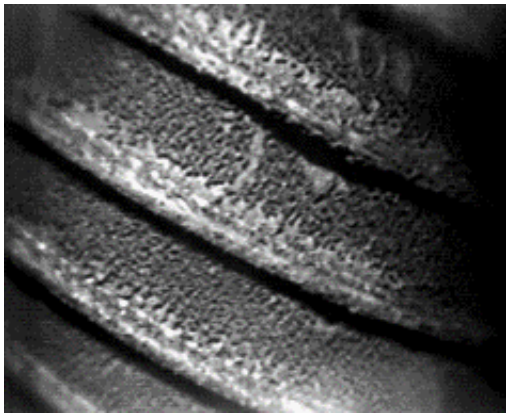

Figure 2.2: Image of real AGR carbon deposits (taken from [14]).

More recent work into the prevention of carbon deposition has been undertaken by Millward et al[15–18] using simpler deposition apparatus. In their work carbon deposition was carried out by flowing a mix of CO_2 with 1% CO and 1000 vpm C_2H_4 through a chamber within a furnace at 550 °C. With this equipment they were able to show that the production of filamentary carbon was due to the presence of Ni particles. The description of the deposits produced by Millward et al would seem to be similar to the description of real carbon deposits found on

AGR fuel described by Sykes et al[13]. This work has lead to the development of a process in which fuel pins are pre-oxidised prior to use [14] by the addition of of 0.1vol% water to the hydrogen atmosphere during the final anneal. Doing this leads to discolouration of the fuel pins with the final colour being dependent upon the oxide thickness. Experimental work has found that an oxide layer of at least 450 nm (giving a green colour) is sufficient to prevent carbon deposition in the lab and the first trials of pre-oxidised fuel in reactors are currently ongoing.

2.4.2 Stainless Steel

Steel is one of the most useful and versatile materials known to man. With its excellent mechanical properties it has found a role in just about every sphere of human life. It does however have one significant drawback; rust. The reddish-brown tinge of corroded steels is familiar to both young and old and is often associated with an object that is old and worn out. Steel is by no means the only material to form corrosion products in air. Aluminium, another metal with a multitude of uses is often regarded as being corrosion resistant being able to spend long periods in open air with no signs of corrosion. However the truth is that aluminium is in fact far more reactive than steels. The apparent difference comes from the properties of the oxides formed when these materials corrode. When bare aluminium comes into contact with the oxygen in air it almost instantly forms an invisible layer of aluminium oxide. This oxide is tough, adherent and non-porous and is able to protect, or passivate, the surface of the metal thus preventing oxygen coming into contact with the bare aluminium preventing further corrosion. When damaged the oxide layer quickly reforms. In comparison, steel, and alloys made predominantly of iron, oxidise relatively slowly in air however the resulting Fe(III) oxides do not have the same protective effect as their aluminium equivalents. Not only is the oxide porous, allowing oxygen to continue to access the iron below but the density of rust is greatly reduced (relative to the base iron) leading to significant swelling which causes rust to fall away in large lumps, often appearing to exaggerate the level damage that has actually occurred.

The corrosion resistance of steels can however be improved by the addition of chromium. Early corrosion resistant blades found at the site of the Terracotta

Army in China have been found to have chromium coatings and in the early 19th century iron-chromium alloys were found to have some corrosion resistance, however it was not until the early part of the 20th century that the the first alloys that would be recognised as what we today call stainless steel were developed.

Today stainless steel is recognised as being an iron base alloy containing at least 10.5% of chromium. At this concentration the alloy is able to form a protecting passivated layer of Cr_2O_3 much the same as the passivated layer formed on aluminium. Modern stainless steel use a wide number of different elements altering the quantities of each gives a vast number of different stainless steel grades with different properties.[19]

Iron-phase Metallurgy In iron-carbon systems the crystal structure of the material formed is dependent on the temperature and carbon content of the alloy present. Figure 2.3a shows the basic iron-carbon phase diagram for an iron alloy containing 0-6.5% carbon at temperatures up to 1600 °C, and the phases that can be formed. For low carbon alloys at relatively low temperatures iron exists primarily as ferrite which has a body centred cubic structure (bcc) and is known as α-iron (fig. 2.4a). As this is heated the structure changes to a face centred cubic (fcc) form known as austenite or γ-iron (fig. 2.4b). Further heating creates δ-iron which once again has a bcc structure.

The phase in which an iron base alloy exists can also be altered with the addition of alloying elements other than carbon which can be seen in a Schaeffler diagram fig. 2.3b.

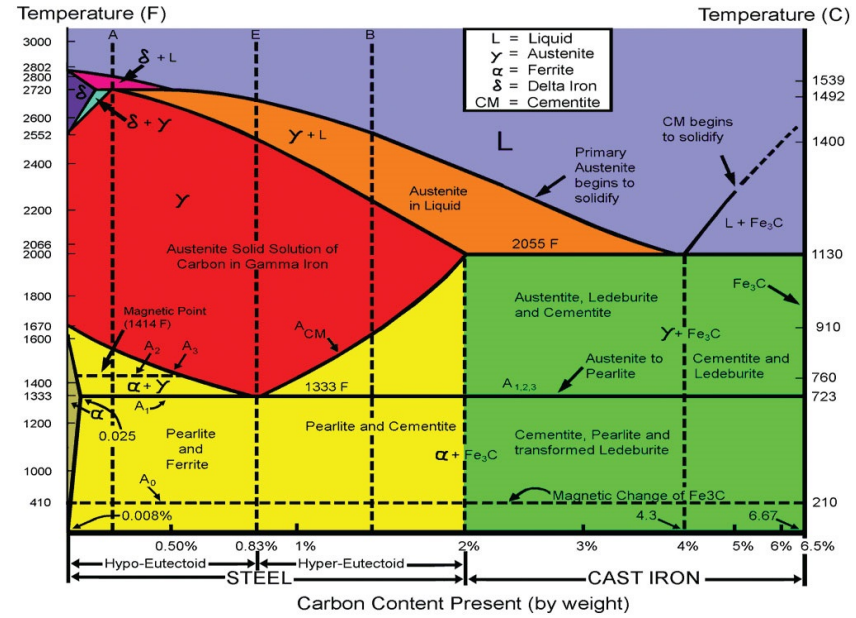

(a) Fe-C phase digram (taken from [20]).

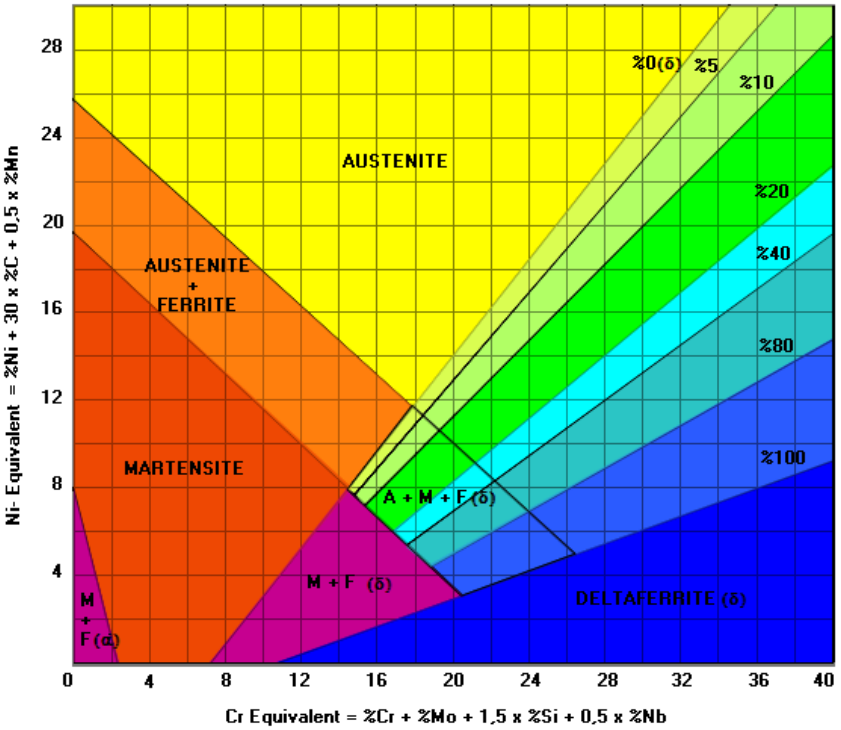

(b) A Schaeffler digram (taken from [21]).

Figure 2.3: Iron base alloy phase diagrams.

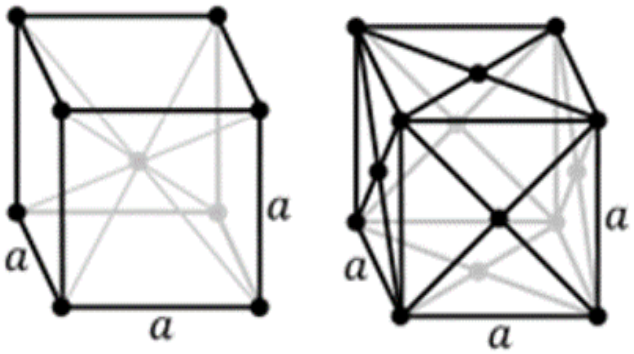

(a) Body Centred Cubic (BCC)

(b) Face Centred Cubic (FCC)

Figure 2.4: The BCC and FCC unit cells[22].

Austenitic Stainless Steel The austenitic stainless steel's contain at least 16% Cr and account for the majority of stainless steel production today as the AISI 300 series alloys are part of this group. The name comes from the austenite phase that is formed thanks to the alloys fcc structure. The fcc structure (which is only stable in iron at elevated temperatures) is stabilised by the presence of at least 8% nickel which ensures that the fcc structure is maintained at all temperatures. A number of other alloying elements can be added to fine tune the alloys properties. The elemental composition of some common stainless steels are shown in table 3.1. The two most common stainless steel's are the AISI 300 series materials which contain around 2% Mn such as 304 also known as 18/8 and 316 commonly referred to as marine which contains an additional 2% Mo for added corrosion resistance. This group also includes a number of other grades designed for use at high temperatures such as 310 which contains 25wt% Cr and 20wt% Ni.[23–25]

2.4.3 AGR Cladding

To cope with the more extreme conditions (higher temperatures and increased neutron flux) found in AGR's stainless steel was used in place of a magnesium alloy for fuel cladding in AGR's. A 20%Cr, 25%Ni, Nb stabilised austenitic alloy[26] is used which has high oxidation resistance at elevated temperatures. Nb is added to help prevent the formation of chromium since niobium carbides precipitate out

at higher temperatures than chromium carbides so the Nb in effect mops up any carbon impurities preventing chromium depletion. The full elemental composition is shown in table 3.1.

At first glance austenitic stainless steel would appear to be the ideal choice for use within a nuclear reactor being hard, strong and highly corrosion resistant over a wide range of temperatures. This is however not entirely true since the high neutron flux within a reactor leads to a number of degradation mechanisms which would not normally be expected or only be found at much greater temperatures than typical of nuclear reactors.

	wt%						ppm				
	Cr	Ni	Nb	Si	Mn	Mo	C	V	S	P	Ti
304L[27]	18.47	8.7	0.01	0.31	1.47	0.28	180	-	20	380	-
316L[28]	17.54	12.3	-	-	1.84	2.47	-	-	10	210	-
310S [29]	24.65	19.41	-	0.605	1.766	-	542	1810	15	160	100
20/25/Nb[30]	19.9	24.5	0.64	0.57	0.72	-	550	-	-	-	140

Table 2.2: Elemental composition of various stainless steels.

2.5 Reactor Damage of Stainless Steels

The following section looks at some of the degradation mechanisms that will affect stainless steel cladding while in the reactor primarily oxidation and radiation induced segregation.

2.5.1 Steel Oxidation in Carbon Dioxide

The oxidation behaviour of 20/25/Nb stainless steel in CO_2 has been studied by numerous authors a general description of which is given by Tyzac and Cowen[31]. Overall this type of steel shows an improved resistance to oxidation when used as cladding compared to 18%Cr steels such as 316 although it has been suggested that this may be due to the very tight controls used in production of fuel cladding which limits impurities rather than any significant effect of the alloying elements[31].

An early study into the structure of the oxide layer formed was carried out by x-ray and electron diffraction[32] and concluded that the final oxide product had a duplex structure consisting of an inner layer of rhombohedral Cr_2O_3 (chromia) and an outer layer of spinel oxide[1]. The rate of diffusion of cations through the Cr_2O_3 is reduced and this controls the overall rate of oxidation. The structure of the spinel oxide means that if two divalent cations replace two Cr^{3+} cations a third divalent cation must also diffuse into a cation vacancy to maintain neutral charge. Once these are filled cation movement can progress more rapidly with movement of cations through interstitial sites rather than vacancies.

The structure of these oxides has also been characterized by Laser Raman Spectroscopy[26]. This work examined oxides formed at a range of temperatures and in either CO_2 or a mixture of 4% CO, 350 vpm CH_4, 300 vpm H_2O and 400 vpm H_2 in CO_2. This work found that all oxides contained iron rich spinel oxides with the exception of those produced at 600 °C (the lowest temperature) in CO_2 where Fe_2O_3 was dominant. Raman spectroscopy showed clear peaks for the various different phases present.

It has since been shown that the oxide scale is actually of triplex form [33]. With a novel method of fractography and by combining the results of numerous other techniques Desport and Bennett were able to show that the inner chromia layer was made up of two distinct bands; an inner more porous silicon rich layer and an outer layer. It was also found that the porosity of the silicon rich layer made it brittle and that consequently it was at this point that oxide spallation would occur.

2.5.2 Effect of Irradiation on Oxidation

The effect of irradiation on the oxidation of 20/25 steel was examined by Bennett et al[34] by exposing samples to a neutron flux and fission fragments within a reactor at a range of temperatures. Comparison of the in reactor samples with unirradiated samples found that irradiation had not increased levels of oxidation by more than a factor of two which was within the limits of reproducibility. This is a contrast to work carried out by the same author on an 18/8/Ti steel which

[1] A spinel oxide is an oxide of the form $A^{2+}B_2^{3+}O_4$ where A and B are metals.

was found to have enhanced oxidation[35] upon exposure to fission fragments at 650 °C.

2.5.3 Diffusion in Metals and Radiation Induced Segregation

In all metals it is possible for atoms to diffuse, with this diffusion being highly dependent on temperature. Nevertheless at the temperatures experienced within a nuclear reactor the rate of diffusion would be expected to be sufficiently low for the detrimental effects to remain at acceptable levels. However the high neutron flux within a reactor is able to greatly accelerate the rate at which diffusion is possible, and diffusion is the cause of several detrimental mechanisms.

Within metals diffusion can occur along one of two pathways. Small atoms such as H, He, B, C and O are able to take an interstitial position within the metal matrix while larger atoms (Fe, Cr, Mn etc) move by jumping from vacancy to vacancy[36]. When exposed to a high neutron flux the number of vacancies is drastically increased and consequently the rate of diffusion is also increased. This increased rate of diffusion leads to a number of degradation mechanisms the most important of which (in the current discussion) is radiation induced segregation

Diffusion normally leads to the reduction of a concentration gradient with atoms moving from areas of high concentration to low. When radiation is present the opposite can occur. Vacancies tend to migrate to grain boundaries which act as a vacancy sink. The rate at which atoms diffuse depends on the strength with which they bind to vacancies. Atoms such as nickel bind tightly to vacancies and consequently diffuse quite slowly but with the concentration gradient. Chromium on the other bonds weekly to vacancies and consequently tend to diffuse away from vacancies at a high rate. Since the vacancies are moving towards the grain boundaries chromium atoms (or other atoms that bond weekly to vacancies) tend to diffuse away from the grain boundaries against the concentration gradient leading to a localised reduction of chromium. This process is known as Radiation Induced Segregation[37, 38] and has been found to be most serious between 400°C and 420°C [39]. Temperatures in this range are experienced by the cladding of the first two elements on each stringer (at the base of the core) [40].

While radiation induced segregation is the most important degradation mechanism in the current discussion, other diffusion/vacancy controlled degradation mechanisms can also occur. Void swelling takes place when vacancies congregate together and fill with H and He (from (n, p) and (n, α) reactions) leading to swelling[38]. Grain coarsening occurs when diffusion causes smaller grains to shrink and larger grains to grow in order to minimise surface area making the material thermodynamically more stable. This can lead to brittle failure of a material. Finally creep is accelerated since the high neutron flux will cause additional point defects which combine to form extra dislocations where creep can occur.

2.6 Corrosion and Oxidation

Upon removal from a nuclear reactor spent nuclear fuel contains a large quantity of decaying fission products which produce a significant amount of heat as well as radiation. Traditionally water storage has been utilised to store this fuel since the water is able to both disperse decay heat and provide radiation shielding. While stainless steel is often used in place of carbon steel due to its corrosion resistance it does not have complete corrosion resistance. This section provides a general introduction to corrosion, how this is affected by radiation and the most common forms of corrosion found to affect stainless steel.

2.6.1 Basic Corrosion Reaction

Corrosion is the common name given to the oxidation of metals (most often) by their environment, with the most common example being the rusting of iron and steel. In this document the term oxidation is used to refer to oxidation in a dry environment while the term corrosion is used to refer to oxidation in an aqueous environment. The corrosion reaction is a redox process in which the metal is oxidised according to

$$M \longrightarrow M^{n+} + ne^{-} \tag{2.2}$$

alongside the cathodic reduction reactions

$$O_2 + 4e^- + 2H_2O \longrightarrow 4OH^- \tag{2.3a}$$

$$2H^+ + 2e^- \longrightarrow H_2 \tag{2.3b}$$

$$H_2O + 2e^- \longrightarrow 2OH^- \tag{2.3c}$$

In aerated conditions eq. (2.3a) is the dominant reduction reaction along with eq. (2.3b) in acidic conditions or eq. (2.3c) in neutral or alkaline conditions. For iron or carbon steel the primary oxidation reaction is

$$Fe \longrightarrow Fe^{2+} + 2e^- \tag{2.4}$$

followed by the redox reaction

$$4Fe^{2+} + O_2 \longrightarrow 4Fe^{3+} + 2O^{2-} \tag{2.5}$$

leading to the production of hydrated iron oxides which are less dense than iron and spall away exposing fresh metal to corrosion. As discussed above alloys of iron with at least 10.5wt% Cr are known as stainless steels and these quickly form a thin layer of Cr_2O_3 which protects the metal from further corrosion under most conditions. Nevertheless stainless steel can still be susceptible to certain forms of corrosion, particularly localised corrosion, the most common examples of which are summarised below.

Galvanic Corrosion

Corrosion is a redox reaction and can therefore be influenced by the flow of electrons. Galvanic corrosion takes place when two dissimilar metals are in contact producing a potential difference between them leaving one metal as an anode and more susceptible to corrosion.

Crevice Corrosion

Crevice corrosion occurs in an aqueous solution when a small gap or crevice produces an area of stagnant solution. Corrosion initially takes place on metal both within the bulk solution and the crevice leading to the creation of both positive metal ions and OH^-. In the bulk solution oxygen is able to diffuse in as oxygen is used up, however, within the crevice oxygen diffusion is prevented leading to a build up of M^+. To maintain charge neutrality Cl^- (which is more mobile than OH^-) diffuses into the gap creating a more aggressive atmosphere in part by the formation of complex ions which produce H^+ according to eq. (2.6) and a subsequent reduction in pH and exacerbation of the problem.[41]

$$M^{n+} + H_2O \longrightarrow MOH^{(n-1)+} + H^+ \tag{2.6}$$

Pitting

Pitting is similar to crevice corrosion in that once initiated corrosion is accelerated by stagnant conditions however the initiation of these conditions comes from metallurgical factors rather than differences in oxygen concentration. Numerous mechanisms have been proposed but the basic principle suggests that a small local anode is created as a result of a scratch or impurity at which the initial rate of corrosion can be high leading to the formation of the initial pit in which stagnant conditions can develop.[41]

Intergranular Corrosion

Intergranular corrosion (IGC) is a form of localised corrosion that takes place at grain boundaries. This is discussed in greater detail in section 2.6.3.

2.6.2 Radiation Corrosion

Numerous authors[42–44] have studied the effect of radiation on the corrosion of stainless steel (and other metals) in aqueous media with the general consensus being that the corrosion rate is generally increased as a result of the production of radiolysis products such as hydrogen peroxide and OH and HO_2 radicals.

However, in aqueous solution Byalobsheskii[42] has reported certain circumstances in which radiation can reduce the rate of corrosion. It was found that crevice corrosion could be inhibited in aqueous solution as a result of ionising radiation acting as an oxidant which creates trivalent iron and chromium which act as oxidizing agents in place of the deficient oxygen. Similarly it was shown that the corrosion of a stainless steel alloy in 65% nitric acid could be reduced with the addition of radioactive Cs-137 but not by other non radioactive Cs isotopes. This was put down to certain radiolysis products acting as reducing agents and shifting the potential of the system to the passivated region.

Atmospheric corrosion (corrosion in air or other gaseous medium) has also been shown to increase under irradiation[42, 45] although overall corrosion rates remained low. Byalobzheskii[42] also discovered unexpected results when corroding stainless steel in a humid environment exposed to radiation. An experiment was designed in which two metal plates were placed in a chamber with a humid atmosphere and exposed to a radiation source. One plate was exposed directly to the source, the second was partly shielded with the other plate. The shielded plate was found to have a greater corrosion rate than the non-shielded plate. It was established that this was due to the heating effect of the radiation on the unshielded plate which prevented the formation of the moisture which formed on the shielded plate and encouraged corrosion.

In the United States a phenomenon known as “hot cell rot” where fuel cladding falls apart upon handling has occurred when stainless steel clad fuel has been left for a period of time in air[46] and anecdotal evidence suggests that a similar phenomenon has taken place with AGR fuel left in the hot cells at Sellafield.

2.6.3 Intergranular Corrosion

IGC (also known as intergranular attack, IGA) is a form of corrosion that takes place at the grain boundaries as a result of chromium depletion and is often aggravated by stresses leading to intergranular stress corrosion cracking (see section 2.6.7). In AGR fuel chromium depletion is the result of radiation induced segregation as described above, however the phenomenon is common in many metals without the influence of radiation. In these cases chromium depletion is the

result of a process known as sensitisation. This occurs when stainless steel is held at elevated temperatures (within the range of approximately 425 °C to 875 °C[47]) for prolonged periods. It is primarily the result of impurities, normally carbon, which tend to migrate to grain boundaries where they form covalently bonded compounds such as chromium carbides. These precipitate leading to chromium depletion in the grain boundary region, locally depleting the chromium and leaving the alloy more susceptible to corrosion[1]. The degree of sensitisation is influenced by both increased temperature (within the sensitisation range) and increased time although extended time frames particularly at high temperatures can lead to healing as chromium diffuses from the centre of the grains to the boundaries.

While the method of chromium depletion in unirradiated samples may differ the basic corrosion mechanism is much the same. Countless authors have studied IGC in a variety of austenitic stainless steel using a number of different methods and fig. 2.5 shows some examples [48, 49]. Despite using different methods, both chemical and electrochemical, these examples clearly show the key feature of IGC with corrosion occurring primarily at grain boundaries.

[1] All alloys have a critical time for maximum sensitisation. Beyond this time chromium is able to diffuse back to grain boundaries from within grains leading to some healing and reduced sensitisation however the time frames required for this are extremely large(∼80,000 hours) and are not considered relevant in this discussion.

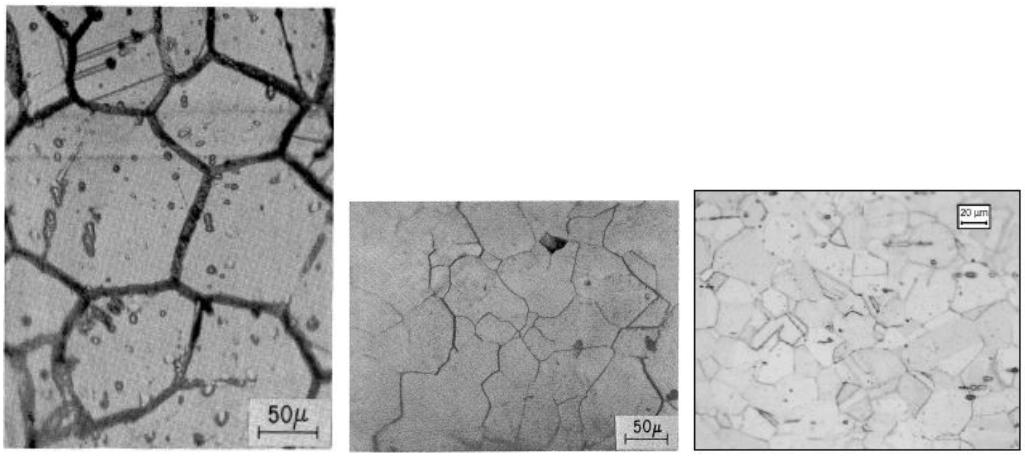

(a) [49] (b) [49] (c) [48]

Figure 2.5: Examples of IGC.

While time and temperature are the underlying causes of IGC as a result of sensitisation it has also been shown that among other things alloy composition[50, 51], impurities[49] and pretreatment[51] all influence the degree and rate of IGC.

2.6.4 IGC Testing

ASTM standard A262-Standard Practices for Detecting Susceptibility to Intergranular Attack in Austenitic Stainless Steels[52] is the main industry standard for assessing IGC and almost all non electrochemical methods for assessing IGC resistance of austenitic stainless steel use one of these tests (or a derivative thereof). The standard consists of six different test methods. ASTM-Practice A also known as the oxalic acid etch test is an electrochemical polarisation test and is used to carry out a quick initial assessment of the samples susceptibility to IGC. The results of this test will then recommend the use of one of the other five tests; practice B-the Streicher test (boiling ferric sulphate and 50% sulphuric acid), practice C-the Huey test (boiling 65% nitric acid), practice E-the Strauss test (boiling copper-copper sulphate-16% sulphuric acid) and practice F (boiling copper-copper sulphate-50% sulphuric acid).

The most severe of these tests (and the only test recommended for use with AISI 310[52]) is practice C-the Huey test. This test involves boiling samples in 65% nitric acid for a total of 240 hours with the samples being removed from the acid every 48 hours, weighed and returned to fresh acid. This method (or derivations thereof) has been used by a number of authors to test the corrosion resistance of stainless steel samples[27, 49, 51, 53–55].

Tavares et al [29] have investigate sensitisation and microstructure in 310 stainless steel. Their work sensitised samples at 600 °C to 800 °C for times of 4, 24, 100 and 210 hours. Corrosion testing was carried out electrochemically. This work found greater σ phase formation at longer sensitisation times and temperatures although the samples held at higher temperatures also show considerable healing.

2.6.5 Reduction of Nitric Acid

The basic mechanism by which IGC occurs has been examined in detail and like all corrosion types is the result of a redox reaction. The oxidation reaction is generally that of the metal, normally the iron matrix but in stainless steel the outer Cr_2O_3 forms a protective layer. In highly oxidising conditions it is possible for an additional oxidation step to be present in which the insoluble Cr(III) (as Cr_2O_3) becomes soluble Cr(VI) (as $Cr_2O_7^{2-}$) removing the protective layer[56].

The key reduction reaction in the process is based on the reduction of nitric acid according to

$$NO_3^- + 3H^+ + 2e^- \longleftrightarrow HNO_2 + H_2O \tag{2.7}$$

While it was well understood that this mechanism was autocatalytic and that the nitric acid molecule was not the electroactive species the exact nature of the mechanism was unclear for many years.

Work by Balbaud et al[57] has now shown that nitrous acid is the electroactive species and is reduced according to the charge transfer step

$$(HNO_2)_{ads.} + H^+ + e^- + s \longleftrightarrow (NO)_{ads.} + H_2O \tag{2.8}$$

where 's' is a free adsorption site. The heterogenous reaction

$$(HNO_3) + NO_{ads.} \longleftrightarrow (HNO_2) + (NO_2)_{ads.} \tag{2.9}$$

then regenerates the electroactive species. The final reaction

$$(HNO_3) + (HNO_2)_{ads.} + 2s \longleftrightarrow 2(NO_2)_{ads.} + H_2O \tag{2.10}$$

also takes place.

At concentrations below 6 M eq. (2.9) is slow leading to a build up of NO from eq. (2.8). Also at concentrations below 8 M NO_2 is unstable so eq. (2.10) is drawn to the left favouring the build up of HNO_2.

Higher HNO_3 concentrations make eq. (2.9) fast and NO_2 is now stable and formed preferentially.

Overall and despite the fact that a higher HNO_2 concentration makes the solution more reducing, an increased HNO_2 concentration is preferable since it increases the rate of reduction of nitric acid (eq. (2.7)), increasing the corrosion potential of solution and hence the overall corrosion rate. Consequently in this solution it is preferable to retain the reduction products (HNO_2 and NO_2).

2.6.6 Nitric Acid with Oxidising Ions

The Huey test is the most severe of all the tests described in ASTM A262, and while it has been shown to be effective and beneficial in many cases there are occasions where the use of boiling nitric acid alone is not sufficient or representative, either because of the times involved or because of other constituents that may be present. Consequently the Huey test has been adapted by several authors by the addition of oxidising cations such as Cr(VII) and Ce(IV)[48, 50, 58].

The thermodynamics of a redox reaction is dependent on the overall redox potential of the reaction according to

$$OX + RED \longleftrightarrow RedPot \tag{2.11}$$

In pure nitric acid the reduction reaction, as described above is eq. (2.7) which has a redox potential $E^{\circ}{}_{25^{\circ}C} = 934mV/SHE$. However when oxidising ions such

as Cr(VI) are added the reducing role played by eq. (2.7) is replaced by that of eq. (2.12).

$$\begin{aligned} Cr^{6+} + 3e^{-} &\longleftrightarrow Cr^{3+} \\ E^{\circ}{}_{25^{\circ}C} &= 1232mV/SHE \end{aligned} \tag{2.12}$$

which has a greater redox potential and is therefore more aggressive.

2.6.7 Stress Corrosion Cracking

According to the National Association of Corrosion Engineers (NACE) "stress corrosion cracking (SCC) is the cracking induced from the combined influence of tensile stress and a corrosive environment" and "the required tensile stresses may be in the form of directly applied stresses or in the form of residual stresses" [59]. The exact mechanism by which SCC takes place is uncertain but several methods have been suggested however the model favoured for intergranular cracking of sensitised stainless steels is the slip dissolution model. In this model oxides layers form on the outside surface of a crack however at the tip this oxide is fractured due to plastic strain leading to localised anodic dissolution before the film repairs and the cycle repeats[60].

As with IGC ASTM standards exist to allow testing of susceptibility to SCC and in this case two standards are of particular relevance. ASTM G38 - Standard Practice for Making and Using C-Ring Stress-Corrosion Test Specimens[61] discusses the production of so called c-rings which allow for the controlled induction of stress within the sample (fig. 2.6. These allow stress or strain to be introduced into a sample in a controlled and repeatable manner.

ASTM G36 - Standard Practice for Evaluating Stress-Corrosion-Cracking Resistance of Metals and Alloys in a Boiling Magnesium Chloride Solution covers the chemical process that leads to the cracking[62]. G36 is far less prescriptive than ASTM A262 (IGA test) and allows for the solution concentration and test time to be chosen by the user. This is likely in part due to that fact that there is some disagreement about the boiling point of magnesium chloride solutions[63] however a 42wt% solution is commonly used[64–66].

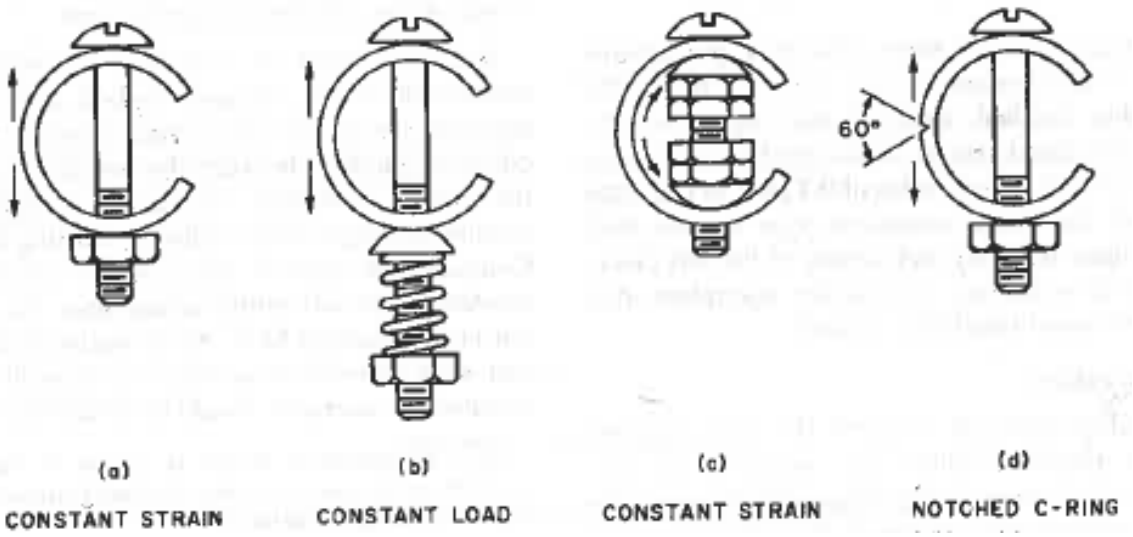

Figure 2.6: C-Rings used for ASTM testing for SCC (taken from ([61]).

2.6.8 Long Stored Fuel Condition

The cooling ponds at Sellafield were initially filled with demineralised water, however in the early years of operation (from 1978) it was found that failures were taking place (see fig. 2.7)[67] leading to the release of soluble caesium and other radionuclides. An investigation into this found that such failures were due to intergranular attack combined with stresses within the cladding leading to intergranular stress corrosion cracking (IGSCC). In demineralised water failures would occur within 200 days [67]. Testing showed that 50% of pins from elements 1 and 2 were found to fail by IGSCC[8, 67].

In order to address this problem a series of corrosion tests were undertaken in the early 1980's to find a corrosion inhibitor and sodium hydroxide (caustic) was identified as most suitable[67]. This led to the dosing of the AGR storage pond to pH 11.4 since when there have been no reported failures. Up until 1993 post storage examination (post storage examination) was carried out regularly and found evidence of limited IGA [40]. Since then there has been only limited post storage examination and that has found no significant degradation beyond that found upon removal from the reactor[8].

The crack seen in fig. 2.7 is in the region of 50 μm in width however there is

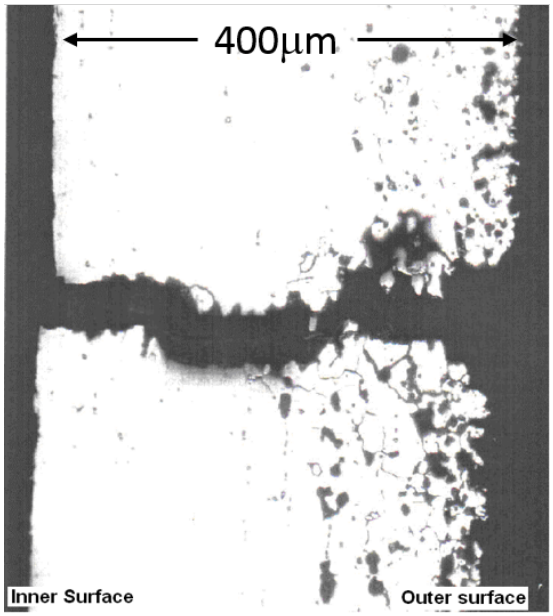

Figure 2.7: Failed cladding pre caustic dosing with significant IGA on the outer surface. The crack width is approximately 50 μm (taken from[8]).

some anecdotal evidence that smaller cracks may exist.

2.6.9 Fenton's Reaction

Fenton's reaction is the catalytic breakdown of hydrogen peroxide by Fe(II) and Fe(III) to form aggressive hydroxyl and hydroperoxyl radicals as seen below[68];

$$Fe^{2+} + H_2O_2 \longrightarrow Fe^{3+}HO^{\bullet} + OH^{-} \tag{2.13a}$$

$$Fe^{3+} + H_2O_2 \longrightarrow Fe^{2+}HOO^{\bullet} + H^{+} \tag{2.13b}$$

For Zircaloy and aluminium clad fuels aggressive radicals are can only be formed by radiolysis. For stainless steel clad fuels, the oxide of which contains Fe(II) and Fe(III) there is the potential for higher concentrations of radicals than would be found in a dry store containing Zircaloy or aluminium clad fuels as even if the initial quantities of water were similar. This may therefore mean than a dry store for stainless steel clad fuel may require a more stringent level of dryness than dictated by ASTM C-1553. There is however no firm evidence of this and

2.7 Analysis Techniques

The following section looks at some of the techniques that have been used to analyse the samples produced in Part 1 of this thesis. It includes a brief description of the technique and in some cases some of the data that has previously been found with them.

2.7.1 X-Ray Photoeloectron Spectroscopy

In general the area of interest when it comes to the analysis of oxide layers is the distribution and concentration of metal atoms and in this case almost all spectroscopy techniques are suitable. In some cases it is necessary to know about the presence of water or hydrated oxides in which case x-ray photoelectron spectroscopy (XPS) is the most useful technique. XPS uses an x-ray to eject an electron from a surface the energy of which can be detected. The general energy of the electron is dependent on the atom from which it is ejected however this varies slightly depending on the speciation of the atom as can be seen in fig. 2.8. While the various peas will all overlap it is possible to use peak fitting to differentiate between oxygen in O^{2-}, OH^{-} and H_2O.

When differentiating between species it is important to consider not only the peak position but also the peak shape and the full width half maximum (FWHM)[1]. While some elements such as oxygen produce symmetrical peaks others such as the transition metals have asymmetric peaks all of which are slightly different. Furthermore the FWHM of a species is normally quite specific and is also used to confirm identification.

The presence of unpaired electrons can complicate this further by leading to what is known as multiplet splitting which causes the same energy level to produce electrons of slightly different energy levels and therefore multiple closely overlapping peaks can be seen rather a single peak from a single species. Biesinger et al[69] have published details of the peak positions, proportions and FWHM for a number of transition elements as metals and a range of oxides and hydroxides which can allow precise identification.

[1]The full width half maximum, commonly abbreviated to FWHM is commonly used in spectroscopy to analyses peaks. It refers to the width of a peak at half of its maximum height

The number of peaks produced by an element varies depending on the number of electrons and electron shells and in some cases a single shell can produce two similar peaks of different magnitude. In some cases the spacing between the two peaks is highly dependent on the bonding. For instance calcium typically produces peaks from the 2p electron shell and when bound to oxygen and carbon in calcium carbonate the two peaks are separated by 3.5 eV[70].

As a further advantage XPS can be used for depth profiling either by argon sputtering of the surface during the XPS measurement or changing the collection angle (and therefore the distance the electron must travel since this distance is finite). Numerous authors have therefore used XPS to analyse the oxide layers formed on stainless steel.

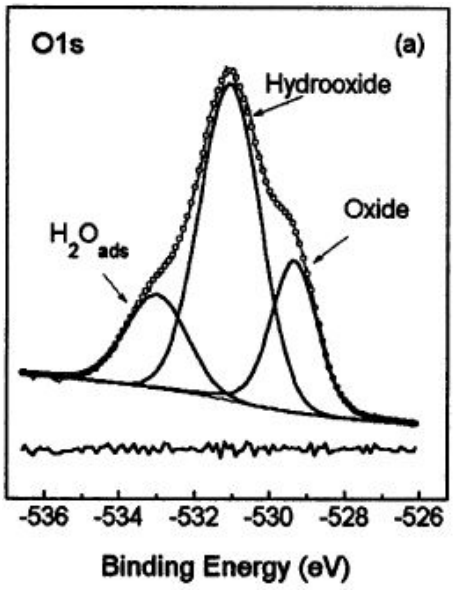

Figure 2.8: XPS plot of an O1s atom in a stainless steel oxide showing energy differences between oxygen from water, hydroxyl and oxide (taken from [71]).

Jin and Atrens[72] oxidised an 18-12 steel in NaCl and found the oxide layer to have a triplex form consisting of a hydrated outer layer, a middle layer of Fe and Cr oxides and an inner metallic layer rich in Ni. The transition from the hydrated outer layer to the middle layer is gradual and the relative concentrations of oxidised Cr and Fe vary being predominantly oxidised Fe with oxidised Cr and and metallic Fe in the outer part and inner part being mainly oxidised Cr.

Overall Cr/Fe ratios vary depending on immersion time with longer immersion times favouring higher Cr concentrations. Comparison of oxide films formed in NaCl and air show slight variations depending on exposure time. This work also found that varying the time the samples spent in contact with air prior to the oxidation in solution changed the overall oxide composition suggesting that the makeup of an oxide was dependent on the whole life of the sample rather than the final step alone, however this became of less importance after longer immersion times.

In electrochemical corrosion work[71] using 316L stainless steel in NaOH Stefanov et al found that the oxide layers had a duplex character consisting of a thin outer layer of nickel hydroxide and an inner layer of nickel oxide. Heating at 350 °C quickly converted the outer hydroxide layer to oxide thinning this layer in the process. In contrast the same author[73] found that immersion of 316L in a solution of CrO_3 in H_2SO_4 produced a duplex oxide consisting of a thin hydrated outer layer of chromium hydroxides and oxyhydroxides and bound hydroxyl and water and an inner layer of predominantly chromium oxide (Cr_2O_3). It was noted that after standing in air or a vacuum the quantity of water in the hydrated layer was found to be reduced.

These are just a few examples of work characterising stainless steel oxides nevertheless they clearly show that the composition of the oxide formed on a stainless steel can vary greatly with time, oxidising media and metal composition although the final conditions appear to be dominant in determining recorded composition.

2.7.2 Electron Microscopy and Energy Dispersive X-Ray Spectroscopy

There are two distinct forms of electron microscopes; transmission electron microscopes (TEM) and scanning electron microscopes (SEM). As the name suggests a TEM involves passing a beam of electrons through a sample causing them to scatter. These scattered electrons can then be constructed into an image. In order for the electrons to pass through the sample the technique requires the use of thin samples which are effectively transparent to electrons and gives a sum nanometer resolution. TEM samples are often produced by cutting a wafer of material out

of a larger sample. A layer of predominantly platinum is layered onto the sample to act as a strap with which the samples can be handled. A focused ion beam can then be used to cut around the sample to leave a wafer of material which is transparent to electrons.

An SEM uses a beam of electrons scanned across the surface of a sample with detectors creating an image from the electrons that are returned. In backscatter mode the detected electrons are high energy electrons from the original beam which are reflected. In secondary electron mode the returned electrons are low energy electrons that are ejected from the sample by inelastic collisions with the electron beam.

A variation of these is the STEM which uses a focussed beam of electrons as in an SEM which are passed through a sample as in a TEM.

Energy Dispersive X-Ray Spectroscopy (EDX or EDS) is a spectroscopic technique that provides elemental information by firing electron beam into a sample and measuring the energy of the X-rays emitted. Since it requires the use of an electron beam they are commonly fitted to SEM and STEM.

Authors such as Maurice et al.[74] have used electron microscopy in conjunction with XPS to show the presence of a duplex oxide layer containing an inner passive hydroxide layer while Mayuzumi et al.[51] have used SEM, TEM and EDX to show that cold working of stainless steels mitigated corrosion of solution treated stainless steel. Electron microscopy has also been used in conjunction with X-ray diffraction to show that pitting preferentially takes place in dendrites of lower Cr content in some laser cladded stainless steel alloys[75], while radiation induced segregation has been observed in stainless steel alloys using STEM and EDX[76].

2.7.3 Thermogravimetric Analysis

Thermogravimetric analysis (TGA) is a thermal analysis technique in which a microbalance within a furnace is able to measure mass change as a function of temperature. The technique can be used to monitor the thermal stability of materials and to calculate the mass of water held within a hydrated compound. The technique is normally carried out under a flow of gas and this can be monitored by online techniques such as mass spectroscopy. The technique is often coupled

with direct scanning calorimetry (DSC) which measures the temperature of the sample in the crucible along with the temperature of an empty crucible and uses the temperarture difference to calculate the specific heat capacity of the sample.

2.7.4 Computed Tomography

Computed tomography (CT)) is an imaging technique used to produce an internal image of a solid object and is most commonly used for medical applications but small scale machines with high resolution (micron scale) are available in a technique known as micro CT.

A tomograph is a cross sectional image of solid body and with the advent of computers it was possible to stitch multiple cross sectional images together to form a 3D image of a solid object. Cross sectional images or slice is produced by taking a series of X-rays while the sample is rotated with the resolution increased by increasing the number of images taken in each slice, and by using thinner slices. The x-ray attenuation is dependent on the density and atomic number of the element.[77]. Synchrotron radiation can also be used.

The technique has been used to study localised corrosion often in real time. Horner et al[78] have used X-ray tomography to study the growth of pits in stainless steel and how stress corrosion cracks will initiate from the pit wall while Babout et al[79] studied the interaction between the microstructure of stainless steel and crack propagation. Synchrotron radiation has been used by King et al [80] to study IGSCC and found that sensitization resistant grains are able to improve resistance to IGSCC.

2.8 Summary

ASTM standard C-1553 is an important document in relation to the drying of spent nuclear fuel. It identifies and defines several different “types” of water” relevant to drying spent nuclear fuel. The two of concern are bound water (both chemisorbed and physisorbed) and trapped water. As a result it is essential that both of these areas are addressed in the drying work that will be carried out.

Historic experience has shown that fuel failures have been as a result of IGSCC and such failures will almost certainly lead to the flooding of fuel pins. While the use of sodium hydroxide dosing has reduced failures, since SCC if it occurs is highly likely to lead to trapped water it is necessary for the drying tests to consider water trapped within cracks so there is a requirement to produce cracks which have a similar morphology to those seen in failed fuel.

The other contributory factor to failures, intergranular corrosion, is also an area that needs to be considered. Not only is it possible that water may become trapped within the gaps left at grain boundaries but some of the corrosion products can potentially be hydrated and consequently bound water is a possibility. It is not however clear how much of an issue the water associated with IGSCC may so it is felt that work is required to assess this. Work should also be carried out to assess whether bound water is likely to be a concern as result of other corrosion phenomenon such as pitting which is one of the most common types of corrosion to affect stainless steel particularly when exposed to high levels of chloride. Similarly some work should be done to assess whether the corrosion products formed in NaOH may be sufficiently hydrated to be of concern.

The use of carbon dioxide coolant results in significant quantities of carbon depositing on the fuel surface. It is also essential that it is established whether the quantities of water associated with this are of concern.

Thermogravimetric analysis is a technique which is believed to be suitable to assess whether the quantities of water associated with various samples are likely to be significant enough to require consideration during drying tests. Since the technique relies upon the measurement of mass changes alone it will not be able to differentiate between bound and trapped water, let alone between the two different types of bound water discussed in table 2.1.

There is however a hope that it will be possible to make this distinction with XPS. The extreme vacuum required by XPS will remove any trapped water that is not removed from a sample by evaporation in the atmosphere prior to testing. The XPS data itself should be able to identify the different species of water allowing physisorbed and chemisorbed water to be identified.

Chapter 3

Experimental Work

3.1 Introduction

As discussed in chapter 1 the main aim in this piece of original research was to produce a method of safely drying spent nuclear fuel ready for interim dry storage. Before drying tests could be carried out it was felt that it was necessary to develop samples that were suitably representative of those likely to be removed from long term pond storage, however since little post storage examination has taken place the condition of such fuel is not known to any degree of certainty. Consequently a number different samples will be produced that replicate some of the key features that are possible and may impact drying.

Table 2.1 shows the different "types" of water that are of concern when drying spent fuel namely bound and trapped water. For bound water the key factor would seem to be the composition of the oxide formed, how much water is associated with this and how easily it can be removed. It is clear from the literature that the composition of an oxide layer is dependent on numerous factors including, the corroding/oxidising media used, the time and temperature at which the corrosion took place and the composition of the alloy itself. It has also been shown that the presence of radiation has an impact although it is unclear exactly what that is. Consequently it is hard to accurately predict the composition of oxides from these factors alone. What has however been observed from examinations of failed fuel is that the few failures that have occurred have been as a result of IGC and

efforts will therefore be made to ensure that samples with clear evidence of IGC are prepared.

Following the early failures of AGR cladding as a result of IGC the preferred storage method has been demineralised water dosed to pH 11.4 with sodium hydroxide (caustic dosed). This is therefore one factor that is known. There was therefore a set of samples that was treated in a way that it is hoped mimics long term (>25 years) storage in such conditions.

Trapped water is a concern in the case of fuel pins that have become waterlogged during long term pond storage due to the presence of pinholes or microcracks. In such a scenario the water that had seeped into a pin over the course of many years under a hydrostatic pressure would need to be removed in much shorter timescales (tens of hours or less). Micrographs of failed fuel have shown evidence of through cladding IGSCC and as such there was a need to produce a number of samples with similar cracks so that the ability to remove water through such cracks could be examined.

This section covers the experimental methodology that was used in producing and characterising samples to assess whether the presence of bound water is a concern and also producing cracked samples for later drying tests.

3.2 Test Materials

Initially two types of stainless steel were used in preparation and characterisation work; AISI 310 stainless steel (referred to as 310) and samples of real fuel cladding (referred to as 20/25 or cladding). The composition of these two materials is shown in table 3.1. Two materials were used as access to cladding was initially limited. The 310 alloy was chosen as it is the closest common alloy in terms of composition. The key difference is the niobium found in cladding. Since in irradiated material sensitisation takes place as a result of RIS the use of thermally sensitised 310 may be regarded as similar to RIS affected 20/25.

The X-ray fluorescence (XRF) analysis shown in table 3.1 indicates that the cladding contains 2.8wt% aluminium. According to the literature the 20/25/Nb steel used for AGR cladding does not contain aluminium and the XPS and EDX data presented later shows no evidence of aluminium. The data shown was the

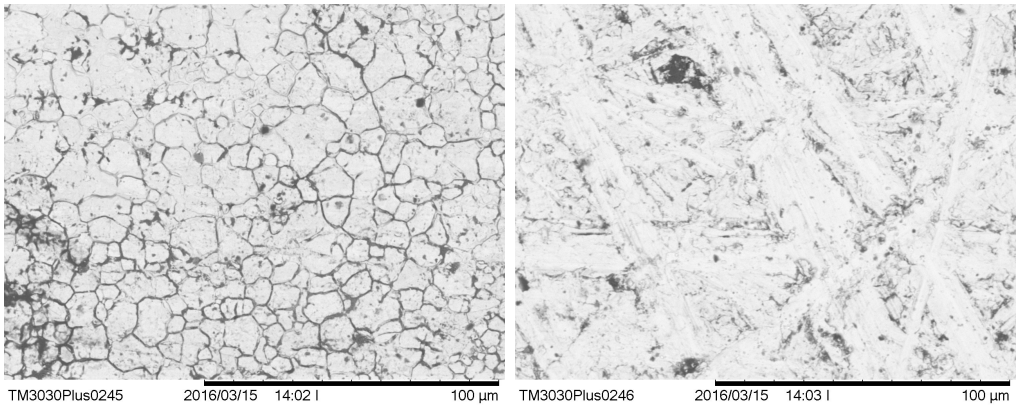

(a) Side A. (b) Side B.

Figure 3.1: SEM Images of as received 310 stainless steel prior to treatment.

the second attempt since the data was being collected with a new machine with which the operator was not yet entirely familiar and the first set of data was clearly wrong. It is therefore believed that the presence of aluminium is an error due to either mis-calibration or potentially a misalignment that has allowed some of the aluminium sample holder to be analysed.

	wt%							ppm			
	Fe	Cr	Ni	Mn	Nb	Al	Si	Cu	Mo	V	Co
20/25	bal.	20.3	22.6	0.8	0.8	2.8	0.55	0	0	0	0
310	bal.	23.8	18.9	1.1	0.0	0.0	0.42	1615	1161	1019	1830

Table 3.1: Composition of sample materials found by XRF.

The 310 samples used were in the form of 0.9 mm plate obtained from Goodfellows Metals Ltd which had been laser cut into 6 mm diameter discs. Figure 3.1 shows SEM images of the metal surface in the as received state. It can be seen that there is a difference in the surface between the two sides with side A showing evidence of grain boundaries. These differences are assumed to be a result of the rolling process.

Real cladding samples were obtained from an unirradiated AGR fuel pin donated by the National Nuclear Laboratory (NNL). AGR fuel pins are approximately 1 m long stainless steel tubes. The pins begin life as smooth walled tubes

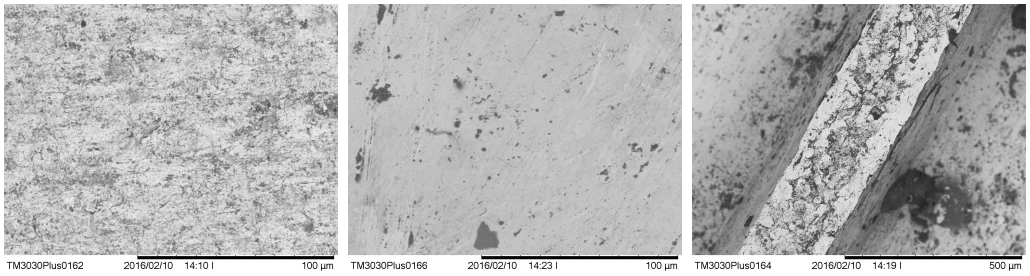

(a) Inner surface (b) Outer Surface (c) Rib

Figure 3.2: SEM images of as received 20/25 stainless steel samples prior to any treatment.

produced by cold drawing which are machined to leave helical ribs. After machining the inner diameter of the pin is approximately 14.5 mm, the wall thickness is around 400 microns and the rib top is around 250 microns wide.

Figure 3.2 shows SEM images of the three different areas of the as received material; the inner surface (inside of the tube), the outer surface produced by machining and the top of the rib. The outer surface appears to have the smoothest finish although machining marks can be seen running parallel to the rib, while the inner surface and rib top both appear rougher however there are no signs of grain boundaries as with the 310 samples.

Real fuel cladding was used in two ways; in some cases small rectangular samples of material were simply cut from the fuel pin using tin snips while in other cases short intact sections of tubing were cut using aluminium oxide cutting discs.

3.3 Accelerated IGC

As described above the need to induce IGC in stainless steel samples was regarded as crucial and the first work concentrated on this. Initial tests were carried out using samples of 310 stainless steel with 20/25 being used once the effectiveness of the method had been confirmed.

3.3.1 Methodology

The standard IGC test for 310 stainless steel described in ASTM A-262 is Practice C-the Huey test and requires holding samples in boiling 65% nitric acid for a period of 240 hours. A review of the literature found that such a test could be accelerated with the addition of oxidising ions such as Cr(VI). As part of an unpublished masters project it was established that the optimum conditions for IGC of a 310 alloy required 65% nitric acid with 0.1% Cr(VI) in the form of potassium dichromate. Holding samples in this boiling solution for thirty minutes led to clear IGC but minimal grain dropping.

The ASTM guide also provides a standard equipment setup for carrying out such tests however as discussed in chapter 2 the addition of oxidising ions changes the chemistry and the requirement to retain reaction products changes. Consequently the corrosion reaction was carried out in a rotary evaporator at atmospheric pressure. This allowed the reduction products (HNO_2 and NO_2) to escape while limiting overall evaporation.

In this work samples were introduced to a cold acid solution and raised to boiling point before rinsing in demineralised water. The time from addition to cold acid to removal and rinsing was forty minutes. PTFE boiling chips were also added to ensure boiling as early tests found failure to do so greatly reduced the corrosiveness of the solution (no IGC observed).

A second factor that influences a samples resistance to IGC is the degree of sensitisation. This was investigated at this time. All 310 samples tested were first heated to 1050 °C for 40 minutes before quenching in water. Samples were then sensitised at temperatures of 600 °C, 650 °C, 700 °C, 750 °C and 800 °C for 4, 24, 100 and 210 hours. Despite the fact that annealing and sensitisation took place in an argon atmosphere a significant scale developed on the surface so after sensitisation the samples were polished to a P2500 grit finish prior to rinsing in acetone and distilled water.

Samples of 20/25 were also tested in the same solution however these were tested in the as received (as received) state.

Samples were visually examined using a Hitachi TM3030 Plus Tabletop SEM. Images were taken in backscatter mode with an energy of 5 kV. This machine and

these conditions were used for all SEM images in this document unless otherwise stated.

3.3.2 Results

Figure 3.5, fig. 3.6, fig. 3.7, fig. 3.8, andfig. 3.9 show SEM images of the 310 samples tested. The degree of sensitisation was judged qualitatively by analysis of the images, with greater sensitisation indicated by greater IGC. The images show that it is hard to give one "ideal" set of conditions since similar results are found for various combinations however the best results appear to between 4 and 100 hours at 650°C at higher temperatures and longer times there appears to be less sensitisation probably due to healing (the diffusion of chromium back to the grain boundaries from the grain centre) while at 600°C for 4 hours there has not been sufficient time for sensitisation.

Figure 3.3 shows images of real cladding held in the solution described above for a period of 1 hr. These samples were treated in the as received state (no heat treatment). The images show that there is a clear difference in behaviour between the three surfaces. While the outer surface of the cladding appears unchanged grain boundaries are clearely visible on the inner surface showing susceptibility to IGC. There is some evidence of IGC on the rib top but considerably less than on the inner surface.

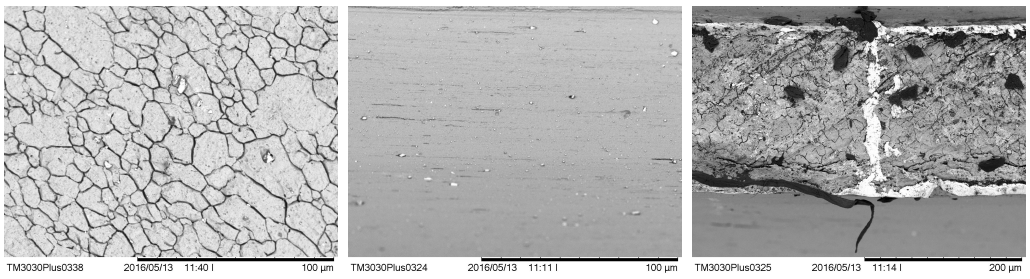

(a) Inner surface (b) Outer surface (c) Rib top

Figure 3.3: SEM Images of 1 hr corroded 20/25 samples.

Increasing the corrosion time to 6 hours increases the degree of IGC present on the inner surface and rib top with grain dropping evident on the inner surface.

While the outer surface still shows no signs of IGC the corroding media does appear to have had some impact with striations from the machining no longer visible.

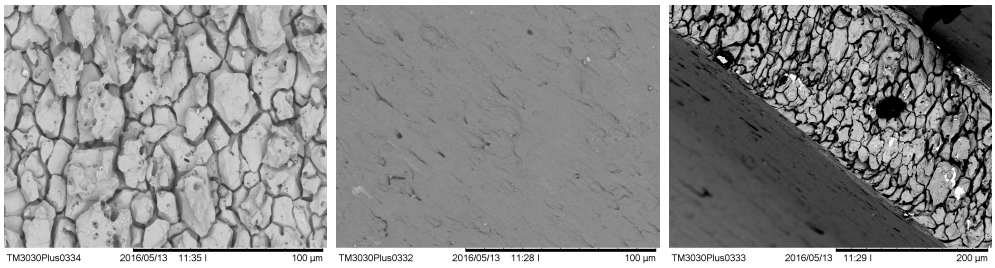

(a) Inner surface (b) Outer surface (c) Rib top

Figure 3.4: SEM Images of 6 hr corroded 20/25 samples.

3.3.3 Discussion and Conclusions

The main aim of this work was to find a reliable method for producing intergranular corrosion (IGC) in 310 and 20/25 stainless steel. The standard test for intergranular corrosion using nitric acid was felt to be too time consuming. It was found that the addition of Cr(VI) ions in the form of potassium dichromate was able to induce IGC in a much shorter period. Consequently this method will be be used to produce samples for later testing.

3.4 Further Sample Preparation

IGC has been identified as a key requirement for sample preparation however long term storage will be carried out in water dosed to pH 11.4 with sodium hydroxide while accelerated IGC can only be achieved with the use of highly acidic media. Consequently a number of samples that had been held in different conditions were also produced to replicate a range of possible fuel conditions.

3.4.1 Methodology

A number of samples were held in an autoclave containing demineralised water dosed to pH 11.4 with NaOH for 28 days. The autoclave was heated to 200°C and

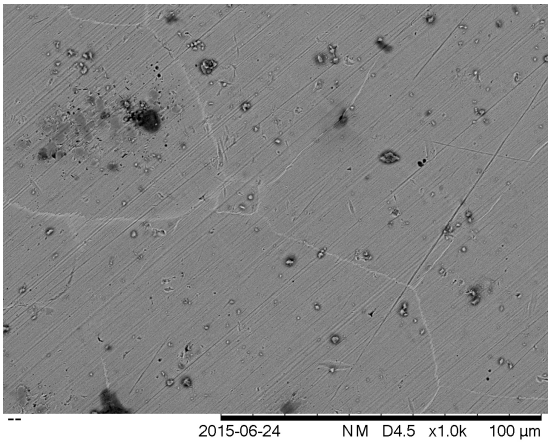

(a) 4 hours

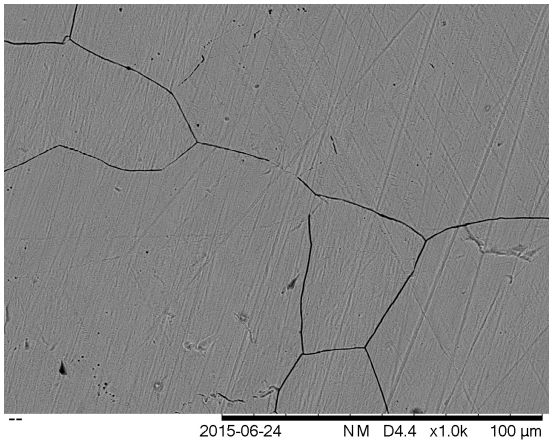

(b) 24 hours

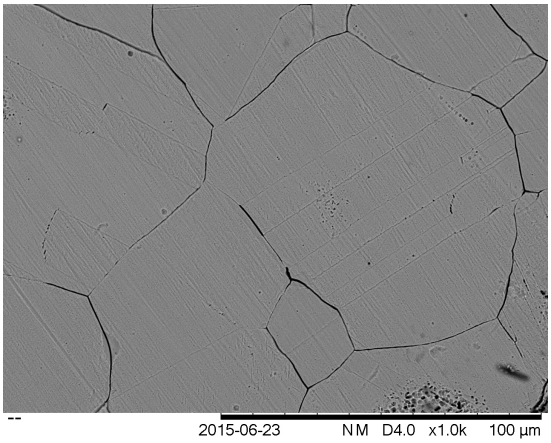

(c) 100 hours

Image unavailable

(d) 210 hours

Figure 3.5: SEM Images of corroded samples sensitised at 600°C.

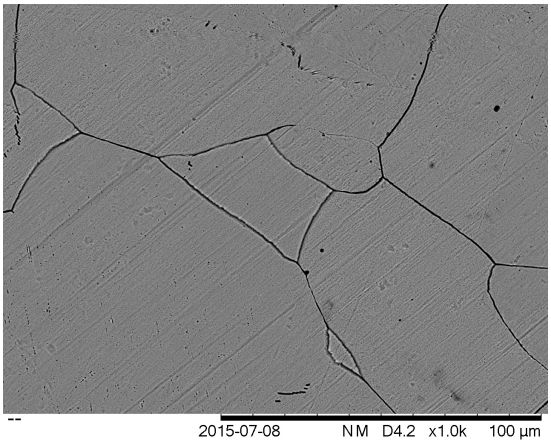

(a) 4 hours

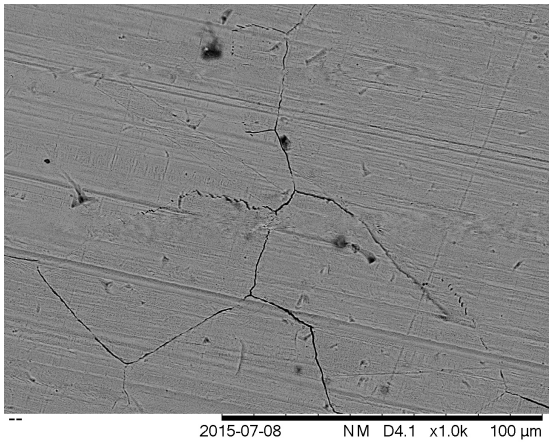

(b) 24 hours

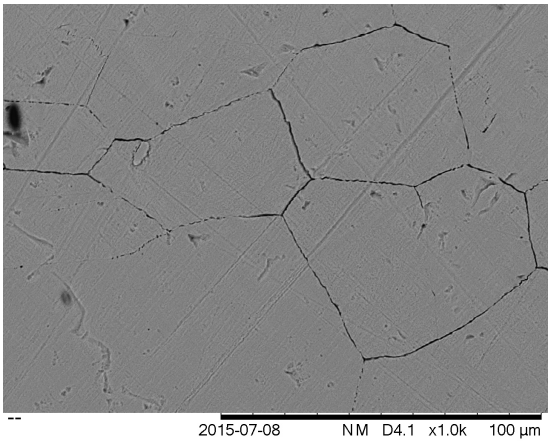

(c) 100 hours

Image unavailable

(d) 210 hours

Figure 3.6: SEM images of corroded samples sensitised at 650°C.

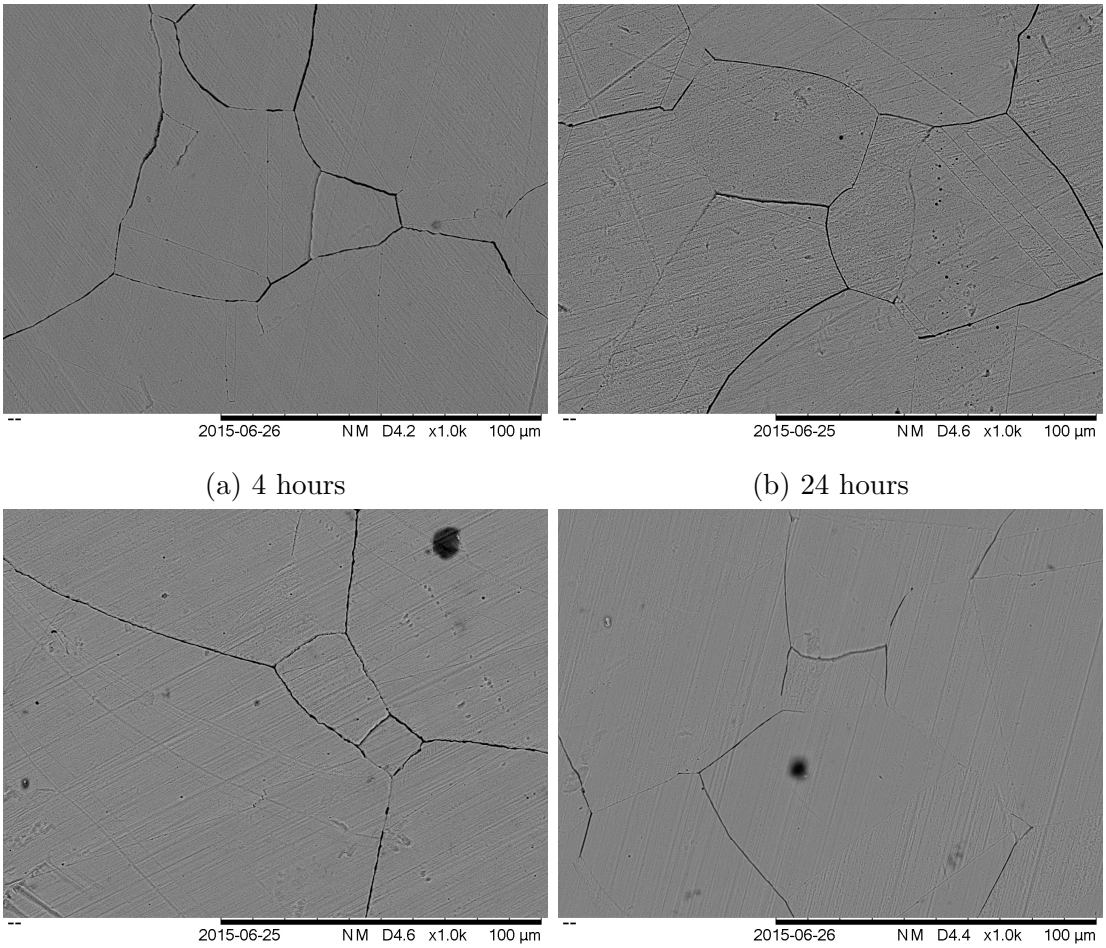

(a) 4 hours (b) 24 hours

(c) 100 hours (d) 210 hours

Figure 3.7: SEM images of corroded samples sensitised at 700°C.

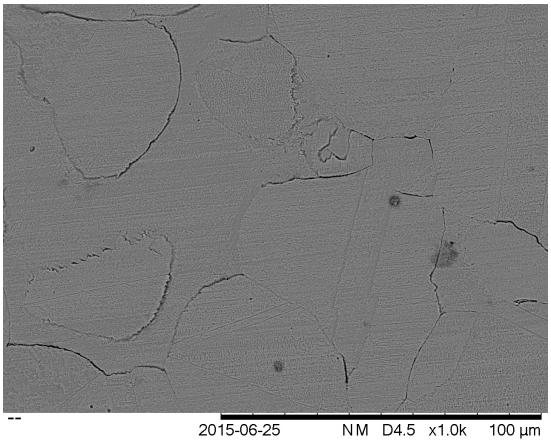

(a) 4 hours

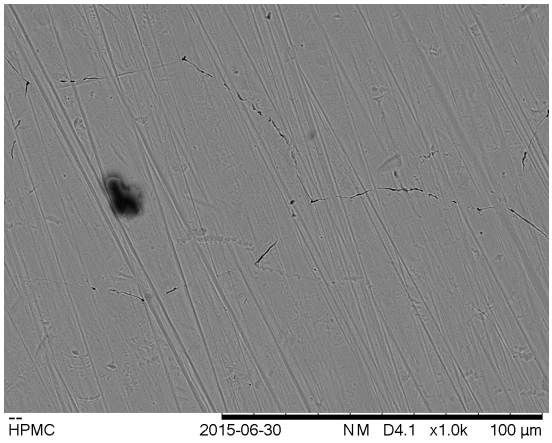

(b) 24 hours

Image unavailable

(c) 100 hours

Image unavailable

(d) 210 hours

Figure 3.8: SEM images of corroded samples sensitised at 750°C.

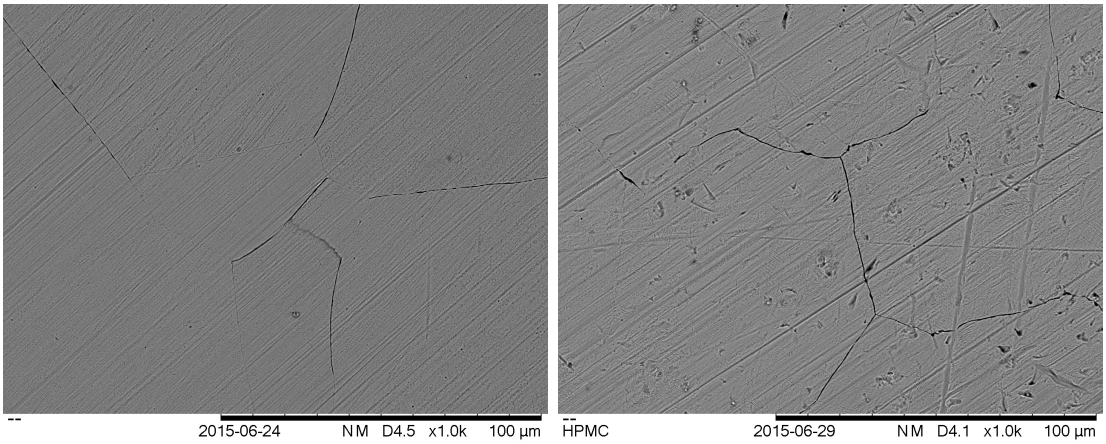

(a) 4 hours (b) 24 hours

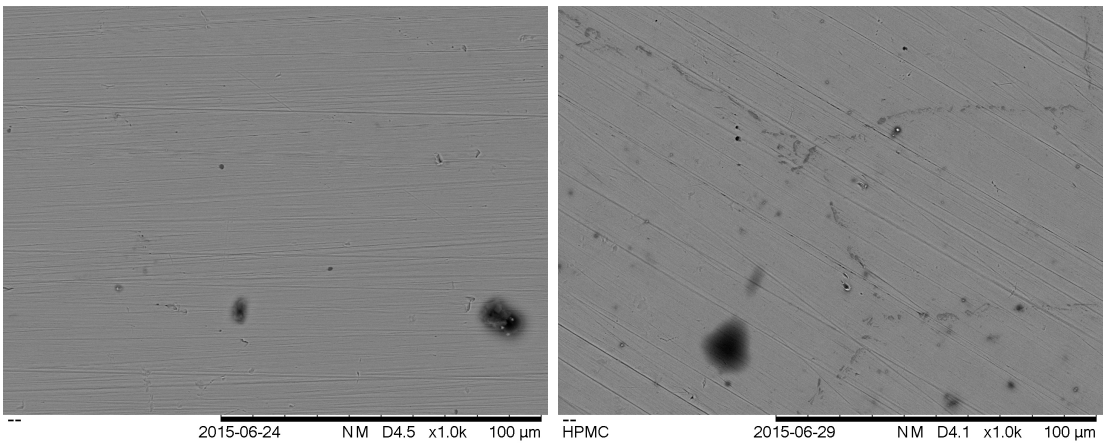

(c) 100 hours (d) 210 hours

Figure 3.9: SEM images of corroded samples sensitised at 800°C.

a pressure of 15 BarG. Samples were held in PTFE beakers inside the autoclave to avoid contact with the stainless steel autoclave walls or with samples of other material (e.g. 20/25 in contact with 310). Since there is no recognised method for replicating long term pond storage this treatment was intended to produce similar effects by increasing reaction kinetics although it is noted that this method is far from perfect.

A further set of samples were held in a solution of 6wt% $FeCl_3$ and 1wt% HCl at room temperature. This is a similar treatment ASTM G48 (Standard Test Methods for Pitting and Crevice Corrosion Resistance of Stainless Steels and Related Alloys by Use of Ferric Chloride Solution). There has been no evidence of spent AGR cladding failing as a result of pitting corrosion however pitting is one of the most common forms of corrosion in stainless steel particularly in high chloride or sulphate containing media. Under normal conditions the water in the Thorpe receipt and storage pond is highly controlled (<1 ppm Cl^-) but there have in the past been unplanned events which have lead to much higher chloride levels for short periods and these have in turn led to an increase in recorded failures due to IGC. Consequently it is felt that this method is worth trying if only for comparison purposes.

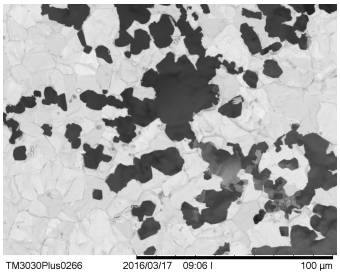

Figure 3.10: SEM Image of 310 samples corroded in $FeCl_3$.

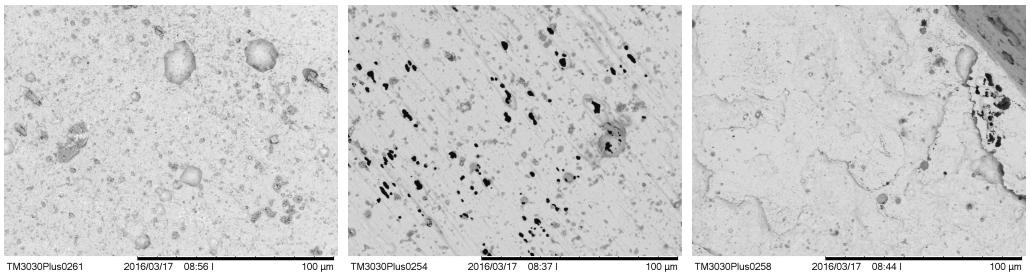

(a) Inner surface (b) Outer surface (c) Rib top

Figure 3.11: SEM Images of 20/25 samples corroded in $FeCl_3$.

3.4.2 Results

The results of 310 and 20/25 samples corroded in $FeCl_3$ are shown in fig. 3.10 and fig. 3.11 respectively. The 310 samples were held in the $FeCl_3$ solution for 24 hours and individual grains can be clearly seen. Pitting corrosion is also clearly visible.

The 20/25 samples were held in the solution for 48 hours as examination after 24 hours showed little evidence of pitting. As with the samples held in the nitric acid solution there are differences in the behaviour of the different surfaces of the cladding however in this case the outer surface of the cladding appears to be more susceptible to pitting than the inner surface. The rib top appears to show some evidence of pitting but substantially less than the outer surface.

The treatment of samples of 20/25 and 310 stainless steel in NaOH are shown in fig. 3.12 and 3.13 respectively. Both 310 and 20/25 samples appear to yield similar results after accelerated storage in NaOH. Neither sample shows any evidence of localised corrosion although the dark colour suggests that a thick oxide layer has been formed. Pyramidal deposits seem to have formed on both materials. For the

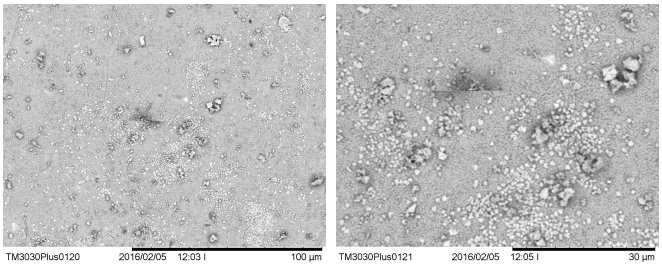

(a) (b)

Figure 3.12: SEM Images of 310 samples held in NaOH.

20/25 samples, all surfaces appear to have behaved in the same manner.

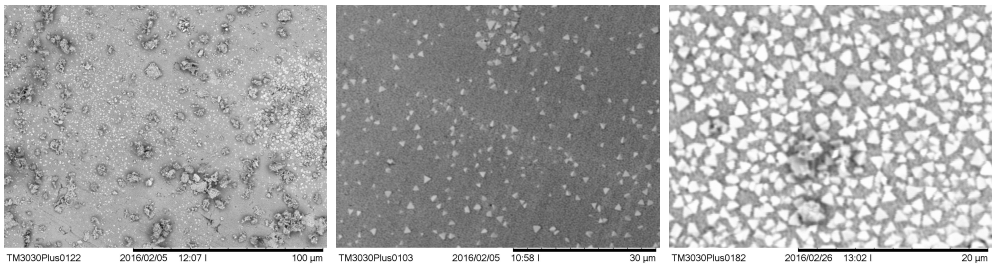

(a) Inner surface (b) Outer surface (c) Surface deposits.

Figure 3.13: SEM Images of 20/25 samples held in NaOH.

3.4.3 Carbon Deposition

In order to prevent oxidation of the graphite core inside an AGR the coolant contains a number of species that lead to carbon deposits forming on metal surfaces such as fuel pins. It was felt that it was important to understand how much water could potentially be held up within a carbon deposit. Carbon deposits were produced using a method similar to that of Walters et al[81]. The samples were first coated in carbon black and then covered in oil before being baked at 200°C for one hour. Images of the carbon deposits formed are shown in fig. 3.14.

The three images above show the nature of the deposits formed. The thickness of these deposits is considerably less than those seen in fig. 2.2 however show

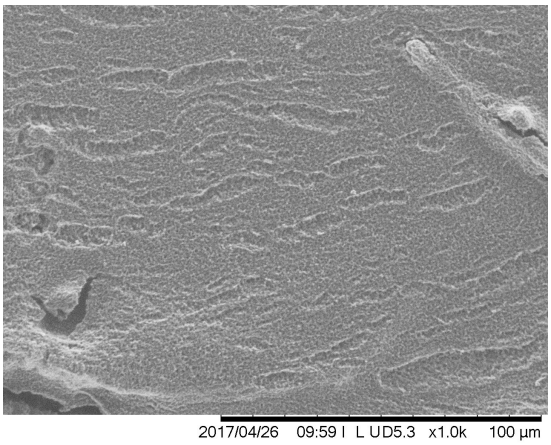

(a) SEM image of deposits on 310.

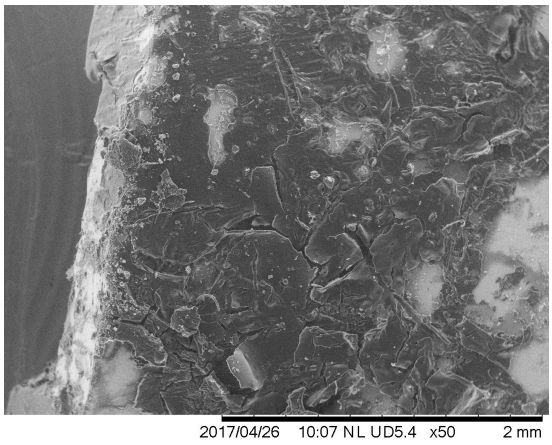

(b) SEM image of deposits on 20/25.

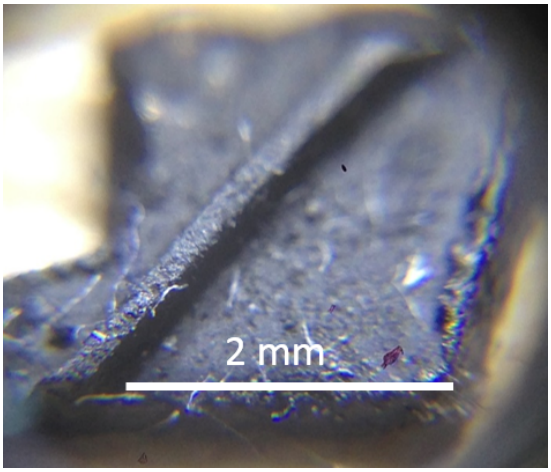

(c) SEM image of deposits on 20/25.

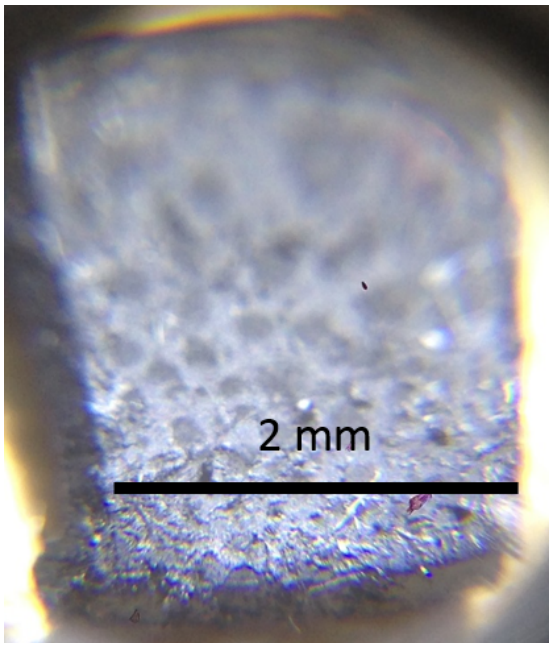

(d) SEM image of deposits on 20/25.

Figure 3.14: Images of carbon deposits.

enough similarities to be considered worthy of testing for their impact on water holdup.

3.4.4 Discussion and Conclusions

Three methods have been used to treat stainless steel to induce IGC, pitting and to replicate long term storage in caustic dosed water. The samples removed from the autoclave (NaOH) were found to have formed a thick oxide layer. While little post storage examination has taken place there is no suggestion that such a layer would be formed and that as expected this method does not produce samples that would be representative of long stored fuel.

post storage examination has however shown that long stored fuel undergoes IGC and the tests carried out have managed to replicate this to one degree or another in both the the surrogate 310 material and also the 20/25 cladding. Samples treated in such a way are deemed to be suitable for further examination. The pitted samples produced in $FeCl_3$ were also deemed suitable for further testing.

The most unexpected result was the difference in behaviour of the three different surfaces of the cladding with the inner surface appearing to be susceptible to IGC but resistant to pitting while the outer surface appeared to be susceptible to pitting but resistant to IGC, while the rib top showed signs of both IGC and pitting but considerably less than the susceptible surface.

Finally a number of samples have been produced which have visible carbon deposits on the surface. While it is acknowledged that the method of formation for these deposits is somewhat different to the catalytic method that takes place within a reactor they are believed to provide enough similarity for testing to be carried out.

For the purposes of drying the important question is how much water is associated with the oxide layers or surface deposits formed and this will be assessed in the following section.

3.5 TGA Analysis

Since the purpose of this work is to look at the drying of metal samples there would seem to be a need to assess the quantity of water that must be removed. As discussed in chapter 5 water is regarded as being present in either a bound or unbound form. As part of an unpublished masters report Thermogravimetric Analysis (TGA) was carried out on samples of aluminium which had been held in demineralised water for 6 weeks leading to the formation of a white powdery oxide layer. Figure 3.15 shows the curve produced with a clear drop in mass around 275°C due to the dehydration of the boehmite oxide layer ($Al_2O_3.3H_2O$) to form bayerite ($Al_2O_3.H_2O$). Since aluminium clad fuel has been dried for dry storage and this technique was capable of measuring the loss of bound water (although it is not able to differentiate between chemisorbed and physisorbed water) and any water trapped within the grain boundaries following IGC, it was felt that it was suitable for assessing the quantity of water found in a stainless steel oxide. While the expectation based on the literature is that the quantity of water associated with a stainless steel oxide will be significantly less than that found on aluminium it was felt that some sort of experimental work was required to confirm this. Note that in the folowoing section each different colour on a thermograph is a different test.

3.5.1 Methodology

TGA/DSC analysis was carried out using a Mettler Toledo TGA/DSC 1100/LF machine. For the initial tests samples were heated from 50 °C to 400 °C at a rate of 10°C per minute. For the follow up tests samples were heated from 50 °C to 500 °C at a rate of 10°C per minute. In some cases the exhaust gas from the TGA was analysed for water using an MKS Cirrus 2 mass spectrometer (MS). The MS was capable of recording data for 14 different masses. Of these it was specifically set to measure a signal for a mass of 17, and OH fragment and 18, water but other masses were also recorded since the machine was already set up to record them. The full list is shown in table 3.2. Upon analysis it was found as would be expected that the OH behaviour was almost identical to that of the water although at a slightly lower intensity. As a result only the data for the water is reported.

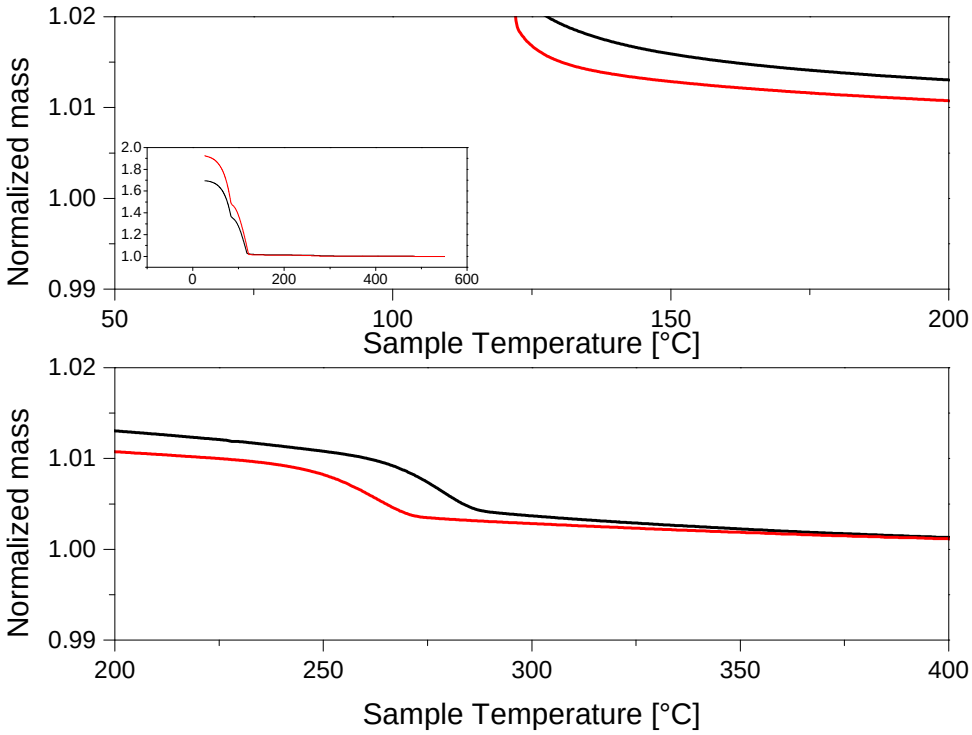

Figure 3.15: TGA curve for corroded aluminium. Expanded scale with the full scale inset. Each line is a different sample.

Four different types of samples were used overall although not all samples were used at all stages; samples treated in the nitric acid solution described in section 3.3 to induce IGC (HNO_3), samples treated in ferric chloride ($FeCl_3$) to induce pitting and in an autoclave (NaOH) as per fig. 3.12 and samples in the as received state.

These samples were tested in two manners. They were either loaded into the TGA machine while still wet or were allowed to air dry beforehand. To allow easy comparison of different samples the data was normalised. Since the starting mass of water was exceptionally difficult to control the data was normalised to the final mass of the samples after the TGA run. For the TGA testing at least three samples were analysed for each sample type.

Mass	Possible fragment	Mass	Possible fragment
4	He	32	O2
12	C	30	C2H6
14	N	41	C3H5
15	NH/CH3	49	CH2Cl
16	O	64	SO2
17	OH	79	Br/SO3
18	H20	81	Br

Table 3.2: Table of all MS masses recorded and their possible identification.

3.5.2 Results

For the initial tests one of each of the four samples of 20/25 was analysed dry. The feeling was that any water that was removed when samples were left to air dry was of no concern since it would not be difficult to remove.

The data from the initial tests can be seen in fig. 3.16. When compared to the data for the aluminium samples seen in fig. 3.15 there is clearly a negligible mass loss in almost all cases with sole exception being the pitted cladding sample.

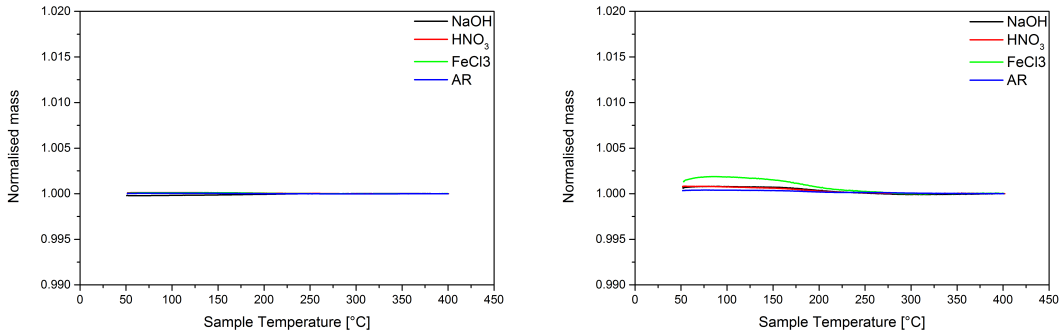

(a) 310 (b) 20/25

Figure 3.16: Initial TGA curves for stainless steel.

The follow up tests were carried out with mass spectrometry of the exhaust gas in an attempt to detect and water being removed below the level of detection. The results for the first experiments are shown in fig. 3.17. These experiments

were carried out dry and on different days (A and B) with the MS disconnected on the days in between. On both occasions a corroded sample was tested first (1) and a non corroded sample second (2). The data would seem to suggest that a water peak was detected from the corroded samples but not from the non corroded samples. The final sample, B3, was another corroded sample and it was found to produce no water peak. After several more tests with similar results it was found that the peaks seen in A1 and B1 were actually due to the removal of bound water to the TGA and capillary line surface and that this water was removed during the first test of the day. For the later tests a single drying run was carried out with an empty crucible before the samples were analysed.

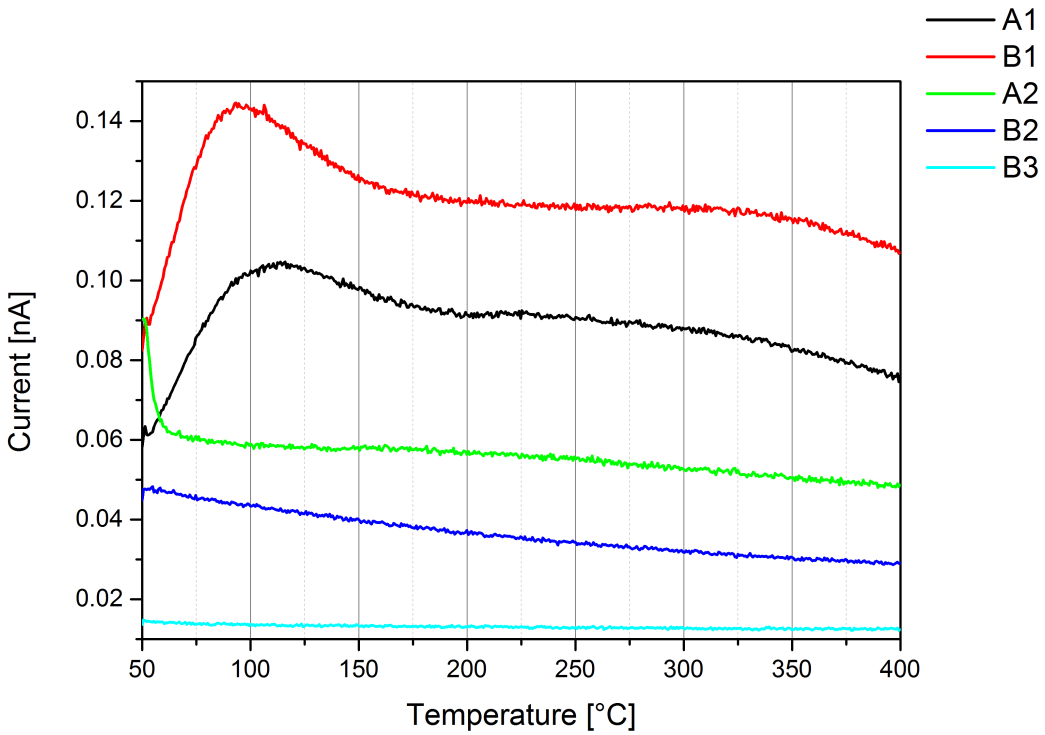

Figure 3.17: MS data from the first TGA runs with MS attached.

Having made this discovery a number of tests were carried out both wet and dry using IGC, NaOH and as received samples of 20/25 (fig. 3.18). These samples were loaded wet to the machine. The MS curves show a large peak in the water that was detected by the MS however the size of this peak varies widely in terms

of both magnitude and duration with no relationship to the sample treatment. It was however noticed that the duration of the peak (the temperature since the heating rate was constant) was related to the initial quantity of water that had been removed. This is due to water being initially evaporated and then boiled off as the sample was heated, being deposited out again on surfaces downstream and then being removed once more. The greater the quantity of water that was initially removed from the sample the more water redeposited down stream and the longer it took to be removed.

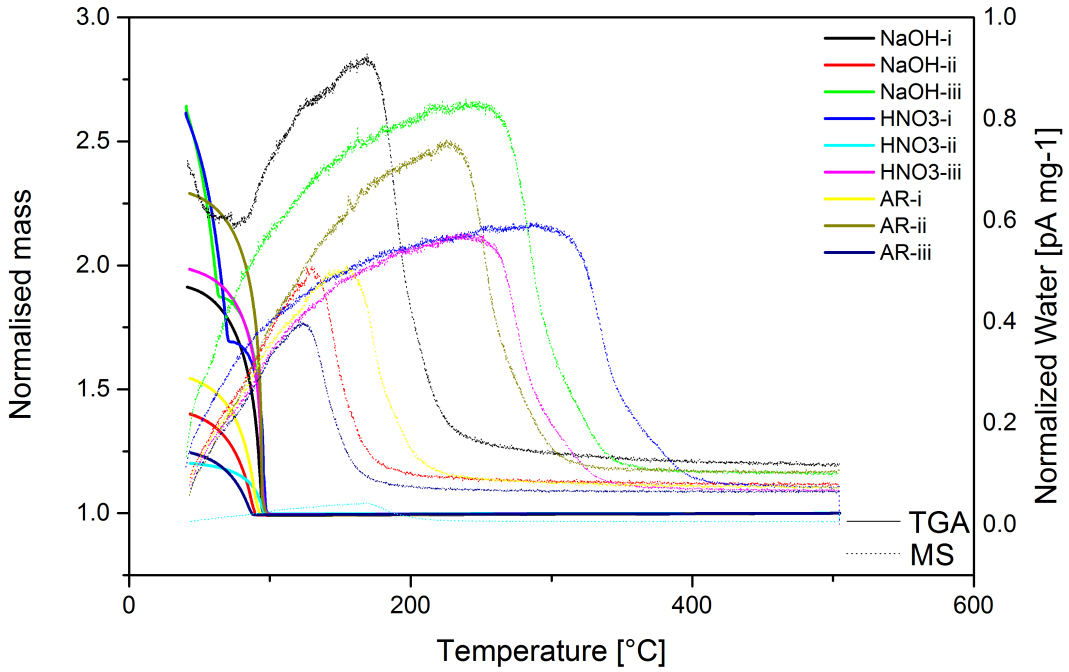

Figure 3.18: MS and TGA data from the second set of TGA runs. The MS curves for the two samples which showed the greatest mass loss also have the greatest duration (temperature since heating rate is constant), while the two shortest MS curves correspond to the smallest mass loss. Three samples (i-iii) were tested for each treatment.

To try and improve the MS data a new capillary line was fitted to the machine and in doing so it was found that the old line had broken within the insulation.

The machine was also baked out for 24 hours prior to use rather than by running a single drying run as had been carried out previously.

The final tests were carried out with IGC, pitted and as received samples in both wet and dry states using both 310 and 20/25 stainless steel.

The plots in fig. 3.19 curves for the as received 20/25 and 310 stainless steel. These samples were completely untreated and placed dry into the TGA. The 310 samples show no mass change while the 20/25 samples remain roughly level until around 200°C and then show a reduction in mass of approximately 0.075%-0.025%. The MS data for both samples shows an initial reduction in water as atmospheric water is removed after which the level of water remains roughly the same.

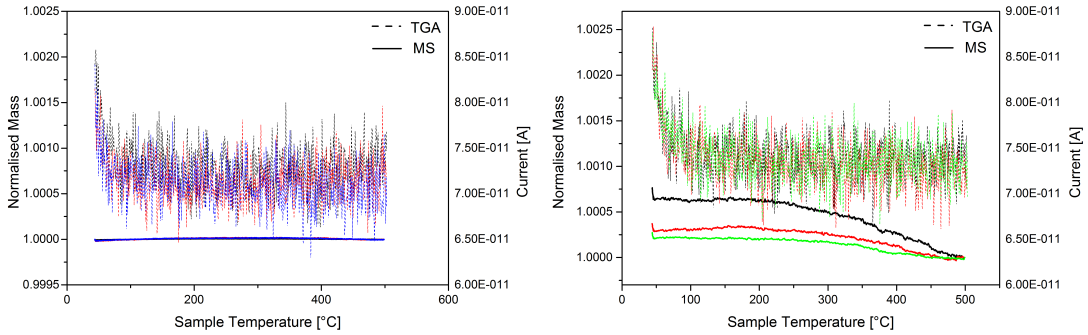

(a) 310 (b) 20/25

Figure 3.19: TGA and MS plots for as received stainless steel. Each colour is an individual test.

The results for dry samples that had been treated to induce IGC and pitting are shown below. The data for these samples is, with the exception of one 310 IGC sample, broadly similar to the as received samples. It is not clear why the odd 310 sample has behaved as it has but this is not believed to be representative and can be discounted.

In fig. 3.22 and 3.23 it can be seen that the initial behaviour of all wet samples is roughly the same with a large drop in mass between 50°C and 100°C as the free water was evaporated and boiled off. From this point on there is a noticeable difference between the cladding and 310. Between 100°C and 200°C the 310 shows a mass change of around 0.025% and then virtually no mass change which is almost

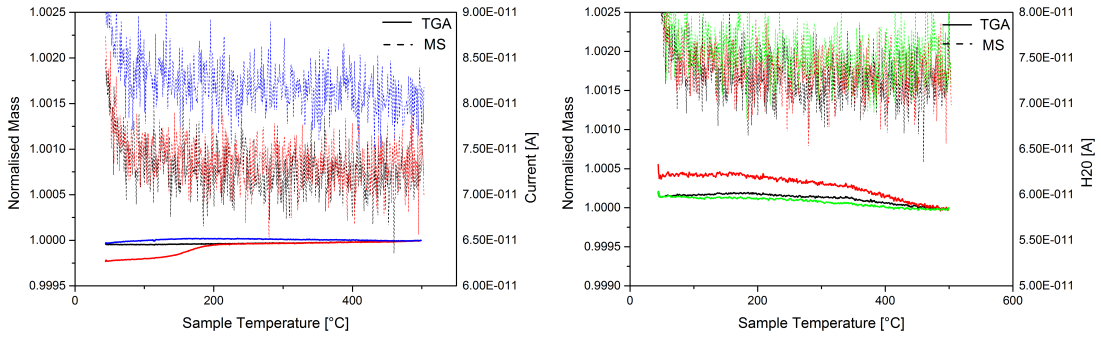

(a) 310 (b) 20/25

Figure 3.20: TGA and MS plots for dry IGC stainless steel.

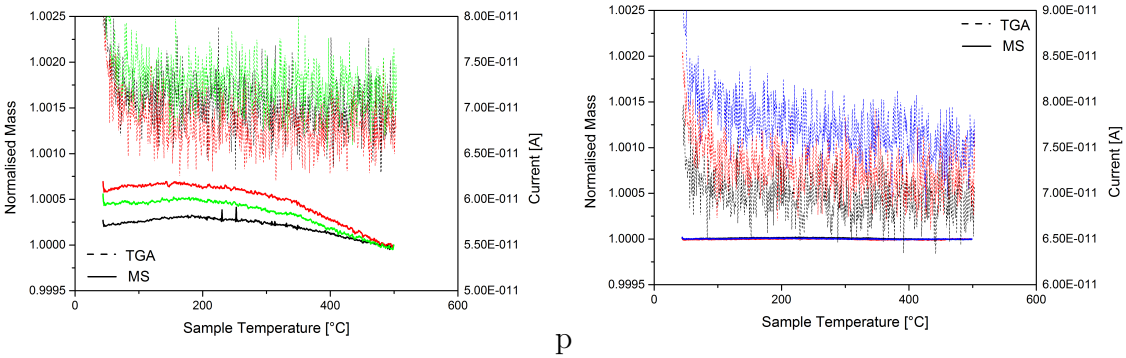

p

(a) 310 (b) 20/25

Figure 3.21: TGA and MS plots for dry pitted stainless steel.

identical to the behaviour of the dry samples in this region. In comparison the 20/25 shows a mass change of approximately 0.3% between 100°C and 200°C. From 200°C the mass loss is much the same as the dry cladding samples with a mass loss of around 0.075-0.025%. The shape of the MS curves is similar to those found previously but with less correlation between the mass of water lost and the peak duration.

One of the three 20/25 IGC samples also exhibited unusual behaviour with a two step mass loss. On some occasions (see fig. 3.15, 3.18 and 3.16) this was observed below 100°C and is thought to be due to water being spilt when the

sample was loaded leading to some water becoming trapped between the crucible lid and rim and underneath the crucible and then being released. On this occasion however the second step was between 100°C and 140°C. This plot also produced unusual MS behaviour with two large spikes in the amplitude.

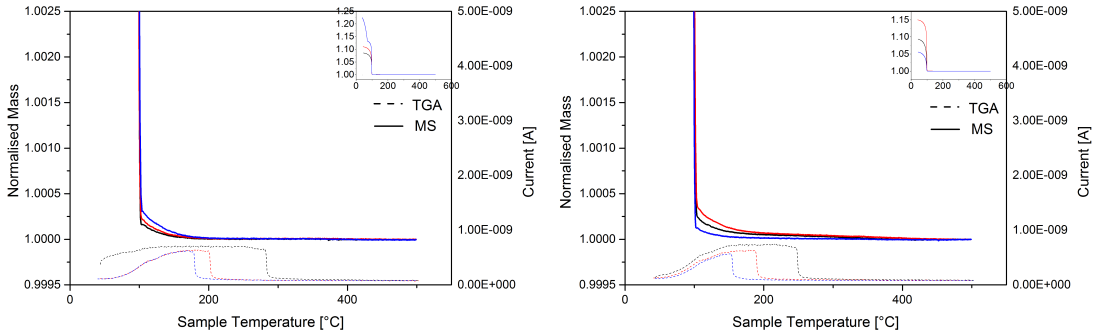

(a) IGC (b) Pitted

Figure 3.22: TGA and MS plots for wet corroded 310 samples.

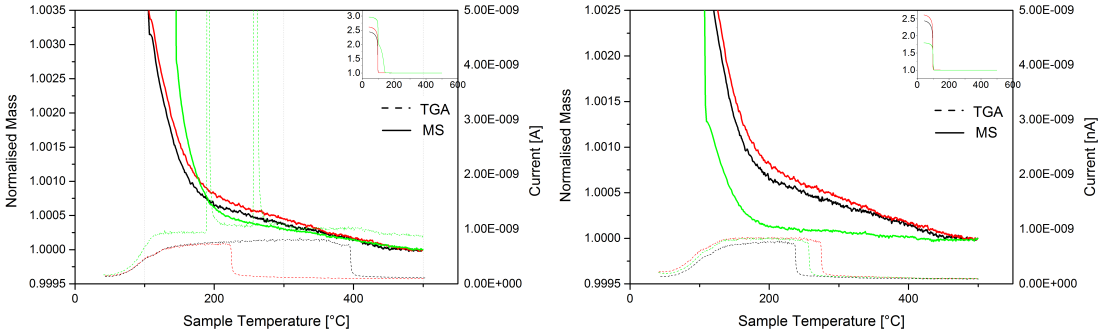

(a) IGC (b) Pitted

Figure 3.23: TGA and MS plots for wet corroded 20/25 samples.

The results for the samples which had carbon deposits are shown in fig. 3.24 and fig. 3.25. The wet samples both show the large drop in mass due to free water seen in previous wet samples. All samples show a further mass loss between around 200°C and 350°C. The MS data for all of the wet 310 samples show a significant number of spikes in intensity.

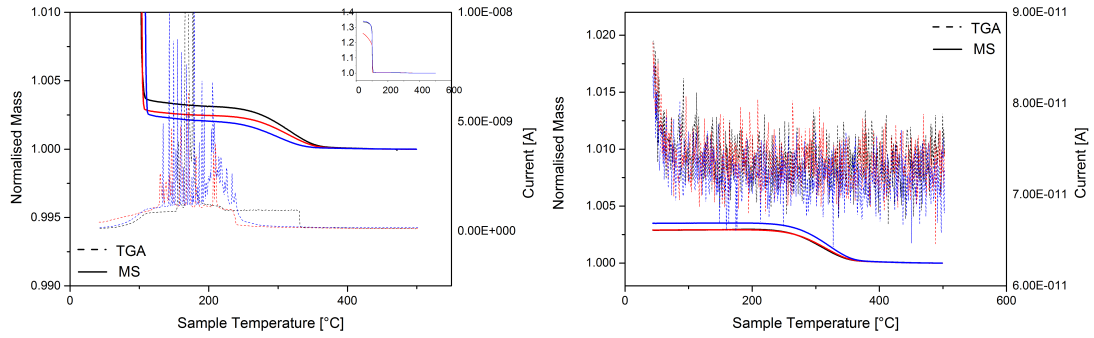

(a) Wet (b) Dry

Figure 3.24: TGA and MS plots for 310 carbon deposited Samples.

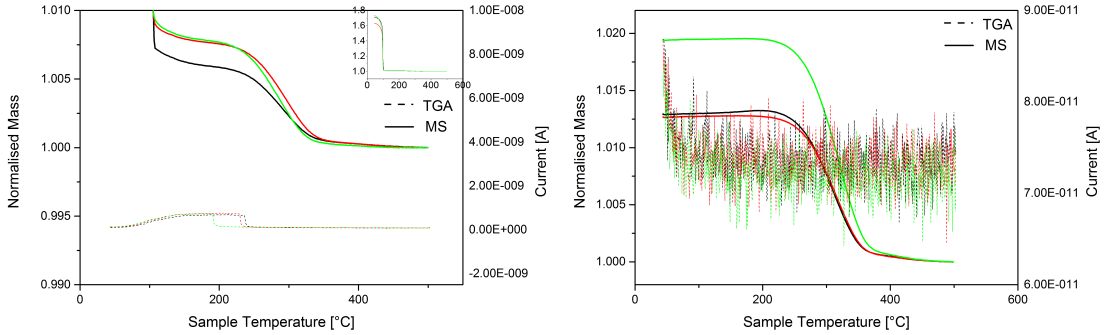

(a) Wet (b) Dry

Figure 3.25: TGA and MS plots for 20/25 carbon deposited samples.

3.5.3 Discussion and Conclusions

Aluminium clad fuels are known to have a thick water containing layer which it was found did not need to be removed for safe dry storage but nevertheless its removal can be detected with TGA. Even allowing for the difference in material it is felt that if the quantity of water released by TGA of stainless steel samples is similar or lower than that found from aluminium the quantities of bound water are likely to be negligible in relation to the impact they may have on dry storage. Despite this when TGA of stainless steel was found to provide little data, MS of the exhaust gas was carried out to try and measure water at lower levels.

The untreated samples of 310 showed virtually no mass change during the TGA run indicating that there was no bound water. The untreated 20/25 showed a mass loss of 0.025-0.07% with the main change occurring above 200°C. This was almost identical to the behaviour of the dry IGC and pitted samples.

The wet corroded samples all show three distinct areas with different rates of mass change. Both 310 and 20/25 show a rapid mass loss up to 100°C as free water is evaporated and boiled off. A reduced rate is observed between 100°C and ∼200°C. Above 200°C the wet corroded samples behave in the same manner to the dry samples with the 310 showing almost no mass change while the 20/25 shows a mass change of ∼0.025%.

The MS data was found to be somewhat disappointing. For dry samples it was found that there was no obvious spike in water beyond the noise observed for as received samples and early on it was found that an MS signal continued to be collected long after the mass change had ended. It was therefore concluded that the MS data would be of little initial value although the was still collected since the effort required to do so was minimal. The later MS data behaved similarly although there were some tests in which large peaks in the MS signal were observed although it is not at all clear what has caused these.

Comparison of all data from the different metals has shown that 20/25 has a greater mass loss than 310 however the degree of mass change is some ten times lower than that observed for the aluminium samples. The most likely source of this mass loss would be due to the loss of water trapped within microscopic imperfections on the sample surface or physiosorbed water. The lack of a distinct drying peak associated with this water can be explained by the Kelvin equation discussed in further section 5.1.5. If the pores present have a normal size distribution then as the sample is heated the water is progressively evaporated from smaller pores as the temperataure rises. It is unlikely to be chemisorbed water since that would be expected to occur as a step change as seen for aluminium in fig. 3.15.

While the MS data is disappointing it did show that water could be detected. Since there was no evident change in the MS signal above 200°C for any of the 20/25 samples there is a thought that this mass loss may in fact be due to something other than water.

A further possibility is that the difference in apparent mass change between the two samples is due to the method of normalisation used. Normalising to the final mass allowed comparison with one sample of 20/25 to another since the samples were cut from the same tube and while the two dimensions may have varied slightly the surface area to mass ration remained around 0.8. Since the 310 samples were cut from thicker material they had a surface area to mass ratio of 0.41. Since any mass loss would be from the surface this ratio difference would have exaggerated any relative difference between the materials.

The results for samples with the wet carbon deposits has similar results to the other wet samples up to 200°C with an initial very high rate followed by a greatly reduced rate. However both the wet a dry samples show step change loss of mass between ∼220°C and ∼350°C. Since there was no noticeable change in the MS signal for water the thought is that this was due to the evaporation of long chain alkanes which had been present in the oil used in production. The samples were baked at 200°C in production so there was no further impact of heating up to this point and it was only when 200°C was exceeded that further mass loss was achieved. With this in mind it raises the question as to whether the mass loss observed for the cladding samples may be due to something similar.

The purpose of this investigation was to establish whether a significant quantity of water was present on a stainless steel oxide. The TGA data collected has indicated that there is likely to be a noticeable difference in the bound water on the surface of the two samples with the AGR cladding appearing to show a noticeable mass drop which is not seen with the 310 samples. However in comparison to the aluminium reference this mass change was of no consequence. This was not affected by either of the common forms of corrosion tested. It is therefore concluded that for the purposes of drying AGR fuel water bound to the surface or held up in carbon deposits can be regarded as negligible and that the only concern is the removal of unbound water.

3.6 XPS Analysis

From the SEM images of corroded cladding shown in section 3.3 and 3.4 it is clear that the two surfaces of the as received cladding behave differently. Since the

corrosion behaviour of a material is a surface phenomenon it was felt that this behavioural difference may be due to differences in the surface composition. As described in section 2.7.1 XPS is a highly surface specific technique which has the added advantage of being able to detect differences in bonding and was therefore felt to be the ideal tool for assessing the differences in the two surfaces. It would also allow the detection of different types of bound water, i.e. chemisorbed water that is held as hydroxides and oxy-hydroxides and layers of physisorbed water bound to the surface.

3.6.1 Methodology

XPS was carried out by Dr Benjamin Johnson of the School of Physics and Astronomy at the University of Leeds with a VG Escalab 250 XPS with monochromated aluminium K-alpha X-ray source. The spot size was 500μm with a power of 150 W. High resolution spectra were taken with a step size of 0.1 eV and an energy of 20 eV. The samples were mounted on carbon tape. Peak fitting was carried out using CasaXPS using Shirley backgrounds and mixed Gaussian-Lorentzian lineshapes (GL(30)) unless otherwise stated. Due to the time involved only a single spot was analysed on each surface.

Prior to analysis the samples underwent a three stage cleaning process to remove as much adventitious carbon as possible. The samples were initially placed into acetone for 10 minutes in an ultrasonic bath followed by a rinse with high purity (>18 MΩcm^{-1}). This was followed by two further periods in a US bath first in a solution of hot high purity water and Topol laboratory detergent and a rinse and then in high purity water alone followed by a final rinse with high purity water.

Two samples were prepared for XPS analysis (one for the inner surface and one for the outer). The rib top was not analysed. Two XPS sessions were carried out using at different times so while the samples were the same the exact areas analysed differed so some variation is to be expected. Before taking a high resolution spectra a survey spectra of each surface was collected. This was used to identify the elements present. High resolution spectra were then collected for each of the elements identified.

3.6.2 XPS Session 1 Results

The survey spectra for the two surfaces are shown in fig. 3.26 and table 3.3 shows the atomic composition of the two surfaces calculated from the high resolution spectra. The survey spectra show a difference in the background level particularly at high binding energy although this is unlikely to be of great significance. The atomic composition of the two surfaces are broadly the same being primarily carbon and oxygen. The inner surface appears to have 50% more chromium than the outer surface however since this is 3.36% compared to 2.09% it is not possible to say whether this is a significant difference or not. The iron accounts for around 2% on of both surfaces.

The likliehood is that the the carbon, silicon, calcium, chlorine and nitrogen and contamination or not major oxide constituents (although silicon is reported to be present in small quantities). The data in table 3.4 shows the values for oxygen, iron, chromium and nickel (the elements one would expect in the metal and oxide) in table 3.3 adjusted to wt%. While this is not entirely accurate since a portion of the oxygen is likely to be organic in origin and associated with the carbon contamination it does allow a more reasonable estimation of the oxide composition to be made and overall the proportions of the transition metals present seem reasonable. There is some suggestion that the outer surface oxide contains less chromium the inner surface, and in the outer surface, while the values are similar the oxide would appear to contain more iron compared to the inner surface

While there is some indication of a difference between the two surfaces the high degree of carbon contamination means that it is unlikely to be possible to produce an accurate picture of the composition of the oxide in terms of the different iron and chromium species present. Nevertheless an attempt has been made to compare the peaks for the two surfaces. This was done by fitting peaks to the high resolution spectra using similar constraints. In some cases these peaks are identified but in others they serve merely to highlight differences. The green lines indicate the region in which peaks were fitted.

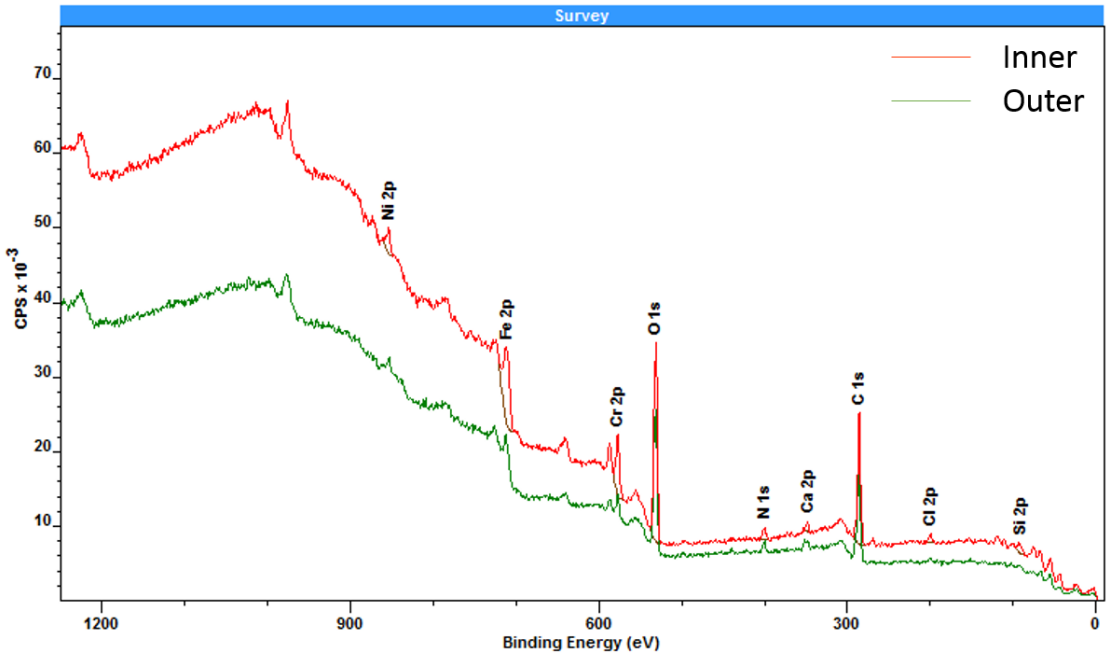

Figure 3.26: XPS survey spectra of the inner and outer surface.

Element	Atomic %	
	Inner	Outer
C 1s	58.04	59.31
O 1s	29.00	27.73
Cr 2p	3.36	2.09
Fe 2p	2.21	2.28
Ni 2p	0.43	0.43
Ca 2p	1.19	1.40
Cl 2p	2.14	1.27
N 1s	2.22	3.21
Si 2p	1.41	2.25

Table 3.3: Surface composition of cladding surface from high resolution XPS spectra.

	wt%	
Element	Inner	Outer
O 1s	61.7	65.6
Cr 2p	20.7	14.3
Fe 2p	14.6	16.8
Ni 2p	3.0	3.3

Table 3.4: Surface composition of cladding surface from high resolution XPS spectra with contaminants ignored and adjusted to wt%.

C1s Three peaks were used to fit both the inner and outer surface for the C1s spectra. No manual constraints were applied yet the FWHM and peak positions vary by between 0.01 and 0.1 eV indicating that the two surfaces are similar in terms of the species present. The lowest binding energy peak has been identified as being the C-C/C-H peak from both the position and FWHM. The remaining two peaks are labelled as C-O and C=O as these will be the two other main types of carbon likely to be found however the peaks are much broader than one would expect for these peaks alone so it is likely that while they have been depicted as two peaks they are in fact a combination of various other peaks (discussed further below). There is however no indication of a significant difference in the two surfaces.

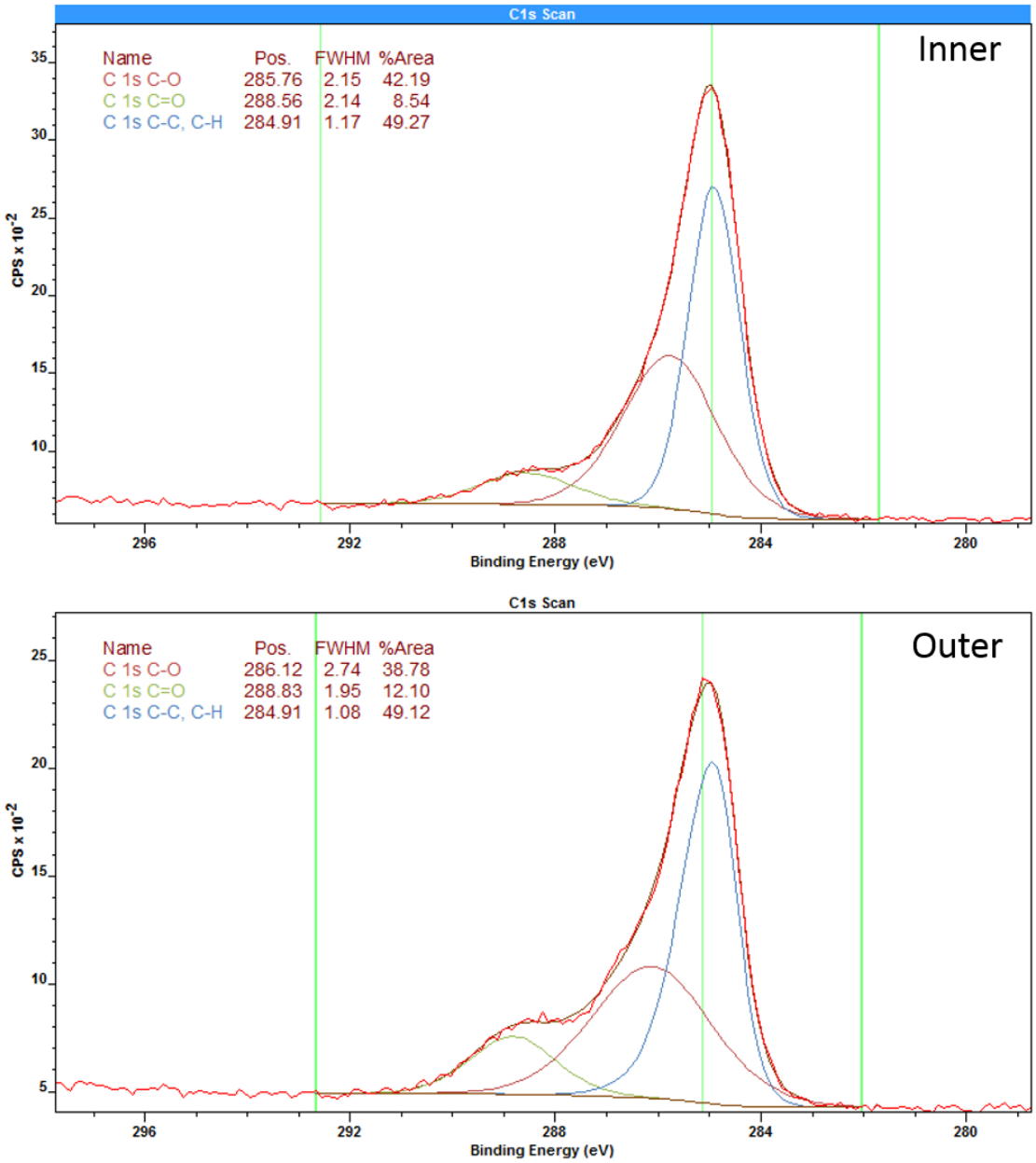

Figure 3.27: C 1s XPS spectra of the inner and outer surfaces.

O1s From the shape of the spectra there is a clear difference in the species that contribute to the total O1s peak. As with the C1s the O1s was fitted with three peaks. The lowest energy of these peaks has been identified as a metal oxide peak based on both the position and FWHM. The remaining two peaks have

been labelled as hydroxide and organic based on there rough position and the knowledge that both of these species are likely to exist and the position of these peaks is broadly correct however like the higher binding energy C1s peaks these are likely to be an agglomeration of many smaller peaks which since the FWHM is quite high.

The relative proportion of oxide and "hydroxide" is somewhat higher for the inner surface than the outer surface while the outer surface has a much higher proportion of organic oxygen.

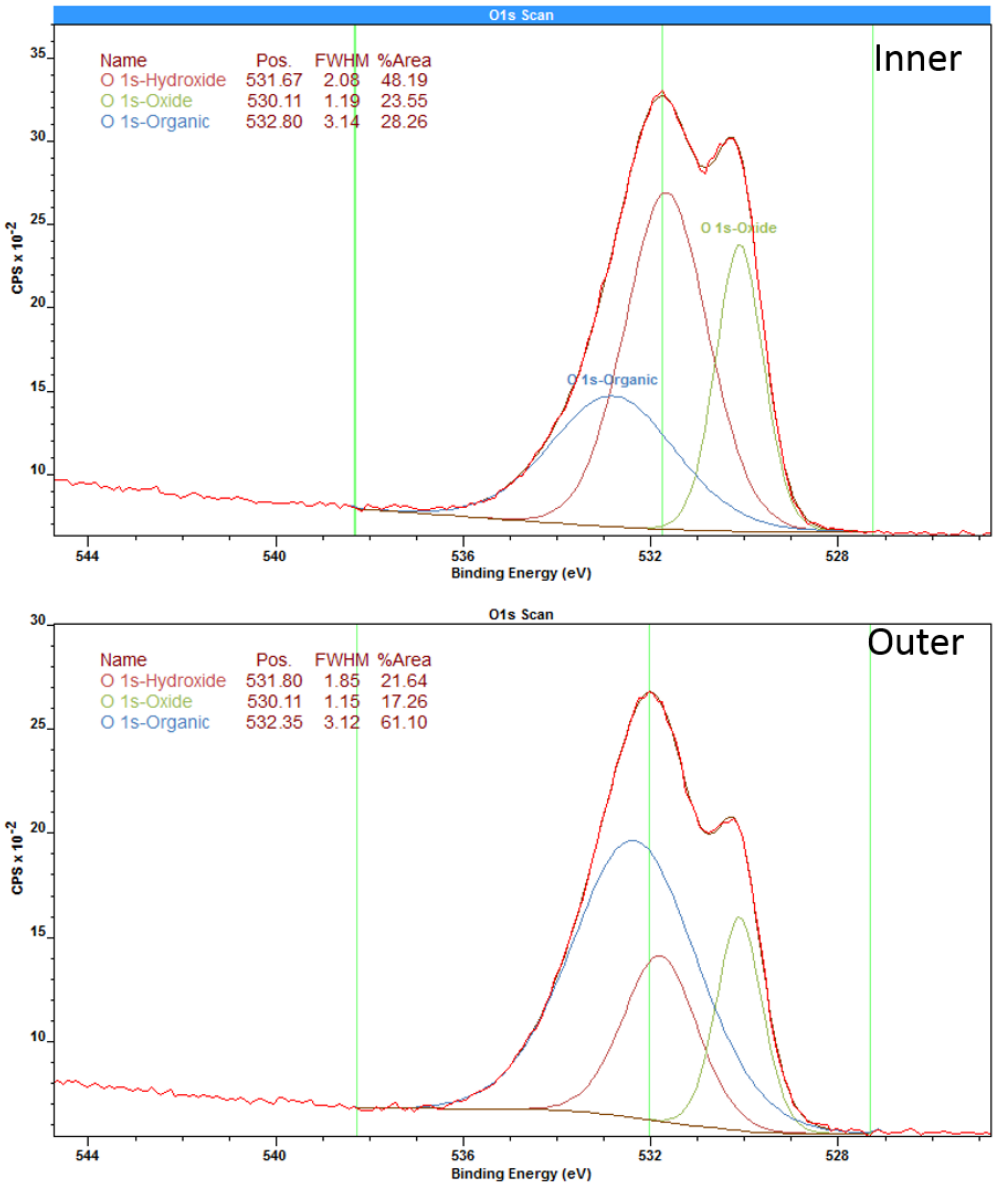

Figure 3.28: O 1s XPS spectra of the inner and outer surfaces.

Minor Elements-Ca 2p, Cl 2p and N 1s In order to explain some of the agglomerated peaks described above fig. 3.29 shows the plots for some of the unexpected elements found.

Calcium shows little chemical shift as a result of bonding so only one peak is apparent however there is distinct spacing between the orbitals with the 3.5 eV

spacing seen being characteristic of calcium carbonate. It is not at all clear what the source of this would be since calcium carbonate is not a typical contaminant.

The main peak for elemental silicon is typically found at 99.4 eV. Since the main peak seen is close to 102 eV and has significant breadth this peak is likely to be a mixture of silicon containing compounds such as silicon carbide, silicon dioxide and silicates.

The shape of the Cl 2p peaks suggests that more than one species is present. The peak around 198.5 eV is typical of metal chlorides while the 200 eV peak is likely to be organic chlorine.

The nitrogen peak is almost certainly a single species and is likely to be gaseous nitrogen adsorbed onto the sample however due to the position it may also be part of a C-NH_2 group.

In order to make an accurate model of the different transition metal species present it is necessary to have an accurate breakdown of the oxide and hydroxide present. It was shown above that this was difficult doe to the large quantities of organic oxygen present although with an ideal sample it may have been possible to work through the carbon sample peaks to do this. However, it is clear that both the C 1s and O 1s peaks will be influenced not only by each other but also by these minor elements.

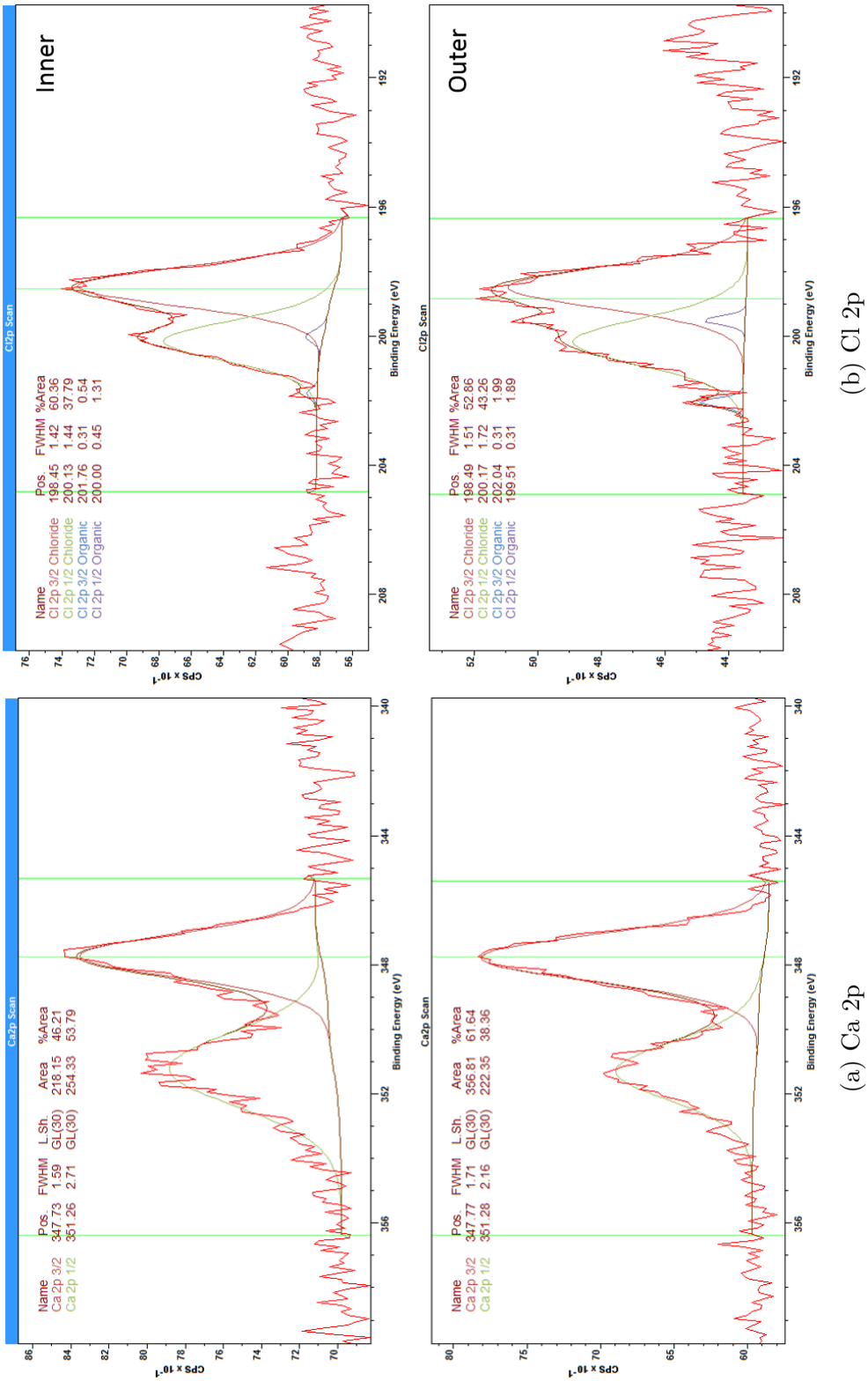
Inner
Outer
Cl2p Scan
Ca2p Scan
Name
Cl 2p 3/2 Chloride
Cl 2p 1/2 Chloride
Cl 2p 3/2 Organic
Cl 2p 1/2 Organic
Pos.
198.45
200.13
201.76
200.00
FWHM
1.42
1.44
0.31
0.45
%Area
60.36
37.79
0.54
1.31
Pos.
198.49
200.17
202.04
199.51
FWHM
1.51
1.72
0.31
0.31
%Area
52.86
43.26
1.99
1.89
Name
Ca 2p 3/2
Ca 2p 1/2
Pos.
347.73
351.26
FWHM
1.59
2.71
L.Sh.
GL(30)
GL(30)
Area
218.15
254.33
%Area
46.21
53.79
Pos.
347.77
361.28
FWHM
1.71
2.16
L.Sh.
GL(30)
GL(30)
Area
356.81
222.35
%Area
61.64
38.36
CPS x 10^-1
Binding Energy (eV)

(a) Ca 2p

(b) Cl 2p

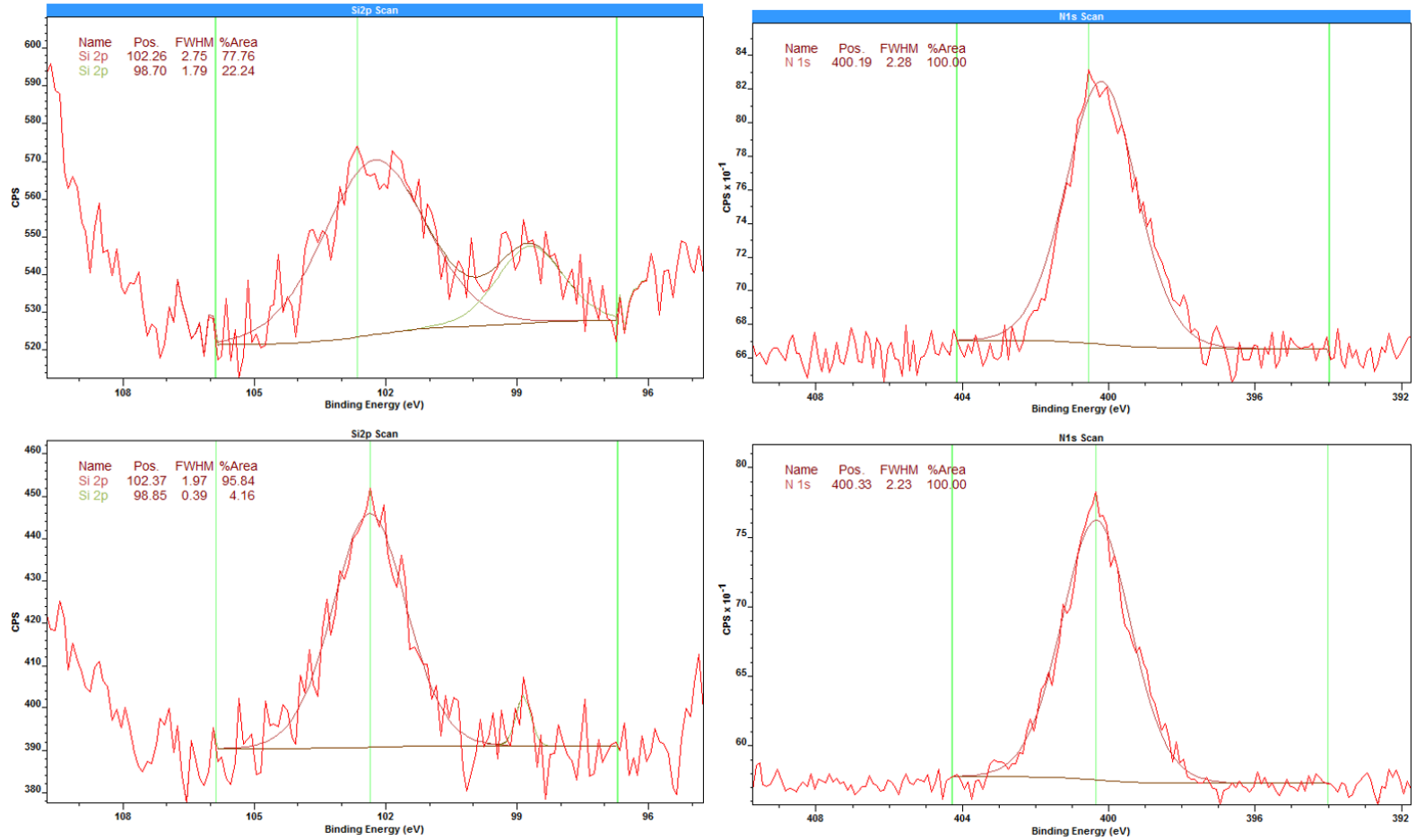

(c) Si 2p

(d) N 1s

Figure 3.29: XPS spectra for minor elements.

Cr 2p The Cr 2p spectra is fitted with three peaks; a metal peak and two higher energy peaks. The metal peak was given the asymmetric lineshape identified by Biesinger et al[69] and constraints were added to limit the FWHM to 0.9 eV. The metal peak accounts for ∼14% of the Cr 2p peak. Chromium hydroxide is one of the few oxidised transition metal peaks (certainly of Cr, fe and Ni) which does not exhibit multiplet splitting. This peak is reported to be at 577.3 eV with a FWHM of ∼2.6 eV[69] and the main peak observed in fig. 3.30 is seen to have values close to this for both the inner and outer surface. These peaks both account for ∼67% of the Cr2p recorded suggesting that the majority of the cladding surface is $Cr(OH)_3$. Chomiu(III) oxide and mixed iron (and nickel) spinel oxides are reported[69] as showing five peaks stretching between 575 and 579 eV with most of the energy at the lower end. The third peak seen at 576 eV is therefore a mixture of these and is but is likely to contain mainly chromium species with some iron containing spinels. Both surfaces are broadbly similar and neither surface shows any sign of a peak relating to Cr(VI) species (∼580 eV).

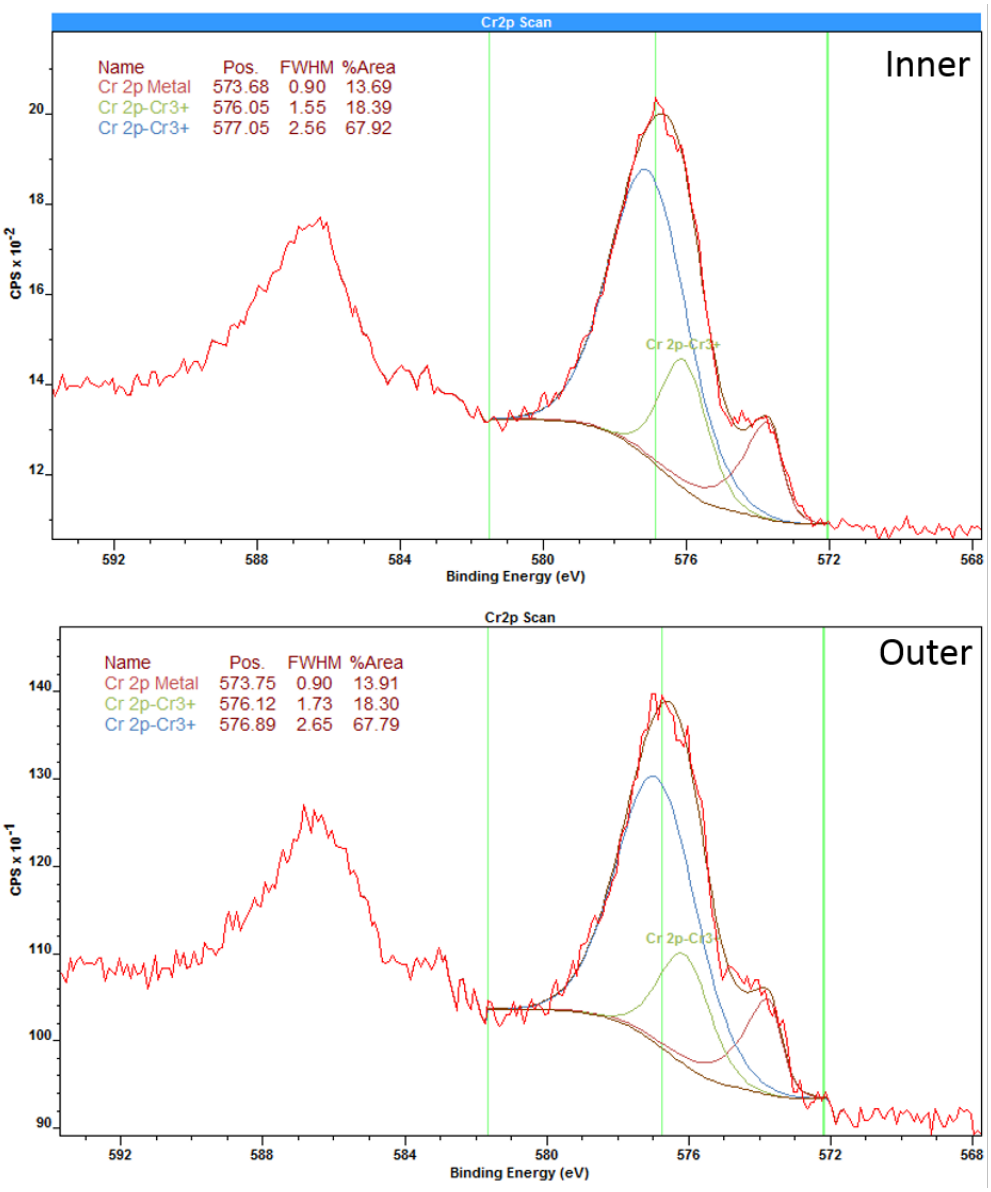

Figure 3.30: Cr 2p XPS spectra of the inner and outer surfaces.

Fe 2p Like the Cr 2p spectra the Fe 2p spectra is fitted with three peaks with the metal peak being given the asymmetric lineshape identified by Biesinger et al[69]. Constraints were added to limit the FWHM of the metal peak below 0.9 eV. With the excpetion of the metal all Fe 2p peaks show multiplet splitting with the 3+ species all covering the same range of roughly 710-720 eV[69] with the bulk of the intensity being at the lower energy. It is therefore safe to say that the iron species are mainly in the 3+ state although further identification is not possible. Fe(II) typically has a BE of ∼708 eV[69]. There is no obvious peak in this location but since this is between the metal and Fe(III) species there may be some present which is obscured. Once again there is no significant difference discernible between the surfaces.

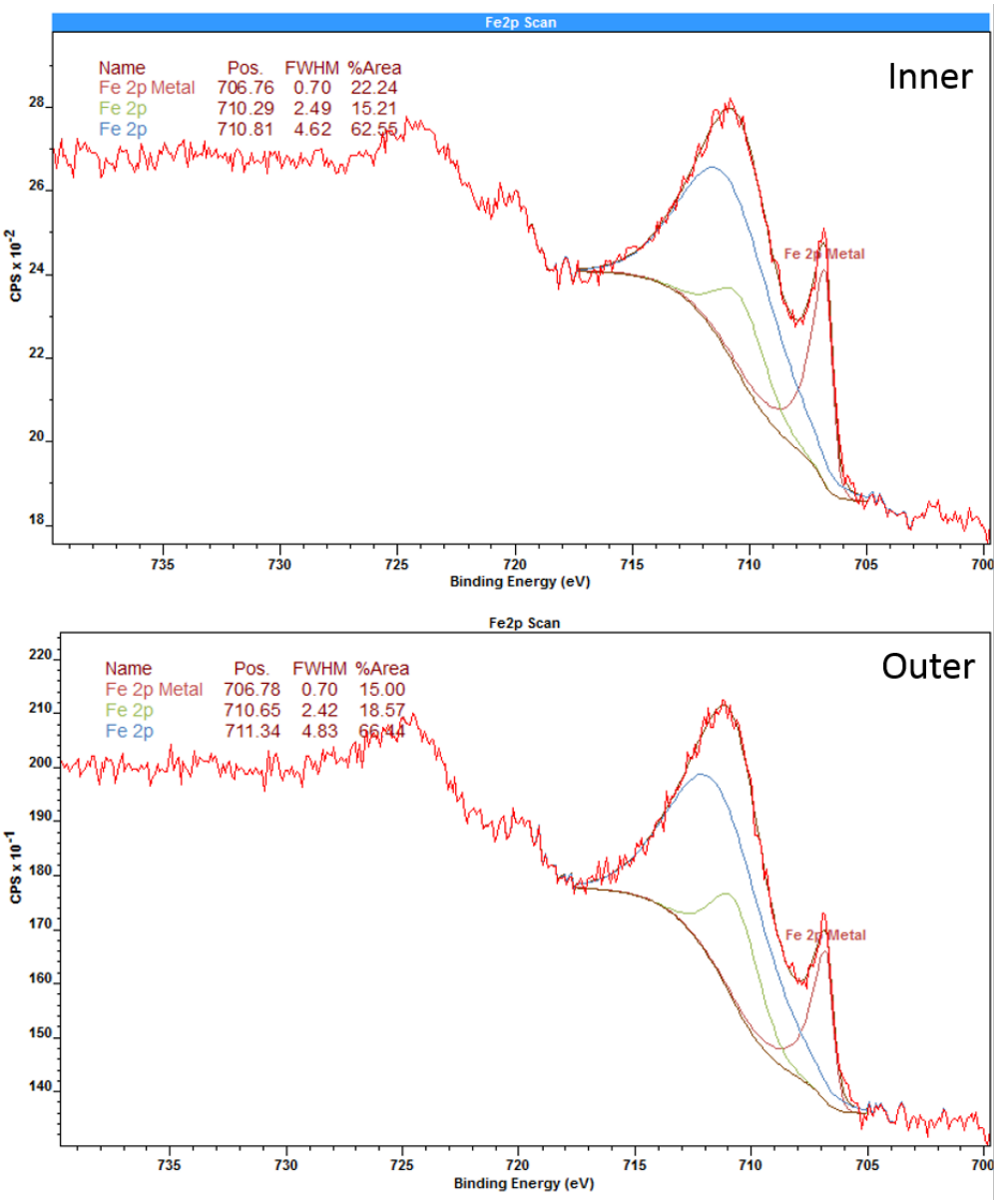

Figure 3.31: Fe 2p XPS spectra of the inner and outer surfaces.

Ni 2p The metal peak for Ni 2p exhibits splitting and typically appears as three peaks. The LA line shape from Biesinger et al[69] was employed as were the peak spacings. The largest nickel metal peak is normally at around 852.6 eV and accounts for ∼80% of the overal Ni2p peak. The fact that this peak is found to account for 90% means that there is virtually no oxidised Ni species present which is as expected. The difference between the expected proportions of each peak and those found could be due to using different machines and settings of the matrix effects as a result of the data presented here being taken from a stainless steel rather than a pure chromium sample. Both surfaces show similar behaviour.

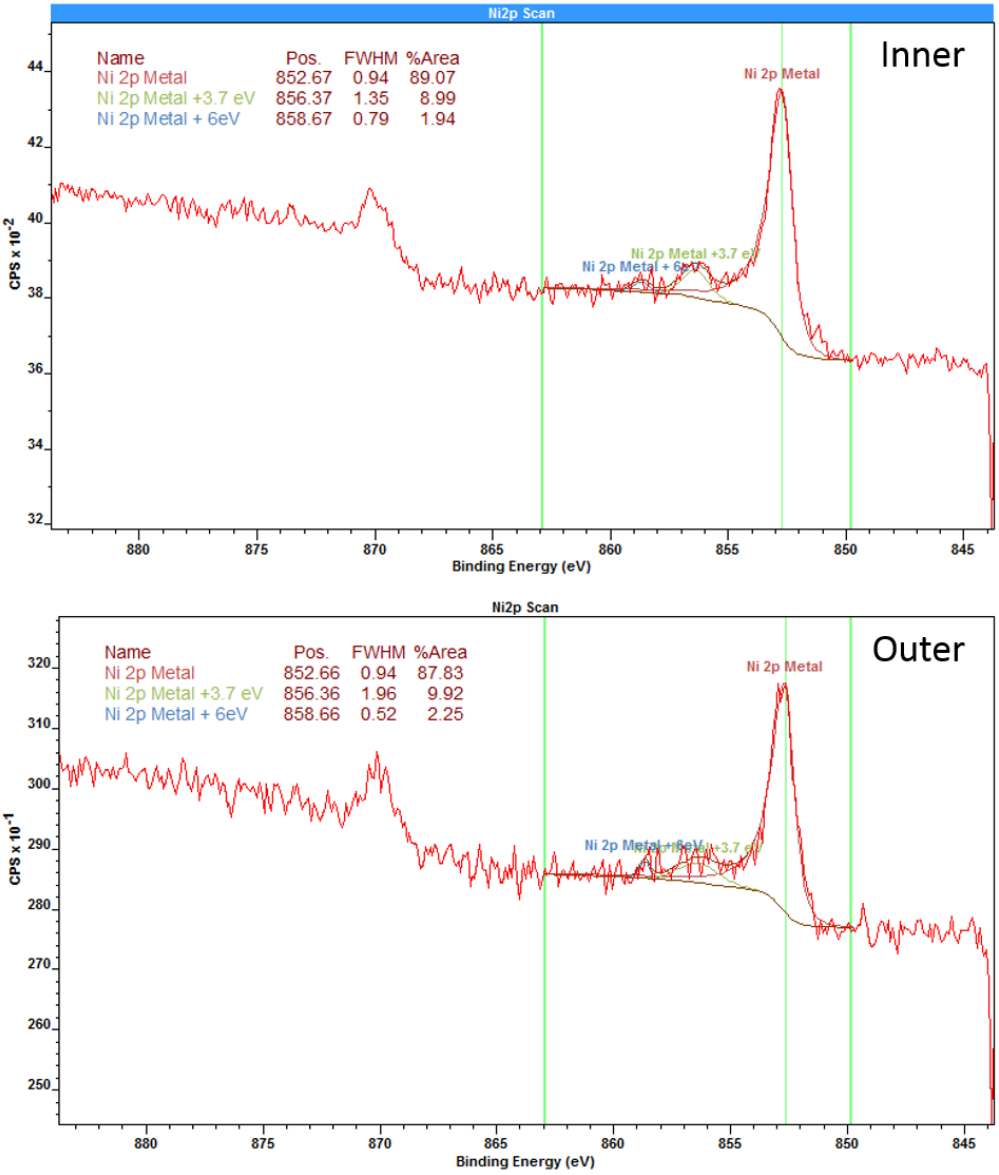

Figure 3.32: Ni 2p XPS spectra of the inner and outer surfaces.

Session 1 Summary The bulk composition of the two surfaces appears to be broadly similar. There appears to be a difference in the quantity of iron and chromium present in the two surfaces. From the high resolution spectra of Cr 2p and Fe 2p the chromium peak is predominantly hydroxide with some metal and 3+ oxide. All Fe(III) species tend to exhibit in the same region and as such it is

difficult to identify specifically what is present (i.e.oxide or oxyhydroxide).

The inner surface C1s peak appears to have a greater contribution from the C-C/C-H peak and consequently less from the C-O and C=O.

3.6.3 XPS Session 2 Results

When the data from the first XPS session was first analysed and the large carbon peak was observed it was decided that a further XPS session would be carried out in which the sample surface was argon sputtered in an attempt to clean some of the carbon from the surface. At this stage detailed analysis of the spectra had not been carried out and the proportion of organic oxygen was not known. The aim was to reduce the carbon peak without significantly altering the oxygen peak since argon sputtering is known to reduce metals which would in turn impact the oxygen peak. Consequently the surface was sputtered in stages with survey spectra being taken after each stage and the relative sizes of the peaks being assessed.

The results of this sputtering is seen in fig. 3.33. High resolution spectra were taken for both samples after 180 s sputtering time as at this time there was no significant impact on the size of the O 1s peak but a significant reduction in the C 1s. Further sputtering carried out beyond this led to a reduction in the O 1s which confirms the high resolution spectra were taken at around the right point based on the criteria described above.

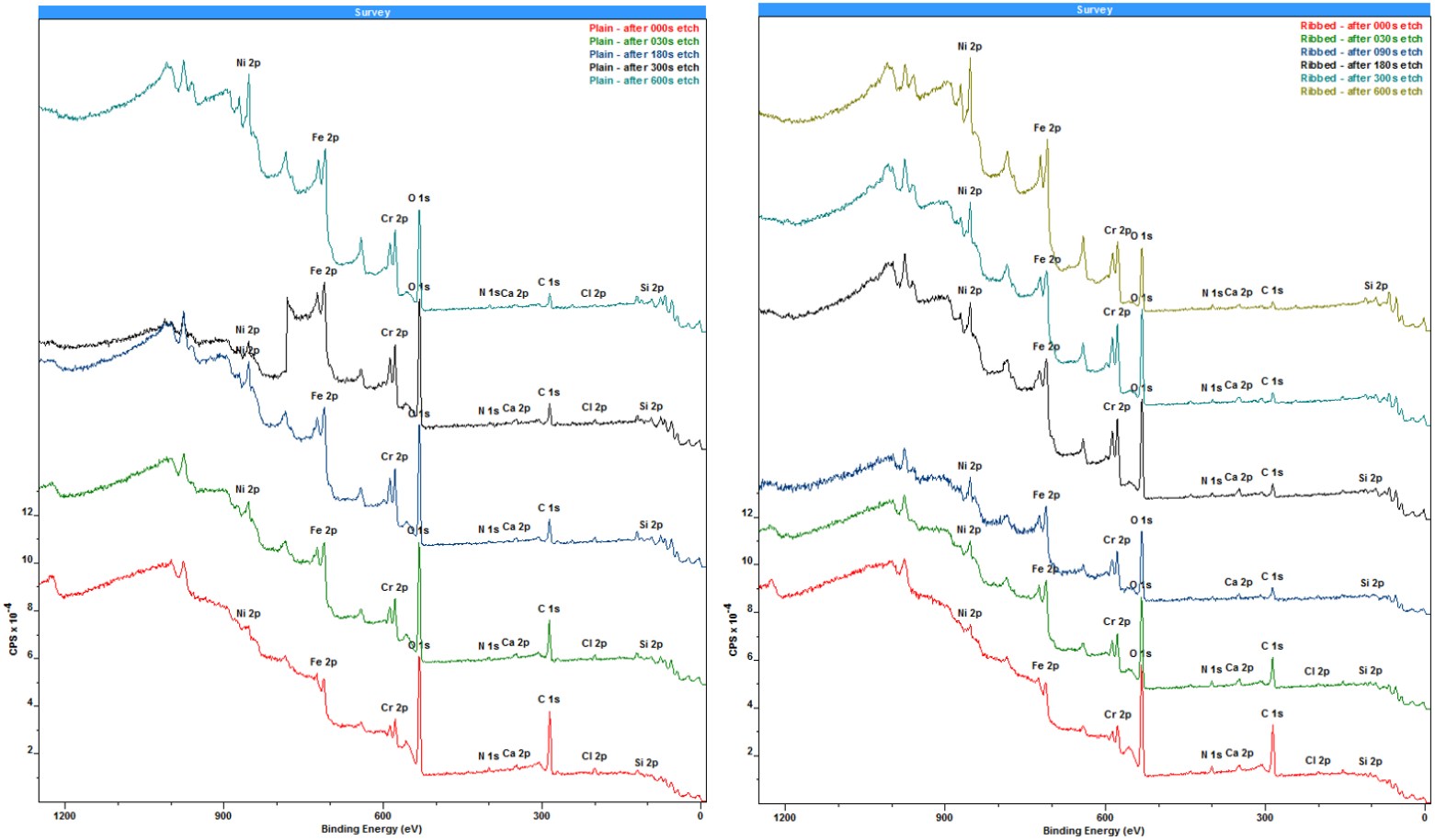

(a) Inner surface.

(b) Outer surface.

Figure 3.33: Survey spectra after various sputtering times.

Element	Atomic %	
	Inner	Outer
C 1s	28.11	22.04
Ca 2p	1.11	2.18
Cl 2p	2.78	1.43
Cr 2p	9.56	12.35
Fe 2p	15.08	17.25
N 1s	1.30	2.41
Ni 2p	1.52	1.96
O 1s	38.36	37.09
Si 2p	2.17	3.30

Table 3.5: Bulk composition after 180 s sputtering time.

The composition of the material after 180 s sputtering (taken from the high resolution spectra) is shown in table 3.5). In comparison to the non sputtered surface there has been an increase in O1s from ∼28% to ∼38%, in Cr 2p from 2-3% to 9-12%, Fe2p from ∼2% to 15-17% and Ni2p from 0.4% to 1.5-2%. These increases have been accompanied by a reduction in C1s from ∼60% to <30%. The remaining minor elements are unchanged.

Once again the atomic composition has been adjusted to wt% in table table 3.6. The quantity of chromium has now increased to 24-28wt%, iron has increased to ∼41wt%, nickel is close to 5wt% and oxygen is 25-30wt%. These values are roughly what one would expect from a stainless steel oxide being enriched in chromium. In both cases the quantity of iron is greater than chromium suggesting that more of the inner Fe rich layer and bulk metal are being detected for both surfaces however the low nickel concentration suggests that little of the bulk metal is being detected. The two surfaces are however more similar than the same data for the non-sputtered samples making it difficult to draw any firm conclusions about the two oxide layer. Nevertheless analysis of the high resolution spectra is presented below.

	wt%	
Element	Inner	Outer
O 1s	30.0	25.6
Cr 2p	24.3	27.7
Fe 2p	41.3	41.7
Ni 2p	4.4	5.0

Table 3.6: Bulk wt% composition after 180 s sputtering time.

C 1s A comparison of the two surfaces would seem to indicate that the outer surface has less carbon and more of the transition metals suggesting that the outer surface began with a thinner carbon layer than the inner surface. This would however be a contradiction to the evidence presented earlier. The difference in the proportions of the various peaks indicates that the inner surface has a greater quantity of C-C than C-O and C=O. This suggests that the carbon layer on the surfaces is itself layered with the outer layer containing more C-C than the inner layer.

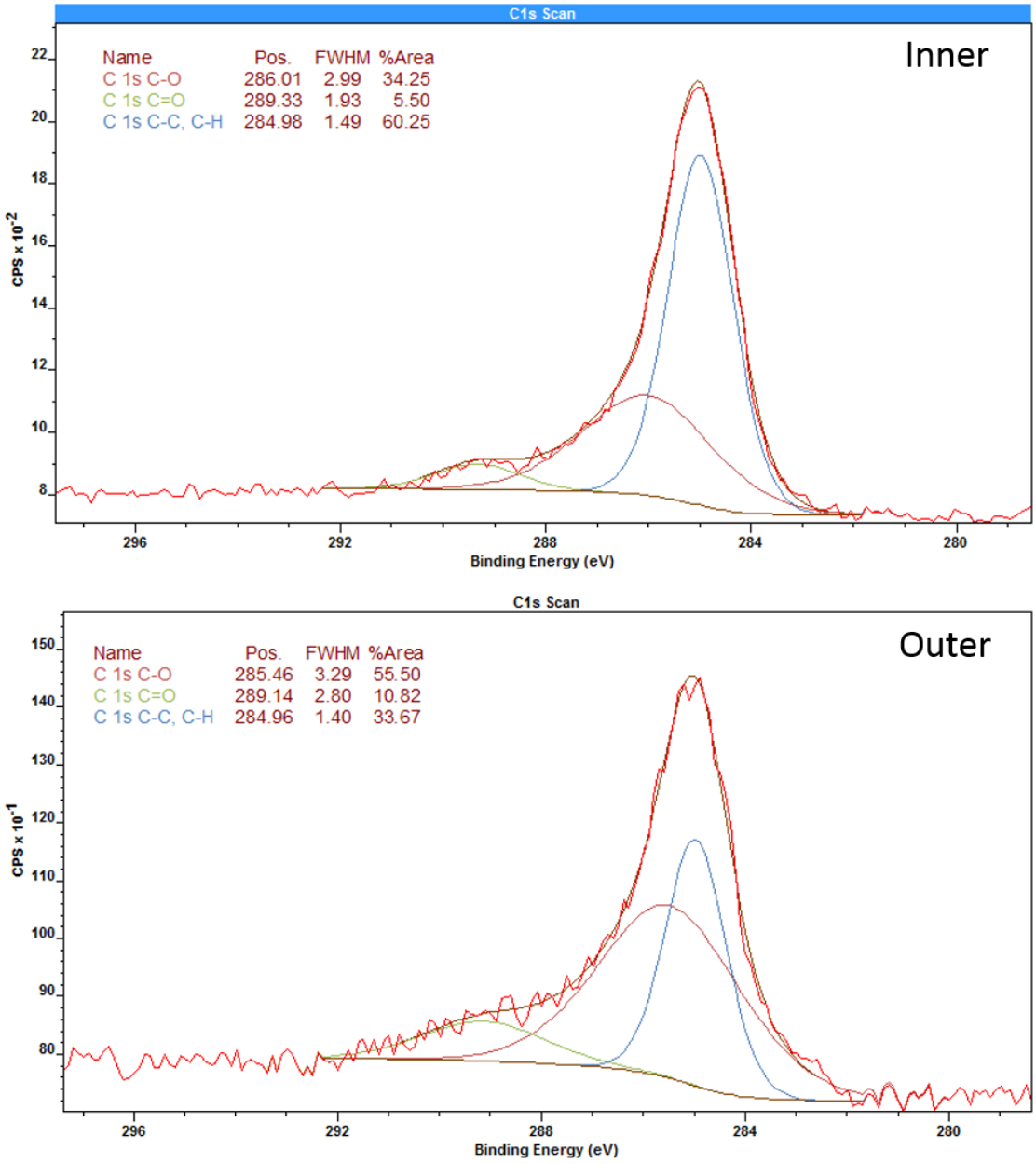

Figure 3.34: C 1s XPS spectra of the inner and outer surfaces after 180 s sputtering.

O 1s The O 1s spectra following sputtering shows a greater proportion of oxide on the outer surface. This may once again be due to the removal of more of the organic carbon overlayer (some of which is included in the hydroxide peak) therefore more of the underlying metal oxide is apparent.

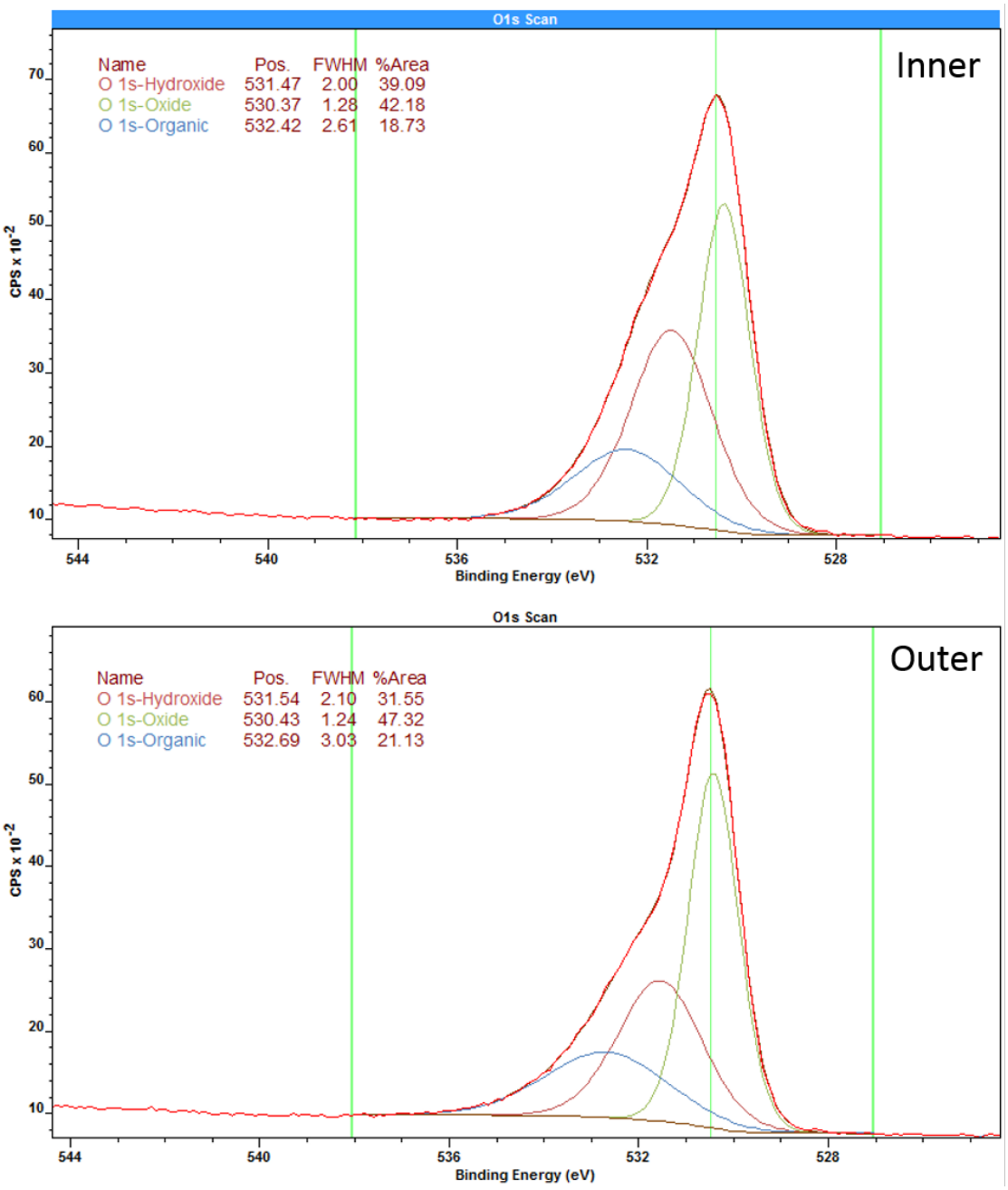

Figure 3.35: O 1s XPS spectra of the inner and outer surfaces after 180 s sputtering.

Cr 2p For both surfaces the peak identified as hydroxide has now increased in FWHM maximum suggesting that a further species is present in this region. Strangely there is also a reduction metallic Cr 2p which goes against expectations

since more penetration into the bulk metal would be expected and is confirmed by the slight increase in nickel seen in table 3.6. There is now an apparent difference between the surfaces with the inner surface having approximately 10% more hydroxide. The inner surface has less metal present which suggests the overall oxide layer (iron and chromium) may be thicker.

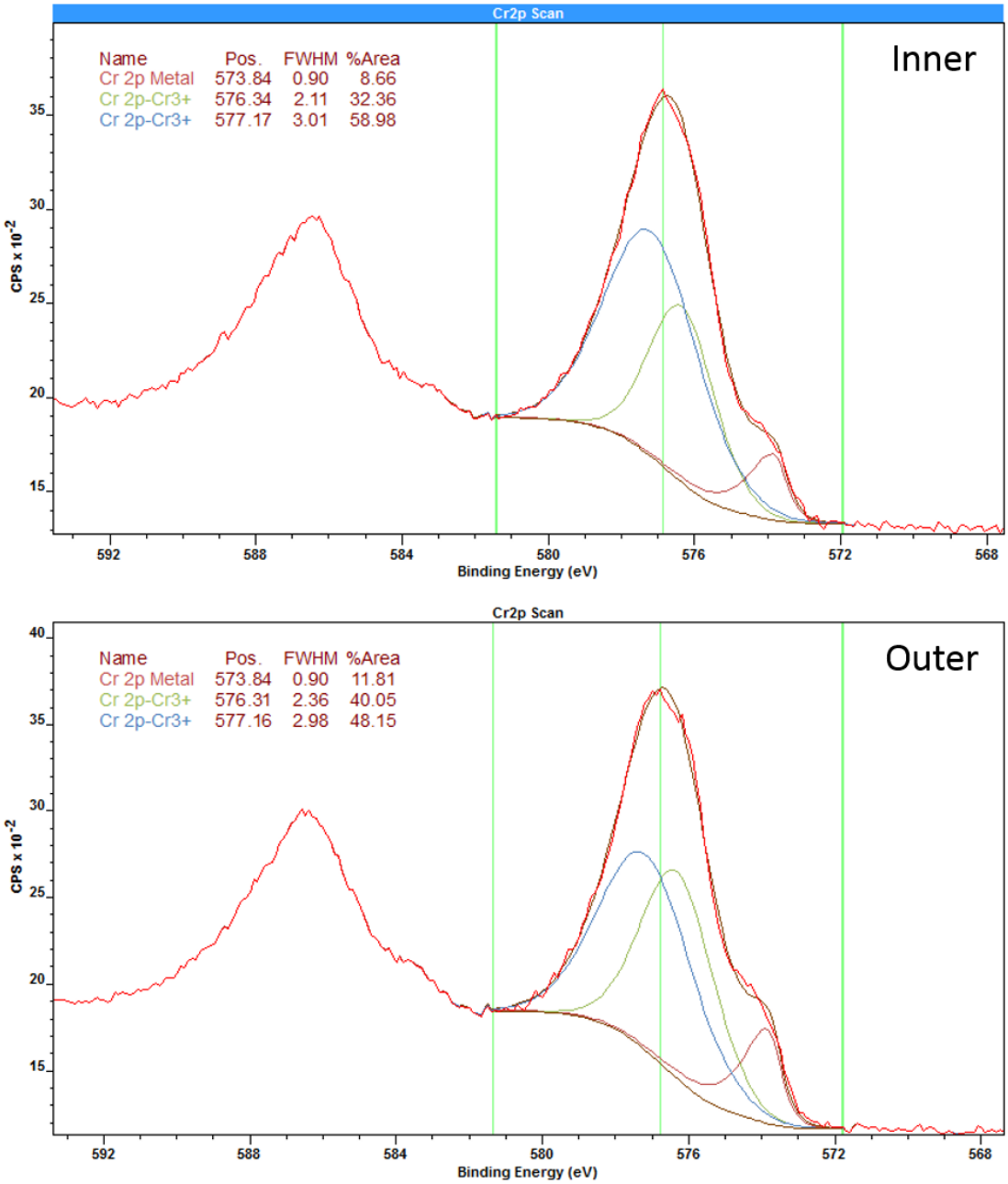

Figure 3.36: Cr 2p XPS spectra of the inner and outer surfaces after 180 s sputtering.

Fe 2p The sputtered iron surfaces appear to contain less Fe metal overall which suggests that the overall stainless steel oxide layer is thicker which is contrary to

expectations since the surface has been sputtered. There are however differences between the two surfaces since the outer surface has more than twice as much Fe metal suggesting that the outer surface oxide is thinner.

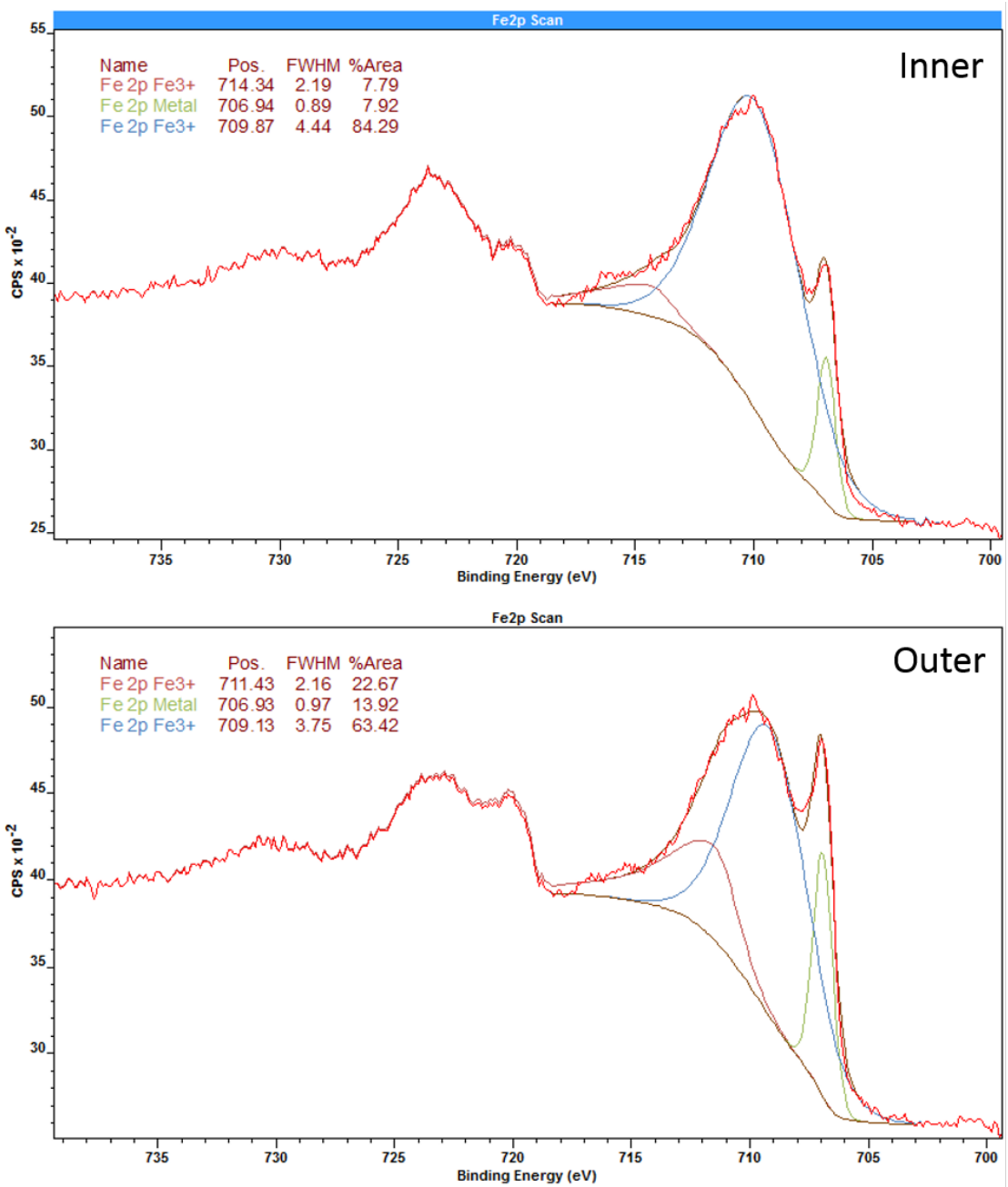

Figure 3.37: Fe 2p XPS spectra of the inner and outer surfaces after 180 s sputtering.

Ni 2p The difference in the relative size of the peaks compared to the literature suggests that there are now more Ni(III) species present particularly on the outer

surface from which more carbon is thought to have been removed.

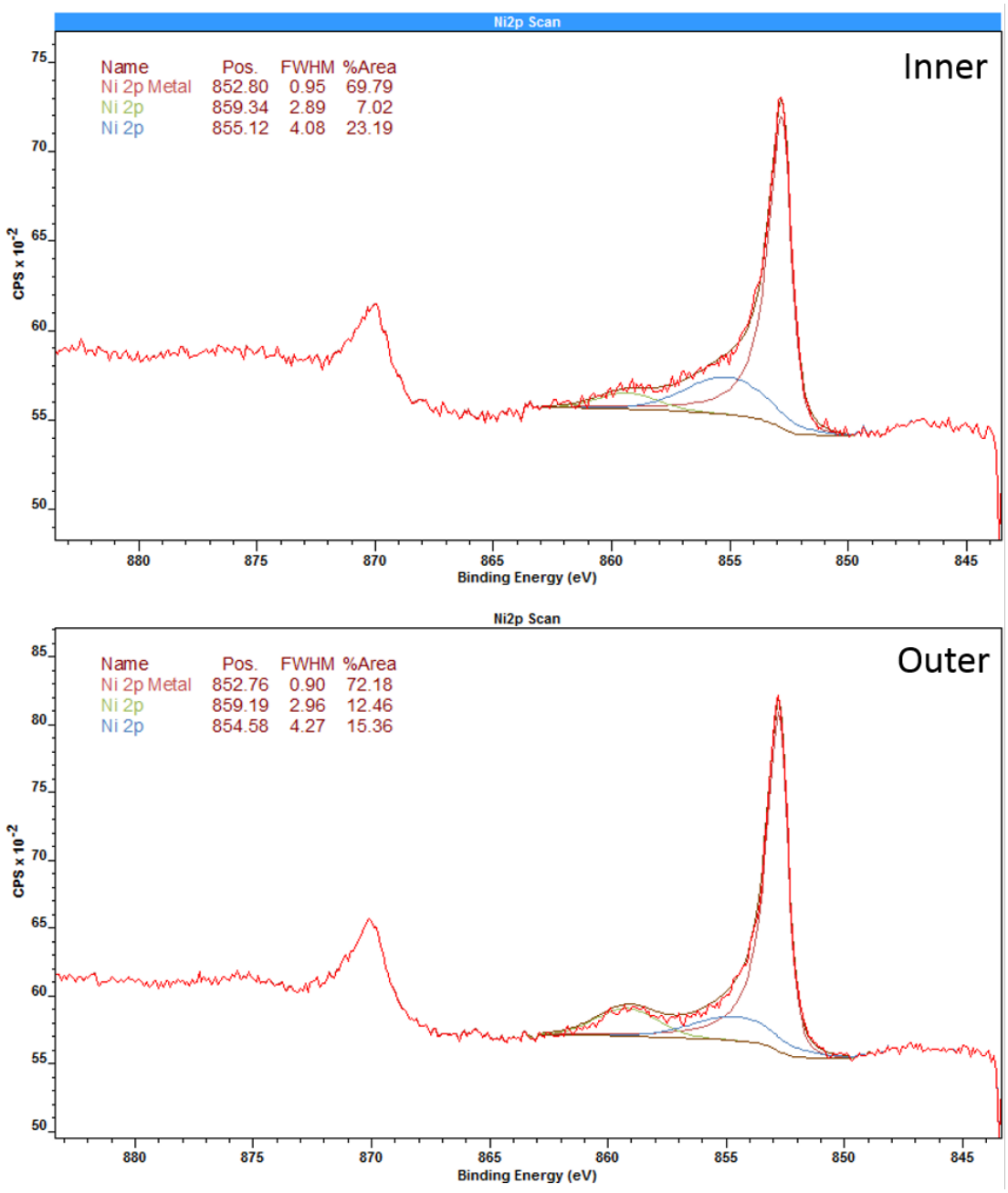

Figure 3.38: Ni 2p XPS spectra of the inner and outer surfaces after 180 s sputtering.

Session 2 Analysis The sputtering of the surfaces to remove carbon contamination has been shown to have some impact with greatly reduced levels of carbon however it has not cleaned the surfaces sufficiently to allow the detailed surface analysis which it had been hoped would allow a detailed comparison of the surface. Comparison of the two surfaces appears to show some differences which were not apparent before sputtering however due to the many variables, some contradictory evidence and the apparent thickness of the carbon layer it is not possible to draw any firm conclusions on differences in oxide composition.

3.6.4 Discussion and Conclusions

XPS is an incredibly powerful tool for surface analysis being highly sensitive to the top ten or so nanometers of a surface. Unfortunately the technique also requires a surface free from contamination. In most cases samples would be mechanically cleaned and polished or subjected to aggressive chemical cleaning techniques before examination to remove any surface contamination which would in this case remove the surfaces of interest so such techniques were not possible. It had been hoped that the cleaning methods used would be sufficient to remove enough adventitious carbon to allow some sort of analysis. The fact that this combined with sputter cleaning did not allow this suggests that the samples have a significant level of carbon on the surface.

In an ideal world it would potentially be possible to produce a better model of the oxide using a number of well characterised reference compounds such as pure transition metals and there oxides and hydroxides in there pure form. although this would be complicated by the presence of several minor elements such as silicon and calcium all of which are likely to contribute to one or both of the O 1s and C 1s spectra to one degree or another introducing yet more unknown variables. It would seem likely that such work could be carried out if it was deemed necessary however based on the time and effort that would be required it was felt to be outside the scope of this work.

The analysis that was carried out seems to indicate that the oxide layers are of the form that would be expected being a mixture of chromium and iron species. The positioning and size of the chromium peak indicates that much of the

chromium oxide layer consists of chromium hydroxide. This indicates that there is likely to be some chemically bound water within the AGR cladding oxide.

Based on the proportion of chromium in the oxide layer and the proportion of that which is hydroxide roughly 20wt% of the overall oxide layer is likely to be chromium hydroxide (12wt%Cr and 8wt%OH).

3.7 TEM/EDX

In addition to the XPS analysis the inner and outer surfaces of the AGR cladding were analysed by TEM/EDX.

3.7.1 Methodology

Three TEM sections were prepared using a focused ion beam and then analysed using an FEI Titan Themis 300 STEM machine operated at 300kV fitted with a Gatan OneView 16 Megapixel CMOS digital camera and the Super-X EDX system. The first section was cut from the outer surface and was not cleaned prior to preparation while the two later sections were cleaned with one coming from each of the two surfaces.

An EDX map was taken of the top surfaces of all three samples and for the two cleaned surfaces a linescan was taken from the platinum strap to a depth of ~20nm into the sample. The linescan was averaged over a width of 10 pixels to reduce the noise.

3.7.2 Results

Uncleaned Samples

Figure 3.39 shows an SEM image and EDX maps of the un-cleaned section. Figure 3.41a is the SEM image and three layers are clearly evident. The EDX maps show that the top layer is the platinum strap used to produce the TEM section. Below this is layer approximately 200 nm thick consisting mainly of carbon but also seems to include particles rich in calcium and oxygen. The metal itself is below this layer.

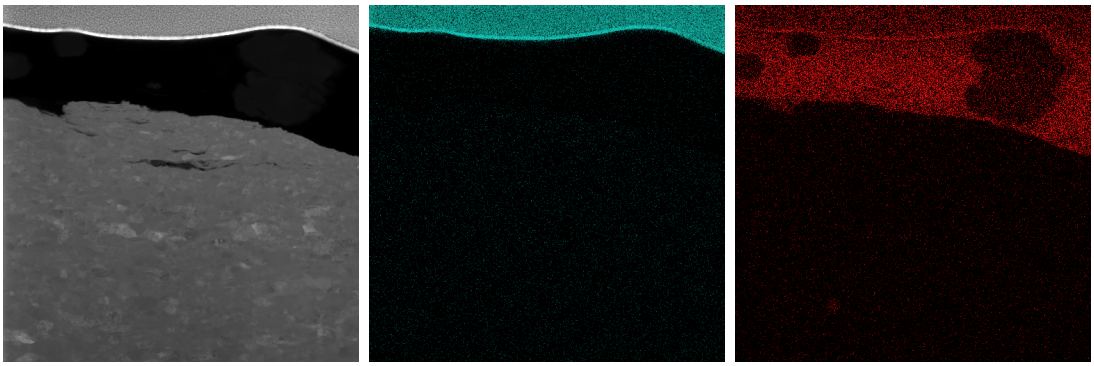

(a) TEM image. (b) Platinum (c) Carbon

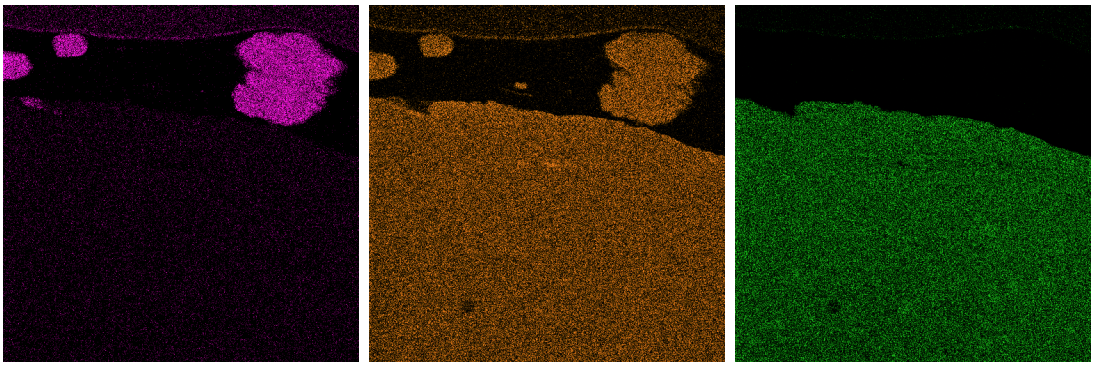

(d) Calcium. (e) Oxygen. (f) Chromium.

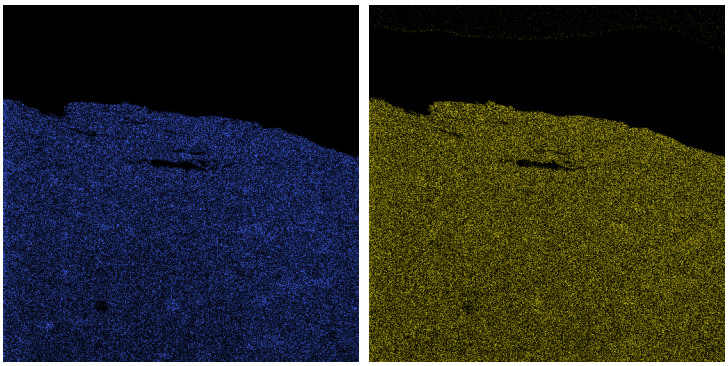

(g) Iron. (h) Nickel.

Figure 3.39: TEM image and EDX maps of the uncleaned cladding sample.

Cleaned Surfaces

Figure 3.40 and fig. 3.41 show similar images for the cleaned samples. There is no apparent evidence of a carbon layer on these samples and also no evidence of any calcium. The inner surface does show an apparent sulphurous inclusion.

Figure 3.42 shows the SEM image and EDX plots for the inner surface with the SEM image of the area examined supper imposed on top. The platinum from the strap used to produce the TEM samples drops steadily and can be considered to have reached zero at around 8 nm (this is important as a datum only). The oxygen starts at around 1.5wt% (which can be regarded as zero), peaks as the Pt reaches zero and then drops sharply back to zero at 10 nm however the magnitude of the peak is minimal reaching a maximum of only 3.5wt%. The three metals all show the same basic behaviour increasing from a negligible level (in the Pt strap) and plateauing at a value equal to its concentration in the bulk metal. The only obvious difference is the distance at which this plateau is reached. The Cr plateaus first again at a depth of 8 nm (which is at the surface of the cladding) followed by the Ni and Fe at ∼10 nm. The Fe peaks at around 43wt%, the Cr at 16wt% and the Ni at 20wt%.

The EDX linescan plots for the outer surface is shown in fig. 3.43. As one would expect the behaviour of the Pt plot on the outer surface is almost identical to that on the inner surface and it even approximates zero at 8 nm once again. The general behaviour of the oxygen plot is also broadly similar showing rising up to a peak before dropping sharply back to zero. The peak is however much higher and broader rising from <1wt% to nearly 8wt% at close to 8 nm and remaining at that level for 2 nm and does not reach zero again until a depth of nearly 13 nm. The shape of the peak suggests it could in fact be two overlapping peaks. Unlike the inner surface the Cr and Ni plot on the outer surface both show clear peaks. The Cr reaches a maximum of 22.5wt% at 8 nm before dropping to a minima of ∼14wt% at 13 nm and slowly rising back to the 17wt% value found in the bulk. The Ni peak is of a similar shape but is somewhat delayed peaking at a depth of 11 nm at 27 wt% holding that for 2 nm and then dropping to the bulk value. The Fe once again rises steadily plateauing after around 15 nm although a slight shoulder is evident at 11 nm.

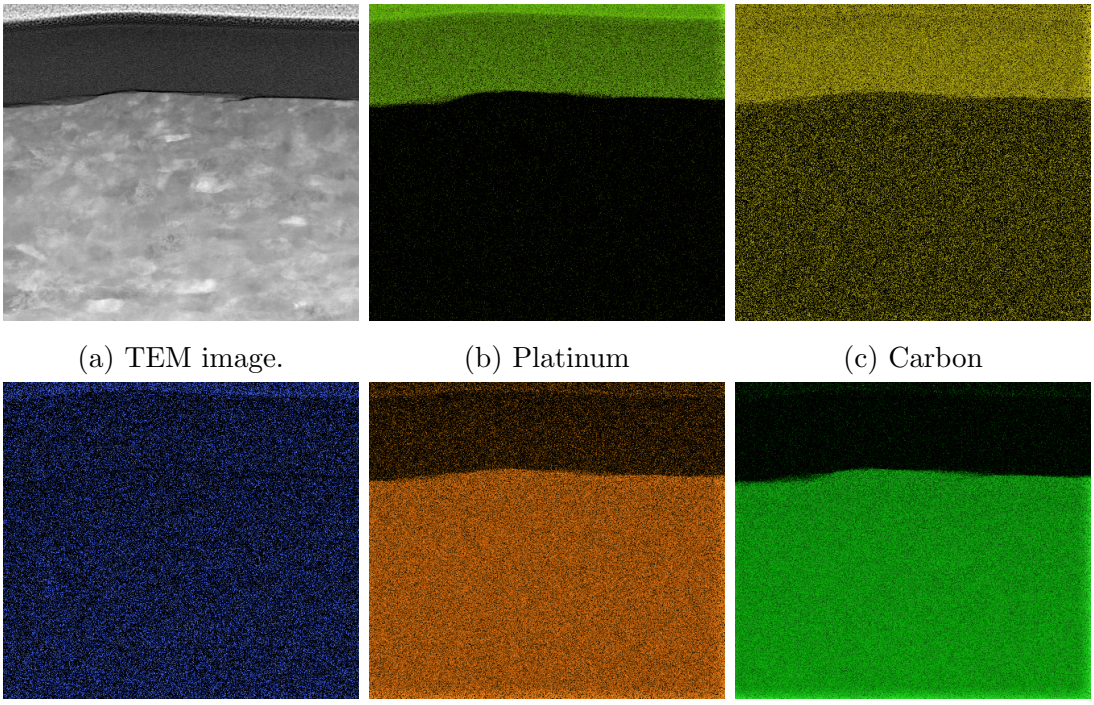

(a) TEM image. (b) Platinum (c) Carbon

(d) Calcium. (e) Oxygen. (f) Chromium.

(g) Iron. (h) Nickel.

Figure 3.40: TEM image and EDX maps of the cleaned outer cladding sample.

Linescans for the minor elements, S, C, Si, N and Ca are shown in fig. 3.42b and fig. 3.43b. For the outer surface Ca appears on the linescan at low levels which were not visible on the map above but are similar to those found by XPS. This disappears at a depth of 8 nm as the oxide layer begins as does the S and N. Only the Si and C seem to play any role in the oxide layer. The Si appears to exhibit a small peak at ∼9.5 nm after which point it drops away abruptly while the C which is used in the production of the Pt strap has reached a background level as the oxide ends and the bulk metal begins. None of the minor elements appear to play any role in the oxide formation of the inner surface as they all reach zero at around 8 nm.

3.7.3 Discussion and Conclusions

The presence of the thick calcium carbonate containing carbon layer on the uncleaned sample is somewhat surprising however it does explain the XPS data despite the XPS spectra being taken on cleaned samples. Due to the thickness of the layer it would be extremely difficult to remove all of this layer across the entire sample. Since the XPS spectra is taken with a spot size of 500 μm the overall area analysed would be in the region of 2.5 x 10^{11} nm^2. In comparison the EDX linescan covers an area of only 5000 nm^2. As a result while it would be easy for the EDX to miss any traces of the carbon layer, it would be virtually impossible for these to be missed by XPS. While this does not explain how the samples have become contaminated in calcium carbonate it does explain the surprising presence of Ca in the XPS spectra taken.

The EDX linescans of the two surfaces show a clear difference in the oxide layer of the two surfaces. On both samples the metal can be regarded as beginning at a depth of 8 nm as the platinum reaches zero and on both surfaces the oxygen peaks at this depth indicating the start of an oxide layer. The outer surface shows a clear peak in the oxygen levels with the width of this peak (at the base) suggesting that the oxide is close to 5 nm thick. The fact that there is a peak in Cr followed by a minima as the oxide ends suggests that there has been chromium diffusion. The slight shoulder in the Fe plot indicating a drop in the rate of increase may be evidence of Fe diffusion but to a much lesser extent. The peak in Ni appears

as the oxide layer ends which would seem to confirm that there has been Cr and Fe diffusion to form an oxide layer that is rich in Fe and Cr leaving a region of Fe and Cr depletion behind it which is in general agreement with the XPS data. The fact that the Cr concentration begins to drop before the O suggests that there are multiple layers within the oxide layer and this would seem to be confirmed with the shoulder in the Fe plot and the apparent peak in Si. The resolution is not sufficient to confirm this but the overall indication suggests that there is an outer layer which is rich in Cr and an inner layer rich in both Fe and Cr separated by a very think Si rich band. This is similar to that observed by Desport and Bennett[33].

In comparison the inner surface showed no signs of peaks for any of the elements except O and even this is only a minor peak. Since the chromium reaches its maximum before the Fe and Cr and at the point at which the O peak begins to decline there is an indication that there is a very thin 2 nm chromium rich layer however there is no sign of the multilayer structure seen in the outer surface.

If the oxide layer is taken to be 10 nm this would mean a 1 cm^3 area of cladding would have an mass of around

3.8 Stress Corrosion Cracking

As discussed in section 2.2 two forms of water are a concern for the drying of spent nuclear fuel. The majority of the work discussed above has looked at bound water however a further issue is that of trapped water. In the early years of fuel storage failures of spent fuel were attributed to IGC and while the changes in pond chemistry appear to have prevented further failures the possibility of microcracked fuel pins becoming flooded over decades in a pond is regarded as being a serious concern. It is therefore felt that tests will have to be carried out on microcracked samples to ensure that water could be extracted through such cracks. In order to this it was flet to be necessary to produce lengths of cracked stainless steel tube in which water could be sealed.

3.8.1 Methodology

SCC tests were initially carried out with small lengths (∼10mm) of 12 and 15 mm outside diameter 304 tube with 1 and 1.5 mm wall thickness respectively. These tests were then repeated with longer lengths (∼60 mm) of 15 mm 304 tube and finally short lengths of AGR cladding. The 304 tube was first heated to 1050°C for 60 minutes in argon and then quenched before being sensitised at 650°C for 24 hours. The AGR cladding was annealed at 1200°C for 30 minutes in argon and then sensitised for 1200 hours at 500°C.

There are two ASTM standards relating to SCC. ASTM G38 uses C-rings to induce stress throughout the wall of a sample which can then be treated to induce SCC. This is not suitable for this work since an intact length of tube is required. Consequently lengths of tube were compressed between two stainless steel plates as seen in fig. 3.44. Compressing the tube in this manner induces stress in the inner surface at 12 and 6 o'clock fig. 3.44 and in the outer surface at positions 3 o'clock and 9 o'clock. These rings were then immersed in boiling 42wt% $MgCl_2$ for 28 days. The stainless steel ring was insulated from the compression plates with PTFE to avoid any galvanic corrosion effects.

For micro CT analysis two sections were cut from the corroded 12 mm outside diameter 304 tube at the 12 and 3 o'clock positions as indicated in fig. 3.45 (samples 304-12 and 304-3 respectively seen in fig. 3.48a and fig. 3.48c).

The sections of tube were then assessed by SEM and micro CT to assess the size and penetration of any cracks formed. X-ray micro CT was carried out using a Bruker Skyscanner 1172 by Dr SJ Brookes, School of Dentistry, University of Leeds (key parameters are shown in table 3.7). Full scale reconstructions and videos were supplied by Dr Brookes as were individual bitmap images of each slice. Further images of the crack were produced by isolating the area containing the crack from the full scale images using ImageJ. The isolated slices were then processed using Digiutilty to isolate the crack from any artefacts produced from the imaging process and then converted into a negative image to allow the crack size to measured and 3D images to be produced. While it was not possible to remove all artefacts without obliterating the crack itself it was possible to clean the image so that the crack was clearly visible.

Parameter	Value
Source voltage	100 kV
Source current	100 μA
Image pixel size	2.82 μm
Filter	Al + Cu
Exposure	2445 ms
Rotation step	0.280 °
Frame Averaging	5 frames
Reconstruction Program	NRecon

Table 3.7: Micro CT Operating Parameters

3.8.2 304 stainless steel Results

Figure 3.46 shows the small length of 304 tubing and the cracks that were formed. The length has been cut in half to increase the visible surface area. Small cracks are visible under SEM at 12 and 9 o'clock The crack at 12 begins at the inner surface which is under stress while the crack at position 9 begins at the outer surface which is under stress.

SEM Imaging

The images in fig. 3.47 show SEM images of the cracks formed in the 15 mm 304 tube. The crack at position 9 is approximately 500μm long. The width of the crack close to the tip is indicated as being less than 4μm but then tapers to a point and appears to stop. From the images obtained the crack does appear to pass fully through the tube wall, however imaging such as this only allows a small section of the crack to be viewed at one time and it is possible that there are points in at which the crack does pass fully through the wall but is not visible. Both of these cracks were visible to the naked eye.

Figure 3.48 shows some of the cracks formed in the 12 mm 304 tube. Small cracks were found at 12, 3, 6 and 9 o'clock although they were substantially smaller than those found in the 15 mm tube with only one crack being visible to the naked eye at 3 o'clock on the outer surface and then only just, however the size at the

crack tip is comparable to that seen in the 15 mm tube. There is however no evidence that the cracks pass fully through the tube wall with no sign of a crack under SEM on the inner surface.

CT Imaging

Figure 3.49a shows one of 2500 slices that were stitched together to form the 3d reconstruction in fig. 3.49b. The slice shows that the crack spans the full thickness of the metal. This image shows the crack seen in fig. 3.48e. In the SEM images it was not at all clear that the crack passed fully through the material but the CT images show that it does in multiple locations. The CT images also show a second crack is present which had not been otherwise observed.

An area containing the crack was cropped from the full size slices (fig. 3.50a) and a stack of 200 slices was then processed to isolate the crack (fig. 3.50b). This allowed a 3d representation of the crack to be created (fig. 3.50c) and 3.50d). It was not possible to completely isolate the crack alone from artefacts but it was possible to produce a 3d reconstruction in which the crack is clearly visible.

Figure 3.51 shows equivalent images from the 304-12 sample. This crack does not pass through the tube wall.

Based on the 3D reconstruction the total crack length in sample 304-3 is estimated to be 1400μm in length compared to a wall thickness of $\sim$1200 μm. The width of the crack is typically seen to be $\sim$20 μm however it is worth noting that in order to isolate the crack, the size in places will have been effectively increased however in some places the crack will have withered away below the resolution of the machine and therefore while the crack is still there it is not necessarily visible.

Figure 3.52 shows CT images of the samples cut from sensitised and SCC treated cladding. These samples show no sign of any cracking.

Figure 3.53 shows a single slice through fig. 3.49 in the ZX plane from fig. 3.50c at the point where the crack is least contiguous. The red line shows the approximate crack path. The open area of the crack at this point is approximately 18% of the total length. It can therefore be assumed that for cracks of this nature the actual crack length is about 18% of that seen. This may of course reduced for smaller cracks but does at least provide a rough estimate.

3.8.3 Experimental Test Piece Production

Having cracked small lengths of 304 tube a longer length of cracked 304 tube was produced to be used for later drying tests. Upon initial removal from the $MgCl_2$ solution a crack was clearly visible along the outside wall of the tube (fig. 3.54c) at the 3 and 9 o'clock position and in cross section (fig. 3.54a) at the 3 o'clock position. Similar cracks could be seen inside the tube at the 12 and 6 o'clock position. A metal plate was welded onto one end of the tube to seal it and a Swagelok cap fitted over the other end. Due to the deformation during production a certain amount of force was required to fit the Swagelok cap and this led to the crack extending slightly as seen in fig. 3.54b however this section of the tube would be within the cap so this is not major concern. The final test piece for use in later drying tests is shown in fig. 3.54d.

3.8.4 Discussion and Conclusions

The ultimate aim of this part of the project was to produce a length of tube with cracks representative of those found in AGR cladding which could be used for drying tests discussed in part 2 of this thesis. The initial tests of small sections of 304 tube found that it was possible to form cracks in such tube and that the size of these cracks appeared to be similar to those observed in failed AGR cladding. Through the use of micro CT it was found that such cracks did penetrate through the tube wall in multiple places, something that could not be proved with two dimensional microscopy alone, and has been attempted unsuccessfully by the National Nuclear Laboratory. Consequently the method developed was used to produce a test piece in which water could be sealed for later testing.

It was unfortunately found not to be possible to induce cracking in samples of fuel cladding with the same treatment. The likelihood is that it is not possible to sufficiently sensitise 20/25 steel thermally for IGA to occur.

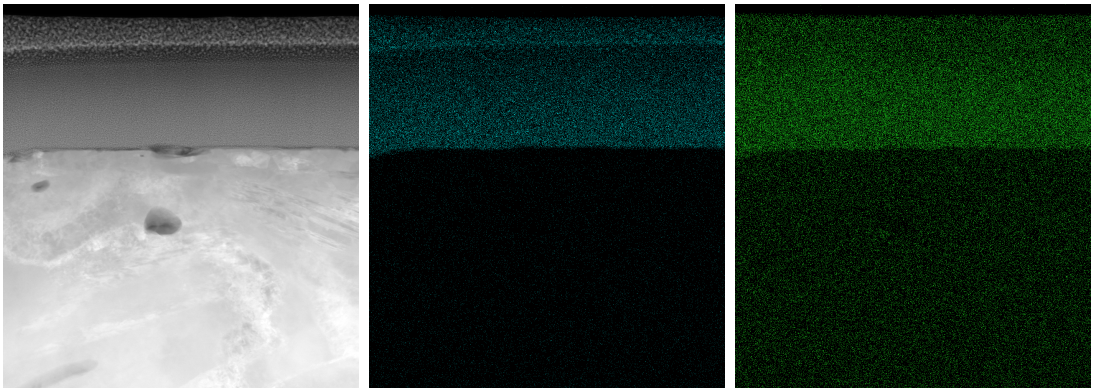

(a) TEM image. (b) Platinum (c) Carbon

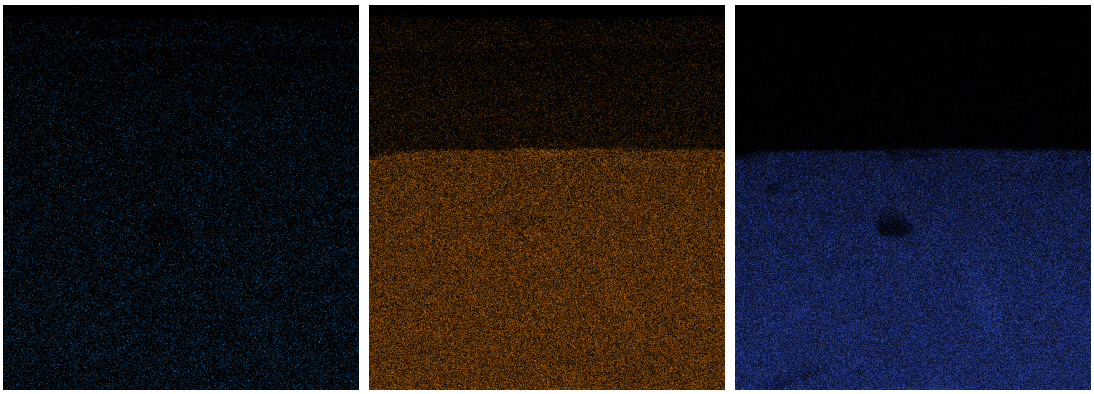

(d) Calcium. (e) Oxygen. (f) Chromium.

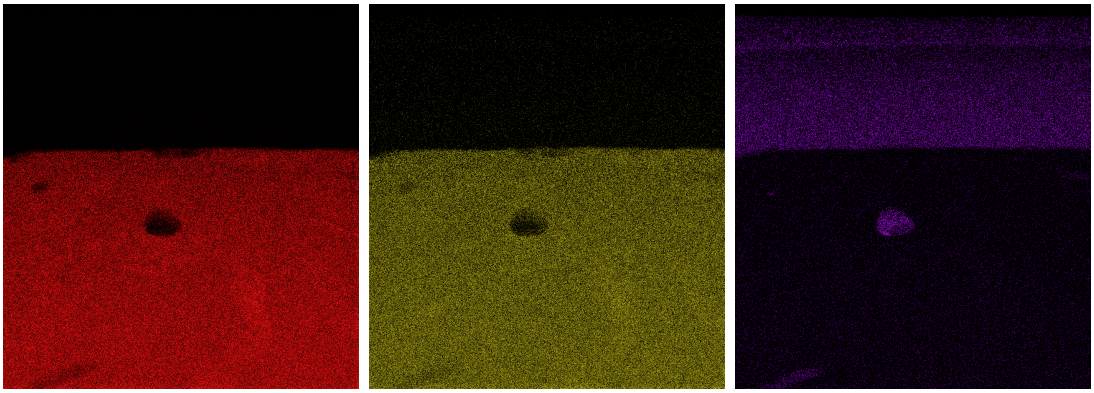

(g) Iron. (h) Nickel. (i) Sulphur.

Figure 3.41: TEM image and EDX maps of the cleaned inner cladding sample.

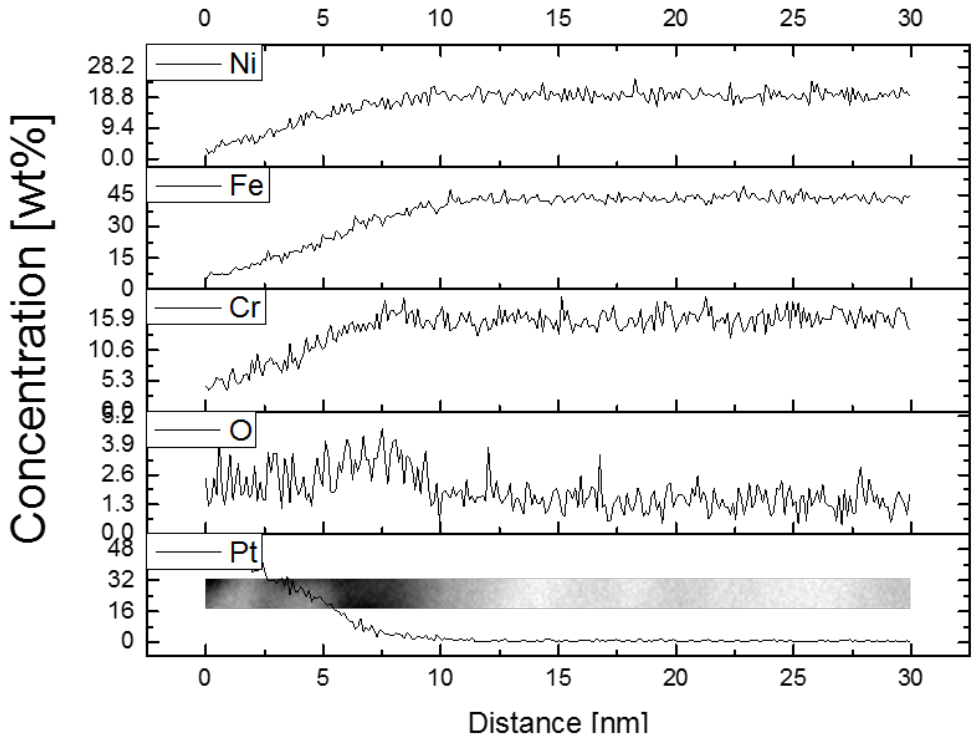

(a) Major elements, O, Cr, Fe and Ni.

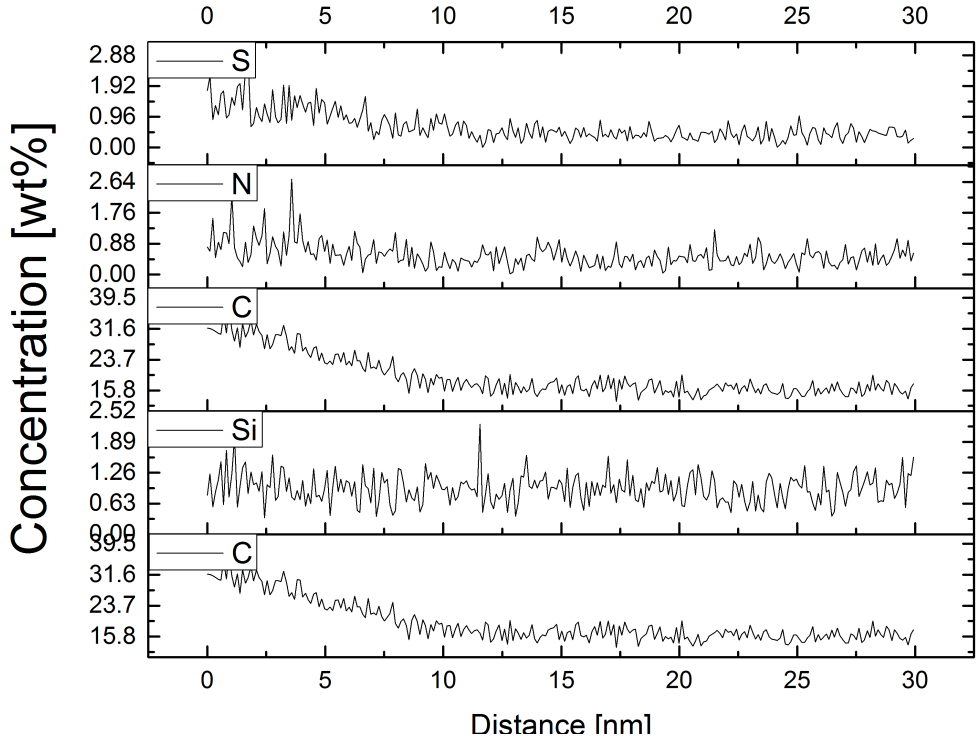

(b) Minor elements S, N, C, Si and Ca.

Figure 3.42: EDX linescan plots of the inner surface. The SEM image of the area scanned has been superimposed.

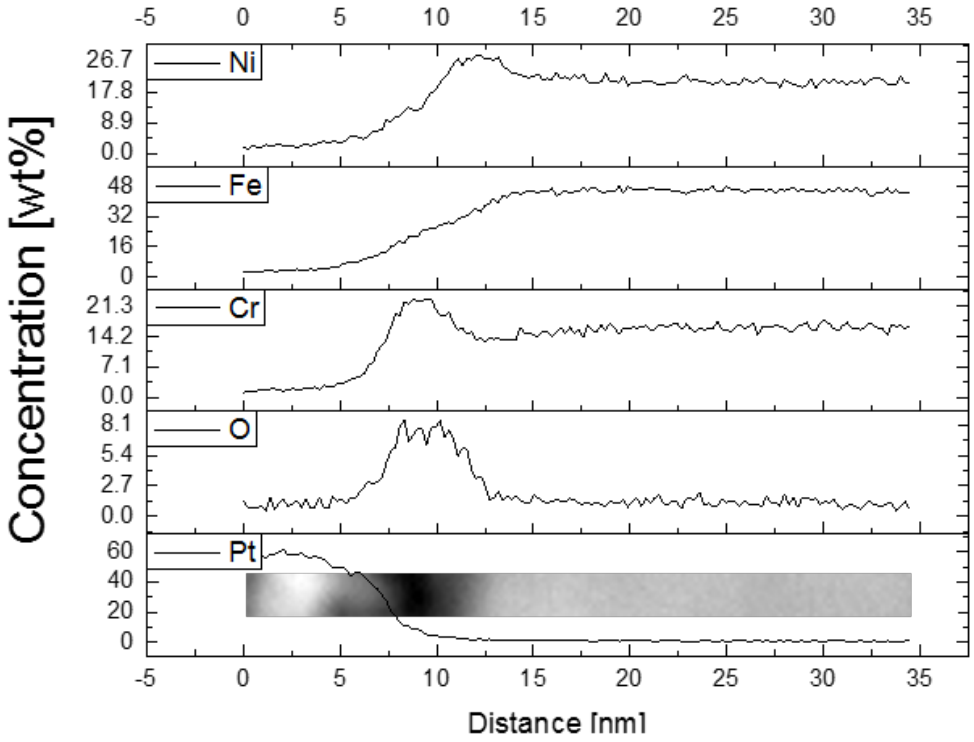

(a) Major elements, O, Cr, Fe and Ni.

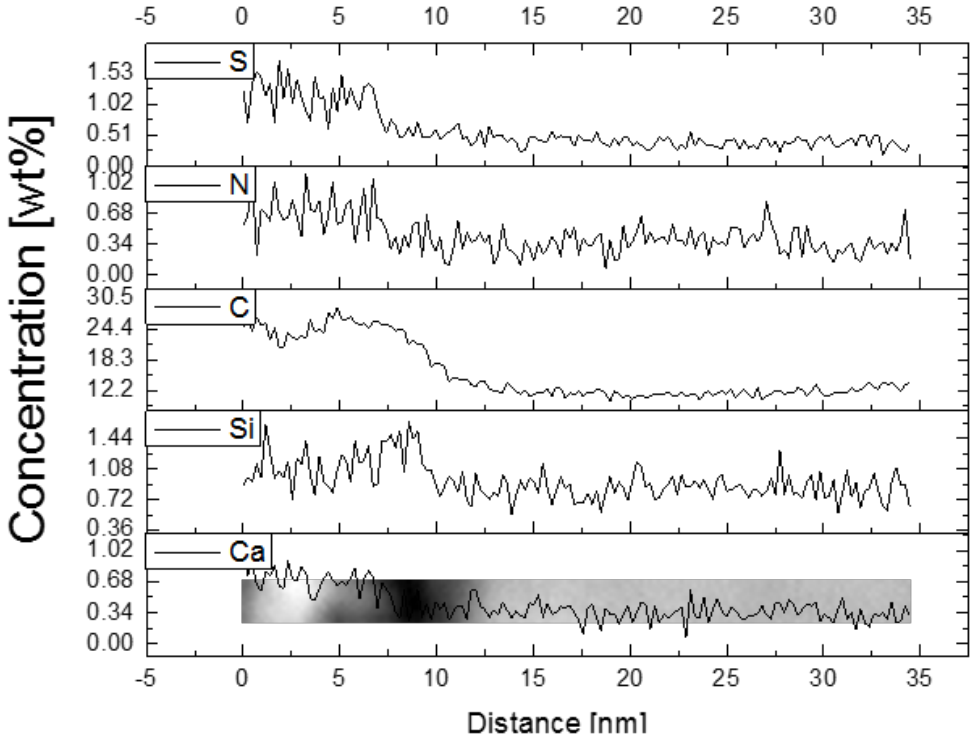

(b) Minor elements S, N, C, Si and Ca.

Figure 3.43: EDX linescan plots of the outer surface.

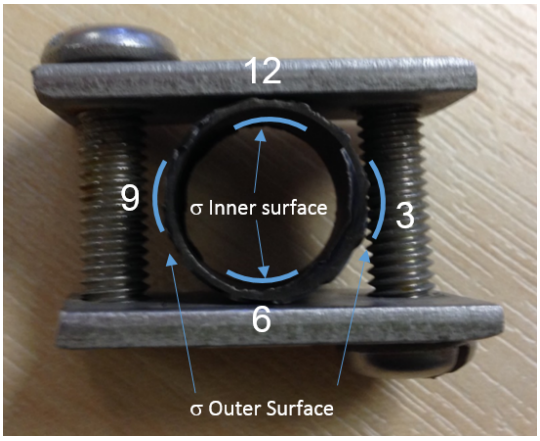

Figure 3.44: The SCC compression ring used showing the areas of stress with a sample of fuel cladding fitted.

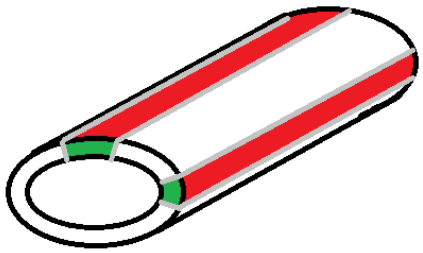

Figure 3.45: Schematic diagram of sections cut for micro CT.

Figure 3.46: The small length of 304 cut for inspection. The crack at 12 o'clock is just visible with the naked eye. Note that the figue has been rotated 90 degrees anti-clockwise.

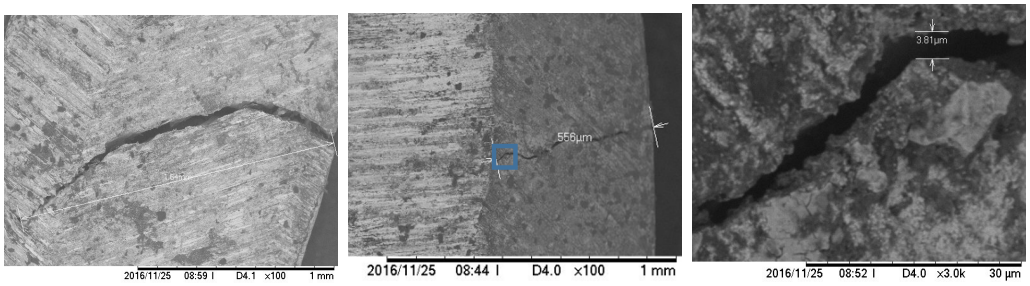

(a) SEM image of the crack at position 12.

(b) SEM image of the crack at position 9.

(c) SEM image of the crack tip at position 9 (as highlighted in fig. 3.47b).

Figure 3.47: SEM images of cracks in 15 mm 304 tube with dimensions indicated.

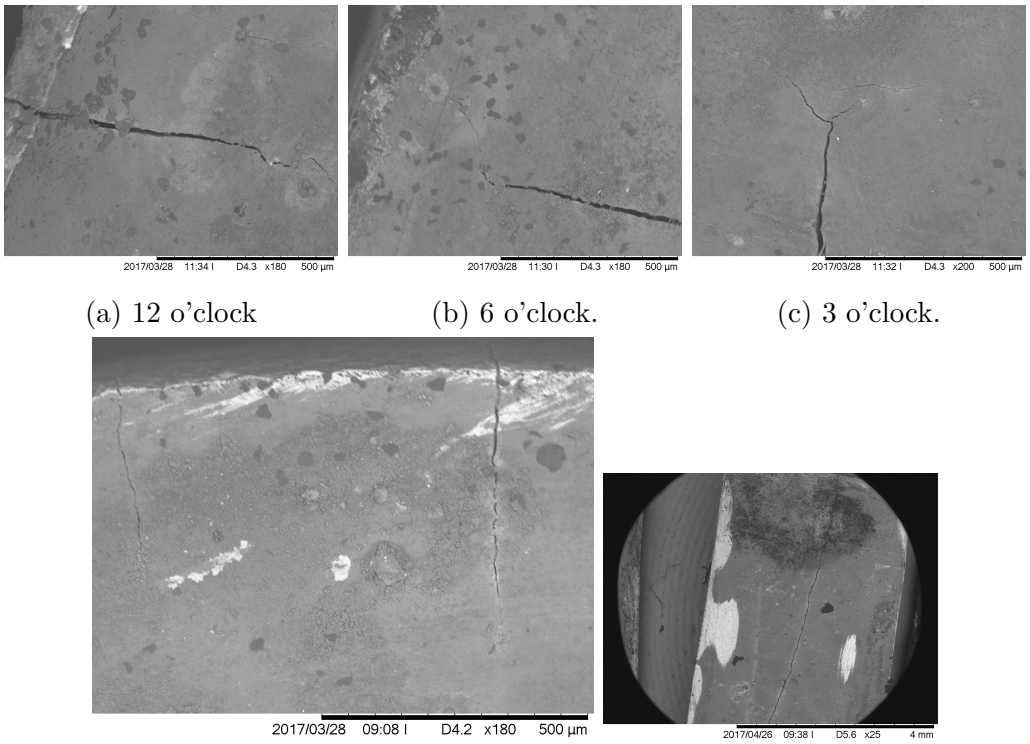

(a) 12 o'clock (b) 6 o'clock. (c) 3 o'clock.

(d) 9 o'clock. (e) 3 o'clock looking at tube wall.

Figure 3.48: SEM images of cracks in 12 mm 304 tube (when looking at a cross section through the tube wall unless otherwise stated).

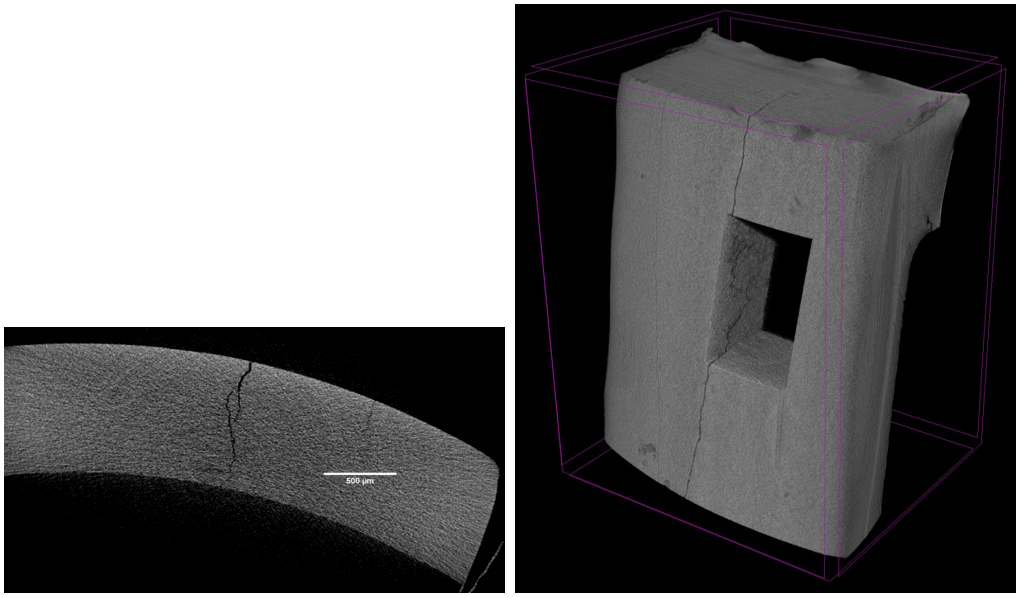

(a) Single slice from CT data. (b) 3D image produced from all slices.

Figure 3.49: Original CT images of the 3 o'clock sample.

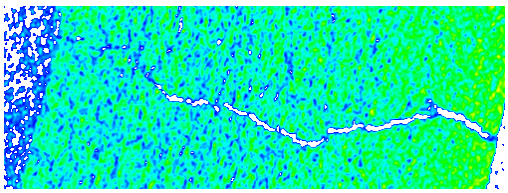

(a) Cropped slice before processing.

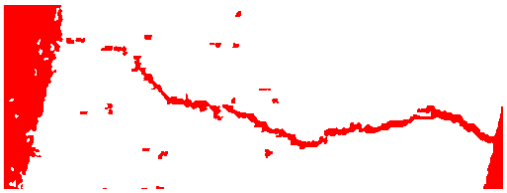

(b) Cropped slice after processing.

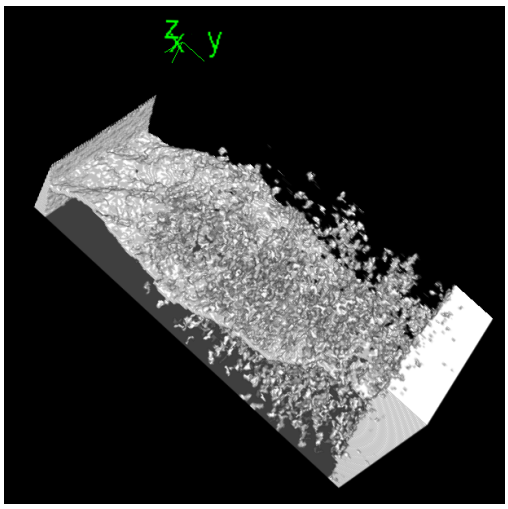

(c) 3D reconstruction of crack.

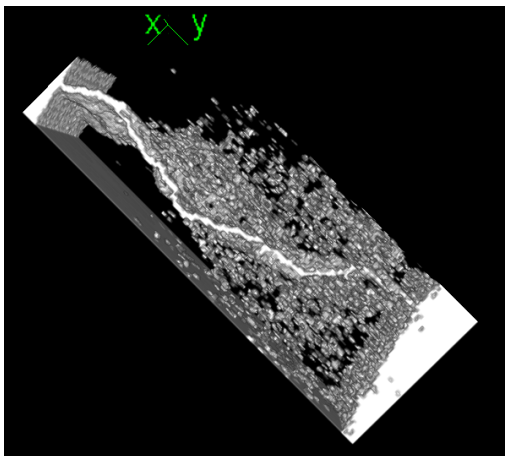

(d) 3D reconstruction of crack

Figure 3.50: Processed CT images of the 3 o'clock sample.

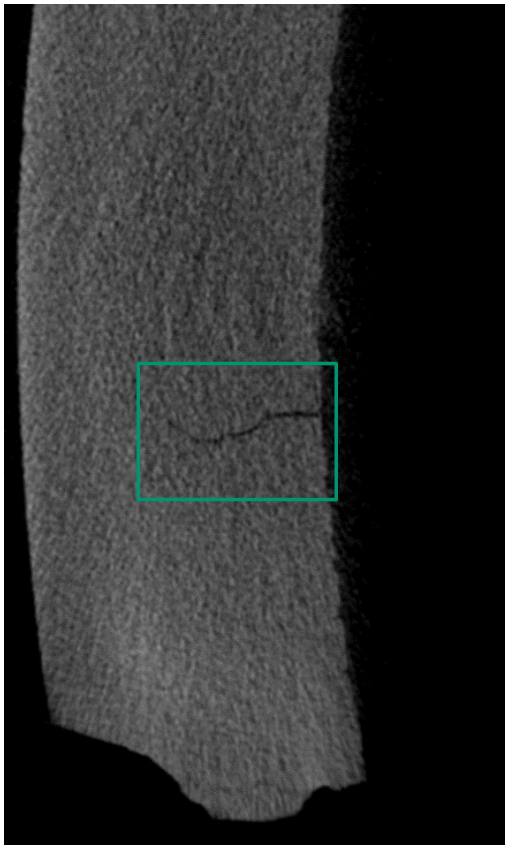

(a) Original single slice image with cropped area highlighted.

(b) Original full size 3d reconstruction.

(c) Cropped image post processing.

(d) 3D image of crack.

Figure 3.51: Processed CT images of 12 o'clock sample.

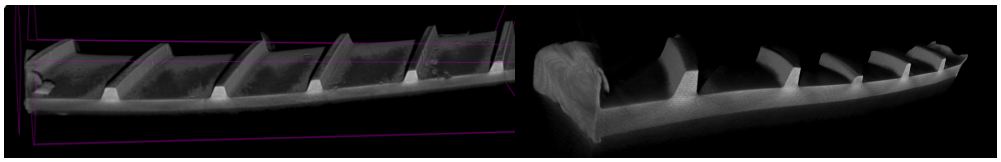

(a) 20/25-12 (b) 20/25-3.

Figure 3.52: CT reconstructions of 20/25 cladding.

Figure 3.53: Slice from fig. 3.49 in the y direction when the crack is at its smallest.

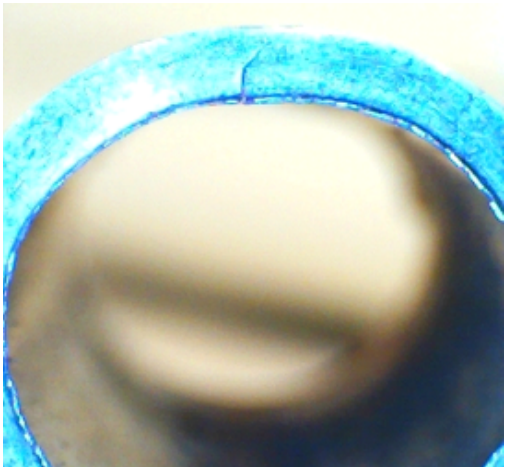

(a) Crack in cross section on removal from $MgCl_2$ solution.

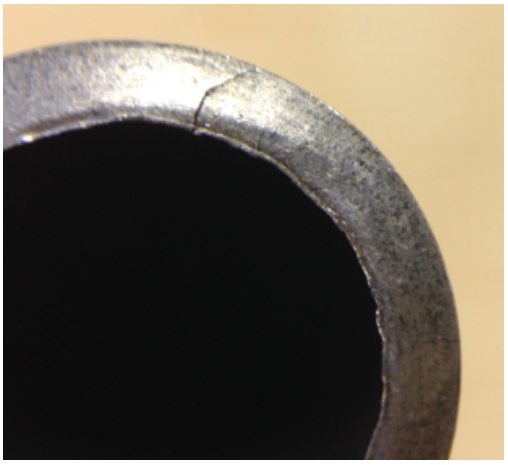

(b) Extended crack after fitting of Swagelok cap.

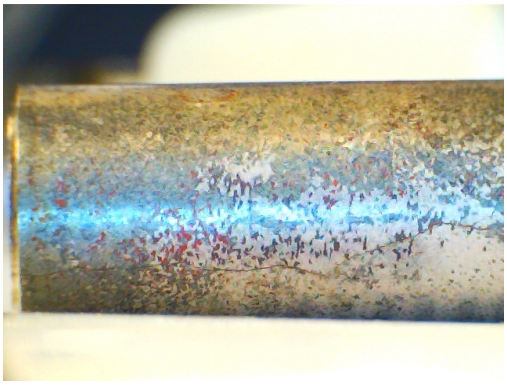

(c) A crack running along the tube wall.

(d) The final SCC test piece (test piece).

Figure 3.54: Cracked 60 mm section of 15 mm 304 tube.

Chapter 4

Summary

The main purpose of part 1 of this thesis is addressing the question of which forms of water are of concern when drying spent AGR fuel ready for dry storage and the preparation of samples that are suitably representative for the drying tests that will be conducted in the remainder of this document. The ASTM standard for drying spent fuel identifies two forms of water as being a possible concern; bound water and trapped unbound water.

Since little post storage examination had been carried out there was little knowledge as to whether bound water was likely to be an issue. Failures when they had occurred had been identified as being due to intergranular corrosion (IGC) and it was decided that the main aim would be to measure the water that could be removed from a sample which had undergone treatment to induce IGC. TGA was found to be capable of measuring water loss from simulant aluminium fuels which have been safely stored and the same methodology was used for stainless steel samples. The results of this found no detectable mass loss from 310 stainless steel samples. The 20/25 samples showed some mass loss but considerably less than for the aluminium samples tested previously. For reference a number of other samples; namely pitted and as received material as well as samples with carbon deposits were also examined with the same results. XPS data has also shown the presence of chromium hydroxide. It is therefore clear that some water is present on the surface of AGR fuel. However since aluminium clad fuels have been safely placed into dry storage and the quantities of bound water on AGR cladding are considerably lower and there is no dryness standard for AGR fuel

storage (one of the reasons why this project is being carried out) and the samples tested showed considerably less bound water than aluminium the conclusion has been made that for the remainder of this thesis the presence of bound water can be disregarded. As noted in section 2.6.9 the presence of Fe(II) and Fe(III) in stainless steel does allow for the possibility that even lower quantities of water may prove to be problematic for stainless steel in dry storage due to it's catalytic breakdown of hydrogen peroxide however research into that field is beyond the scope of this thesis.

Having concluded that bound water could be disregarded the next step was to produce lengths of cracked tube that could be used in the drying tests in part 2. The cracks that are known to have lead to failures previously have been attributed to intergranular stress corrosion cracking (IGSCC). Typical techniques for inducing SCC using C-rings were not suitable for this work and as such a compression method was used along with a method similar to ASTM G36. This method was found to produce cracks similar in dimensions to those in the few images in the public domain of cracks in real pond stored AGR fuel. The length of tube produced was made into a test piece inside which water could be sealed for later testing.

In the course of producing these samples it became clear that there were some differences in the corrosion behaviour of the two surfaces of as received AGR cladding. The hope had been that XPS would highlight differences in the oxide layer of the two surfaces and ideally give some indication as to the quantity of water present however this has not been possible. The TEM/EDX data of an uncleaned sample highlighted the presence of a thick carbon layer on the surface which makes analysis of the oxide layer by XPS difficult.

Linescans of a cleaned sample showed a clear difference in the nature of the oxide composition of the two surfaces of fuel cladding. The outer surface appeared to have a total depth of around 5 nm and a multilayer structure while the inner surface has much thinner oxide layer. This information is of course true for untreated cladding only and differences in the surfaces may be much reduced following the final anneal and also after irradiation, nevertheless it indicates that differences in behaviour are clearly possible and are something that should at least be considered when the corrosion behaviour of fuel is being studied.

Part II

Drying

Chapter 5

Literature Review-Drying and Dry Storage

The following section reviews existing literature that relates to the drying aspect of this research. It begins with an introduction to the science of drying looking at the factors and parameters that can be altered to change drying rates. This is followed up with a look at the methods that have been used to dry spent nuclear fuel and the little research that has been published in the field and is finished with a description of the various types of dry storage that are available.

5.1 Phases of Matter and Phase Changes

The process of drying involves the removal of water from a surface, material or environment. In some cases this may be as simple as wiping water off a surface or at a more complex level it may involve extracting water from other liquids by adsorption to a solid material such as a molecular sieve, however the most common method involves the removal of liquid water by evaporation or boiling. This is the process that takes place when we hang clothes out to dry and it is likely that any nuclear fuel drying process will take place in this way and as such it is vital to have an understanding of the science of phase change and the factors that can affect it.

5.1.1 Phases of Matter [82]

From an early age we are all aware that matter can exist in one of three phases; solid, liquid or gas. Thanks primarily to water we quickly learn that these phases are all related to temperature as water turns to ice when cooled and vapour when heated. As our scientific understanding grows we learn that these changes are in turn related to the energy carried by the various atoms (or molecules) within a substance. The descriptions below are given using water as an example as it is a substance that we all understand however the basic processes are true for all pure substances which have a consistent and homogeneous chemical composition (pure substances).

At low temperatures the atoms in a substance have little energy and are held close together in fixed positions adjacent to each other as a solid. As the system warms up the atoms gain more energy and vibrations increase until the energy of the molecules is sufficient to begin to break some of the intermolecular bonds holding the atoms together and while the atoms are still relatively close together they are free to move around relatively independently of each other. As the temperature increases further the final bonds holding the atoms together break and the liquid becomes a gas.

The process of phase change can however be described in greater detail and once again water is used as an example and atmospheric pressure is assumed. When heat is applied to ice it initially begins to warm until it reaches a temperature of 0 °C. At this temperature continued heating no longer raises the temperature instead a phase change takes place. The energy that was being used to make the water warmer is now used to break bonds instead and this continues until all the ice has melted and only liquid water remains. At this temperature the liquid water is known as a compressed or subcooled liquid.

The following phase changes are dependent on two factors known as saturation temperature, T_s and saturation pressure, P_s and these are the temperature, at a given pressure at which a substance begins to vaporise, and the pressure, at a given temperature at which boiling occurs.

When heat is applied to water in the compressed liquid phase it will begin to warm. Water will continue to warm until the temperature reaches 100 °C by which point the volume has increased slightly (by about 4% in water) but more

importantly the liquid water is now known as a saturated liquid. As a saturated liquid the water has reached a temperature at which it is about to vaporise, and this is the saturation temperature, T_s. In a similar manner to the melting point, as the water is heated further the temperature remains constant with the heat energy being used to vaporise a portion of the water to give a saturated vapour and creating a saturated liquid-vapour mixture. This is accompanied by a substantial increase in volume and will continue until all water has been vaporised. Only then will further heating of the water, now as a vapour, lead to further temperature increase and the formation of a superheated vapour. In the saturated vapour phase any loss of heat will cause the vapour to condense back to liquid water while in the superheated phase some energy loss can be take place with only a loss in temperature but without condensation.

For the case of water this process is reversed upon cooling however for some substances hysteresis takes place and there may be a difference in melting and freezing or boiling and condensing points in the reverse direction

The description above is true for water being held at atmospheric pressure however similar effects can be be observed by changing pressure rather than temperature. The boiling point of a liquid can be increased by increasing the pressure or inversely decreased by reducing the pressure. This is because by altering the pressure you alter the saturation temperature, T_s. This can be described through consideration of water being heated in a sealed vessel. If water is placed into a sealed container and heated it will initially begin to vaporise at 100 °C. As this happens the volume of the water will increase significantly and, since the container is sealed this will lead to an increase of pressure. As the pressure inside the chamber increases T_s increases allowing water to remain as a liquid beyond 100 °C without vaporisation (until the new T_s is reached).

While changing the pressure a liquid is exposed to can change its boiling point, it is also possible to cool a substance by changing the pressure and it is this phenomenon that allows refrigeration plants and air conditioning units to work. These systems contain refrigerant gases that have highly tuned properties, the most famous of them being the (now banned) Chloroflurocarbons or CFC's. These are substances that are gases at room temperature and pressure however will become liquids when compressed or cooled. If a quantity of such a refrigerant is compressed

Temperature [$^{\circ}C$]	$\mathbf{P_s}$ **[kPa]**
0	0.6105
5	0.8722
10	1.228
20	2.338
30	4.243
40	7.376
50	12.33
60	19.92
70	31.16
80	47.34
90	70.10
100	101.3

Table 5.1: Water saturation pressure with increasing temperatures[83].

and held in a sealed container at room temperature it will remain as a liquid. If the container is now opened leading to a reduction in pressure the refrigerant will start to vaporise but this will be accompanied by a drop in temperature down to the refrigerants saturation temperature at atmospheric pressure. In the same way that boiling water will stay at 100 °C when heated until fully vaporised, the refrigerant will stay at its saturation temperature until fully vaporised. The vaporisation process must also take in heat from its surroundings to allow the vaporisation to take place. This heat is known as the latent heat of vaporisation and it is this factor that allows it to be used as a refrigerant.[84]

It also means that low temperatures can be maintained through the use of vessels immersed in liquid gases such as nitrogen and helium which will stay at there saturation temperature as long as they are open to atmosphere. By well insulating the containers in which the liquid gases are kept through the use of vacuum flasks or Dewars it is possible to prevent the liquid getting the required latent heat from its surroundings, thus reducing the rate at which the gas is vaporised and its life as an effective coolant.

The same phenomenon can be used in the form of vacuum cooling. In this

scenario a vacuum is applied to a liquid until the saturation pressure is reached. At this point the liquid will begin to flash into vapour taking heat from the surroundings until the saturation temperature is reached. T_s is maintained and heat is continually taken up (but at a slower rate) until all the moisture has evaporated.

5.1.2 P-v, T-v and P-T Diagrams [85]

The most common way to study the changes of phase of a pure substance is graphically through the use of diagrams. These diagrams normally concentrate on the liquid and gaseous regions where properties are more interesting. Figure 5.1a shows a temperature-volume diagram for a pure substance. The T-v diagram consists of a curve peaking in the centre. To the left of centre the substance exists as a compressed liquid and to the right as a superheated vapour. In the region in the middle beneath the curve is the saturated liquid-vapour, or mixed region. As the pressure increases the size of this mixed region decreases until what is known as the "critical point". At the critical point the properties of the saturated liquid and superheated vapour are identical and the phases can not be distinguished. In this region the properties of the substance may change dramatically and they are known as supercritical fluids. Figure 5.1b shows another T-v diagram showing lines of constant pressure.

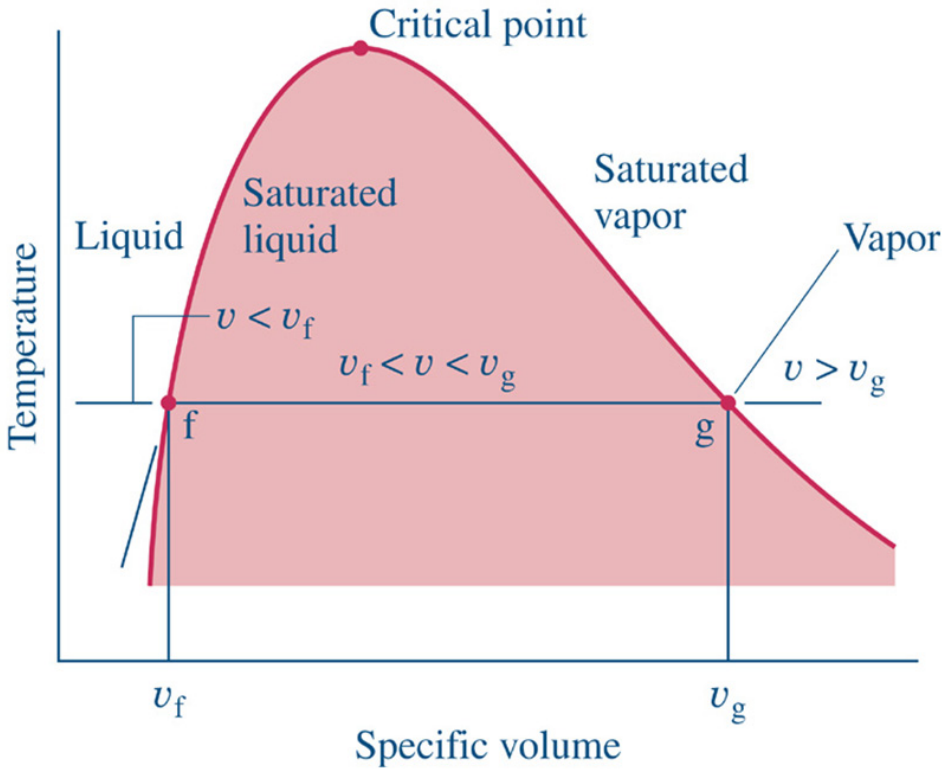

(a) Standard diagram (taken from [86]).

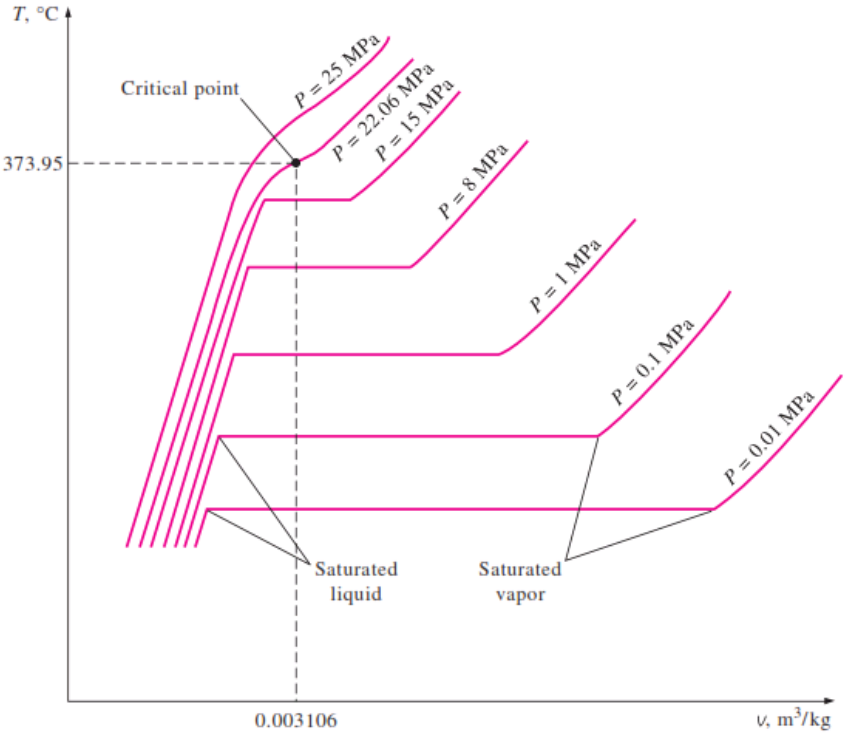

(b) With lines of constant pressure (taken from [85].

Figure 5.1:12Tv diagrams.

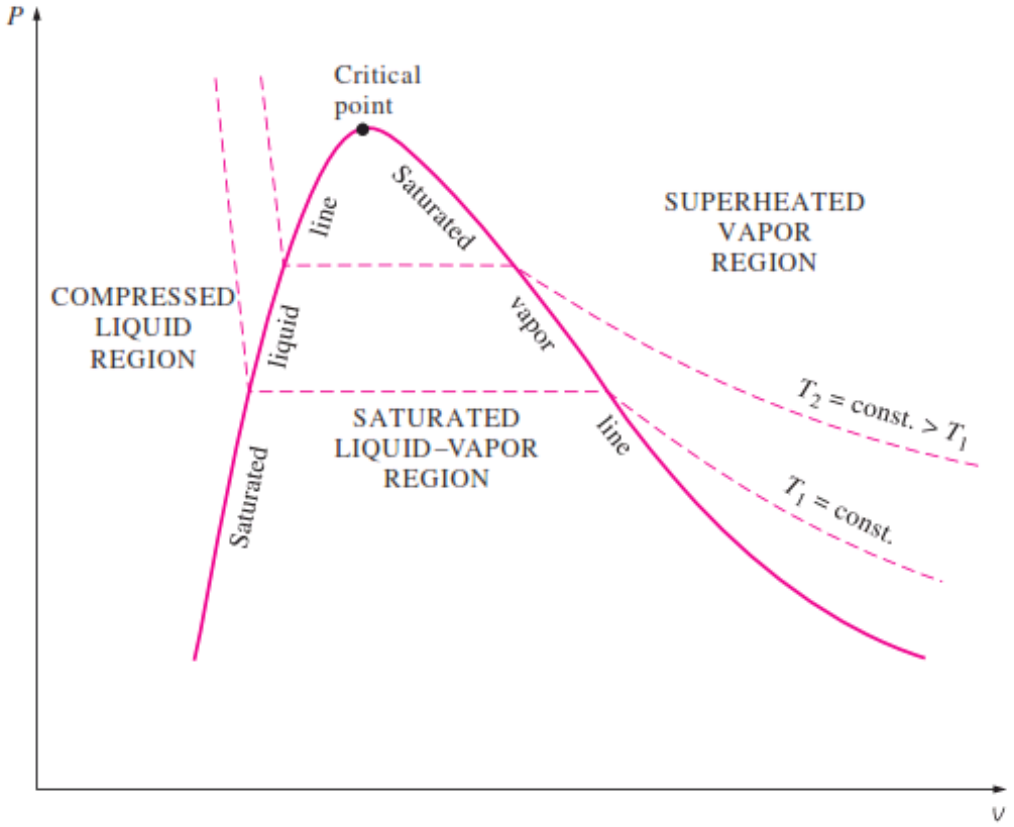

Figure 5.2: P-v Phase Diagram (taken from [85]).

A similar diagram is the P-v diagram (fig. 5.2). The diagram once again shows a curve separating the different regions with a critical point at the apex. The key difference is that the lines of constant temperature curve in the opposite direction to the lines of constant pressure in a T-v diagram. Some phase diagrams can be extended to include the solid phase. For the vast majority of pure substances the density is inversely proportional to temperature with greater jumps as the phase changes. There are however some substances, including water, which expand when they solidify allowing them to float on the surface of the liquid. It is this property of water which has allowed life to develop on Earth. When this occurs different diagrams are required for substances that contract on freezing and those that expand (fig. 5.3).

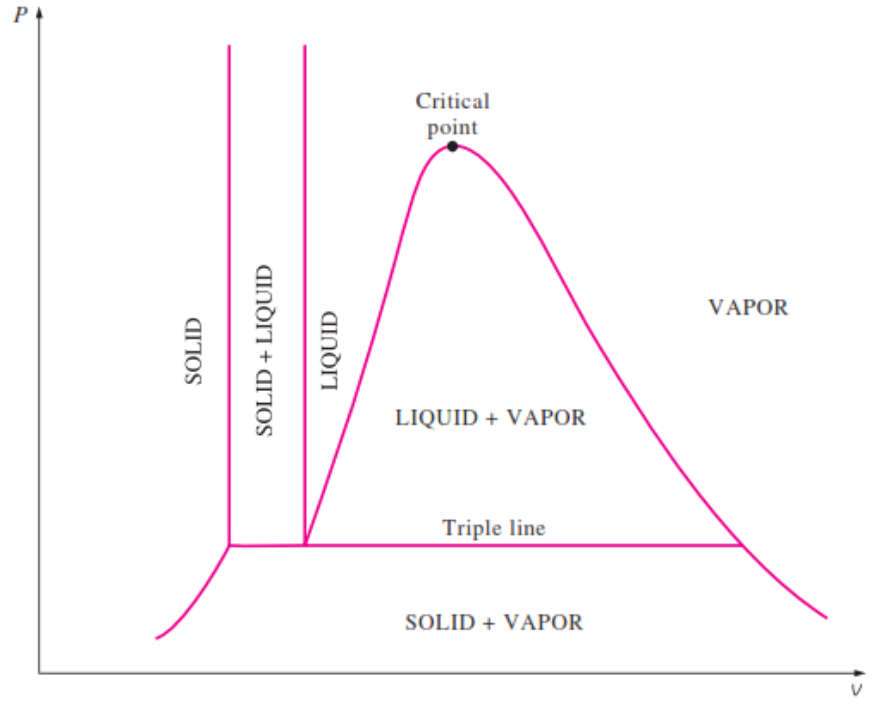

(a) A substance that contracts on freezing.

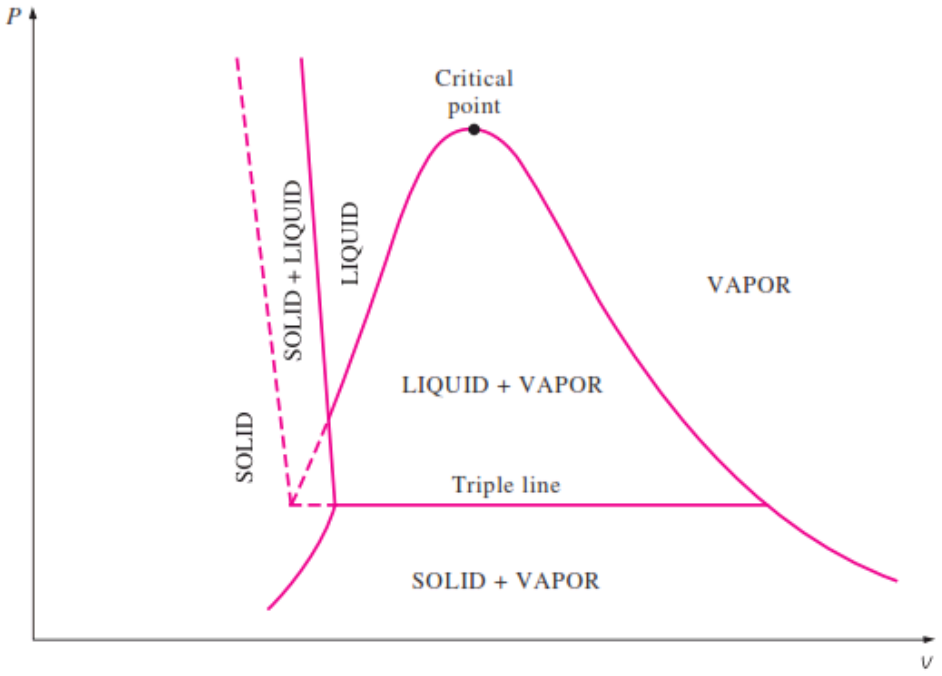

(b) A substance that expands on freezing.

Figure 5.3: P-v diagrams including the solid phase (taken from [85]).

The final type of diagram is the P-T diagram also known as a phase diagram, fig. 5.4. This diagram shows how the phase of a substance relates to pressure and temperature and as such includes all three phases. Like the P-v and T-v diagrams the critical point is shown however P-T diagrams also show a point known as the "triple point". This is the combination of conditions at which a substance will exist as a solid, liquid and gas. A similar point is shown by the "triple line" in fig. 5.3.

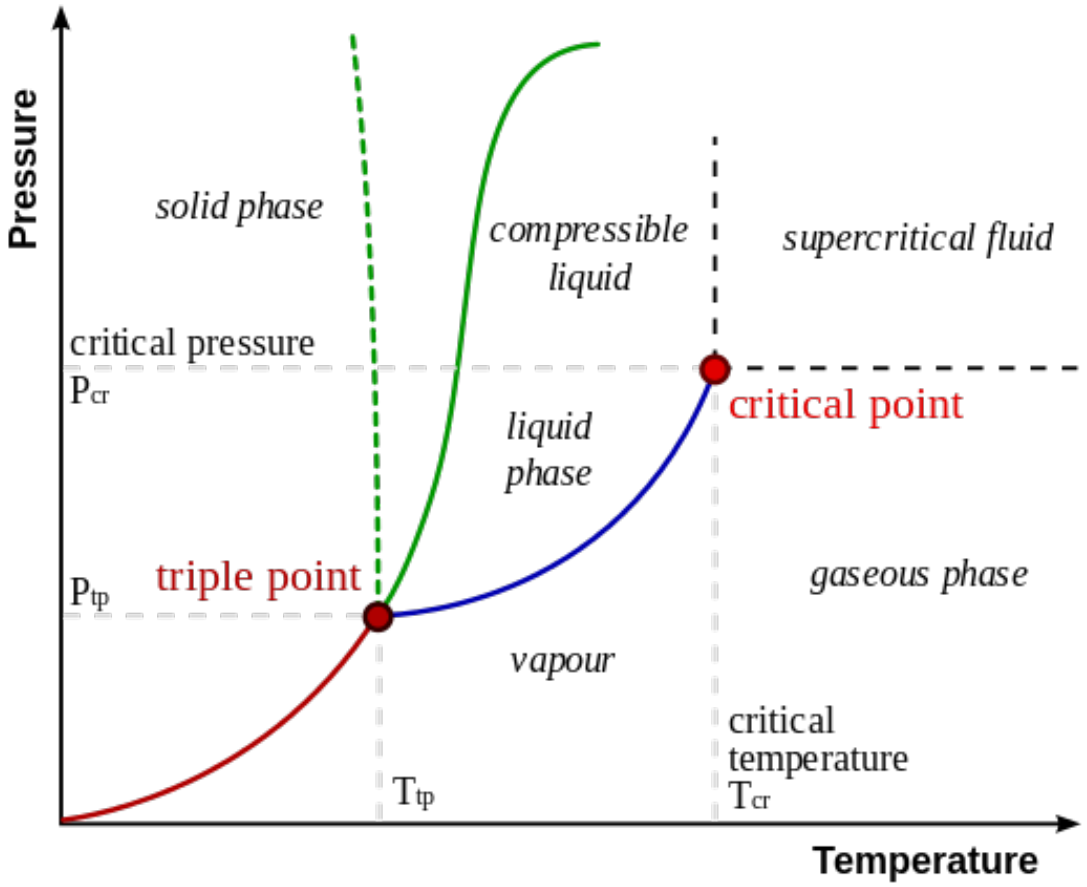

Figure 5.4: P-T Phase Diagram (taken from [87]). The green line shows the change from solid to liquid while the dashed green line shows the same change for a liquid which expands upon freezing such as water.

The P-T diagrams also show conditions in which solids will convert direct from solid to gas with no liquid phase. In everyday life the most common example of

this is carbon dioxide which is known as dry ice and is used as a coolant. This solid material changes directly from solid to gas at atmospheric pressure in a process known as sublimation.

5.1.3 Partial Pressure and Vapour Pressure [88]

The pressure exerted by a gas is a result of the individual molecules of which it is made colliding with the surfaces surrounding it. In the case of a single gas, such as xenon, within a cylinder, the overall pressure of the gas is equal to the force of the xenon molecules colliding with the walls. For a gas mixture the overall pressure is equal to the sum of the partial pressures of the individual gases in the mixture. In the case of dry air at atmospheric pressure the overall pressure. P_{air}, is approximately 1 Bar as a result of a partial pressure of 0.79 Bar from the nitrogen and 0.21 Bar from oxygen (minor constituents ignored for the sake of simplicity) (eq. (5.1)).

$$P_{air} = P_{N_2} + P_{O_2} \tag{5.1}$$

In the case of normal atmospheric air a similar situation is found in which the total pressure, P_{atm}, is the sum of the partial pressure of the dry air, and the partial pressure of the gaseous water, which is known as the vapour pressure, to give eq. (5.2). P_v is generally low since water vapour makes up only a small proportion of air and therefore has little impact on overall pressure however the quantity of water vapour in the air can have a dramatic impact on the perceived temperature and the rate at which water will evaporate. This is a result of the limited quantity of moisture that can be held by air (or other gases) at a fixed temperature and is commonly referred to as relative humidity (RH).

$$P_{atm} = P_v + P_{air} \tag{5.2}$$

The relative humidity ranges from 0% for dry air to 100% for air that can hold no more water, or saturated air. At 100% RH the vapour pressure of saturated air

is equal to P_s at that temperature. Consequently the vapour pressure of water is related to RH by

$$P_v = RH \times P_s \tag{5.3}$$

One of the most obvious effects of these factors is felt in countries with hot tropical climates. The process of evaporation normally takes place as a result of water taking heat from its surrounding and changing phase from liquid to vapour and the body uses this mechanism to cool itself. However, in tropical climates with close to 100% RH water is unable to vaporise into the saturated air and the temperature feels much warmer. Similarly clothes hung out to dry in such climates will not dry despite the high temperatures. Conversely it is possible to dry clothes in temperatures below freezing as the humidity can be so low that the evaporation of water is energetically favourable.

These factors also mean that conditions can be altered to encourage drying. When air is heated the quantity of moisture it can hold is increased leading to a reduction in RH and consequent drop in vapour pressure. Similarly reducing the overall pressure will reduce the P_v and since $P_v = P_s$ and $P_v \propto T_s$ these two factors encourage vaporisation.

Vaporisation is encouraged because water wants to enter into a state of phase equilibrium. In the scientific world we are used to processes in which materials move from areas of high concentration to low, such as diffusion, and the concept of entropy whereby a system wishes to become more disordered and this is in effect what is happening when water strives for phase equilibrium. For liquid water to be in phase equilibrium, the vapour pressure must be equal to the saturation pressure at the system temperature. If the vapour pressure is reduced some water will evaporate to maintain phase equilibrium. This loss of water will in turn cool the liquid reducing P_s and eventually a steady state will be formed (in ideal conditions).

When a pool of water is in contact with air the air at the interface is always saturated. As a result the rate at which the water evaporates is controlled by the difference between the vapour pressure at the interface and the reduced vapour pressure some distance away. In this scenario turbulent air flow will encourage

drying by mixing the air and removing the saturated air from the interface. This can again be seen with drying clothes which will dry much more quickly on a windy day than a still one as the wind continually moves the saturated air away.

5.1.4 Boiling and Evaporation.

While boiling and evaporation are both situations in which a liquid is converted from a liquid to a gas phase they are distinct processes. The process of evaporation occurs at a liquid gas interface when water evaporates from a liquid phase with a P_s that is higher than the P_v of the surrounding gas. In contrast boiling takes place at a solid liquid interface when a liquid comes into direct contact with a surface that is a considerably higher temperature than the boiling point of the liquid causing it to instantaneously form vapour bubbles within the liquid.[88]

5.1.5 Capillary Condensation

Capillary condensation is a phenomenon which allows vapour to condense out of the gas phase below the saturation pressure and occurs in capillaries as a result of surface tension[89]. Water vapour enters a pore and the increased Van der Waals forces cause the water to condensen [90] resulting in a miscus forming thanks to the surface tension of the water. If the pore is narrow enough then the surface tension can then in effect be stronger than the liquids thermodynamic wish to evaporate and an equilibrium forms below the vapour pressure. The size of the this force is goverened by the pore dimensions with narrower pores leading to a greater force and a greater difference between the saturation pressure vapour presure and the equilibrium pressure. As a result of this the boiling point of the water is increased.

The change in vapour pressure due to capillary action can be modelled with the Kelvin equation;

$$ln\frac{P_v}{P}_{sat} = \frac{-2H\gamma V_l}{RT} \tag{5.4}$$

where P_v and P_{sat} are the equilibrium vapour pressure and saturation vapour pressure respectively, H is the mean curvature of the mensicus, γ is the surface

tension (0.072 Nm^{-1}) V_l is the molar volume of water ($\sim 1.8x10^{-5} m^3 mol^{-1}$, R is the ideal gas constant (8.314 $Jmol^{-1}K^{-1}$) and T is the temperature.

Figure 5.5 shows how pore size is impacts upon boiling point (assuming a round pore). It can be seen capillary condensation can have a significant effect but only once the pores are in the region of nanometres in radius.

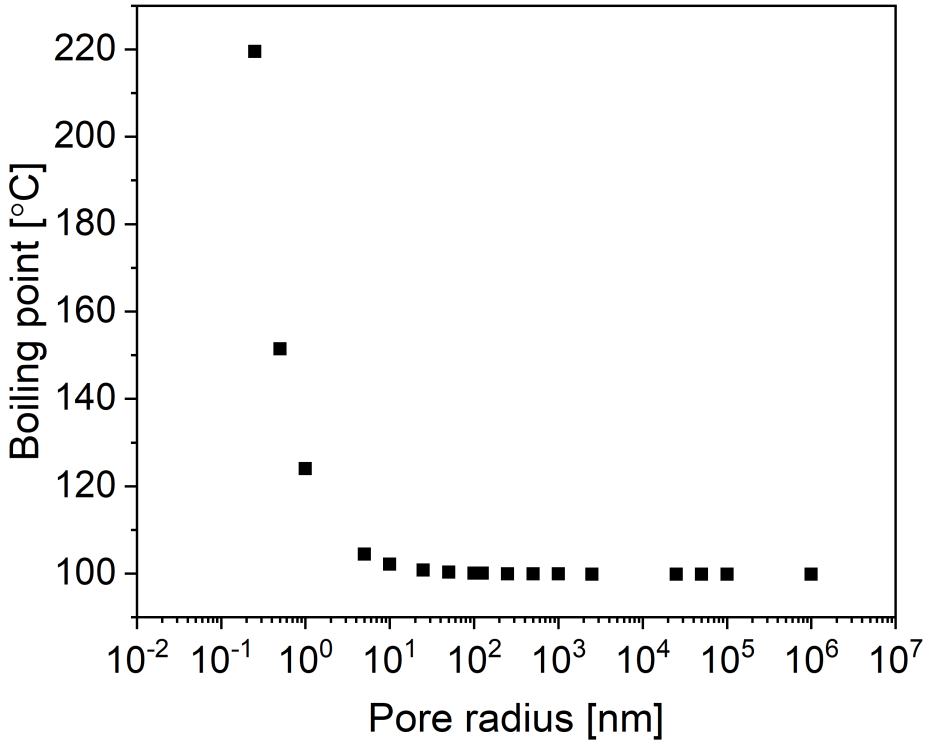

Figure 5.5: Influence of pore size on boiling point of water.

5.2 Heat Transfer

In the previous section it has been shown that drying requires a change of phase and that the driving force behind this in most scenarios is an increase in temperature. The following section looks at the ways in which temperature can be increased in a system by discussing the basic science behind heat transfer.

5.2.1 What is Heat and Heat transfer [91, 92]

We are all aware of the different forms of energy that exist from the potential energy of a stretched elastic band, to the kinetic energy of falling stone as well as the thermal energy of hot objects, and heat transfer is the movement of thermal energy. We are all aware that hot objects will cool down in a cooler environment and cold objects will heat up in a hotter environment and this effect is a clear demonstration that in order for heat transfer to take place there must be a temperature gradient. This is in contrast to other forms of energy transfer which can take place adiabatically (without a change in temperature), or will lead to the warming of an object as result of work done rather than heat transfer (such as when gas is compressed by a piston at room temperature).

While all of these subjects can be studied through thermodynamics this is not always suitable as thermodynamics is interested in the study of the overall quantities of heat transferred at equilibrium. In many situations we are more interested in the rate at which things occur or at times before equilibrium. In these situations we are interested in the science of heat transfer. Heat transfer can be described as the movement of thermal energy as a result of a temperature gradient.

The following three sections look at the three main forms of heat transfer; conduction, convection and radiation.

5.2.2 Conduction [91]

Conduction is the movement of thermal energy as a result of particle interactions. The primary cause, which takes place in all phases is the result of direct interactions between particles on the microscopic scale in which the more energetic particles give up some of their energy. In solids a secondary form of conduction comes about as a result of free electrons and in liquids and gases diffusion also plays a role. Whatever the situation the rate of heat transfer from one point or surface to another is related to three variables; the area, A, the Distance, x and the

temperature gradient ΔT (eq. (5.5)).

$$rate \propto \frac{A\Delta T}{x} \tag{5.5}$$

Equation (5.5) shows that increasing the area exposed to the heat source and increasing the temperature difference will increase the rate at which heat is transferred while increasing the distance between surfaces will reduce the rate. The final factor which affects the rate of heat transfer is the thermal conductivity, k, of the material in question which is a constant and varies from material to material (see table 5.2) and this gives the full equation (eq. (5.6)). It is important to note the negative sign which ensures that thermal energy always flows from areas of high temperature to low.

$$\dot{Q} = -kA\frac{\Delta T}{x} \qquad [Wm^{-2}] \tag{5.6}$$

The thermal conductivity of a material can be defined as the rate of heat transfer through a unit thickness of the material per unit area per unit temperature difference[93] and in most scenarios this is the critical factor for controlling heat transfer. We all understand that metals, which have a high k value are excellent at heat transfer and as such are used for objects such as saucepans. In comparison materials such as wood and plastics have low k values and poor heat transfer characteristics so are better suited for saucepan handles.

On the whole solids are best suited to heat transfer by conduction. Since the atoms are packed closely together the increased lattice vibrations that result from heating are passed on to neighbouring atoms or molecules more easily than in liquids or gases. This is particularly true for crystalline solids, such as diamond, which have the highest thermal conductivity due to their highly ordered nature. In metals heat conduction is primarily due to the secondary process of free electron movement. However in both cases the overall value is the sum of the two parts.

It is worth noting that while some substances such as metals are excellent thermal and electrical conductors, others such as diamond are poor electrical conductors and are therefore ideal for use as heat sinks on electrical circuit boards. Also while pure metals have excellent thermal conductivity properties the addition of other alloying metals even in only small quantities can lead to dramatic

Material	k $[Wm^{-1}k^{-1}]$
Diamond	2300
Copper	401
Gold	317
Aluminium	237
Iron	80.2
Water (l)	0.607
Helium (g)	0.152
Glass fibre	0.043
Air (g)	0.026
Stainless steel [95]	16

Table 5.2: Values for thermal conductivity for some common materials (taken from [91] unless otherwise indicated).

reductions in conductivity. An alloy of iron and 1% chromium has a a thermal conductivity of $62\,\mathrm{W\,m^{-1}\,^{\circ}C^{-1}}$ compared to 83 and $95\,\mathrm{W\,m^{-1}\,^{\circ}C^{-1}}$ for iron and chromium respectively.

In liquids the thermal conductivity is generally reduced compared to that in solids as the atomic spacings are increased and even more so in gases. Conduction occurs as a result of molecular collisions and diffusion in both cases with this conductivity decreasing with increased molar mass however as liquids increase in temperature, k decreases with the opposite being true in gases. The kinetic theory of gases has been found to provide a reasonable estimation of k at relatively low temperatures and shows it to be related to the square root of the absolute temperature. The literature values for conductivity are also valid over a wide pressure range as long as ideal gas behaviour is maintained. In solids and liquids the complexities are such that theoretical predictions are much more complicated.[94]

On the the whole for all substances thermal conductivity is assumed to be the same in all directions however for some materials such as wood and laminates this is not the case[91].

5.2.3 Convection [96–98]

Convection is the combined result of conduction and fluid motion and as such is not technically a mode of heat transfer in its own right however for the ease of description it is generally described as being so. It occurs as the result of heat transfer by conduction to (or from) a fluid in a localised area followed by bulk movement of the fluid. This bulk movement of the fluid transfers heat throughout the fluid. This differs from diffusion and molecular collisions since the heat transfer results from the fluid movement on the macro scale. The phenomenon is clearly limited to taking place in gases and liquids although phase changes such as boiling are also held in this class as there is fluid motion.

Despite the seemingly complex nature of convection the rate of convection can be expressed relatively simply with Newton's law of cooling eq. (5.7)

$$\dot{Q} = -hA_s(T_s - T_\infty) \qquad [W] \tag{5.7}$$

in which the rate of cooling is related to the convection heat transfer coefficient, h, the area of the surface across which heat is transferred, A_s, and the temperature difference between the surface, T_s and at some point a sufficient distance away, $-T_\infty$.

There are two general forms of convection that are considered to take place. When the bulk movement of gas occurs as a result of buoyancy changes then the process is known as free or natural convection however if a fan or other mechanical means is used to induce gas movement the process is known as forced convection. In either case the study of convection generally comes down to analysis of the heat transfer coefficient.

5.2.4 Radiation

The final form of heat transfer is radiation and is heat transfer as a result of electromagnetic radiation. Despite being most effective in a vacuum this form of heat transfer is believed to be of little importance in relation to the drying of spent nuclear fuel so will not be discussed further.

5.3 Diffusion

As discussed in section 5.1, in any system where drying takes place water must change from the liquid to the gas phase. If the gas surrounding the water is

Process	h $[Wm^{-2}K^{-1}]$
Free Convection	
Gases	2-25
Liquids	20-1000
Forced Convection	
Gases	25-250
Liquids	100-10,000
Phase Change	2500-100,000

Table 5.3: Typical values for the convection heat transfer coefficient (taken from [98]).

saturated with water vapour, water will no longer vaporise and drying will not occur. In the majority of systems the voidage is suitably large to allow the removal of saturated vapour by convection or advection (the bulk movement of gas such as by a fan) however in some areas where pores or crevices exist this may not be possible. The following section looks at the process of mass transfer by diffusion which becomes the key factor in this situation.

5.3.1 Basic Diffusion

Diffusion is a form of mass transfer that leads to the mixing of two materials as a result of a concentration gradient. The process is most closely associated with gases and liquids although it also takes place in solid solutions such as metals (although by a slightly different mechanism). Diffusion takes place due to the random nature with which particles move. Figure 5.6 shows an environment containing two different particles separated by a partition. When the partition is removed the likelihood of a red particle moving to the left is equal to that of it moving to the right. More red particles move across the plane (dashed line) from left to right than move across the plane from right to left since there is a higher concentration of red particles on the left leading to a net movement of red particles from left to right. The same is true, but in the opposite direction for the blue particles. This mechanism continues until the particles are fully mixed when net movement is no longer possible.[99, 100]

The simplest equation related to diffusion is Fick's law which relates the trans-

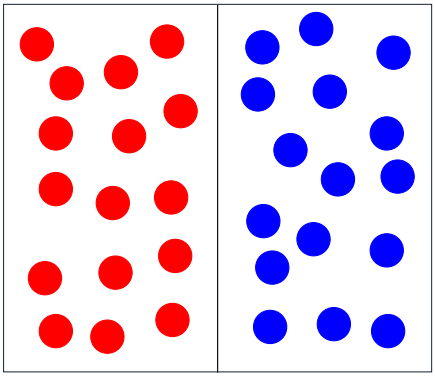

(a) Two different gases are initially separated by a partition.

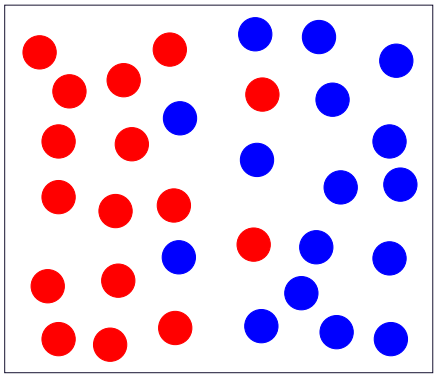

(b) After removal of the partition the gases at the boundary begin to mix.

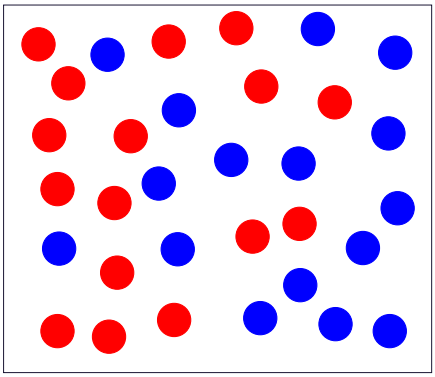

(c) The centre becomes mixed and gases slowly diffuse through.

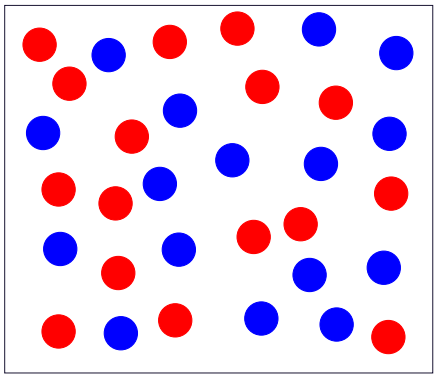

(d) Eventually complete mixing is achieved.

Figure 5.6: Stages of diffusion

fer of a species, A in a binary mixture with B. The equation can be given in terms of mass,

$$j_A = -\rho D_{AB} \nabla M_A \qquad [kg\, s^{-1} m^{-2}] \tag{5.8}$$

where j_A is proportional to the species mass density, $\rho = \rho_A = \rho_B$ and the gradient is the species mass fraction $m_A = \rho_A/\rho$, or in terms of moles

$$j_A^* = -C D_{AB} \nabla x_A \qquad [kmol\, s^{-1} m^{-3}] \tag{5.9}$$

where j_A^* is proportional to the total molar concentration, $C = C_A + C_B$ and the gradient in the species mole fraction $m_A = \rho_A/\rho$.[99, 101]

The common factor to both diffusive mass and molar flux is the binary mass diffusion coefficient or the mass diffusivity, D_{AB}. Several methods have been developed to predict D_{AB} theoretically in gases where the ideal gas law can be applied along with empirically calculated constants or physical properties such as Lennards-Jones potential. The common factor in all of these is the direct relationship to temperature and the inverse relationship to pressure.[102, 103]

The existence of so many different methods for predicting D_{AB} gives some idea of the complexity and accuracy of such methods and consequently tabulated empirical values are used preferentially when available.

5.3.2 Pore Diffusion [104, 105]

When diffusion of a gas is taking place in a porous solid the mean free path may become relevant. This can be assessed with reference to the Knudsen number

$$Kn = \frac{l}{d} \tag{5.10}$$

In this case l is the mean free path and d is the pore diameter. When the mean free path, and therefore Kn is low wall effects are minimal however as the mean free path becomes larger collisions with the pore wall become more common than collisions with other particles. In liquids where l is measured in fractions of a micron Kn remains low and wall affects play little role. In gases l can increase dramatically and can be estimated from

$$l = \frac{k_B T}{\sqrt{2}\pi d_c^2 P} \tag{5.11}$$

where d_c is the collision diameter of the two particles.

When Kn is small (<0.01) diffusion in pores is similar to diffusion in the bulk media and diffusivity is found from

$$D_{eff} = \frac{m_A D_{AB}}{\tau} \tag{5.12}$$

where τ is the tortuosity of the pore network. When l is similar to the pore diameter Kn becomes large (>10) and the wall effects play a much greater role

and Knudsen diffusion predominates. In this situation the mass diffusivity can be found from

$$D_{Kn} = 48.5\, d \left[\frac{T}{M}\right]^{0.5} \tag{5.13}$$

where M is the molecular mass.

It is worth noting that since l is related to the gas pressure and temperature a reduction in gas pressure, or increase in temperature will increase l allowing Knudsen diffusion to be dominant for even relatively large pore diameters.

5.4 Dry Storage of Spent Nuclear Fuel

As discussed above the key requirements for the dry storage of spent fuel are the maintenance of the integrity of the fuel to prevent the release of fission products, ensuring that the fuel can be safely retrieved at a later date and the prevention of criticality during storage. Corrosion must be prevented since failure to do so may lead to cladding failure which may will release fission products's and in extreme cases may allow geometrical reconfiguration of the fuel to a point where criticality can achieved. The presence of water may also lead to the production of a flammable hydrogen atmosphere as a result of the reaction between water and metal fuel cladding or the direct radiolysis of water. A final danger when metallic uranium fuel is present is the risk of uranium hydride production which is pyrophoric. Such an atmosphere is a potential risk when spent fuel is being recovered for permanent disposal.

There are two basic types of drying which can be used for spent nuclear fuel, forced gas drying in which a hot pressurised gas is forced through the canister and vacuum drying where the canister is evacuated this reducing the vapour pressure. The following sections look at these methods in more detail.

5.4.1 Cold Vacuum Drying

Cold[1] vacuum drying similar to that used for drying commercial power reactor fuel was used at the US Department of Energy's (DoE) Hanford site for the drying of Zircaloy clad, uranium metal fuel. This was carried out as part of a project to remove around 2100 tons of fuel from basins in which it had been stored for 10-25 years. The fuel was first washed to remove crud[2], corrosion products and sediment and loaded underwater into Multi Canister Overpacks (MCO)[3]. These were in turn loaded into shielded transport casks. The canisters were drained and then evacuated to an initial pressure of approximately 13 mBarA (10 torr)[107]. Hot water (50 °C) was flowed in the annulus between the canister and transport cask and vacuum drying was continued for 24-48 hours [108]. Once the pressure reduced to 0.7 mBarA a vacuum rebound test was used to confirm adequate dryness. The vacuum was isolated and the pressure monitored for 1 hour. A pass required the pressure to remain below 4 mBarA. The fuel was ultimately stored in sealed containers with the intention of transfer to a geological disposal facility when possible.

The parameters for this method were developed by Pajunen et al [109]. Pajunen's aim was to develop a set of drying parameters for which a vacuum rebound test would be a suitable test for dryness. It was assumed that all unbound water except that retained within cracks and pores was removed by the vacuum drying process. Three separate models were used to model water retained in these cracks and pores and numerous drying parameters were analysed to develop parameters that would reduce trapped water (described as residual free water) to <200 g. Four sets of conditions were developed that matched this, three involving vacuum drying and one using a helium flow. These four methods were further analysed to assess whether a vacuum rebound test could be used to prove that the volume of

[1] The technique is commonly known as cold vacuum drying since compared to some methods relatively little heat is supplied but warm vacuum drying is probably a more suitable term.

[2] Within the nuclear industry crud is a term used to describe unidentified deposits left on fuel after irradiation. First seen at Chalk River hence the name Chalk River Unidentified Deposits [106].

[3] An MCO is a stainless steel canister into which several spent nuclear fuel assemblies can be loaded for transport and storage.

water retained had reached <200 g. Of these, two were found to meet the requirements. The final parameters were decided upon due to the predicted overall cycle time that would be required.

In an overview of the project at Hanford, Loscoe [110] discussed some of the major challenges. Since the N-reactor fuel at Hanford utilised uranium metal not all of these challenges will apply to oxide fuels however two that do are the dangers of over-pressurisation and the production of a flammable atmosphere with the cask.

Since the Hanford remediation project intended to create a dry storage system that did not require any monitoring there was a need to prevent the over pressurisation of the canister due to gas build up since over pressure valves were not feasible[1]. The two potential sources of gas were from breakdown of water or from fission products (xenon, krypton) and alpha emitters. Gas could be evolved from water by either radiolysis to yield hydrogen and oxygen (a total of 1.5 moles of gas from 1 mole of water) or by a reaction between uranium and water to yield 1 mole of hydrogen. From estimates of the maximum conceivable volume of water in the MCO following drying and the worst case of all water broken down by radiolysis it was possible to show that the volumes of gas from fission products etc were negligible and that overall the total worst case pressure increase was well below the design pressure.

In regard production of a flammable atmosphere within the cask, the limiting factor was stated as being an oxygen concentration of 4% or greater. A method was described in which it could be shown that there were no combinations of decay power, water content or temperature that could yield an oxygen concentration of 4% or higher since any oxygen produced tends to react with uranium. For an oxide fuel the likliehood would be even lower since there would be no uranium metal present.

The Chalk River Laboratory in Canada used a similar method to the cold vacuum drying process during a remediation project for fuel that had been in dry storage for up to 25 years [111–113]. While similar to the Hanford process periodic cycles of vacuum heating followed by pressurisation were carried out to

[1]Use of an Over Pressure Valve would require monitoring of gas to assess whether any OPV was lifting and releasing fission products. Any lifting OPV would require investigation and remedial work which would in part defeat the purpose of sealed storage.

prevent freezing, and the end point (extent of dehydration) was established from equilibrium pressure measurements. Chalk River Laboratory carried out a series of tests using a fuel element removed from storage to assess drying characteristics and process parameters [111]. They concluded that the vacuum drying process was capable of completely removing free water as well as some physiosorbed water. Vacuum rebound tests were carried out periodically but no correlation was observed between rebound test results and equilibrium pressure.

Hot Vacuum Drying

A hot vacuum drying method was developed for use on aluminium clad fuel stored at the Idaho National Engineering and Environmental Laboratory (INL, interchangeably known as Idaho National Engineering Laboratory, INEL and Idaho National Engineering and Environmental Laboratory, INEEL). The first stage was to remove free water and was similar to the Hanford cold vacuum drying. Fuel was loaded into self-draining canisters underwater and then transferred to the drying facility. A lid containing vacuum lines and thermocouples was then added and the canister evacuated. The pressure was maintained above 6.7 mBarA (the triple point of water) to prevent freezing and electric band heaters surrounding the canister were used to maintain the internal temperature at 50 °C. Once the pressure reached 4-6.7 mBarA the system was isolated for a pressure rebound test (initial pressure maintained for 1-2 hours). The second stage involved heating the fuel to 150 °C in a flow of 2% oxygen 98% argon for two hours [107].

The parameters for this method were developed from work by Lords & Crepeau [114–116] who carried out a number of tests using a half scale mock up drying rig, simulated corrosion product and fuel elements. The key difference between the Hanford cold vacuum drying and hot vacuum drying method was due to the presence of corrosion products and crud on fuel from INEEL. The geometry of the fuel prevented an effective washing step from being completed prior to the drying step, and consequently a more aggressive drying method was required to dehydrate the corrosion products as well as remove free water.

It was estimated that the first 16% of water contained in the corrosion products sludge was released in the first thirty minutes under vacuum. Extending this to

four hours increased water release to 28% but further extensions had little effect. The use of a two hour heating period alongside vacuum increased this to over 60%. Thermocouples placed in various positions on the mock fuel elements showed that element temperatures may lag behind those of the air temperature by up to 10 °C even after several hours heating [115, 116]. Further work involved simulating the effect of aggressive drying on flooded pores [115]. Pores were replicated by drilling small holes into the mock element surface, gluing aluminium foil over the top and injecting water. It was found that even with the most aggressive conditions no damage was observed to the cladding (foil) from the flashing of steam in the pore as the canister was evacuated.

Later work by Crepeau et al [114] experimented with a series of vacuum and heating cycles. For each cycle the canister was evacuated down to 665 Pa and then held for five minutes before being backfilled and heated with the heaters set to 220 °C before being evacuated once again. The heating phase for the first cycle was 30 minutes with this increasing by five minutes for each of the next three cycles. It was shown that this method was capable of removing all free water but higher temperatures were required to dehydrate corrosion products. Dryness can be measured from the temperature behaviour of thermocouples attached to the centre of the mock fuel elements. It was shown that if moisture was present during the vacuum hold period at 665 Pa the temperature would remain constant however once all residual moisture was removed the temperature would increase during the hold period. It was further shown that after four drying cycles 72% of fuel elements were completely dried and that with an extra drying cycle all fuel was dry. Thermogravimetric analysis of the simulated corrosion products after drying suggested that the dried corrosion product was drier than ambient as it appeared to absorb water from the atmosphere. A final interesting observation from an assessment of deliberately inadequately dried fuel elements showed the existence of a sharp drying front from the outside of the fuel plates towards the centre rather than a gradual increase.

While AGR fuel will be largely free from corrosion products and crud the potential need to remove water from microcracks and flooded fuel pins is likely to provide a similar challenge suggesting that more aggressive conditions than those used in cold vacuum drying will be required.

5.4.2 Hot Gas Drying

An hot gas drying method has been used by the French to dry fuel from their Uranium Naturel Graphite Gaz (UNGG) reactors[117, 118] prior to storage. This magnesium alloy clad, uranium metal fuel similar to British Magnox fuel had been left in wet storage for up to 25 years where corrosion occurred leading to the production of pyrophoric uranium hydride. Unlike other drying methods the first step involved the mechanical removal of cladding to leave bare uranium fuel. This was followed by several heating steps in an atmosphere of argon, the first at 100°C to remove liquid water and the second at 430°C to pyrolyse any uranium hydride. A final drying step involved partially oxidising the uranium at 250°C in an atmosphere of argon and oxygen (increasing from 5-20% O_2 with time). The fuel would finally be sealed in aluminium canisters and then transport casks prior to shipping to either a reprocessing plant or for long term storage.

The US firm Holtec have developed a method of fuel drying known as Forced Helium Dehydration (FHD)[119]. This system involves flowing a hot gas stream, normally helium through the fuel canister and condensing out the entrained water. The system utilises a closed loop to reduce helium usage and prevent the release of fission products. This system is widely used in the US at commercial dry fuel stores. The end point for the drying process is determined through use of an inline dew point sensor.

With Magnox reprocessing at the Sellafield site due to end in 2014 before all UK Magnox fuel has been processed a number of these drying methods (Hanford cold vacuum drying, INEEL hot vacuum drying and Hot Gas Drying) were assessed as contingency options for dealing with remaining fuel [120]. It was noted that all methods were initially suitable but with some limitations. Vacuum drying methods relied upon reaching a standard of sufficient dryness. While this may be acceptable for zircaloy or aluminium clad fuels which, in comparison to magnesium clad fuels, are relatively resistant to corrosion, no level of sufficient dryness has been set for magnox fuels. Also problems related to hydrogen and UH_3 were of less concern since the fuel was intended for permanent geological disposal with no recovery (Hanford) or for vented storage with no hydrogen (and therefore UH_3)

build up (INEEL). Hot gas drying has been shown to dry fuel to a sufficient standard although the time and costs involved would be substantially greater.

5.4.3 Types of Dry Storage

Dry storage of spent nuclear fuel has been described by Sindelar et al [121] as existing in two distinct types; sealed and unsealed systems. A sealed storage system is generally regarded as being the ideal candidate however seals must either last for the entire storage period or allowance must be made for seal replacement or potential repackaging. Furthermore a sealed system allows the build up of hydrogen and formation of UH_3 particularly when storing damaged fuel. This is not possible in an unsealed system where the flow of gas through the system removes hydrogen and also helps to minimize fuel temperature. There is however an increased risk of fission products release requiring an increased level of monitoring of gas and unfortunately as fuel cladding is generally used as the first layer of confinement to prevent fission products release unsealed storage is not suitable for damaged fuel.

As well as sealed and unsealed systems dry storage can be classified according to the use of either vaults, silos or casks. Morris et al [120] described the three systems as follows. A vault store is a large concrete structure capable of storing hundreds or thousands of fuel assemblies, in which fuel is stored in a number of storage tubes with the shielding provided by the concrete structure of the building. Such a vault is used for the storage of Magnox fuel at the Wylfa site in North Wales. Casks and silos are both designed as modular storage systems with new casks or silos being added to a site as required. The shielding and structural strength is provided by steel/concrete structures each capable of holding a much smaller number of fuel bundles ($\ll$100). The key difference between the two is that casks are generally multi-purpose transport and storage containers whereas silo's require separate transport casks.

Chapter 6

Drying Rig Construction, Commissioning and Behaviour

6.1 Introduction

The first part of this thesis has covered the preparation of samples that can be used in later drying tests. This second part of the thesis focuses on the drying of these samples. In chapter 5 it was shown that two methods have been used to dry zircaloy or aluminium clad fuel on a commercial scale. These methods are vacuum drying and flowed gas drying. There is however little evidence as to the relative effectiveness of each method since there has been no controlled testing on comparable fuels. The purpose of this thesis is to address this by building and operating a multipurpose drying rig capable of both vacuum drying and flowed gas drying.

A simplified version of the concept rig is shown in fig. 6.1. The concept was to construct a drying vessel in which simulant fuel samples could be placed and dried. A vacuum drying system is much simpler and requires only an outlet line to a vacuum pump and a heated drying vessel. When the heater is turned on the vessel will warm the fuel and the vacuum pump will extract the water vapour. A flowed gas drying system is more complex. Gas must be flowed through the vessel so an inlet and outlet line are required and the gas is often heated before entering the vessel. In its simplest form a once through system would be utilised with the

wet gas simply being released to atmosphere however since helium may be required and the gas usage is high a recirculation system will likely be utilised which will therefore require a recirculation pump and a system with which gas can be dried. A method of increasing the system pressure will also be required. The following sections look at the rig design, development and construction in more detail.

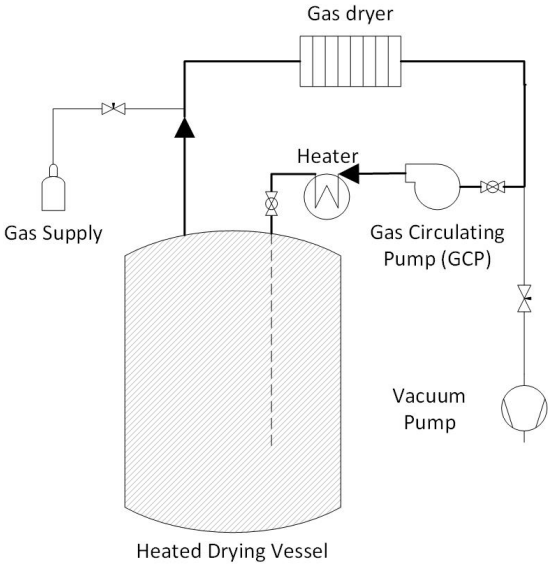

Figure 6.1: Basic concept design for a multipurpose drying rig.

6.2 Envisaged Operating Procedure and Initial Design

Before a detailed design and specification was put together the basic operating procedure for the system in both vacuum drying and flowed gas drying was compiled. The various steps envisaged are discussed below and are based on how fuel would arrive and be treated in a real life scenario.

6.2.1 Bulk Water Removal

The first step of the drying process is shared for both vacuum drying and flowed gas drying. The fuel will arrive inside a cask which will be flooded with water to

provide shielding and cooling. The first step will be to remove this bulk water. In order to achieve this the vessel will require two connections one of which will have a dip tube to the base of the vessel. Gas will be flowed into the top of the vessel forcing the bulk of the water out of the vessel to leave only a heel of water behind.

6.2.2 Vacuum Drying Operation

When vacuum drying, after removal of the bulk water one of the two lines used to remove the bulk water will be closed off with a valve as will the line to the gas supply used to displace the water. A vacuum will then be drawn on the vessel removing water vapour from the system. The water vapour could theoretically go directly to the vac pump but since the drying system will be in place for the flowed gas drying it should be used to protect the vac pump.

6.2.3 Flowed Gas Drying

When carrying out flowed gas drying the dip tube that was used to remove bulk water will be used to flow hot dry gas into the vessel. Wet gas will removed from the system through the same line used to pressurise the vessel. The wet gas will be passed through a drying system and then returned to the vessel via a gas pump and then a gas heater.

6.3 Initial Design

An initial design for the rig was produced and a hazard and operability study (HAZOP) was carried out to ensure the design was safe. Several minor changes were made leading to the final design seen in fig. 6.2.

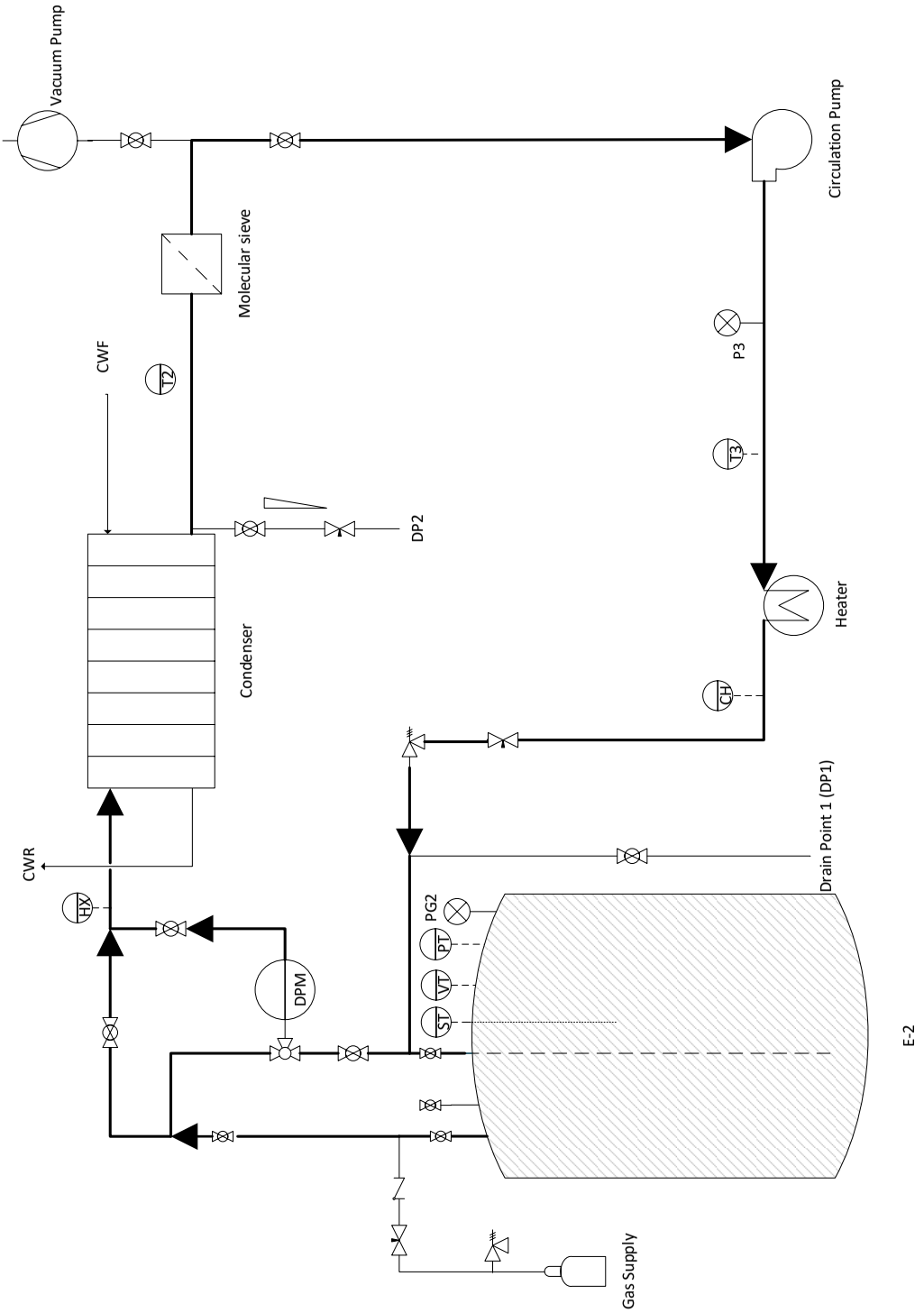

Figure 6.2: Schematic drawing of the final rig design following HAZOP.

6.4 System Parameters

As discussed above the intention is to design a rig that is capable of undertaking both vacuum and flowed gas drying tests. The system parameters are in part based on the details of commercial systems available. No infirmation is available as to the conditions used within the Holtec or other current commercial flowed gas methods in relation to pressure and flow rate which are two of the key parameters. As such the choice of these will be based around technical parameters, i.e. what can be reasonably be achieved. The method used for drying UNGG fuel has a drying step at 100°C (other higher temperature steps inthis method having other purposes beyond drying) and this is therefore regarded as being the minimum temperature that should be achievable.

A little more information is available regarding vacuum drying system but still not a significant quantity. Of the methods reviewed the highest temperature used was 150°C. This was chosen as being a suitable temperature to use when designing the system as it met the requirements for flowed gas drying and yet is easily achievable. The other critical vacuum drying parameter is pressure. The methods used typically used pressures in the range of 0-4 mBarA and the aim is to meet these values.

6.5 Rig Components

Having produced a final design the following parts were obtained for construction.

6.5.1 Drying Vessel

The design and specification of the drying vessel came about from a number of factors. The two key design parameters were the operating pressure and temperature. The hot vacuum drying process used at INL used an operating temperature of 150°C and this was used as a starting point for the operating temperature. The vessel was constructed from a length of 2.5' schedule 10' stainless steel pipe with a domed cap and flange welded in place to give a vessel with an internal volume close to 500 ml. A blank flange was to be used as a lid with stainless steel tubes

welded into place to act as the inlet and outlet lines (10 mm internal diameter) and instrumentation lines (fig. 6.3).

The maximum pressure is only relevant for flowed gas drying and since this information is not publicly available a pressure of 10 BarG was chosen. This pressure was felt to be higher than would actually be necessary but this would allow plenty of room for testing to be carried out. It was also found to be close to the maximum operating pressure for schedule 10 pipe at 150°C. Consequently the design temperature and pressure were taken to be 10 BarG at 150°C.

A 4" band heater with an integral thermocouple was purchased from Watlow and was fitted around the outside of the vessel to provide heating. The band heater (and the circulation heater discussed below) was controlled by a digital temperature controller purchased from Watlow and made into a control unit in house. The integral thermocouple was designated as being the process temperature (this was used as the vessel set point and taken to be an approximation of the vessel wall temperature). The vessel and heater were wrapped in lagging and placed into a stainless steel tin to function as a stand.

The vessel itself was fitted with four further thermocouples. A thermocouple was fitted in the gas at the top of vessel and this was designated the vessel temperature (VT). A third was a flexible thermocouple which could be used to record the surface temperature (ST) of the test piece within the vessel. Finally thermocouples were fitted at the inlet (Vin) and outlet (Vout) of the vessel.

The vessel was fitted with an analogue pressure gauge and a port for a pressure transducer. Two digital pressure transducers were purchased one with a range of 0-2 BarA (high resolution) and another with a 0-15 BarA range (low resolution) with the transducer changed according to the test being carried out.

A spare line with a valve was also fitted to the vessel to allow for further modifications if required.

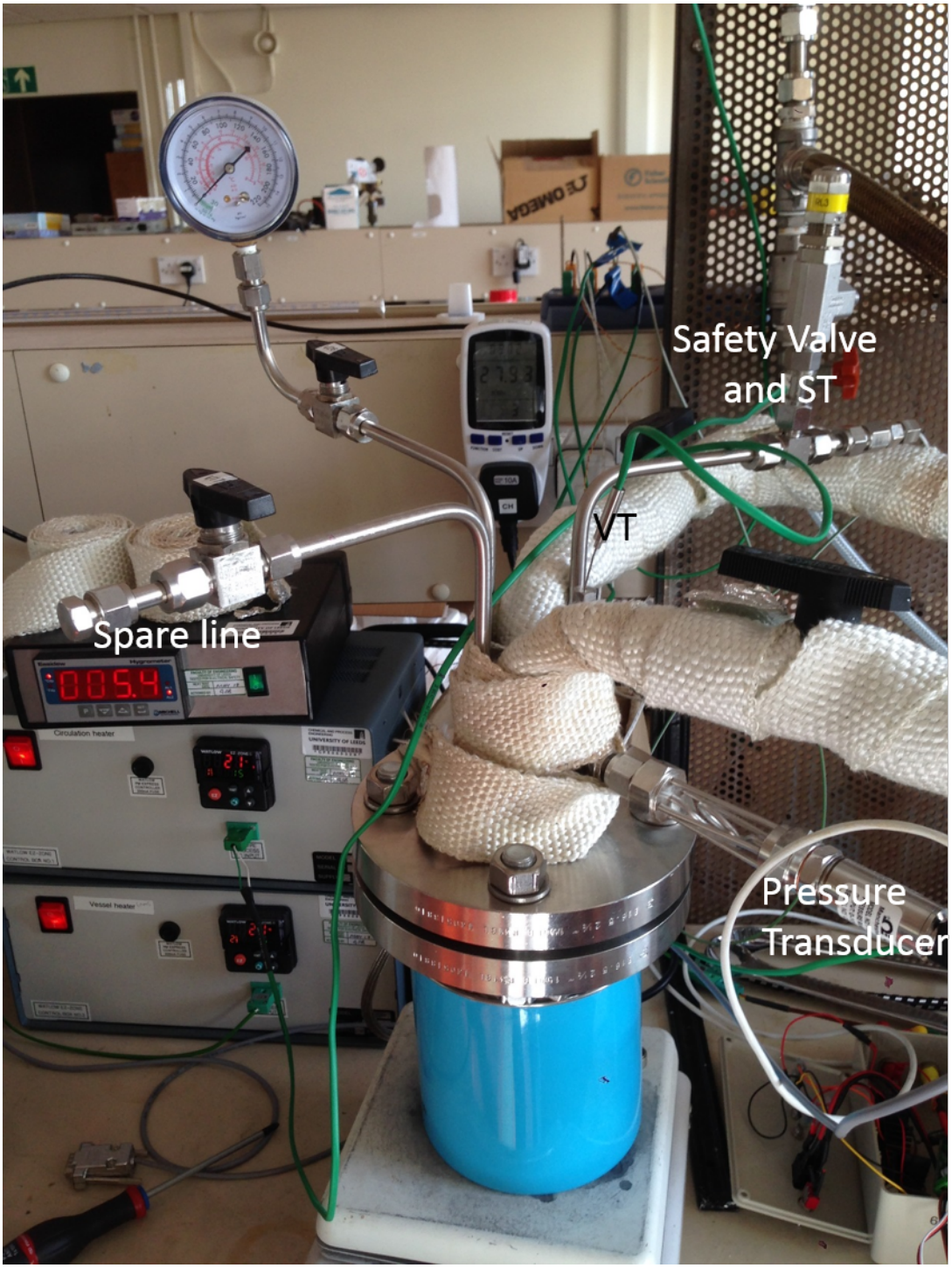

Figure 6.3: The drying vessel.

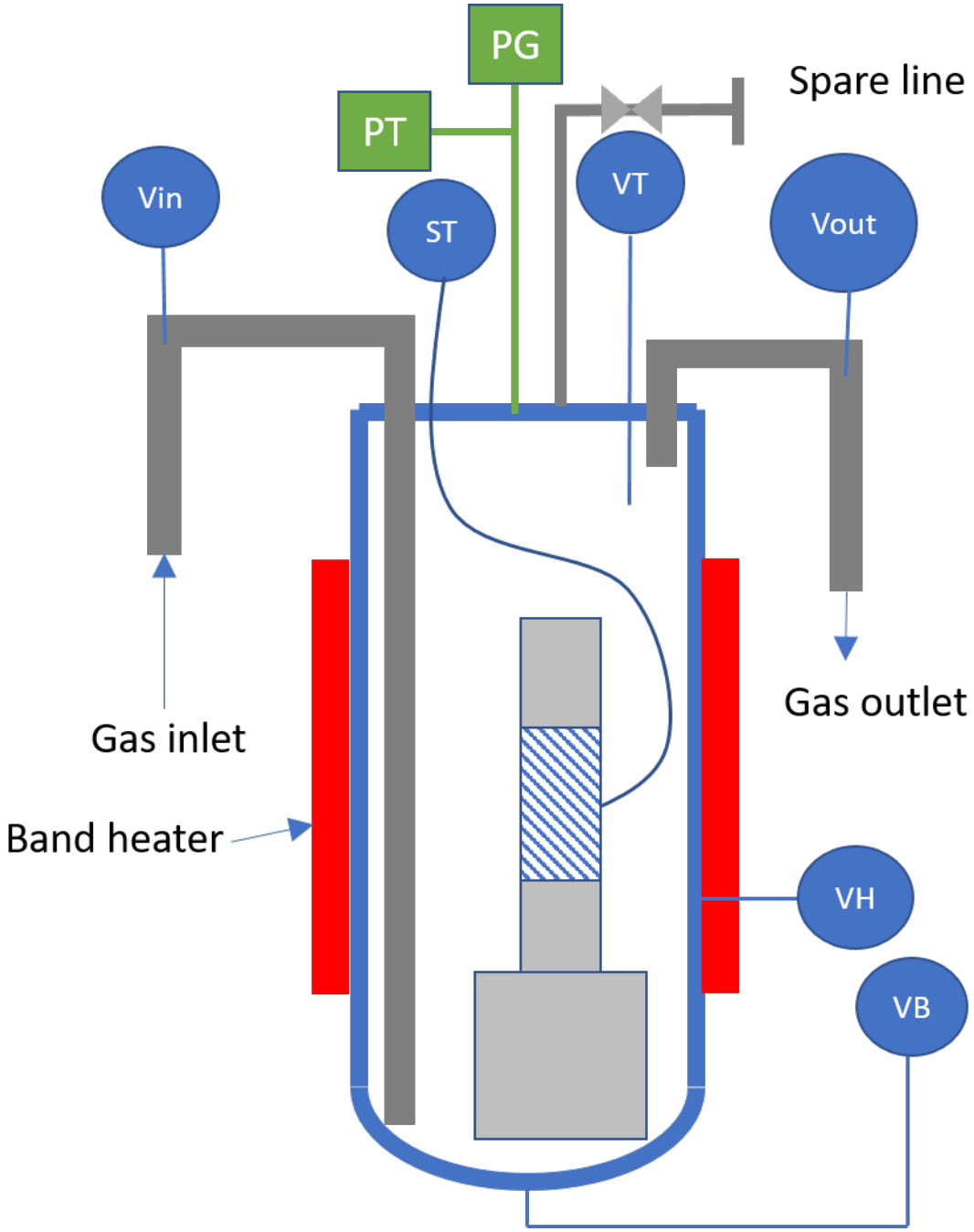

Figure 6.4: A schematic diagram of the drying vessel showing layout of thermocouples (blue circles), and pressure gauge and transducer (green rectangles).

6.5.2 Pipework and Fittings

The pipework was constructed from stainless steel tube using a combination of twin ferrule compression and threaded fittings (Tee pieces etc). For the primary loop pipework 12 mm outside diameter (OD), 10 mm internal diameter (ID) stainless steel tube was used alongside primarily 1/2" BSPT fittings although in some places other sizes were used. Vacuum and gas supply were through 6 mm flexible hose. Stainless steel flexible hoses were used to connect the vessel to the pipework and these had 1/2" BSPP fittings.

6.5.3 Gas Drying System

For flowed gas drying a method for drying the gas is required. In the Holtec method this is achieved with the use of an air cooled condenser and a demoisturising module that freeze dries the air. For this bench top rig a simpler system was decided upon. This consisted of a water cooled condenser and a filter column packed with molecular sieve. The water cooled condenser was intended to remove the bulk water from the system with the molecular sieve being able to carry out the final drying step. A small plate heat exchanger was sourced to act as the condenser (or heat exchanger, condenser). Water could be removed from the system during operation through drain point 2.

The molecular sieve was packed into a 6" length of 1" stainless steel pipe. Later this was replaced with a length of 1.5" pipe with sanitary fittings to ease disconnection when the sieve required changing. The molecular sieve was regenerated after use by heating to 300°C.

6.5.4 Gas Heater and Pump

The system ultimately used three types of heater; a band and circulation heater which were obtained from Watlow and a number of lengths of heating tape.

The recirculated gas was heated with a Cast-X 2000 240 V, 1 kW circulation heater purchased from Watlow. This had a built in thermocouple for over temperature control. The vessel inlet thermocouple was used for process temperature control (see fig. 6.4).

Two lengths of heat tape with built in adjustable thermostats were also purchased from Omega Engineering Ltd. One length was used to prevent cooling of the gas before the vessel and prevent condensation of water vapour in the pipework prior to the condenser. This was set to run at around 50°C which was the maximum operating temperature of the flowmeter. The second length was placed on the inlet line to the vessel. This was also initial initially set at 50°C but was later set to higher temperatures.

A D10K gas pump was purchased from TCS Instruments. This had a maximum flow rate of 11 l min^{-1} and maximum differential pressure of 6 psi (∼400 mBar) for air at atmospheric pressure. The pump was supplied with a speed control board and a control unit was made in house.

6.5.5 Instrumentation

Temperature As an experimental drying rig the system was fitted with several instruments. Thermocouples were fitted in multiple locations around the pipework to allow temperature changes to be measured as the gas was circulating. In addition to the thermocouples on the vessel, thermocouples were placed midway between the vessel and condenser (T1), at the inlet to the condenser, between the condenser and molecular sieve (T2) and between the circulation pump and heater (T3). Analogue pressure gauges were also placed alongside T1, T2 and T3 (P1, P2 and P3 respectively). thermocouples were also fitted to record the temperature of the cooling water flow and return (CWF and CWR).

K-type mineral insulated thermocouples were used throughout with the tip located in the centre of the pipework.

Flow An El-Flow mass flowmeter from Bronkhorst UK limited was fitted to the recirculation pipework between the condenser and the molecular sieve. This location was chosen as the flowmeter had a maximum operating temperature of 60°C and since the intention was to have a temperature of up to 150°C being down stream of the condenser would protect the flowmeter. A mass balance would theoretically be possible by recording the volume of water removed from the condenser.

Before the rig was constructed there was little knowledge of the flow rates that would be obtained. Consequently the flowmeter range was based on the maximum capacity of the recirculation pump.

Humidity Since the purpose of the rig was to dry spent nuclear fuel it was felt necessary to be able to monitor the humidity of the flowing gas. This was to be achieved with a Michell Instruments Easidew Online dew point meter (dew point meter). This had been purchased for an earlier drying project and had a dew point range of -100°C to +20°C. The dew point meter came with a display module which was placed into a control box in house.

In an ideal world two dew point meter's would have been available to allow the dew point of both the dry and wet gas to be monitored however due to the high cost of these units this was not possible. The recirculation pipework was therefore designed to allow dry gas to be fed to the dew point meter. The pipework was also designed to ensure that the maximum operating pressure was not exceeded. The dew point meter could be bypassed along the route containing T1 mentioned above. T1 was located such that the temperature there would be be similar to at dew point meter if that route was taken. For high temperature tests the dew point meter would initially be bypassed to allow the gas temperature to be measured and if it was found to be below the operating temperature of the dew point meter the gas would be flowed along that route.

6.5.6 Gas Supply and Vacuum Source

The gas to increase the system pressure will be supplied from a regulated gas cylinder. The vacuum source was an Edwards E2M5 vacuum pump. The ultimate vacuum of the pump was stated as 2.5 x 10^{-4} mBar.

6.5.7 Valves

As with all systems of this type numerous valves will be required. Where the purpose of the valve was to be isolation only ball valves were used. When some degree of flow control was thought to be required needle valves were used. A single check valve was used to prevent the flow of fluid back towards the regulator.

The system used two Swagelok RL3 series pressure safety valves.

6.5.8 Data Logging

Multiple data logging systems were used. The flowmeter was connected directly to a PC and data was recorded using FlowDDE and FlowPlot software which was supplied by the manufacturer.

Two data loggers were purchased from Omega engineering, one for recording the pressure transducer and dew point meter data and one for recording thermocouple data. The Tracerdaq software supplied limited the total number of channels to 8. Consequently further channels were recorded using a combination of handheld digital thermometers and two Labview programmes written in house. On occasions two PC's were used. One of the heater controllers could also be logged through Labview. The total number of channels that could be recorded changed during the course of experimentation as different methods of operation were assessed.

Data was generally recorded at 1 Hz with the exception of some longer tests when it was reduced to 0.5 Hz and flow data which was always at 10 Hz.

6.6 As Built Rig

Figure 6.6 and 6.5 show a process and instrumentation drawing (P&ID) and picture of the as built rig. Table 6.1 gives a full list of all instrument and parameter abbreviations.

The pipework was put together in sections with leak tests carried out on each section by immersion in water. Once the system was completed initial positive and negative leak tests were carried out by filling the system with gas to a pressure of about 0.5 BarG and observing the behaviour on the analogue gauges. When leaks were found they were isolated to a specific section by closing some of the valves. Once the leak had been traced to a specific section the exact location was found with a soapy bubble test.

Once all leaks had been found in this manner final extended leak tests were carried out by reducing the system pressure and leaving the system to stand overnight.

For the system as a whole several small leaks were found to still exist within the pipework. These were regarded as acceptable since the critical leak test related to the drying vessel which would be required for vacuum rebound tests. This had been identified prior to design and construction so only compression fittings were used up to the isolation points on the drying vessel. Leak tests on the drying vessel gave no noticeable rise in vessel pressure once isolated when left overnight ($\sim$18 hours). Some other commissioning tests were carried out in parallel to leak tests.

Abbreviation	Short name	Description
ST	Surface Temperature	Flexible thermocouple inside vessel to measure sample surface temperature.
VT	Vessel Temperature	Temperature of the gas at the top of the vessel.
Vin	Vessel inlet temperature	
Vout	Vessel outlet temperature	
T1	Temperature 1	Temperature midway between vessel and condenser.
T2	Temperature 2	Temperature between condenser and sieve.
T3	Temperature 3	Temperature between circulation pump and heater.
HX	Heat Exchanger	Temperature at condenser inlet.
CWF	Cooling Water flow	
CWR	Cooling Water return	
DPM	Moisture Indicator or Dew Point Meter	
PI	Pressure Indicator	
DP1	Drain Point 1	For bulk water removal.
DP2	Drain Point 2	For condenser water removal.
S1	Sieve 1	thermocouple on molecular sieve casing upstream.
S2	Sieve 2	thermocouple on molecular sieve casing downstream.
VH	Vessel Heater	Integral vessel heater thermocouple. Approximates to vessel wall temperature.
VB	Vessel Base	Thermocouple attached externally to base of vessel.
CH	Circulation heater	Gas heater for flowed gas drying.

Table 6.1: Abbreviations for rig parts and instruments some of which are found in later chapters only.

Figure 6.5: Picture of the as built rig. The heat tracing and lagging have not yet been fitted. 1-Drying vessel, 2- Dew point meter, 3-Condenser, 4-Flowmeter, 5-Molecular sieve, 6-Vacuum supply point (line not attached), 7-Position of circulation point (not shown), 8-Circulation heater.

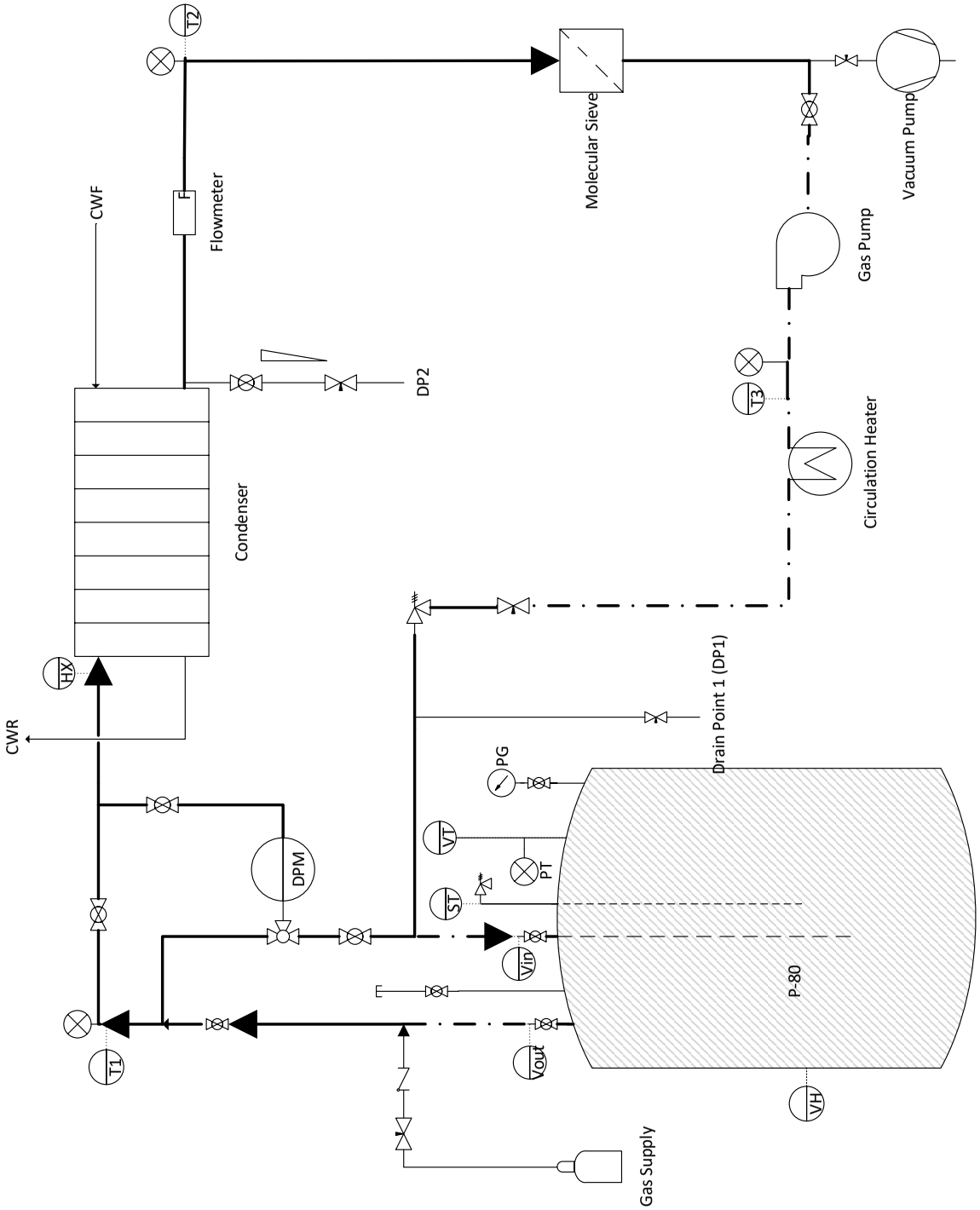

Figure 6.6: P&ID of the as built rig.

6.7 Commissioning Tests

6.7.1 Bulk Water Removal

The first tests carried out related to the bulk removal of water. These tests were carried out to ascertain what volume of water was left in the vessel after the removal of bulk water via the dip tube and how much water hold up took place. This was achieved by filling the vessel with ∼500g of water and then removing it. The mass of water collected via the drain point was then recorded, as was the mass of water remaining in the vessel. The mass of water remaining in the vessel was calculated by placing an empty beaker and a piece of blue lab roll on a balance. The free water was poured into the beaker and any drips on the surface of the vessel mopped up. The mass change was then recorded. The data from these tests is in table 6.2.

Starting Water in Vessel [g]	Bulk Water Collected [g]	Water Remaining in Vessel [g]	Holdup [g]
500.00	472.30	7.20	20.50
500.05	488.20	11.60	0.25
500.50	496.75	7.20	-3.45
499.90	482.60	8.25	9.05
500.90	481.60	13.05	6.25

Table 6.2: Initial water hold-up in system following bulk water removal.

From the data it can be seen that there was considerable variation in the volume of water held up within the system. Unsurprisingly the initial bulk test showed the greatest water hold up. It had been expected that after several tests the quantity of water held-up within the system would reach approximately zero however it was found that water continued to be held up within the system. The mass of water that remained in the vessel was between 7.2 g and 13.15 g with an average of 9.46 g.

The continued hold-up of water suggested that water was being routed and held-up somewhere expected. By reviewing the pipework it became clear that very

specific valve sequencing was required to prevent water being directed into lengths of pipework where it could become trapped. This would occur if the system was pressurised (to displace water) before the line to the drain point was opened. The operating procedure was therefore updated to ensure that system pressurisation was the final step.

After making operational changes the results found in table 6.3 were obtained. While the level of hold up was greatly reduced there was still found to be some variation. This was felt to be due to changes in the curvature of the hoses used to connect the vessel to the pipework. Based on this it was decided that a fixed mass of water would be added to the vessel to act as heel water since ensuring the position of the hoses would be extremely difficult and offer little advantage.

Starting water in vessel [g]	Bulk Water Collected [g]	Water Remaining in Vessel [g]	Holdup [g]
500.90	499.50	4.9	-3.5
501.30	493.10	7.15	1.05
498.40	494.25	7.05	-2.9
500.00	495.65	5.05	-0.7

Table 6.3: Water hold-up in system following bulk water removal using modified method.

6.7.2 General Behavioural Tests

A range of initial tests were carried out. These tests were carried out with no particular objective other than to observe the behaviour of the rig and assess what data could be collected and if any initial changes would be required. Some of these findings are discussed below. These tests were almost all vacuum tests since they were carried out before a section of the recirculation pipework was in place.

Cooling Water and Mass Flow An early test was carried out with 250 g of water in the vessel and no vessel heating (fig. 6.7). The cooling water to the

condenser was not initially flowing. The lower resolution pressure indicator was in use and the flow rate is given as the percentage of full scale.

During the first 1200 seconds there were several changes in flow rate. These were due to the valves that allow the dew point meter to be bypassed being opened and closed. The large spike in flow at 2000 s was due to the cooling water being turned on. Since the mass flow meter was immediately downstream of the condenser this was thought to be due to an initial cooling of the gas leading to an increase in density and greater mass flow. This also lead to an initial pressure drop across the flow meter or condenser leading to an apparent rise in the vessel pressure.

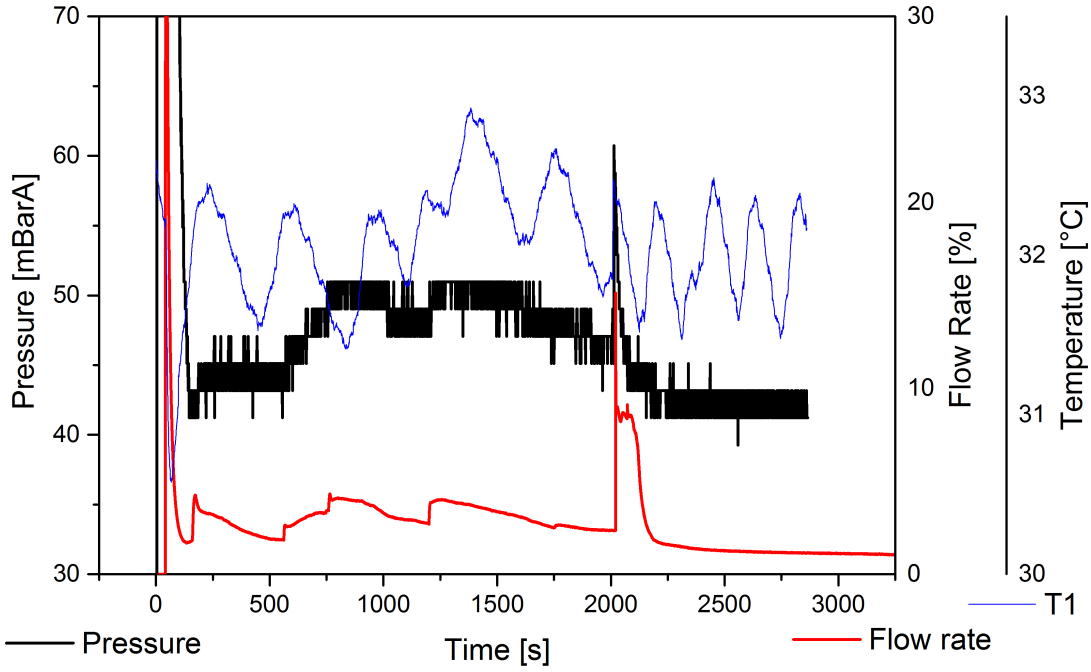

Figure 6.7: An early test showing the impact of opening and closing dew point meter bypass valves, the effect of cooling water and behaviour of heat tracing.

The initial design of the rig envisaged using a mains water cooled condenser. Unfortunately the lab was based on the fourth floor and the mains water was found to be close to 27°C and was therefore ineffective. To avoid this water was pumped

around in a closed cycle from a water tank which was held at room temperature giving cooling water of around 17°C.

Behaviour of Heat Tracing The heating behaviour of the heat tracing can be seen from the temperature of T1 in fig. 6.7. The thermostat functions by powering the heat tracing for a short period leading to a rise in temperature before shutting off allowing the tube to cool. This process repeats leading to the wavelike behaviour observed.

Temperature Control Difficulties The vessel heater was initially to be controlled using the thermocouple monitoring the vessel gas temperature, vessel temperature and this was not initially logged. Figure 6.8 shows a plot of a test in which the vessel was filled with water and heated. No sample was present in the vessel so the surface temperature thermocouple was hanging, free lying against the vessel wall and was initially submerged. The vessel temperature was set to 150°C. The vessel was then evacuated.

Since surface temperature was in the water it was recording the water temperature which since the vessel had been evacuated was the boiling point of the water. As more water is boiled off the pressure increases leading to an increase in surface temperature. Once all the water has been removed surface temperature begins to record the wall temperature which increases to 400°C. The set point temperature was 150°C however the vessel gas temperature (which was not logged since it was being fed into the controller) did not reach 150°C so the heater kept operating.

Vacuum Level During a number of tests it was found that the ultimate vacuum for the system was in the region of 20 mBarA. While this was not as low as may be liked it was felt that it was low enough for the initial tests considering the time that would be required to improve this.

Dew Point Meter Failure During one of the commissioning tests water was accidentally condensed around the dew point meter causing it to fail. A dew point meter such as that used is not able to deal with liquid water. As the system was brought from a vacuum to atmospheric pressure while still containing saturated

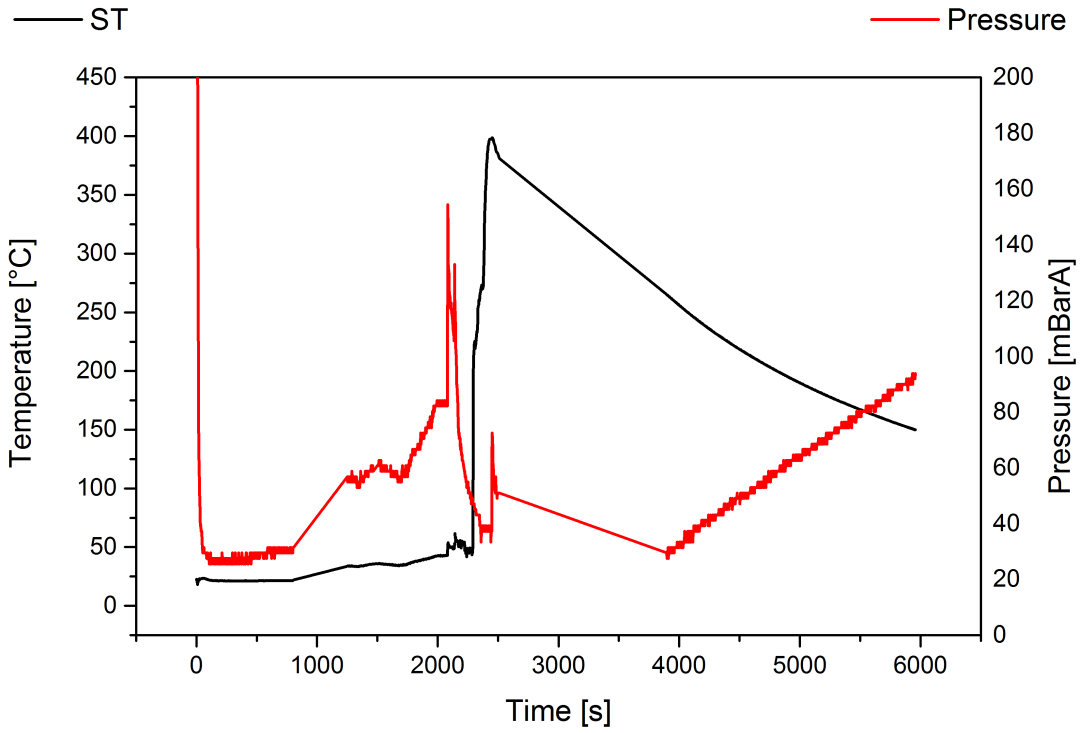

Figure 6.8: An early test showing the ineffectiveness of using vessel temperature as the process control.

gas, water condensed due to the sudden pressure rise. The positioning of the dew point meter at this time meant that water was able to pool around it leading to its failure.

The dew point meter was repaired and the pipework modified to prevent water pooling around the dew point meter. The dew point meter was then tested again this time during an elevated pressure (FGD) test. The dew point meter now failed almost immediately. After discussions with the manufacturers it was concluded that the Easidew was not suitable for this purpose. A different model with a dew point range of -40°C to +60°C was discussed however we were informed that this would still not be suitable for a saturated liquid. Since we could not guarantee that a saturated liquid could be avoided it was decided that carrying out further repairs would not be a sensible course of action since further breakdowns were still likely.

Flow Meter Range Part of the early testing was used to understand how the flow meter software functioned. The dew point meter was calibrated by the manufacturer for air at 11 l min^{-1} and atmospheric pressure. Before use the software was programmed with the system pressure at both inlet and outlet and also the test gas. Once these had been established the maximum value for the flow meter could be chosen. The flow meter then displayed the flow and recorded the data as a percentage of the maximum flow rate. The software would read no higher than 131% and as result the plots for flow tend to begin with sharp initial spikes that go off the scale and then drop back down.

The minimum value that the pressure could be set to was 0.8 BarA. Since this is somewhat higher than the pressure to be used and the flow meter is not designed for measuring water vapour the flow rate is not entirely accurate in numeric terms however it was valid in relative terms i.e. the flow in test A was twice that in test B. This was felt to be suitable for the work in hand as values such as this would be specific to this system. Should the precise value be required it is possible to calculate an accurate value on an individual basis.

Chapter 7

Initial Drying Tests

7.1 Introduction

Once a sufficient number of tests had been carried out to gain a basic understanding of the how the drying rig functioned a number of drying tests were carried out. These tests were carried out as part of a contract with NNL to produce data for an unpublished NDA report. Perhaps more importantly it provided crucial information into the behaviour of the drying rig that could not be obtained by simple commissioning tests and this information was used to make changes and upgrades to the system and guide further testing.

Tests were carried out at room temperature, 60°C and 150°C. 150°C was chosen as this was the hottest test the vessel was designed for so was an upper limit. The coolest we could achieve was room temperature with no supplied heat and this was used as the other extreme. 60°C was chosen as it was roughly between the other two temperatures while also being close to the temperatures used elsewhere.

7.2 Methodology

The initial tests were carried out to compare vacuum drying with flowed gas drying at a range of pressures and to assess whether the type of gas used in the system has an impact. Tests were carried out at three temperatures. For room temperature tests no heat was supplied to the vessel and the temperature began at around 19°C

but tended to drop as the test progressed. For the 60°C and 150°C tests these temperatures represent the set point of the vessel heating and also the set point of the circulation heater where applicable. Tests were carried out at three different pressure. For low pressure or vacuum tests the recirculation line was closed and the vacuum pump was turned on to give a vacuum of around 20 mBarA. For the atmospheric (1 BarA) and high pressure (8-10 BarA) tests the recirculation line was opened and the gas pump used to circulate gas through the circulation heater and to the drying vessel. For the high pressure tests gas was introduced to the system until the system pressure was 10 BarG. It had initially been planned to increase the system pressure and then shut off the gas supply however it was found that there were several small leaks that meant it was necessary to leave the regulated gas supply to the system open. This combination of three temperatures and three pressures gives a combination of nine different tests. At least one test was carried out for each different set of conditions and for some conditions multiple tests were carried out.

Four different gases were used to assess whether the cover gas impacts the drying rate. Flowed gas drying methods are utilised in part as they greater heat transfer due to forced convection. The effectiveness of a gas is in terms of heat transfer is down to its specific heat capacity, which is in effect how much energy it can carry. Gases with higher specific heat capacities can carry more energy and are therefore more effective at heating since they cool slower. The aim was to asses how significant the impact of different drying gases, with different heat capacities was.

Three gas flushes were used before each test to remove any atmospheric air from the system. This was achieved by reducing the system pressure to around 50 mBarA and then pressurising to 1700 mBarA (for vacuum and atmospheric pressure) tests or by increasing the pressure to 5 BarA and then venting to atmospheric pressure for the high pressure tests. This was repeated three times to give a purity of ∼99%. The four gases used were nitrogen, argon, carbon dioxide and air. The use of four gases meant there were a total of 36 different test conditions.

Drying tests were carried out using the test piece shown in fig. 7.1. This particular test piece was produced from a short length of fuel cladding with a 300 μm hole drilled into the side to represent a pinhole. A metal plug was welded into

one end and a short length of 15 mm stainless steel tube welded into the other end. A Swagelok type cap was fitted over the tube to allow water to be sealed inside. This design was later found to be similar to that used by Holtec when testing RBMK fuel[122]. Comparison of vacuum drying and flowed gas drying was carried out by calculating a drying rate which was determined by weighing the sample at the beginning and end of each test to ascertain the water loss and dividing this by the length of the test. For these tests pinholed stainless steel test piece typically held 1-2 g of water since this kept the water below the level of the pinhole. The heat capacity of the test piece is around 71 J °C $^{-1}$.

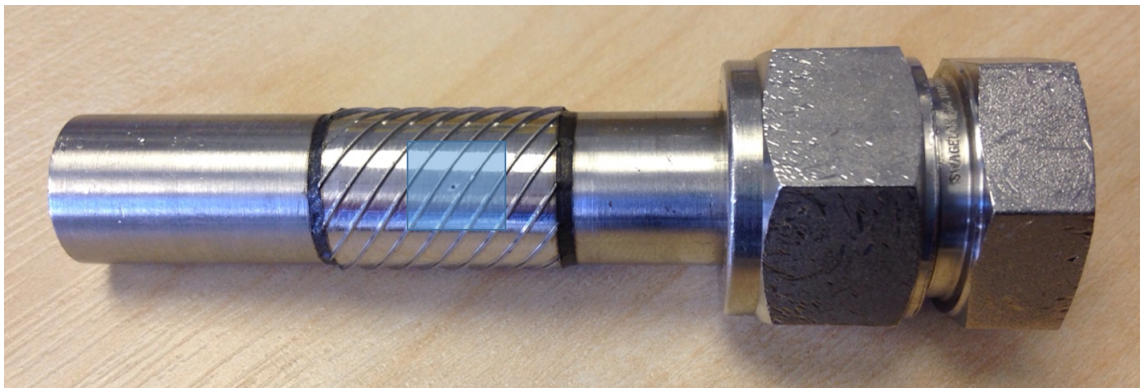

Figure 7.1: Picture of the pinholed stainless steel test piece. The pinhole is just visible in the approximate centre of the cladding in the area highlighted.

For the room temperature and 60°C tests each test had a nominal duration of 60 minutes, while for the 150°C tests this was reduced to 30 minutes to prevent all water being removed and making the calculation of a drying rate impossible. The actual drying time was measured from the end of the gas flush until the point at which the vessel was vented. The test process was carried out as follows:

1. 5g heel of water added to vessel.
2. Test piece weighed to ensure minimum mass of water present.
3. Surface temperature thermocouple clamped to test piece touching cladding section.
4. Test piece lowered into vessel and lid fitted.

5. Lid bolts tightened.
6. Various data loggers started.
7. Gas flushes carried out.
8. Pumps/heaters started and test run for nominal period of 30/60 minutes.
9. Vessel returned to atmospheric pressure and lid removed.
10. Data loggers stopped.
11. Test piece weighed. Mass loss calculated and recorded.
12. Mass of water remaining in vessel recorded.

7.2.1 Estimated Heating Rates

Attempts have been made to model the heating rate of the test piece however it should be noted that numerous assumptions will have to be made which means that the figures produced are broad estimates only.

Vacuum Drying When vacuum drying the assumption is that all heating is by conduction since there is low gas density. The contact area is hard to judge but is assumed to be in the region of 3 mm^2. The test piece is assumed to be 0.01 m from the heat source (the vessel walls) and the conductivity value from table 5.2 will be used. Based on this assumption the test piece will heat to 60°C in around 580 s and to 150°C in 390 s. These times appear quite fast. In reality the vessel walls will take some time to warm which will slow the heat rate but how long this will take is known.

Forced Gas Drying When vacuum drying the assumption is that all heating is by forced convection. The surface area of the test piece will be modelled as a long thin cylinder on top of a short fat cylinder to give a surface area of 6.23 x $10^{-}3$ m^3. Since the gas flow conditions are unknown a value of 150 $Wm^{-2}k^{-1}$ will be used which is in the middle of the range shown for forced convection in section 5.2.3. The gas is assumed to be the set point from the beginning of the test. Based on

these assumptions the test piece is expected to take 220 s to reach 60°C and 280 s to reach 150°C. These times seem more plausible than the vacuum drying times but are still expected to be somewhat quicker than will be achieved, again in part due to the fact that the gas flow will take some time to warm.

7.3 Individual Experiment Data Output

7.3.1 Standard Vacuum Drying Data Plot

For each individual test, data was analysed in the form of data plots which monitored how the different measurements varied over time. An example of a standard data plot is shown in fig. 7.2. The standard data plot contains the data streams (pressure, flow, surface temperature etc) that were found to be of most interest on a regular basis. The experiment internal diameter (bottom right corner) records the test date and number, the test temperature, nominal pressure and cover gas used as well as the calculated rate at which water was found to be removed through the pinhole. Other data plots showing other data streams were available and analysed where necessary.

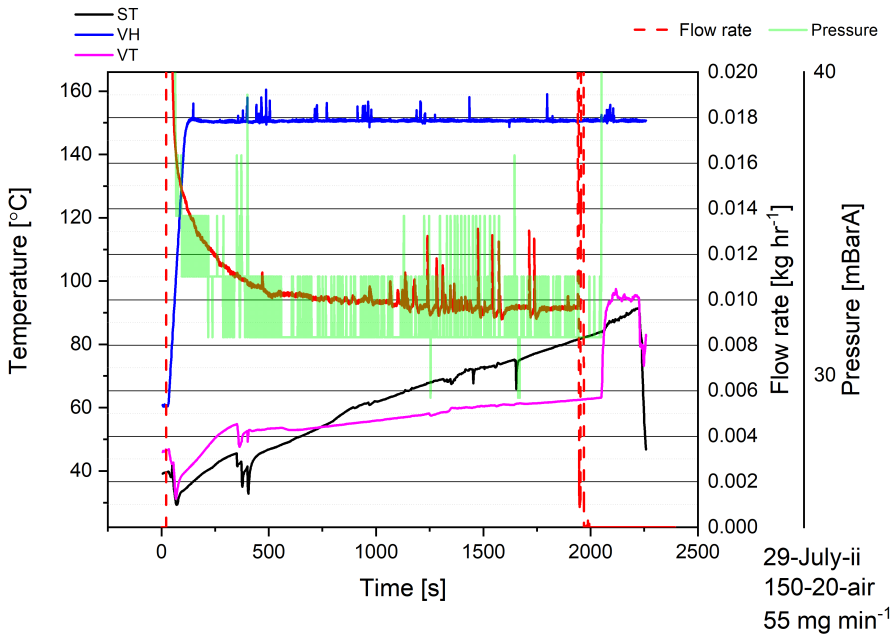

Figure 7.2: A standard data plot used throughout the drying tests. The experiment ID in the bottom right hand corner shows that this is the second test carried out 29th July at 150°C and 20 mBarA with air as the cover gas. The overall drying rate was found to be 55 mg min^{-1} (0.92 mg s^{-1}).

7.3.2 Observable Drying Events

When viewing the data on a PC it is relatively easy to zoom into the various different regions of the plots where different events occur but this is obviously more difficult in a written document. In fig. 7.3 a number of regions are highlighted and these regions are discussed below.

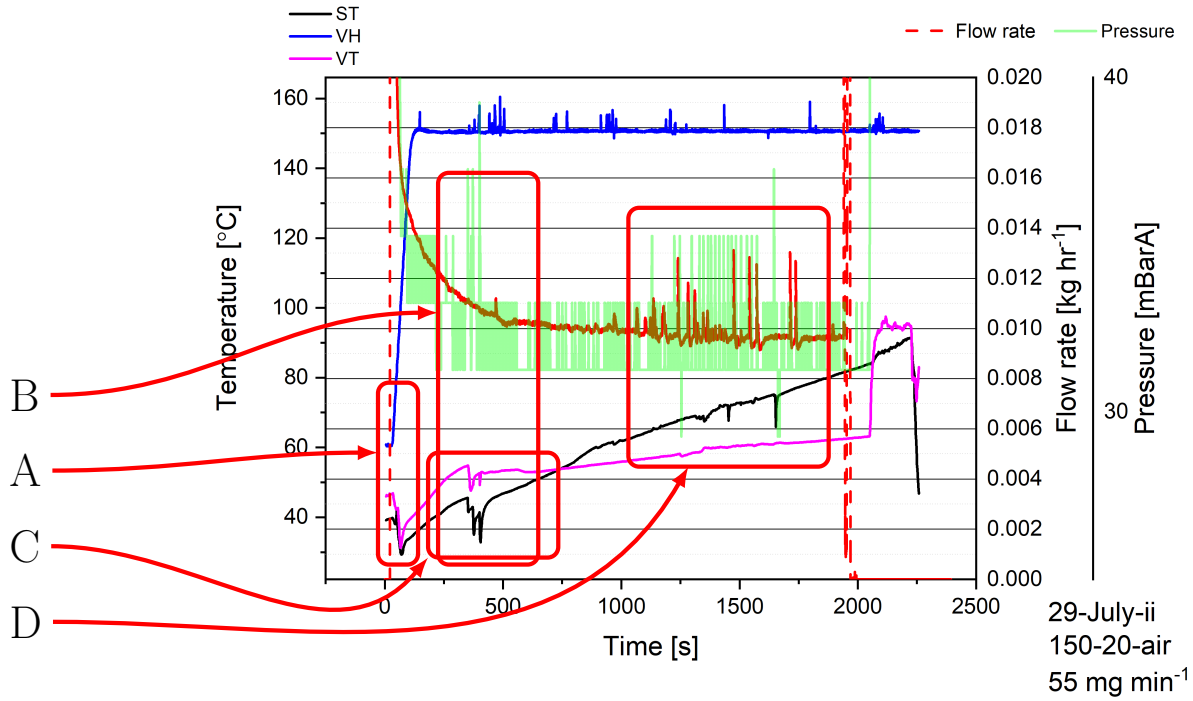

Figure 7.3: Regions of fig. 7.2 that are shown enlarged below.

Region A Region A (fig. 7.4a) shows the behaviour as the vessel is initially evacuated. The vessel temperature begins higher than the surface temperature as the air inside the vessel warmed more quickly than the test piece once the lid was replaced, and the thermocouple which measured vessel temperature was close to the lid which was warmed thanks to its proximity to heat tracing. Once vacuum was applied to the vessel both vessel temperature and surface temperature dropped rapidly due to adiabatic cooling. The shoulders apparent around 50 s are due to the vent line being closed after the vacuum was applied.

Thermocouples downstream of the vessel all show an increase in temperature as vacuum is applied as warm air from the vessel passed across them as seen in fig. 7.4b.

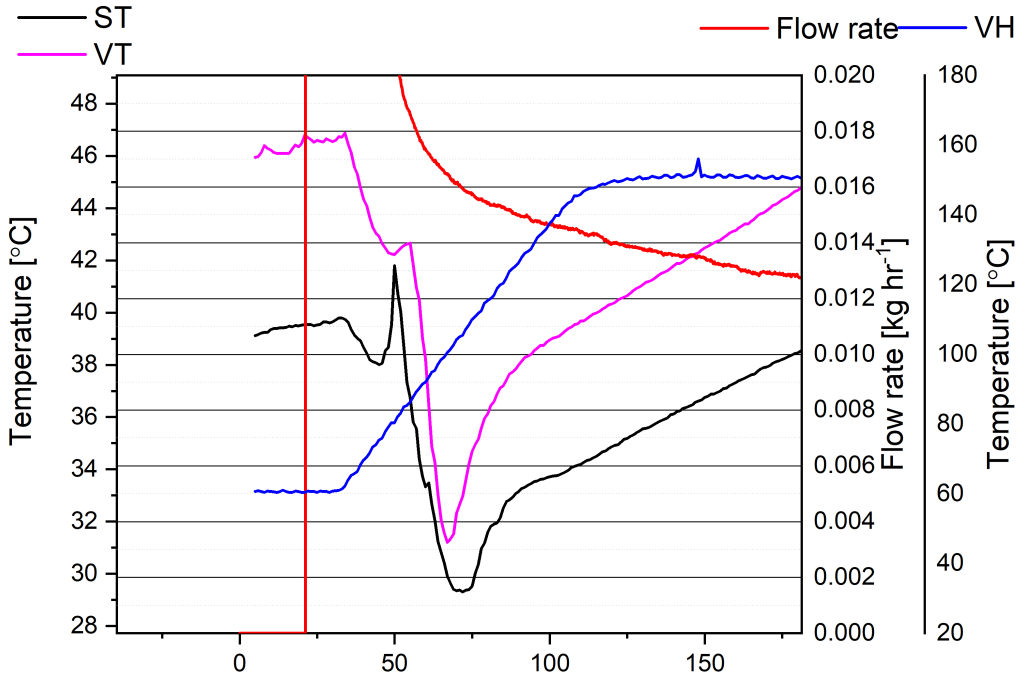

(a) Enlarged view of area A.

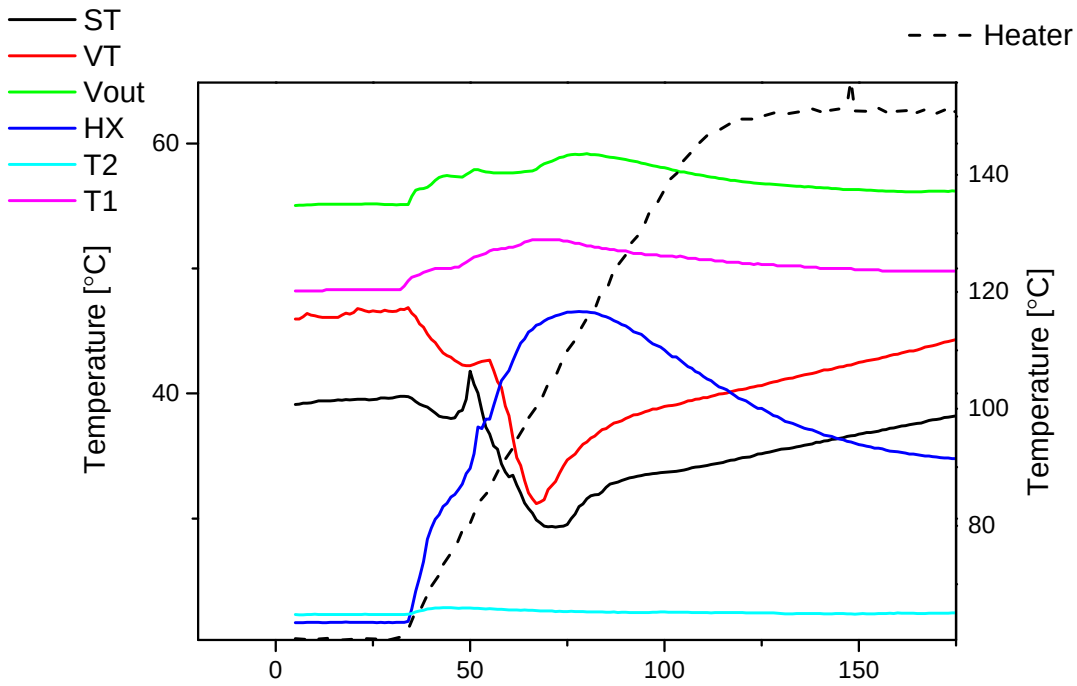

(b) Other thermocouple data for region A.

Figure 7.4: Enlarged view of area A and associated thermocouple data.

Region B The drop in both vessel temperature and surface temperature in region A is believed to be due to the heel water in the vessel bottom beginning to boil. When the vessel was evacuated the temperature of the heel water (not measured) is believed to be below the boiling point which at this pressure was around 26°C. The water was around 17°C when it was added to the test piece and cools slightly when the vessel was initially evacuated. The vessel warmed as did the water although its temperature lagged somewhat behind that of the test piece. When the water begins to boil both surface temperature and vessel temperature drop. This was accompanied by a spike in pressure within the vessel and shortly after by a spike in the mass flow rate. The spike in flow rate is delayed since the flow meter is downstream of the vessel and the condenser.

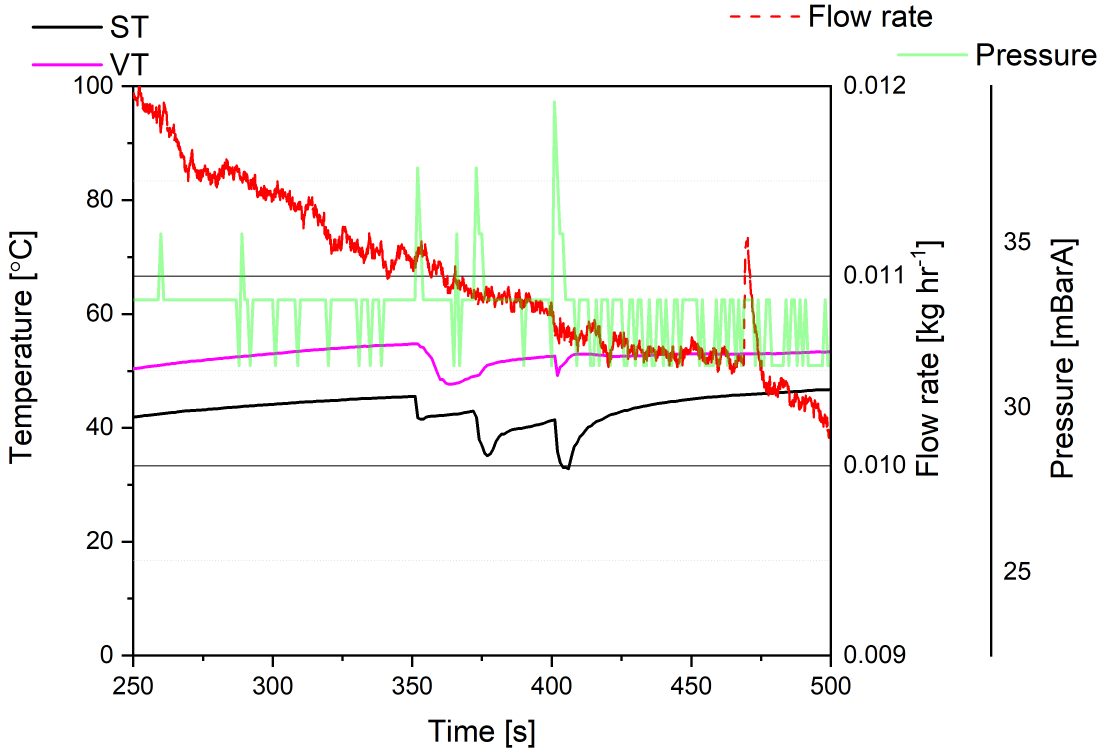

Figure 7.5: Enlarged view of area B.

Region C There is a significant difference in the gradient (rate of increase) of the vessel temperature plot before and after the heel water begins to boil. Before

boiling, vessel temperature was increasing much faster than surface temperature however after boiling vessel temperature has become almost constant. In contrast the rate of change of surface temperature was roughly the same before and after the boiling occurs.

Prior to the heel water boiling there was a relatively large quantity of water vapour in the vessel which acted as a heat transfer fluid and vessel temperature increased. Once the heel water had boiled away the mass of water vapour in the vessel is reduced as was the heat transfer ability of the fluid within the vessel so the gradient of vessel temperature drops dramatically. Surface temperature increased due to conduction from the vessel walls to the test piece and this was unaffected by the loss of water vapour from the vessel.

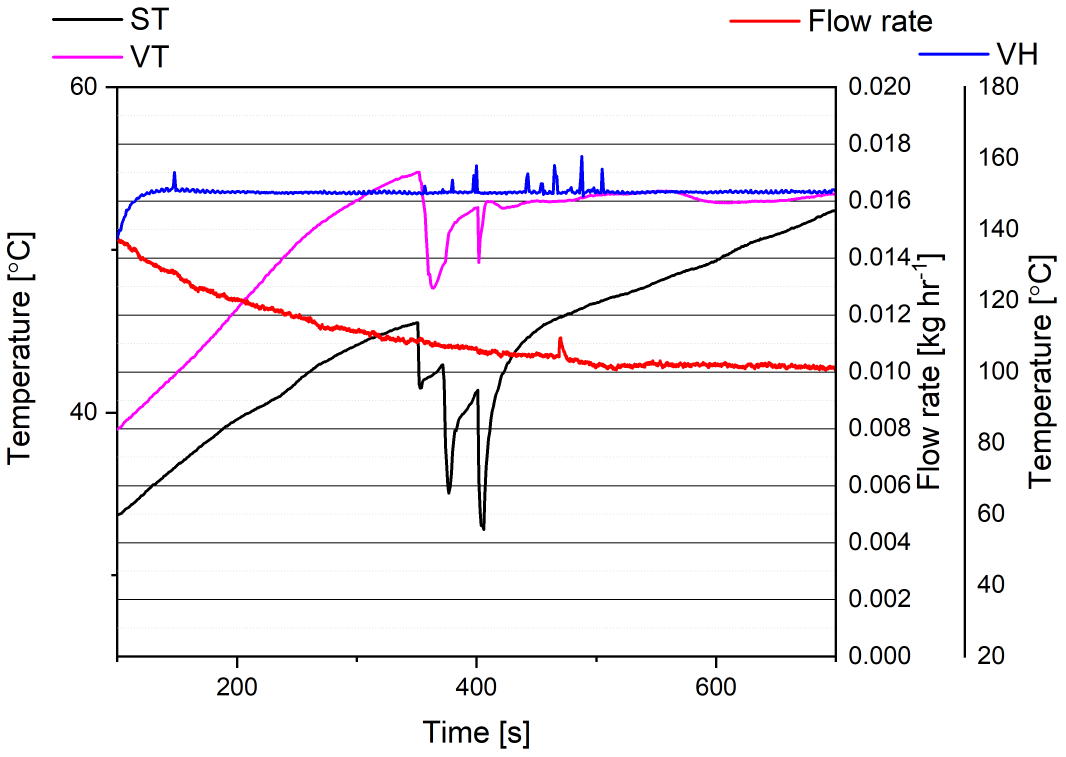

Figure 7.6: Enlarged view of area C.

Region D In region D the water within the test piece began to boil. This had heated more slowly than the heel water since it had been reliant on the test piece heating up while the heel water was warmed by the vessel wall. Once it began to boil there were once again spikes in pressure and flow rate.

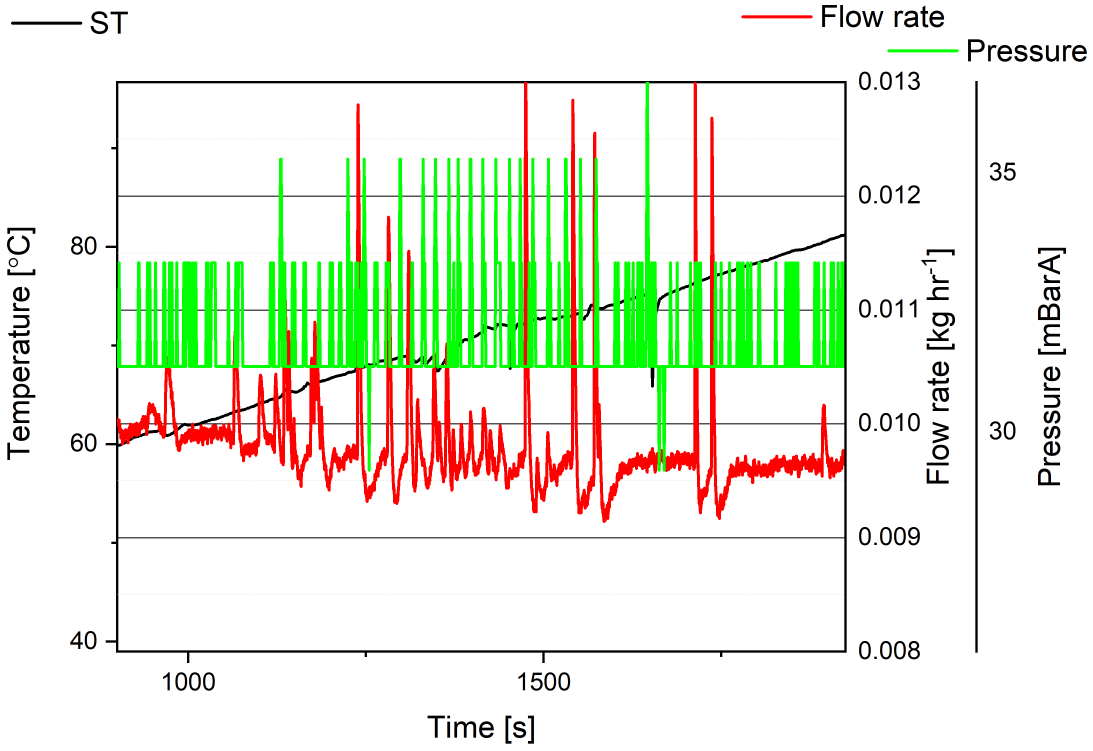

Figure 7.7: Enlarged view of area D.

7.3.3 Ambient Pressure Drying Plot

A typical data plot for 60°C atmospheric pressure flowed gas drying drying is shown in fig. 7.8. The surface temperature clearly rose with time. A shoulder is visible in surface temperature around 250 s when the gas backfills have been completed and the pump speed was set. The flow rate fluctuates somewhat with time and in places it would seem that these fluctuations can be paired with changes in pressure and thermocouple readings but this is far from certain.

As can be seen the data plot for 60°C atmospheric pressure drying shows relatively little about the drying behaviour of the system. This was found for all examples of data plots for atmospheric pressure and high pressure most likely because the boiling point was not as easily achieved.

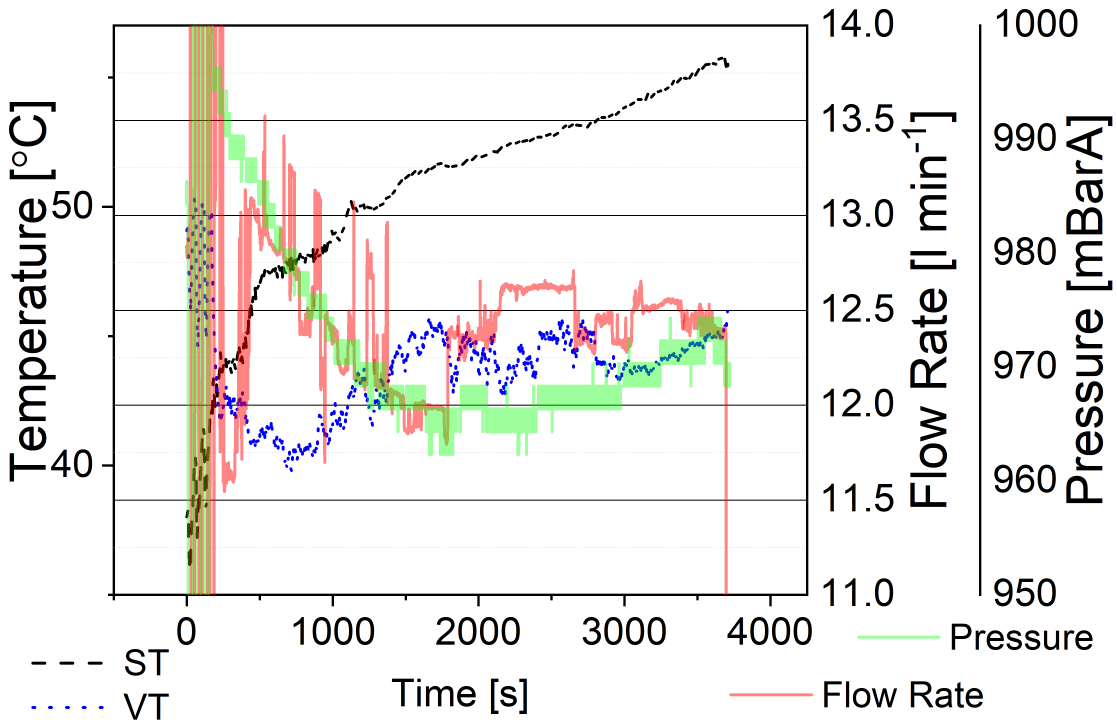

Figure 7.8: Data plot for 60°C atmospheric pressure flowed gas drying drying.

7.4 Overall Drying Results

The overall results for the drying tests discussed here are shown in three different ways in figs. 7.9 to 7.11 and also in table 7.1.

The most obvious outcome from the drying tests carried out is that 150°C vacuum drying is clearly the most effective method with drying rates in the region of 35-50 mg min^{-1} (0.58-0.84 mg s^{-1}) for all gases tested. This can be seen in fig. 7.9a and 7.10c. Atmospheric pressure 150°C and 60°C vacuum drying are the next most effective methods consistently giving results in the region of 12-17 mg min^{-1} (0.2-0.28 mg s^{-1}) for all gases tested. High pressure 150°C drying was also found to have some effect particularly when using air and nitrogen.

		11 BarA	**1 BarA**	**20 mBarA**
		[mg min^{-1}]	[mg min^{-1}]	[mg min^{-1}]
CO_2	RT	0	0	0
	60°C	0.15	0.5	15
	150°C	2.96	12.5	42.5
Argon	RT	0.34	0.33	0
	60°C	1.02	1.8	15
	150°C	1.48	16.6	40
air	RT	0	0	0.33
	60°C	0.48	0.71	13.4
	150°C	7.72	15.2	49.5
N_2	RT	0	0	0
	60°C	0.82	0.34	15.2
	150°C	13.6	16.4	35

Table 7.1: Maximum drying rates under different conditions.

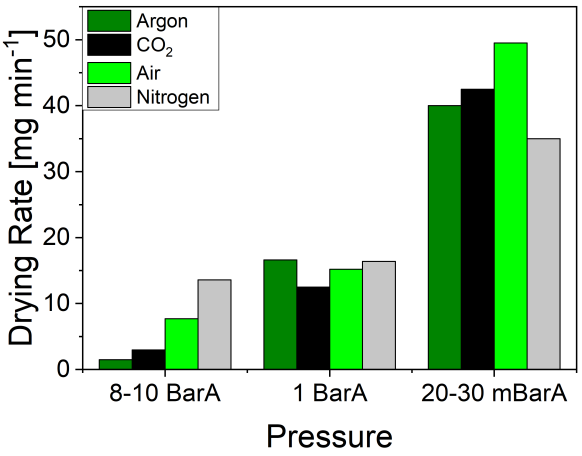

(a) 150°C drying.

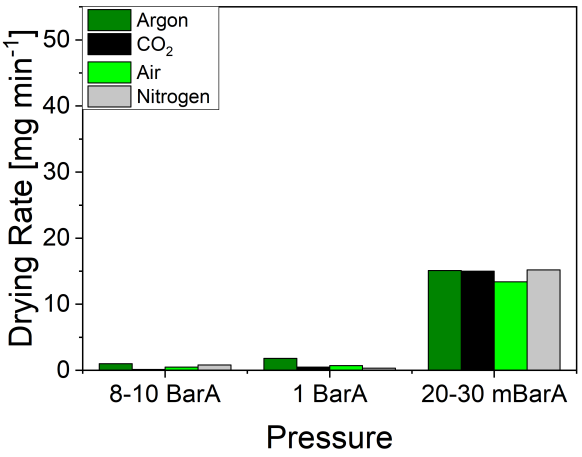

(b) 60°C drying.

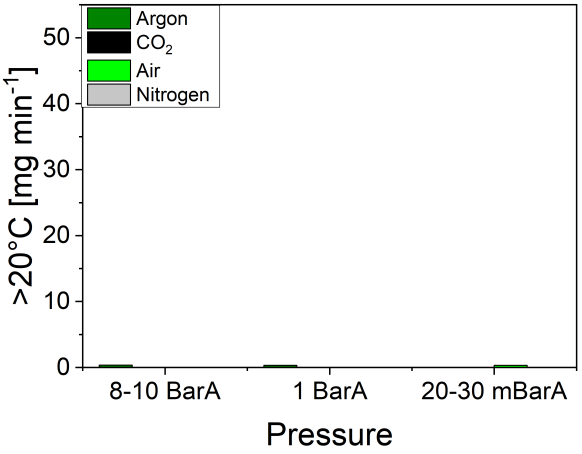

(c) Room temperature drying (no additional heat supplied<20°C).

Figure 7.9: Drying rates at different temperatures.

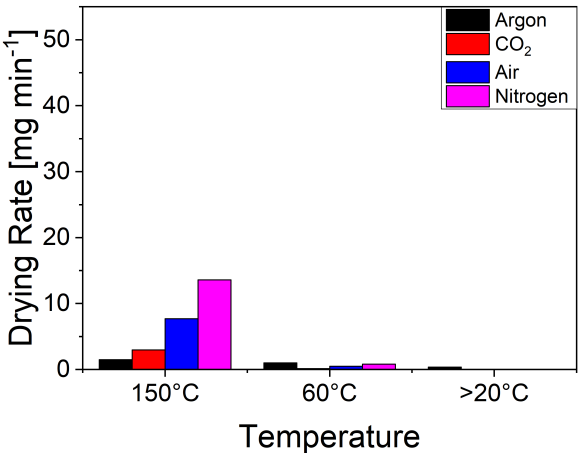

(a) 8-10 BarA drying.

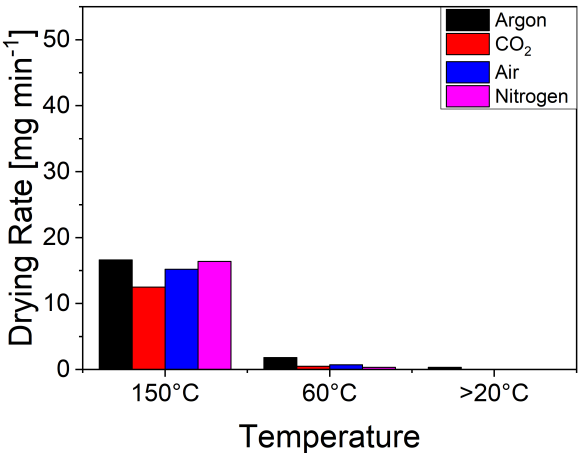

(b) 1 BarA drying.

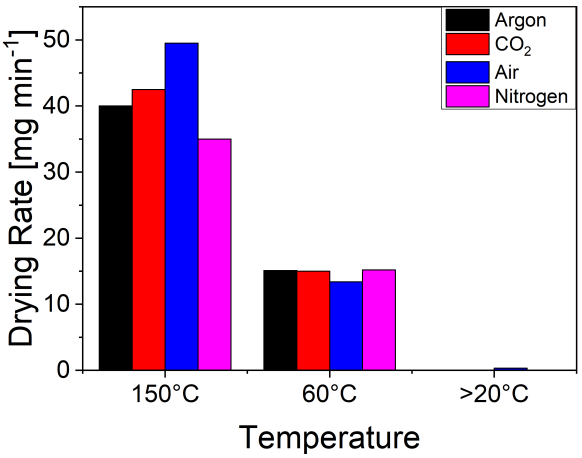

(c) Vacuum drying (20-30 mBarA).

Figure 7.10: Drying rates at different pressures.

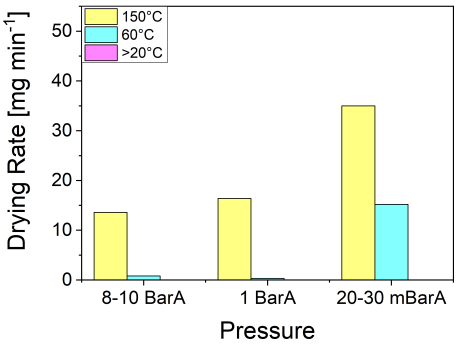

(a) Nitrogen cover gas.

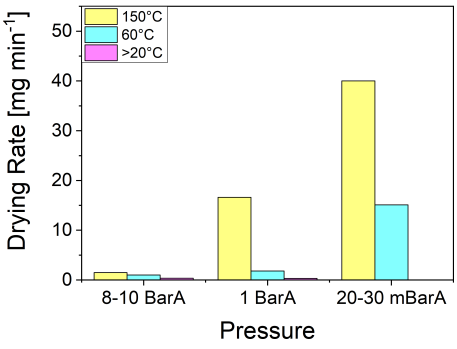

(b) Argon cover gas.

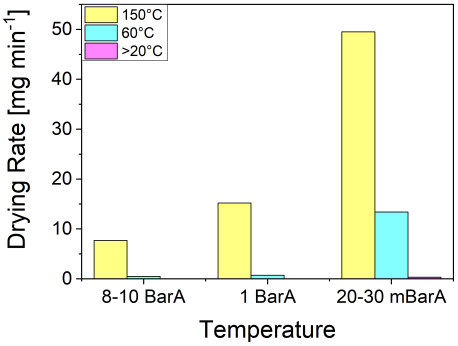

(c) Air cover gas.

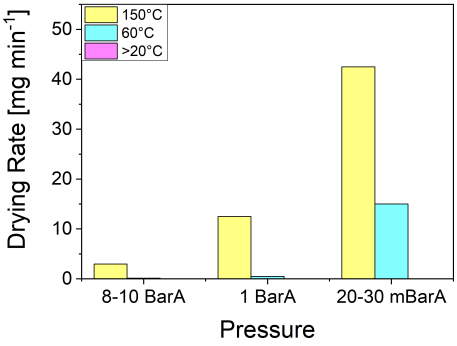

(d) Carbon dioxide cover gas.

Figure 7.11: Drying rates with different cover gases.

The quantity of heel water remaining in the vessel following the various tests is shown in fig. 7.12. For the 150°C and 60°C vacuum drying tests all heel water was removed in all tests but a significant quantity of water remained for room temperature vacuum drying. The room temperature atmospheric pressure and high pressure tests found that virtually no water was removed from the vessel. 150°C and 60°C atmospheric pressure drying removed the majority of water from the vessel while 150°C high pressure drying was more effective than 60°C high pressure.

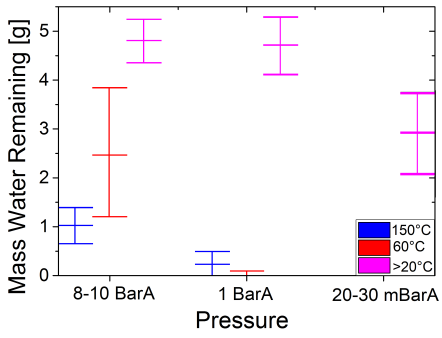

(a)

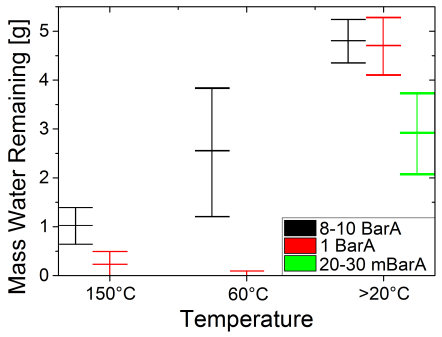

(b)

Figure 7.12: Quantity of heel water remaining.

7.4.1 Discussion

The data has shown that vacuum drying was considerably more effective than the flowed gas drying methods. There were however three areas that were believed to be reducing the effectiveness of flowed gas drying. It was found that obtaining the required temperature at the vessel inlet (the set point) was exceptionally difficulty and thus the temperature of the flowed gas is not as hot as may have been liked. This was due to the narrow bore of the pipework (low mass flow rate and high surface area to volume ratio) and the length of pipework which led to considerable heat loss.

A further issue found for the flowed gas drying drying related to the circulation pump. The pump was supplied with a variable speed controller which was designed

to protect the pump by cutting off if excessive current was drawn. Unfortunately the controller was far too sensitive, tripped out regularly and meant that the achievable flow rates were much lower than had been hoped. The manufacturers were consulted and it was advised that this was a known issue and a new pump controller was under development.

Finally the temperature of the cooling water was such that the condenser was ineffective and the molecular sieve is therefore thought to have been overwhelmed leading to the recirculation of already saturated gas reducing the effectiveness.

It should also be noted that the heating rate of the test piece was significantly lower than had been predicted particularly for the flowed gas drying. In this case it is due to the flowed gas being unable to reach anything close to the planned temperature. A similar effect was found for the vaccuum drying as a result of the vessel taking time to heat up however once it had warmed the heating rate of the test piece was noticeably quicker.

7.5 Minor Changes

For some of the later flowed gas drying tests the circulation heater was routed directly to the vessel cutting out some redundant pipework. This went some way to increasing the temperature at the vessel inlet but not as far as would have been liked.

One of the concerns relating to the accuracy of the results was the variation in the drying rates found. A detailed analysis of the data plots for the 150°C vacuum drying tests, and to lesser degree the 60°C vacuum and 150°C atmospheric pressure tests showed that a major factor was the impact of starting temperature, with small variations being found to have a surprisingly large impact. In order to address this problem a more controlled starting procedure was introduced to remove these variations.

Three key changes were made to the start up operations. Firstly the vessel was preheated to 60°C before each test. It had been found that previously some tests had been started from room temperature and while others had begun with a preheated vessel. 60°C was chosen since it was cool enough to allow the test

piece to be fitted and removed but 60°C enough to allow cooling between tests in a reasonable time.

Another factor that was thought to be impacting the drying rate was the gas flushes. Since gas type did not appear to have any significant impact on the drying rates it was decided that further tests would be carried out using air therefore negating the need for gas flushes.

Finally ice was added to the cooling water thus increasing the effectiveness of the condenser and reducing the load on the molecular sieve.

7.6 Vacuum Drying 2

Having made these minor changes a number of 150°C and 60°C vacuum drying tests were carried out. The results of these and the original drying tests are shown in fig. 7.13. The drying rate for the 150°C vacuum drying tests increased to 55-65 mg min^{-1} (0.92-1.08 mg s^{-1}) while the 60°C vacuum drying tests were now between 9.5 and 11 mg min^{-1} (0.16-0.18 mg s^{-1}). This shows far less variation between tests than had been previously observed.

It was also found that water could now be collected within the condenser and a mass balance could be carried out that accounted for all water within the limitations of the balance used (0.05 g).

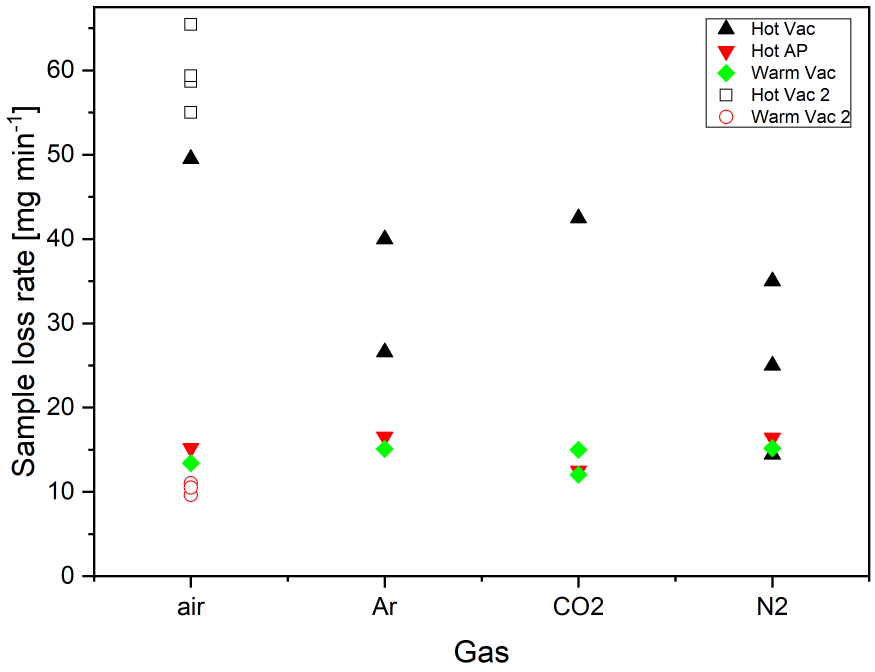

Figure 7.13: Variation in drying rates. Each point is a single test.

7.7 Conclusions

The data presented in this chapter was produced for the NNL to provide some preliminary data into the relative effectiveness of vacuum drying and flowed gas drying. The data collected found that 150°C vacuum drying was by far the most effective of the methods investigated with drying rates 2-3 times greater than for the next two most effective methods. The initial tests did however seem to indicate significant variation between the tests for the 150°C vacuum drying. In all cases the quantity of heel water removed was much greater than of water within the test piece which confirms the belief that removing free water is not a concern when drying spent fuel. In only one set of conditions did the type of gas used appear to have any impact.

While 150°C vacuum drying was unquestionably the most effective method

there was initially some concern in the variation in the values obtained however it was clear from analysis of the data plots that there were minor differences in the experimental conditions and operation that may have lead to these differences. When minor changes were made to the operating procedure it was possible to dramatically reduce this variation.

Although the purpose of this work was to compare the two methods since this has not been carried out previously there was some surprise that vacuum drying was found to be so much more effective than flowed gas drying. One of the rationales for flowed gas drying being more effective than vacuum drying is that while from a thermodynamic standpoint it is much easier to boil water under vacuum thanks to the lower vapour pressure, the reduced heat flow means that the fuel being dried may cool dramatically and may lead to ice formation. With flowed gas drying one of the aims is to drastically increase heat transfer. However the data plots showed that there was no significant difference in the surface temperature of the test piece between any of the test pressures (20 mBarA, 1 BarA and 8-10 BarA) which suggests that the dominant form of heat transfer is conduction from contact with the vessel walls rather than by convection. It is not however clear whether the poor performance of the pump and inability to reach the required set point had a significant impact on this.

While the data did indicate that vacuum drying was more effective than flowed gas drying and that the data plots were able to provide some information as to what was happening at certain points in the drying cycle perhaps the most useful output from this data was in fact some of the deficiencies found since these guided development of the rig and its operation and these are discussed in the following chapters.

Chapter 8

Rig Modification and Testing

Chapter 7 described the initial drying tests that were carried out with the rig. These tests showed vacuum drying to be more effective than flowed gas drying however in many ways the most useful result was some of the learning points that arose from the rig performance and operation. The following chapter discusses the development and modifications that arose as a result of this initial testing and that would be used in the second phase of drying tests.

8.1 Rig Changes

8.1.1 Movement of Flowmeter

Perhaps the largest change to the system was the movement of the mass flowmeter (FM). In the initial design the flowmeter was positioned downstream of the condenser so that hot gases could be cooled to below the flowmeter's maximum operating temperature before entering the flowmeter with the water condensed being collected. This did however limits its effectiveness as it was unable to measure any water that would be condensed out. This was not regarded as being an issue when the intention had been to use a dew point meter as that would provide information as to the gas water content. However the initial testing showed that the temperature of the gas reaching T1 was well below the operating temperature of the flowmeter so it was felt to be safe to move the flowmeter where it would be able to record all water vapour.

Since this involved a change to the pipework the opportunity was taken to remove other pieces of redundant pipework specifically that relating to the dew point meter. During initial testing it was found that the inlet vessel isolation valve V17 was passing internally to the recirculation pipework thus limiting the ultimate vacuum. Since another valve was not readily to hand this section of pipework was completely isolated for vacuum testing and the lines capped. An updated P&ID is shown in fig. 8.1.

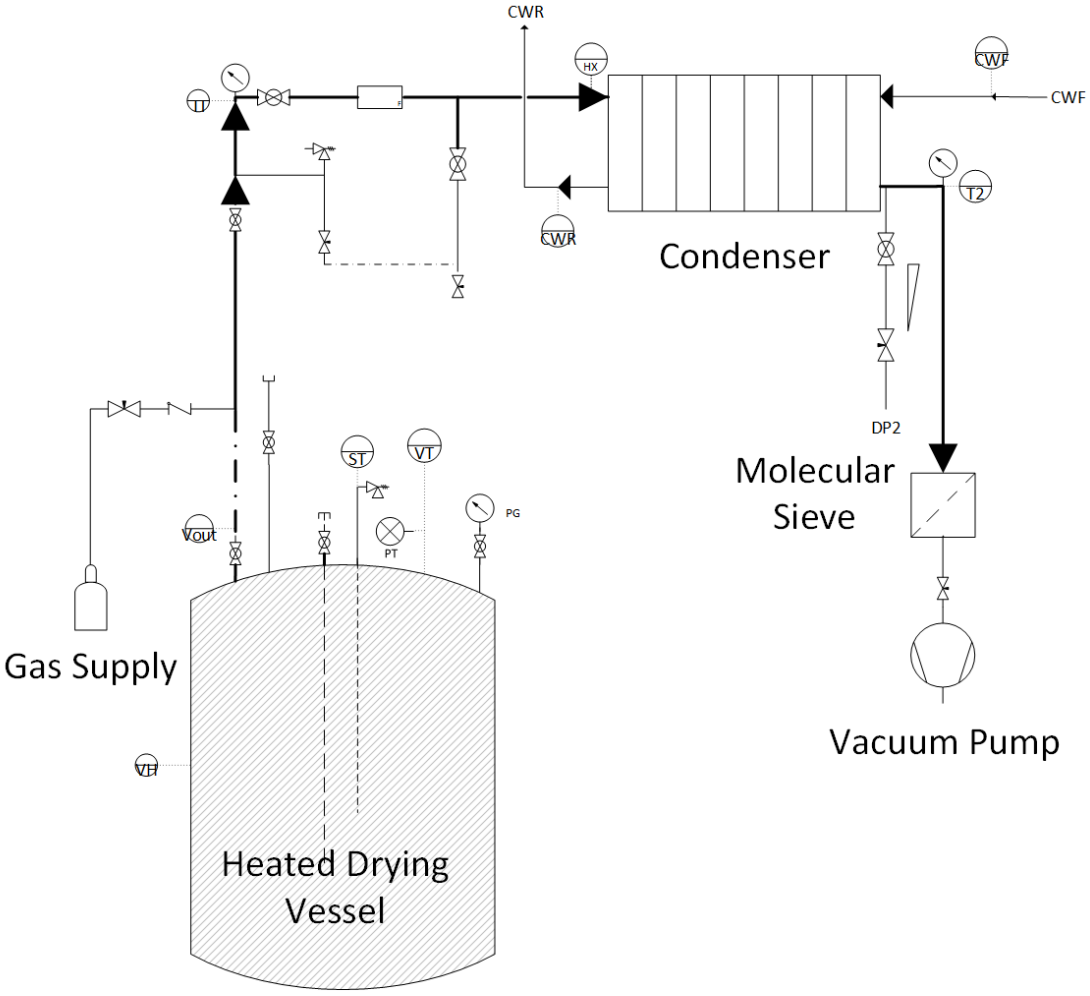

Figure 8.1: P&ID of updated rig.

8.1.2 Heat Tracing

During the initial testing the thermostat of the heat tracing failed leading to the heat tracing being either on or off. This caused the pipework to heat up to in excess of 120°C. One advantage of this was that the pipework and hose between the circulation heater and vessel was hot enough to allow the temperature at the vessel inlet (the circulation heater process temperature) to reach set point. This did however cause the stainless steel hose to fail since it was not suitable for external heating. Consequently the heat tracing was turned off. It was later noted that this allowed minor changes in temperature to be detected by downstream thermocouples as drying progressed which gave an additional data stream. Consequently the heat tracing was not replaced.

8.1.3 Pump Controller

As discussed the pump controller was found to regularly trip out and it was thought to be running far from full power. As a result the pump controller was replaced for later flowed gas drying testing.

8.1.4 Molecular Sieve

Towards the end of the vacuum drying tests it was found that a significant quantity of water had condensed out into the vacuum pump oil. This indicates that the molecular sieve had become saturated. The original design for the molecular sieve was found to make replenishment difficult so a 1.5" diameter pipe with sanitary triclamp fittings was fitted instead of the 1" threaded pipe. The molecular sieve was weighed at the end of each test. The theoretical water capacity of the molecular sieve was in excess of 20 g but the sieve was replaced once the sieve had increased in mass by $\sim$10 g from its dry weight.

8.2 Operational Changes

8.2.1 Temperature

Temperature control was found to provide a challenge for several reasons. At the start of the test the test piece is first placed in the vessel and the lid secured. The experiment would then be started (data loggers started and pressure adjusted and/or pumps started). In an ideal world the temperature of the vessel would always be the same when the test piece was added and the time between the test piece being placed in the vessel and the experiment started would be fixed. It is however difficult to achieve this since a cold vessel could only be guaranteed for the first test of the day and if the vessel was preheated first to 150°C it was too hot to safely add the test piece. During the more controlled set of testing discussed in chapter 7 this issue was addressed by preheating the vessel to 60°C before the testing but this did not address the issue of the time between the test piece being added to the vessel and the experiment being started.

In the end of the decision was taken to greatly reduce the temperatures being used with the majority of vacuum testing being carried out at 30°C but with some at 60°C. 30°C was sufficiently 60°C to require heat to be provided and prevent the drop in surface temperature observed in the room temperature tests in chapter 7, however the temperature gradient was low enough to prevent the test piece being heated at a high enough rate for differences in the starting delay to be significant.

8.2.2 Additional thermocouples

An additional thermocouple was fixed to the base of the drying vessel (VB) for the second phase of drying tests and by rearranging some connections it was found to be possible to record the vessel heater temperature (VH). It was also found to be possible to place the surface temperature thermocouple inside a short length of copper tube and thus collect a reasonably accurate indication of the temperature of any water in the base of the vessel and this could be used in free water drying tests (fig. 8.2).

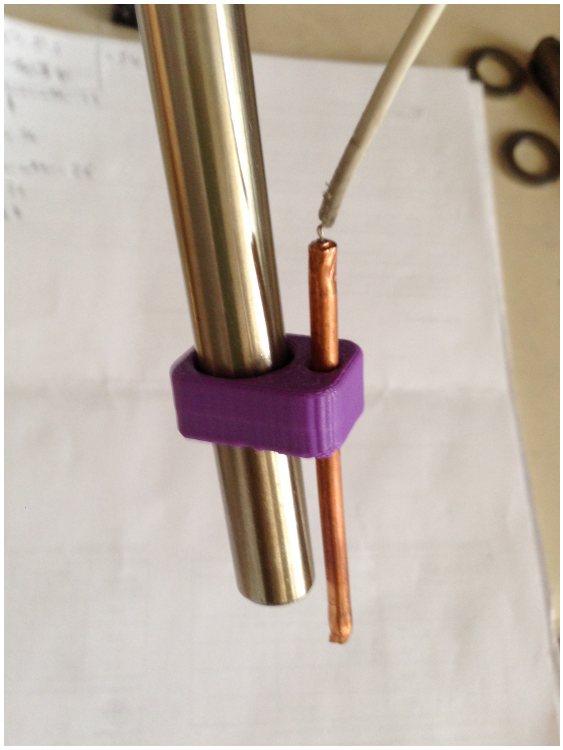

Figure 8.2: The surface temperature thermocouple could be placed inside this copper tube attached to the tube. Due to the high thermal conductivity of copper it would very quickly reach a temperature similar to that of any water in the base.

8.3 Commissioning Tests

A number of commissioning tests were now carried out with the aim of characterizing the behaviour of the system in more detail than before.

8.3.1 Vacuum and Pressure Rise Testing

After modifications the vessel when evacuated would sit comfortably between 1.7 and 4.6 mBarA averaging around 3.2 mBarA. During testing the ultimate vacuum was regarded as being reached when a single value of 2.5 mBarA had been recorded. During the the test shown in fig. 8.3 the vessel was isolated from the vacuum at around 1200 s. The leak rate after this point is highlighted. In multiple tests the leak rate was found to be less than 10^{-3} mBar s^{-1}. The jump in pressure at the

end of the highlighted region was due to a valve on a spare line fitted to the vessel being opened. The line ws fitted in case an additional port was required. This ultimate vacuum and leak rate were found at both 30°C and 60°C.

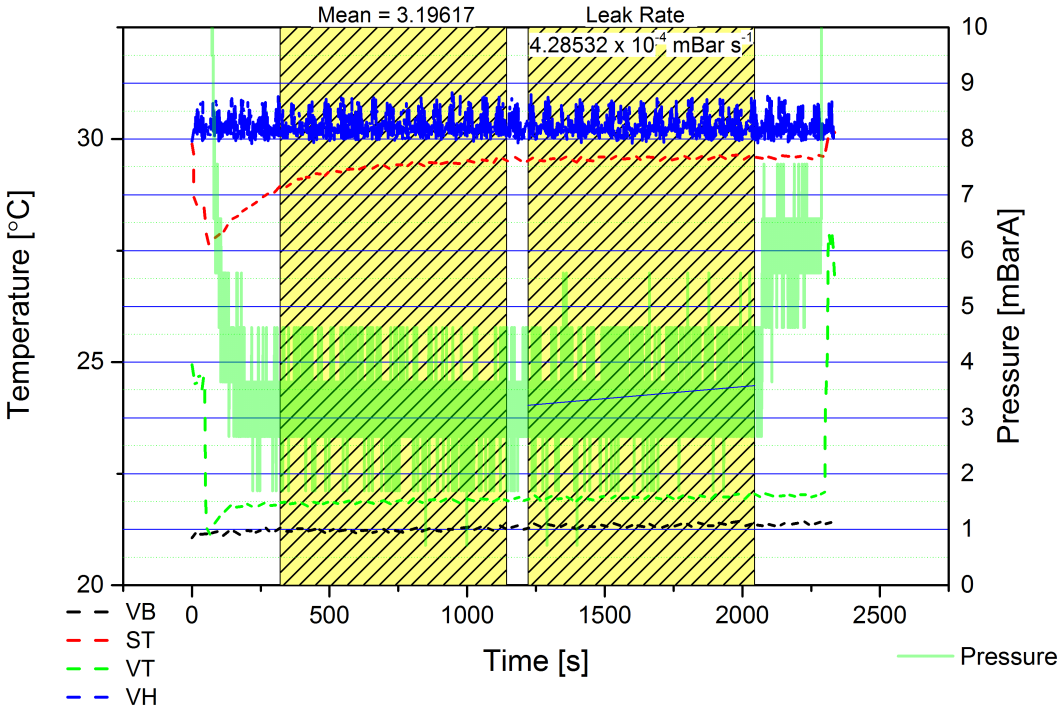

Figure 8.3: Ultimate vacuum and leak tightness.

8.3.2 The Effect of Water Addition

The effect of water being introduced to the vessel once ultimate vacuum had been reached was investigated. This was done in the following manner.

1. Ensure spare line valve closed and vessel at ultimate vacuum.
2. Isolate vessel.
3. Remove cap from spare vessel line.
4. Add known mass of water to pipe ahead of spare line valve.

5. Replace cap and open spare line valve.

By following this procedure the spare line could effectively be used as an airlock. When the airlock was opened there was a rise in the vessel pressure which was significantly greater than that observed when there was no water in the airlock. A number of tests were carried at 30°C and 60°C using varying amounts of water and the pressure rise was recorded. The results of these tests show an initially linear increase in pressure (fig. 8.4) as the mass of water introduced to the air lock is increased from 0 to ~9.5 mg with an increase of 15.9 and 20.5 mBarA at 30°C and 60°C respectively but with no further pressure rise as more water is added. The pressure rise is limited as the gas within the vessel becomes saturated and the difference in temperature accounts for the pressure difference. This data shows what will happen if the vessel is isolated before all water is removed during a vacuum drying test.

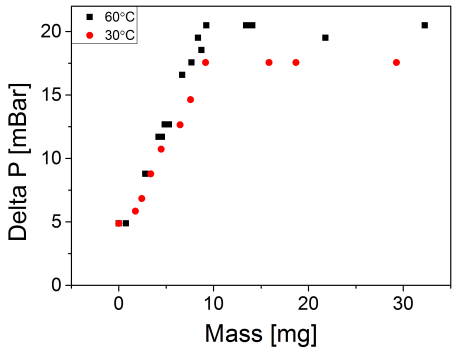

Figure 8.4: The impact of adding water to the evacuated vessel via the "airlock".

8.3.3 Free Water Removal

A number of tests were carried out to show the behaviour of the system when free water alone was being removed under vacuum. In the first of these 20 g of water was added to the vessel and the vessel evacuated. The results of one of these tests is shown in fig. 8.5. The test as a whole lasts nearly 6000 s with the vessel being evacuated for the first ~4000 s and then isolated. During the first two minutes there is a rapid drop in surface temperature (which is now measuring

the water temperature), vessel base temperature and pressure as the vessel is evacuated. The line labelled "b.p." is the theoretical boiling point of water based on the recorded pressure. Since a liquid can never be warmer than its boiling point the maximum temperature surface temperature can reach should remain within the region. The plot shows that surface temperature closely matches the lower range of this temperature suggesting that it is quite accurately recording water temperature. During the course of the test the pressure drops with surface temperature following it as more water vapour is removed. The flow rate also drops as more water is removed. Once the vessel is isolated the flow rate drops to zero almost instantaneously after which the pressure rises from 20 to 28 mBarA. This is a similar pressure rise to that observed when water was added to the evacuated vessel through the airlock indicating that there must be at least 9.5 mg of water within the vessel which was confirmed at the end of the test.

The vessel base is slightly warmer than surface temperature throughout the test as it is recorded on the outside of the vessel wall and the wall itself is heated however the trend follows that of surface temperature.

The brief drop in flow at 3000 s is due to the condenser drain valve being opened. It was now found not to be possible to remove any water from the condenser. This is because the pressure is low enough for the dew point of the vapour to below the temperature of the cooling water even with the addition of ice.

Similar behaviour was observed when 10 g of water was placed in to the vessel. When 5 g of water was used the general behaviour was similar but all water was evaporated away. This can be seen in the data plot (fig. 8.6) with a relatively sudden drop in pressure to the system ultimate vacuum reducing the water temperatures boiling point (surface temperature) until all the water has been removed and surface temperature begins to rise as it is now recording the vessel wall temperature.

Figure 8.7 shows how the overall free water drying rate changed as the mass of water in the vessel is reduced. It shows that as the starting mass of water is reduced the drying rate drops. This is likely to be due to the lower mass of water cooling more quickly than the larger mass thus the water evaporates more slowly.

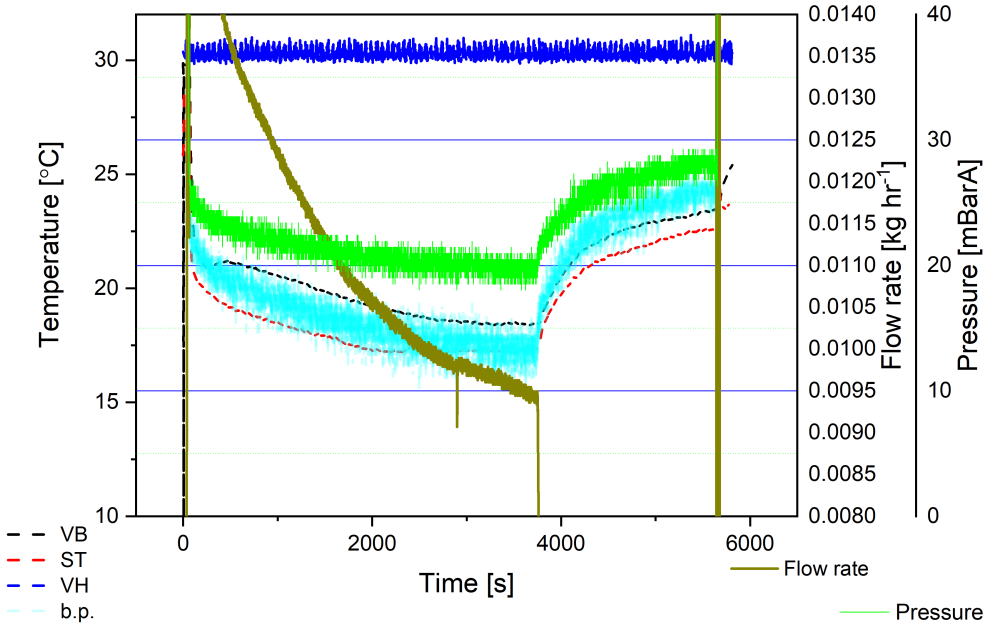

Figure 8.5: 20g free water test.

8.4 Conclusions

The most significant impact of the modifications made to the drying rig was the reduction in the ultimate vacuum of the system from ∼20 mBarA to ∼3 mBarA. This reduction in the system pressure allowed vacuum drying to be carried out effectively at much lower temperatures and this removes a factor that was introducing error to the system. One of the negatives of this was that the water cooled condenser no longer functioned and this meant that the molecular sieve alone was responsible for collecting water vapour. The absorption of water is an exothermic reaction and the temperature of the sieve increased noticeably becoming almost too hot to touch in some circumstances and necessitated a more frequent change in the sieve media.

Having made these changes and carried out the above testing it was felt that the system was ready to be used for a second phase of vacuum drying tests.

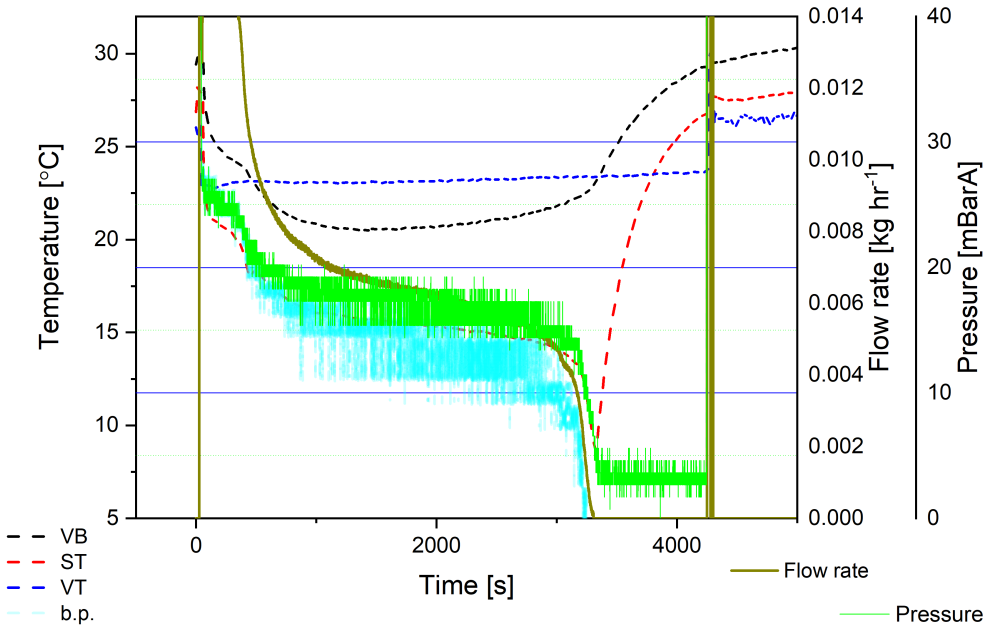

Figure 8.6: 5g free water test.

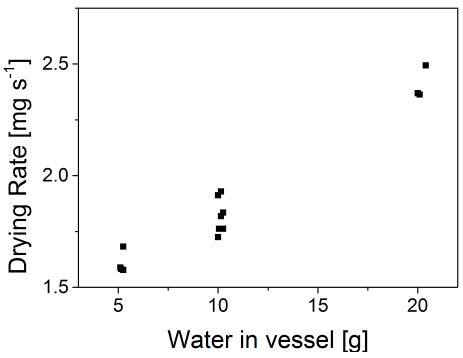

Figure 8.7: Free water drying rate with starting mass of water. Each point is a single test.

Chapter 9

Detailed Vacuum Drying

Chapter 7 described the initial drying tests that were carried out with the rig. These tests showed vacuum drying to be more effective than flowed gas drying. The following chapter is devoted to the second phase of vacuum drying tests carried out which looked at vacuum drying in more detail. This section also addresses some of the differences in drying rates that will occur when the size of a defect is changed. The initial drying tests were carried out entirely with a test piece containing a 300μm pinhole and while this piece is still used here a test piece with SCC microcracks, the production of which is discussed in section 3.8 is also introduced.

9.1 Vacuum Drying Operations

9.1.1 Water Quantity

For the second phase of vacuum drying tests it was decided to dispense with the use of heel water. It had been found that its presence confused the data plots, made the identification of specific events more difficult and since it was easily removed it was felt that further study was not necessary. It was also felt that since the molecular sieve was now the sole means of collecting water it would be better to limit the quantity of water that it was required to collect.

In the initial testing the test piece used was filled with 2-3 g of water since this kept the water level below the level of the pinhole and thus prevented any loss

prior to the test however in the following section a sequence of drying tests were normally carried out. The test piece was completely filled with water for the first test of the sequence (∼7 g) at the end of which it was weighed and then replaced for the next test in the sequence without being refilled. This was continued until the final test in the sequence in which the final drops of water were removed from the test piece and the weight of the test piece had returned to its empty weight.

9.1.2 Test Time and Temperature

The standard test conditions for vacuum drying were a vessel heater set point of 30°C (based on the thermocouple in the vessel heater) and a nominal duration of 1 hour. Some testing was however carried out at a temperature of 60°C and the effect of longer and shorter durations investigated.

9.2 Pinholed Stainless Steel Test Piece

The following section reviews the results obtained with the pinholed test piece and covers the behaviours observed with the drying rig and instrumentation and also some of the conclusions that can be drawn from the data of all the drying tests carried out.

9.2.1 Vacuum Drying

When carrying out vacuum drying tests on the pinholed test piece the data plots varied depending on the quantity of water that was in the test piece at the beginning of the test.

First Test of Sequence.

In the first test of a sequence (fig. 9.1) when the test piece was full there was typically a period of steady decay in both pressure and flow rate. This was followed by a period in which the flow rate and pressure show no upward or downward trend but both spike frequently and erratically. Towards the end of the test there was often a period in which no flow was recorded and the pressure remains constant. Further details are described below.

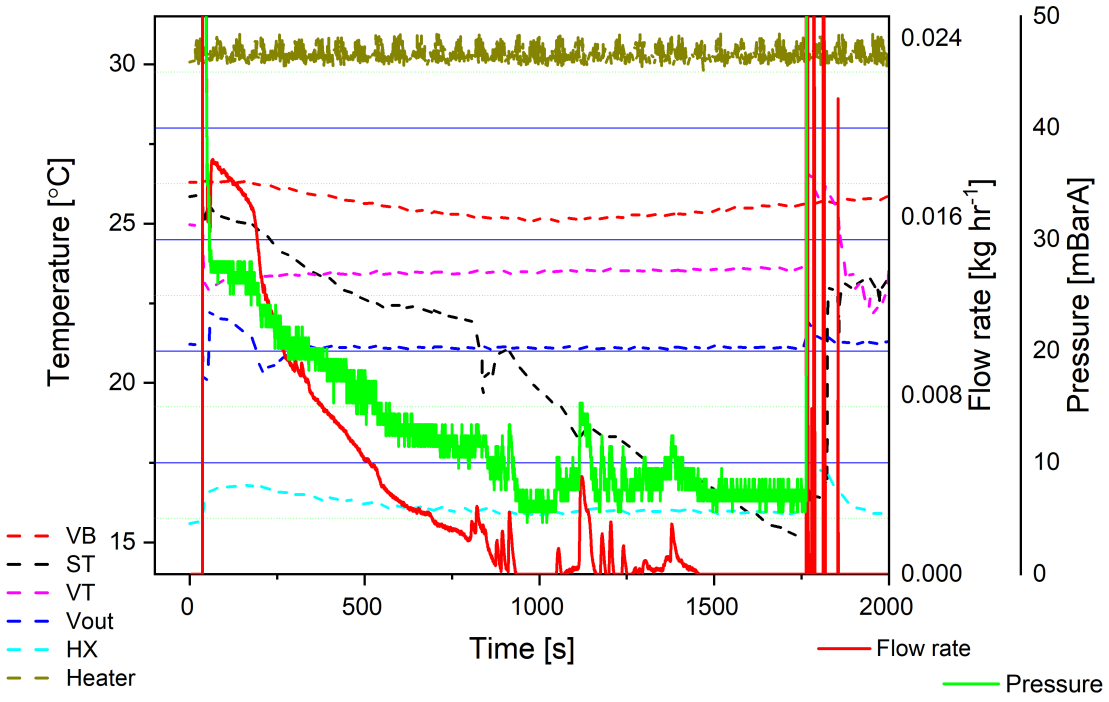

Figure 9.1: Full scale plot.

0-70 s There is an initial delay between starting the data loggers and the test beginning of around 35 s. Once the vacuum pump is started the pressure shows exponential decay and drops rapidly while the flow rate goes off the scale as the vessel is evacuated. The flow rate hits a minima as the vessel is evacuated then shows a slight peak at 55 s before reaching another minima and then rising slightly and decaying slowly. Because of the way the test piece is filled the peak at 55 s

thought to be due to a tiny amount of free water on the outside of the test piece vaporising as the pressure drops. The second rise is due to the more sustained removal of water from inside the test piece. There is a shoulder in the pressure plot at 54 s which would not be observed in a perfect exponential decay curve. At 70 s the vessel pressure appears to level off at 25-27 mBarA (but is actually decaying slowly).

As the vessel is evacuated surface temperature, vessel temperature and vessel outlet all drop due to adiabatic cooling. Surface temperature soon begins to rise as the test piece is in contact with the vessel walls so is warmed by conduction peaking at around 25.8°C at 54 s, the same time that the shoulder on the pressure plot is observed and a second before the peak in flow occurs although the flow meter is downstream of the vessel so a delay is expected. The pressure at this point is 33 mBarA which equates to a boiling point of water of 25.7°C which would seem to confirm that this peak in flow is due to water vapour. Surface temperature then begins to drop slowly.

After adiabatic cooling, vessel temperature levels off at 23°C. This equates to a vapour pressure of 28 mBarA. The vessel outlet temperature rises to level off at 22°C but also shows a slight shoulder at 55 s.

The condenser inlet temperatures is slightly cooler than the majority of pipework since it is next to the iced water cooled condenser. It shows an increase in temperature as the vessel is evacuated rather than adiabatic cooling as warm air from the vessel heats the thermocouple.

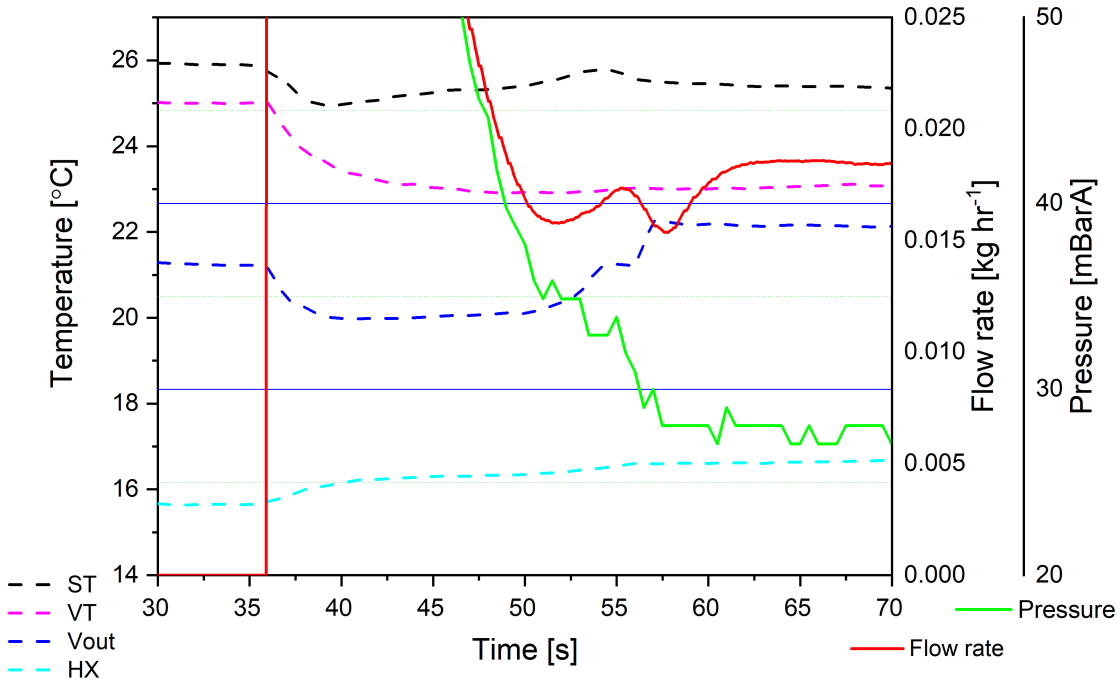

Figure 9.2: 0-70 s.

70-800 s Between 70 and 200 s flow, pressure, vessel outlet and surface temperature all decay. There is a shoulder at 200 s after which vessel outlet levels off while the remaining values continue to drop steadily. It is not entirely clear what happened at 200 s.

The condenser temperature drops throughout as the cooling water lowers the temperature of the adjacent condenser. Vessel temperature rises slowly.

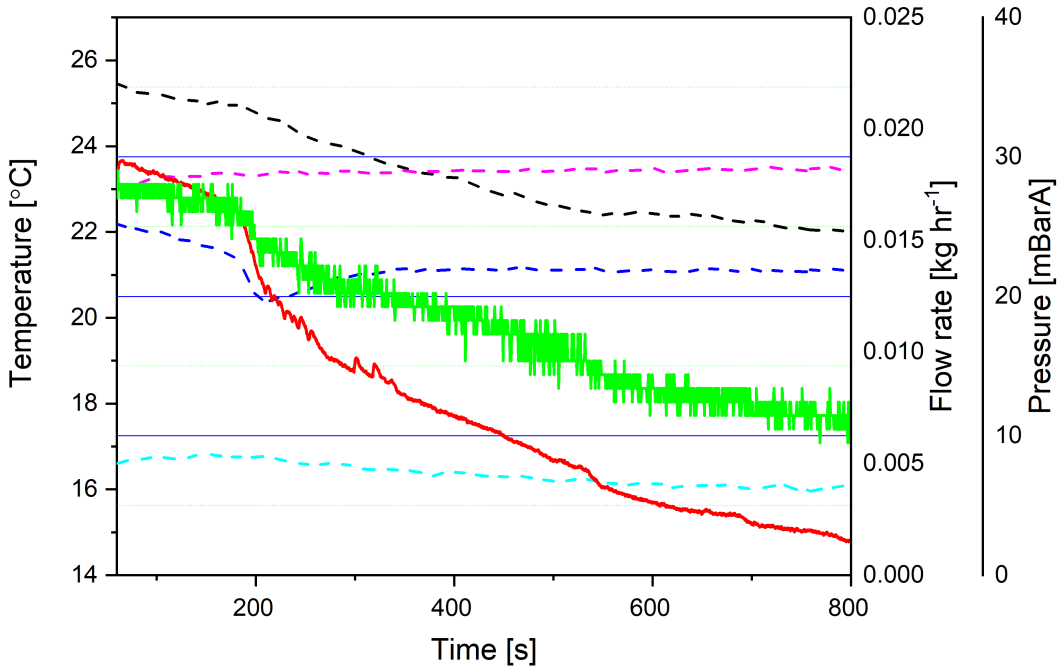

Figure 9.3: 70-800 s.

800-1500 s Between 800 and 1500 s the flow rate and pressure both behave erratically with large spikes in flow coinciding with spikes in pressure. Surface temperature generally drops but the spikes in flow and pressure are also accompanied by troughs in surface temperature.

Vessel outlet and vessel temperature both remain level. The condenser temperature appears to remain level but there are in fact fluctuations that broadly match the spikes in flow and pressure.

The observed spikes in flow and pressure are believed to be due to water boiling hence their erratic nature. The boiling is cooling the test piece hence the drops in surface temperature. Conversely the denser water vapour leaving the vessel is a better heat transfer fluid leading to spikes in condenser temperature.

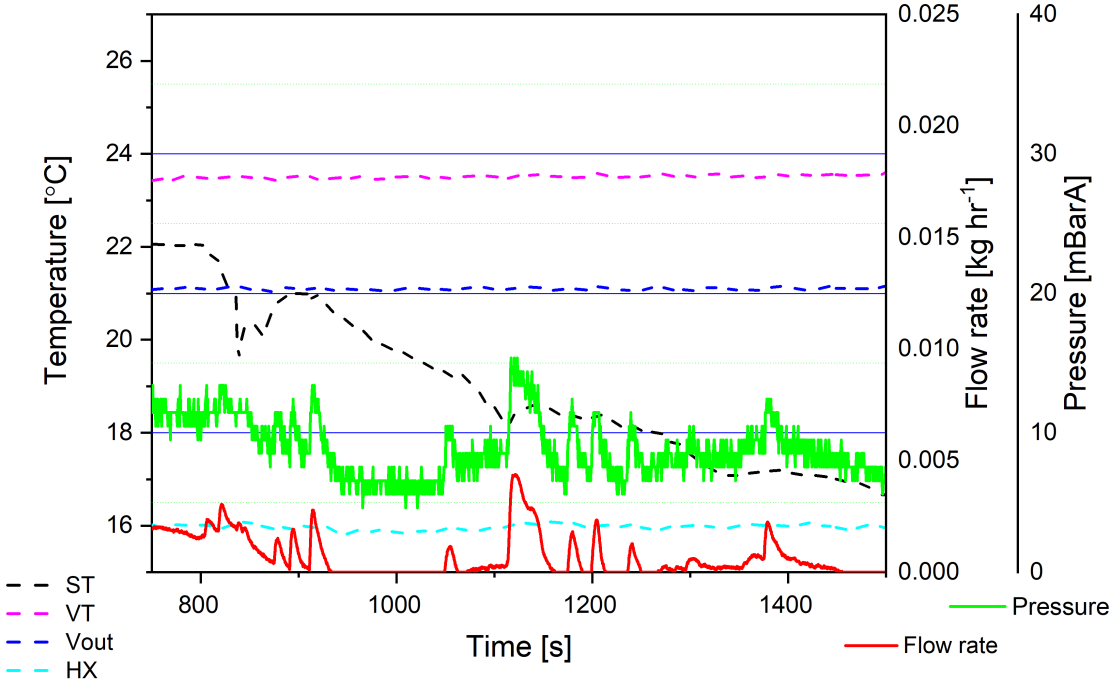

Figure 9.4: 800-1500 s.

1500-1800 s The flow rate appears to be zero since it is below the level of detection and the pressure remains level. All temperatures remain level except for surface temperature which continues to drop. This suggests that energy is still being used to boil water within the test piece. The vessel is brought back to atmospheric pressure and the test ended at 1760 s.

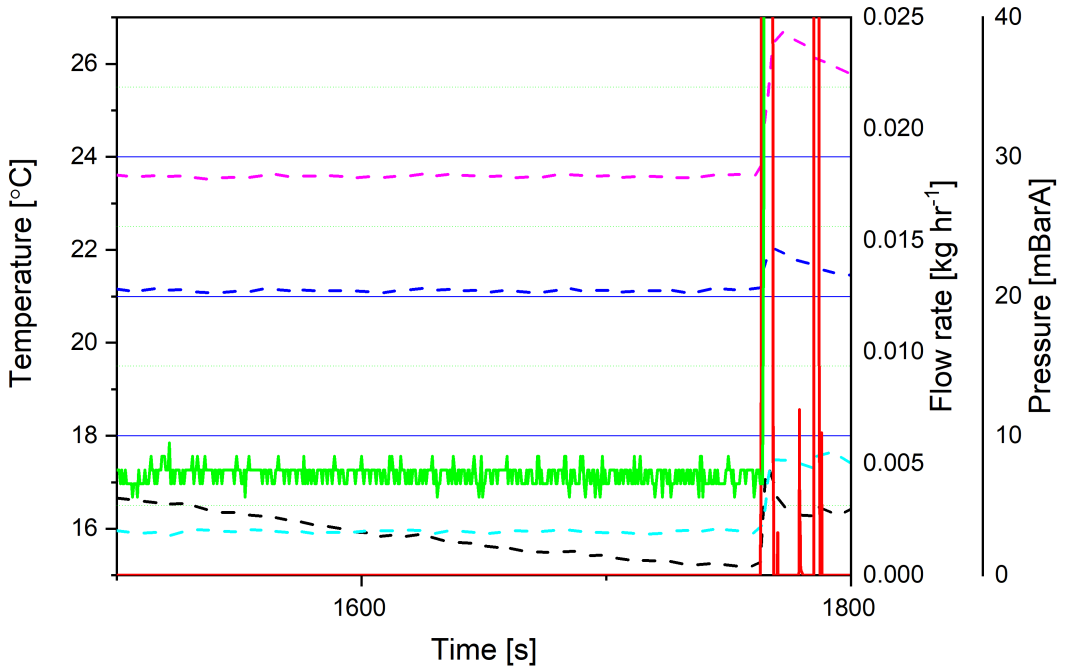

Figure 9.5: 1500-1800 s.

Second Test of Sequence.

The second test in a sequence is typically similar to the first but the first period of decay is much shorter. The detailed data plots are therefore similar in behaviour so are not shown.

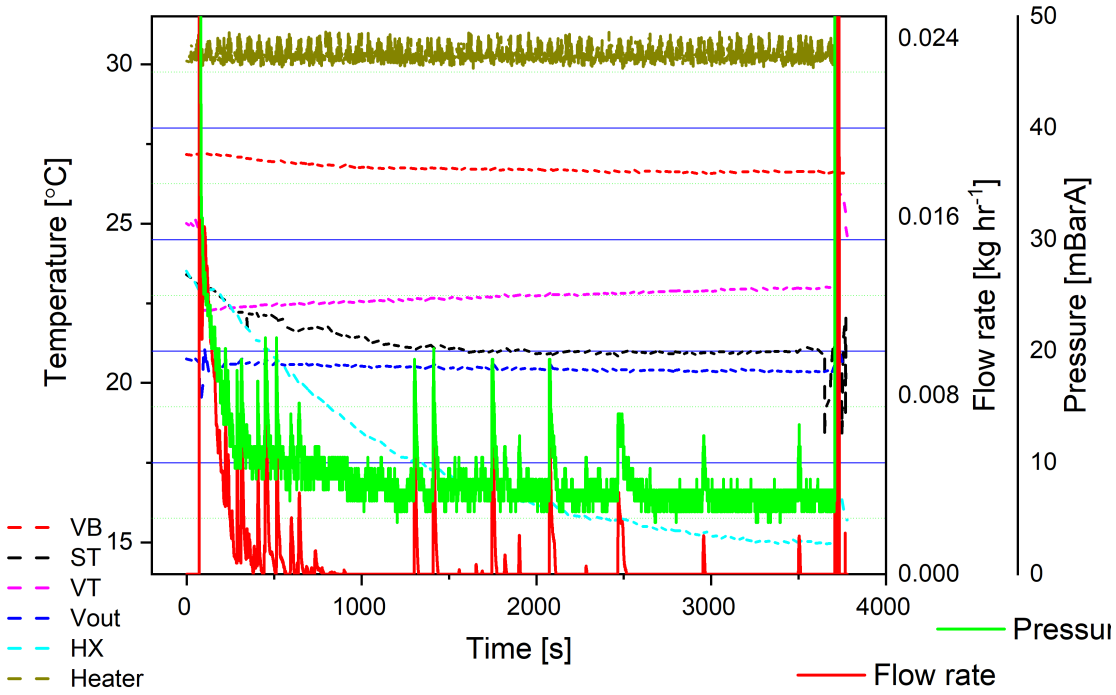

Figure 9.6: Data plot for the second test of a sequence.

Mid sequence tests.

The tests in the middle of a sequence (fig. 9.7) show relatively little. Almost all of the plots remain roughly level although when the temperature scale is expanded it becomes clear that both vessel temperature and surface temperature rise slightly and the erratic behaviour of surface temperature is seen here as in other tests being indicative of boiling.

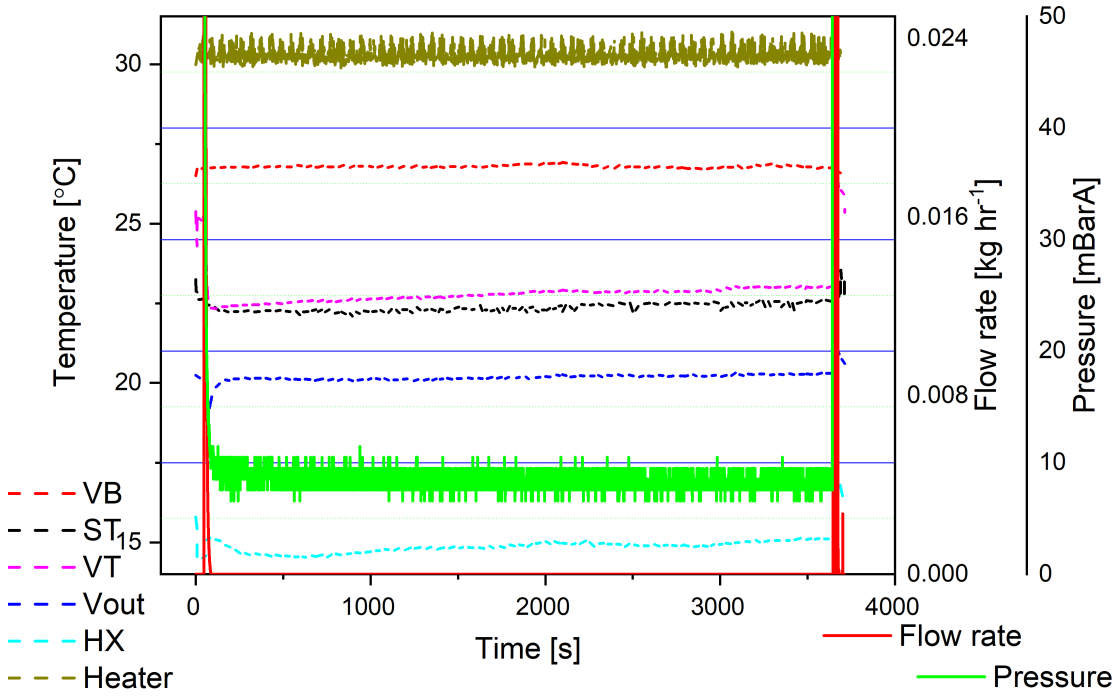

(a) Full scale plot.

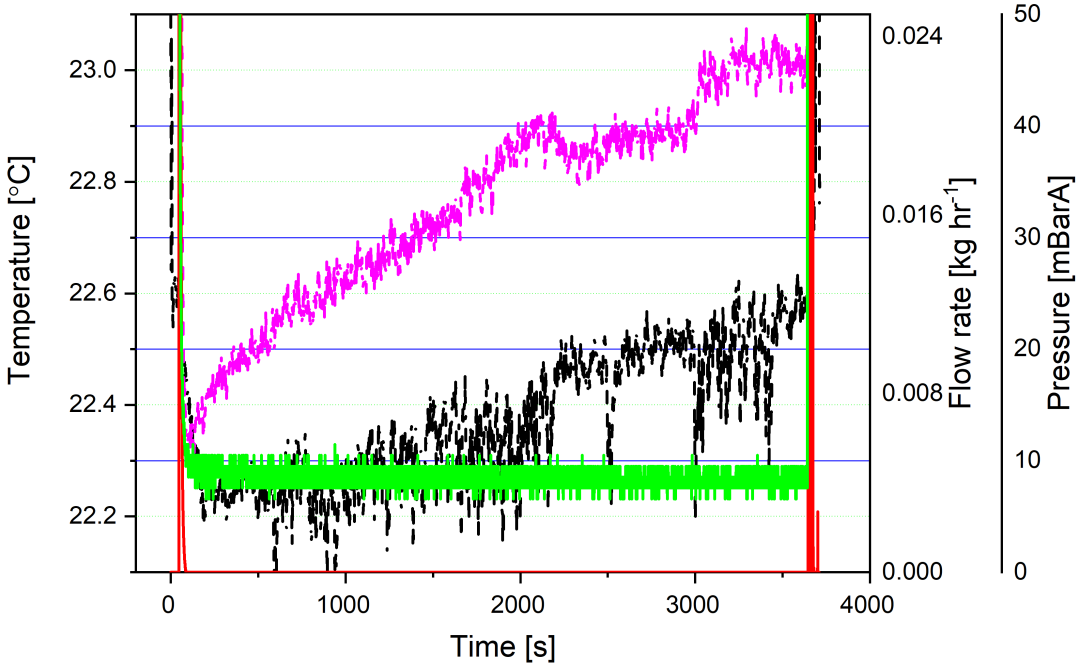

(b) Expanded temperature scale showing surface temperature.

Figure 9.7: Data plot for a mid sequence test.

Final Test of Sequence

The final test of a sequence (fig. 9.8 and 9.9) is very similar to the tests immediately preceding it however there is a clear step in the pressure plot at 1000 s which was initially believed to be the point at which the last of the water is evaporated. There is a noticeable drop in condenser temperature at this point as less heat transfer takes place and surface temperature becomes less erratic. Surface temperature does however show some erratic behaviour later when another change in condenser temperature is observed. This may indicate that at 1000 s the last of the bulk free water is removed since there was no water present in any test which showed this drop in pressure however since the pressure recorded here is somewhat higher than the ultimate vacuum there would appear to still be some water within the system. It was later established that there was holdup of water within the condenser and that the system ultimate vacuum could only be established by running hot water through the condenser to remove this water. It is however interesting to note that despite there being water holdup downstream of the vessel (where the pressure transducer is mounted) which effectively limits the system pressure a pressure drop is still noted when the last of the trapped water is removed.

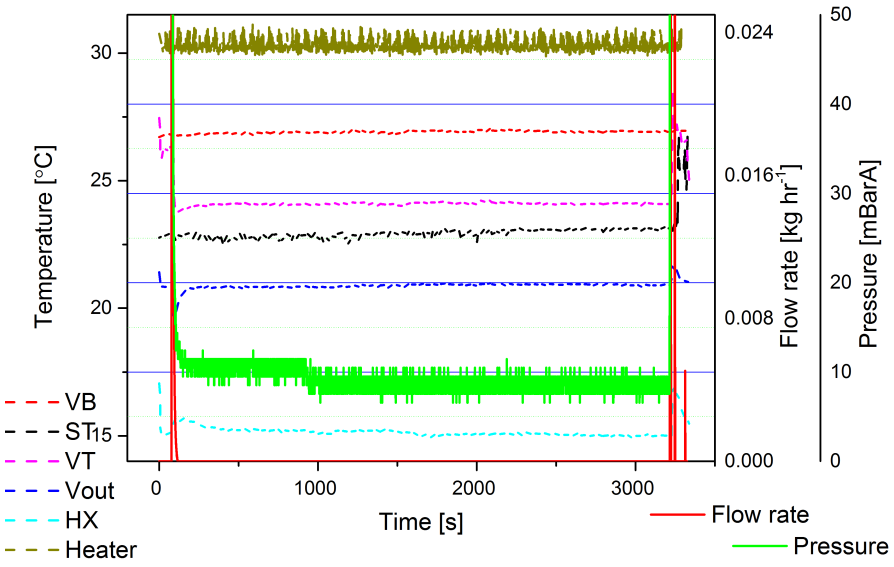

Figure 9.8: Full scale data plot for the final test of a sequence.

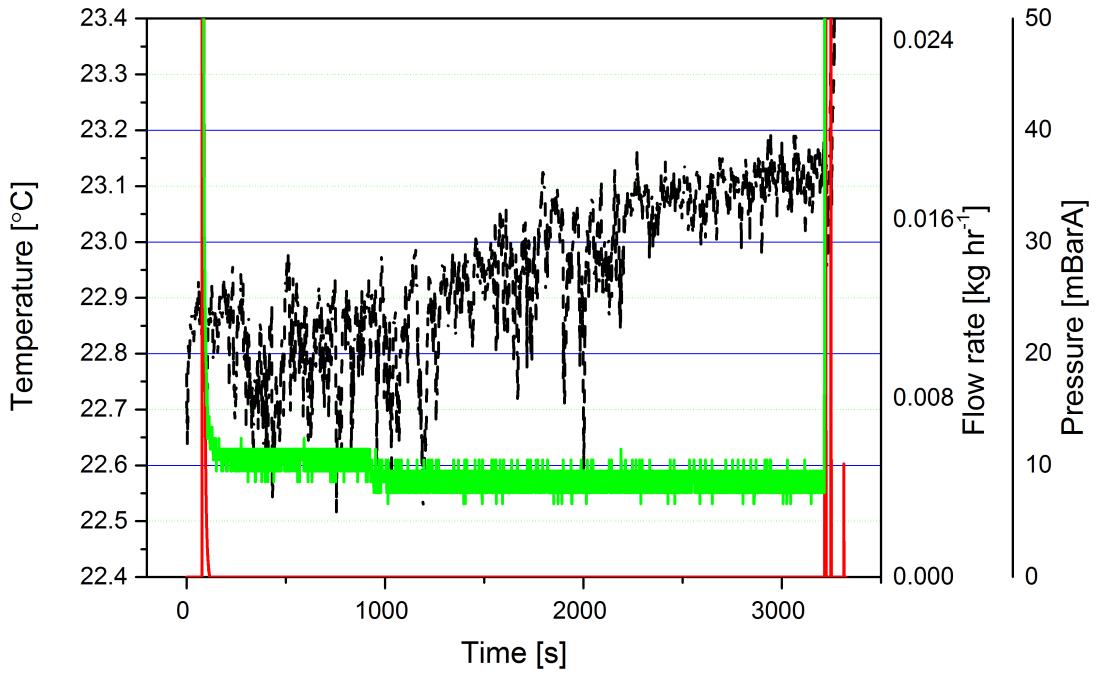

(a) Expanded temperature scale showing surface temperature.

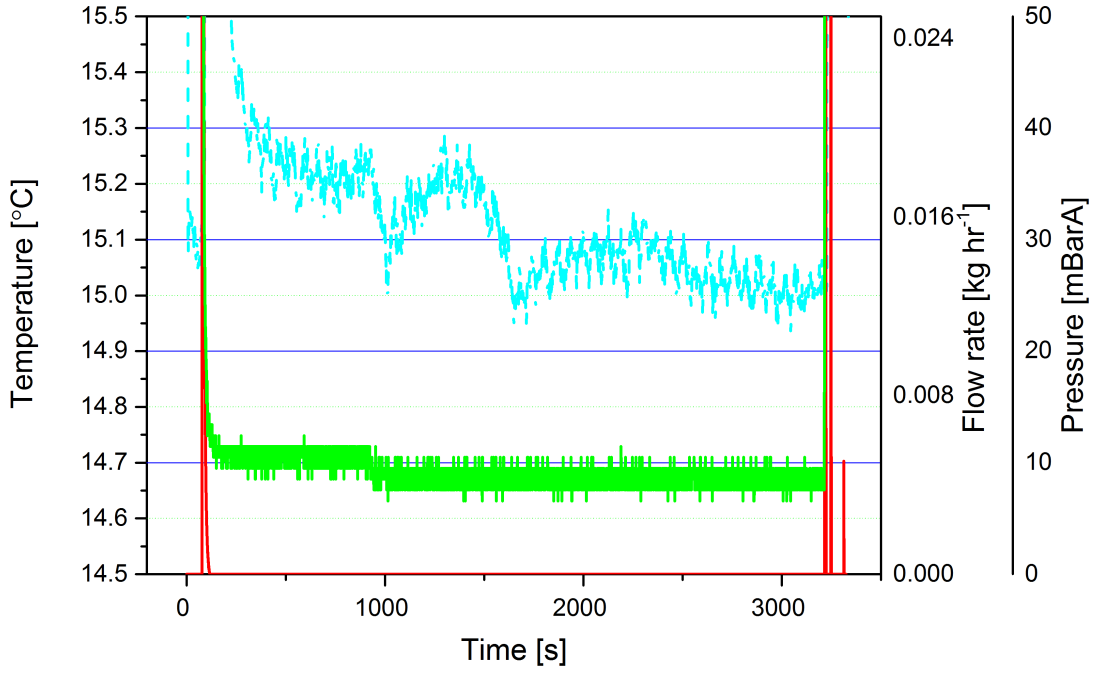

(b) Expanded temperature scale showing condenser temperature.

Figure 9.9: Expanded scale plots of fig. 9.8.

9.2.2 Overall Vacuum Drying Data

The data plots above have shown that with the instrumentation used it is possible to make some deductions about what is happening with the vessel and also identify key points in the drying process. Each data point on the plots below is a single test.

The Impact of Water Quantity Figure 9.10 shows how the quantity of water in the test piece at the beginning of a test impacts the drying rate for that test. When the test piece was full of water (∼7 g) the drying rate varied between 0.4 and 0.5 mg s^{-1} however when the test piece contained 0.9-4 g of water at the beginning of a test the drying rate was always around 0.15 mg s^{-1}. For the tests beginning with 4-7 g of water an intermediate drying rate was obtained.

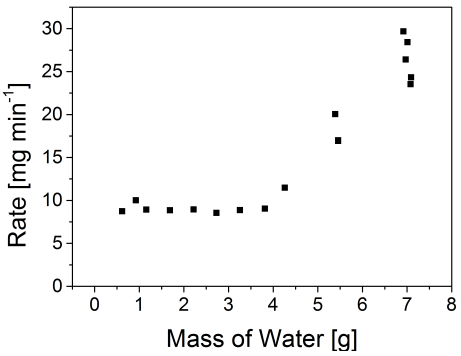

Figure 9.10: The effect of water quantity on drying rate for 60 minute, 30°C tests.

The Impact of Pressure Figure 9.11 shows how the drying rate is affected by the system pressure at both 30°C and 60°C when a full test piece was in the drying vessel. At low pressures (<10 mBarA), 60°C tests gave a rate between 0.65 and 1 mg s^{-1}. Not only was the rate considerably higher than that found for the 30°C test but the range was also larger. At 80 mBarA the drying rate at 60°C was 0.32-0.37 mg s^{-1} which was still higher than at 30°C (0.22-0.29 mg s^{-1}) but was proportionally less so and the range covered was similar. At higher pressures (240-590 mBarA) the drying rate was 0.15-0.32 mg s^{-1} at both 60°C and 30°C.

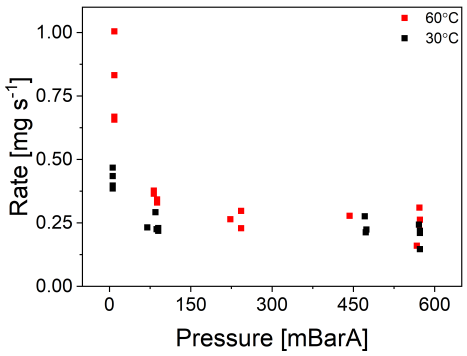

Figure 9.11: The effect of pressure on the drying rate for 60 minute tests.

However the drying rates shown are calculated from mass lost from the test piece and what is not shown in fig. 9.10 is the quantity of water that remained within the vessel. In all cases at the higher pressures used water was found to remain in the vessel after being ejected from the test piece as seen in fig. 9.12. At 30°C there is no apparent correlation between the pressure and the mass of water remaining while at 60°C there is an apparent reduction in the quantity of water remaining as the pressure increases which is somewhat counter intuitive and it is not entirely clear why this should be the case.

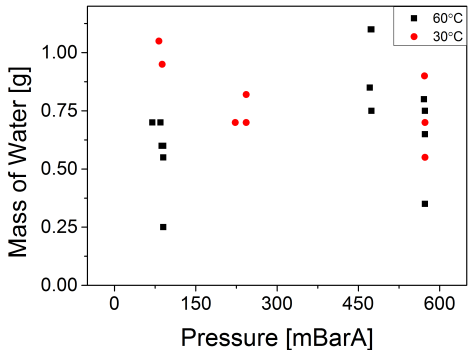

Figure 9.12: The quantity of water remaining in the vessel after tests at different pressures.

The Impact of Test Time The effect of the test time on the drying rate for 30°C tests is shown in fig. 9.13. The drying rate is clearly higher and more varied

for shorter tests than longer tests. The reason for this can be seen in the drying plots where the flow rate, which is an indicator of how much water vapour is being removed from the vessel, is initially high and drops with time. A much greater proportion of a short test will consist of a period with a high flow rate and will therefore increase the calculated drying rate while a longer test will have a longer period with a flow rate below the level of the detection and this will bring the average down.

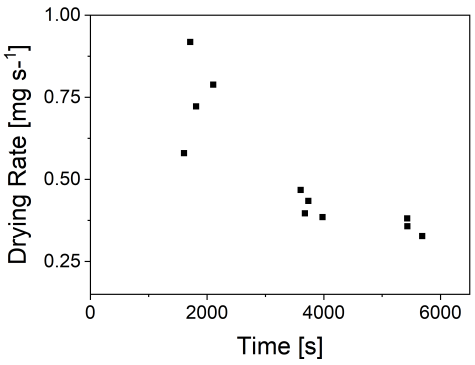

Figure 9.13: The effect of time on the drying rate for 30°C tests.

9.2.3 Comparison to Initial Testing

To allow a comparison with the initial testing a small number of tests were carried out at 60°C using 2-3 g of water in the test piece. While these tests are not completely comparable since there was no heel water used it did allow a rough comparison of the rates obtained following the rig modifications.

For the tests carried out at 60°C the drying rate was found to be between 0.25 and 0.36 mg s^{-1} which was slightly higher than found in the initial testing (0.16-0.18 mg s^{-1}) when the rig pressure was higher indicating that a lower pressure increases the drying rate although the presence of heel water at this point may have reduced the rate somewhat in the initial testing.

9.2.4 Discussion

One of the most obvious observations from the results shown is that the test conditions which show the highest drying rates, at whichever temperature, tend to also show the greatest variation. In some cases a detailed analysis of the data and the experimental set up can find some reason for this. For instance the low pressure 60°C tests show a range of 0.65 to 1 mg s^{-1} and while these were all nominally identical tests with the test piece being full of water, closer inspection shows that the highest rate was found when the test piece contained the most water (6.929 g), while the lowest rate contained the least water (6.371 g).

One of the reasons for this impacting the drying rate is the result of the air space left within the test piece. When the lid is being secured the air space is compressed ejecting water from the hole until the water level drops below the level of the hole. Besides the fact that it was difficult to ensure that exactly the same quantity of water was added into the test piece in the first place other factors are believed to impact the amount of water ejected such as the rate at which the lid was fitted, how tightly the lid was held in place while the locking nut was tightened and even the angle at which it was held during tightening.

9.2.5 Proposed Model of Drying Behaviour for the Pinholed Test Piece

With the data plots shown above three distinct drying regimes are observed.

Regime 1 When the cap is attached water is unable to escape from the tube since the airspace in the top can not expand without forming a vacuum. As the drying vessel is evacuated the air space in the test piece expands and forces water out of the hole until the water level is below that of the hole. This water pools at the base of the vessel and is responsible for the high flow rate towards the beginning of each full test piece test as seen in **??**. Since this water can not be hotter than its boiling point which is less than 24°C the temperature of the base of the vessel (VB) drops while this water is present. Once this water has been removed the flow rate is greatly reduced.

Regime 2 This behaviour is also occurring during regime 1 but is obscured. It is thought that the peaks in flow and pressure observed beyond this point are due to the water within the test piece boiling with the bubbles rising and spitting water upwards. On occasions this water is spat towards the pin hole in the test piece leading to a slug of water being ejected from the test piece. It is possible that during this period a pressure gradient exists between the inside of the test piece and the vessel with a greater pressure existing inside the test piece. As a result the test piece does not cool as much as may be expected.

Regime 3 Over time the water level drops and there comes a point at which the water level is too low for water drops to reach the hole and slugs of water are no longer ejected thus the spikes in flow and pressure are no longer observed. Water is removed by evaporation only.

9.3 Cracked Acrylic Test Piece

A number of tests were carried out using the cracked acrylic test piece test seen in fig. 9.14. This piece was made from 15 mm outside diameter acrylic tube with 1.5 mm walls. It was slowly compressed in a vice until a crack formed along its length.

The cracked acrylic test piece was an early attempt to produce a tube with crack which could be sealed and was inspired by a broken tube found in the laboratory. The experimental procedure used was identical to that used for the pinholed stainless steel piece with the exception that the surface temperature thermocouple was not used. Previous testing with the pinholed stainless steel test piece had shown that while some useful data was collected from this thermocouple when attached to acylic which has a much lower thermal conductivity than stainless steel ($\sim$0.17 $Wm^{-1}K^{-1}$ compared to $\sim$17$Wm^{-1}K^{-1}$) little useful data would be obtained.

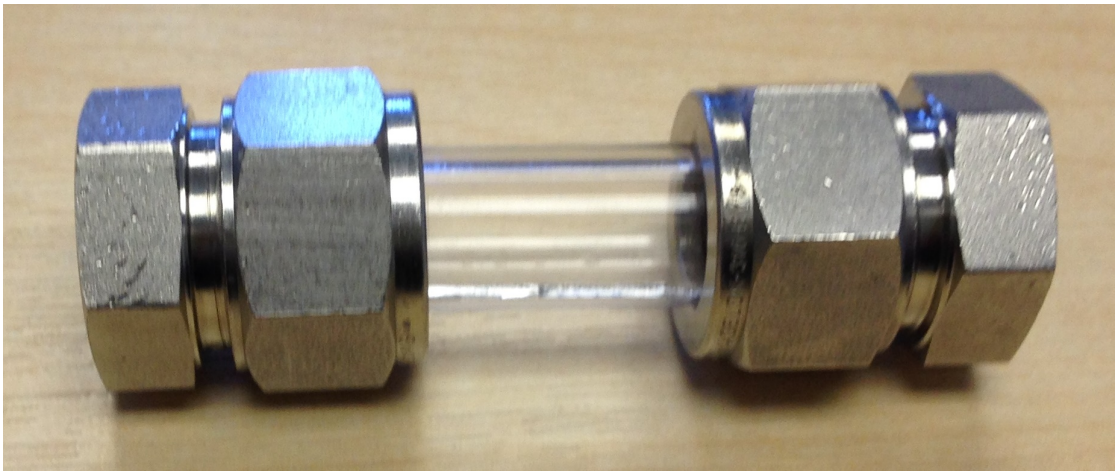

Figure 9.14: Cracked acrylic test piece.

9.3.1 Data Plots and Drying Rates

The data plots for the crackaed acrylic test piece show three distinct drying regimes and these can be seen in fig. 9.15 along with the drying rates obtained. These regimes closely match those described above for the pinholed stainless steel test piece but with some differences in places.

The first drying regime is seen in fig. 9.15a and is very similar to the first test of a sequence with the pinholed stainless steel test piece with an initial drop in flow and pressure however this drop is substantially larger and over a longer time span than previously observed. This test has a high drying rate of 0.91 mg s^{-1}.

The next two tests are almost identical and both show the second drying regime (also seen towards the end of A). They show erratic behaviour with spikes in flow and pressure. This is similar to that described for the pinholed stainless steel test piece however the spikes are much greater in magnitude and more frequent but of much shorter duration. These two tests both show a drying rate of 0.28 mg s^{-1}. Regime 3 in tests E, F and G, is almost identical to the mid sequence tests described above with constant pressure and zero recorded flow. The drying rate was 0.13-1.14 mg s^{-1}. Test D shows the transition from drying regime 1 to 2.

Test D which shows the transition between regime 1 and 2 has an intermediate drying rate. Test H shows a drop in pressure as the final free water is removed.

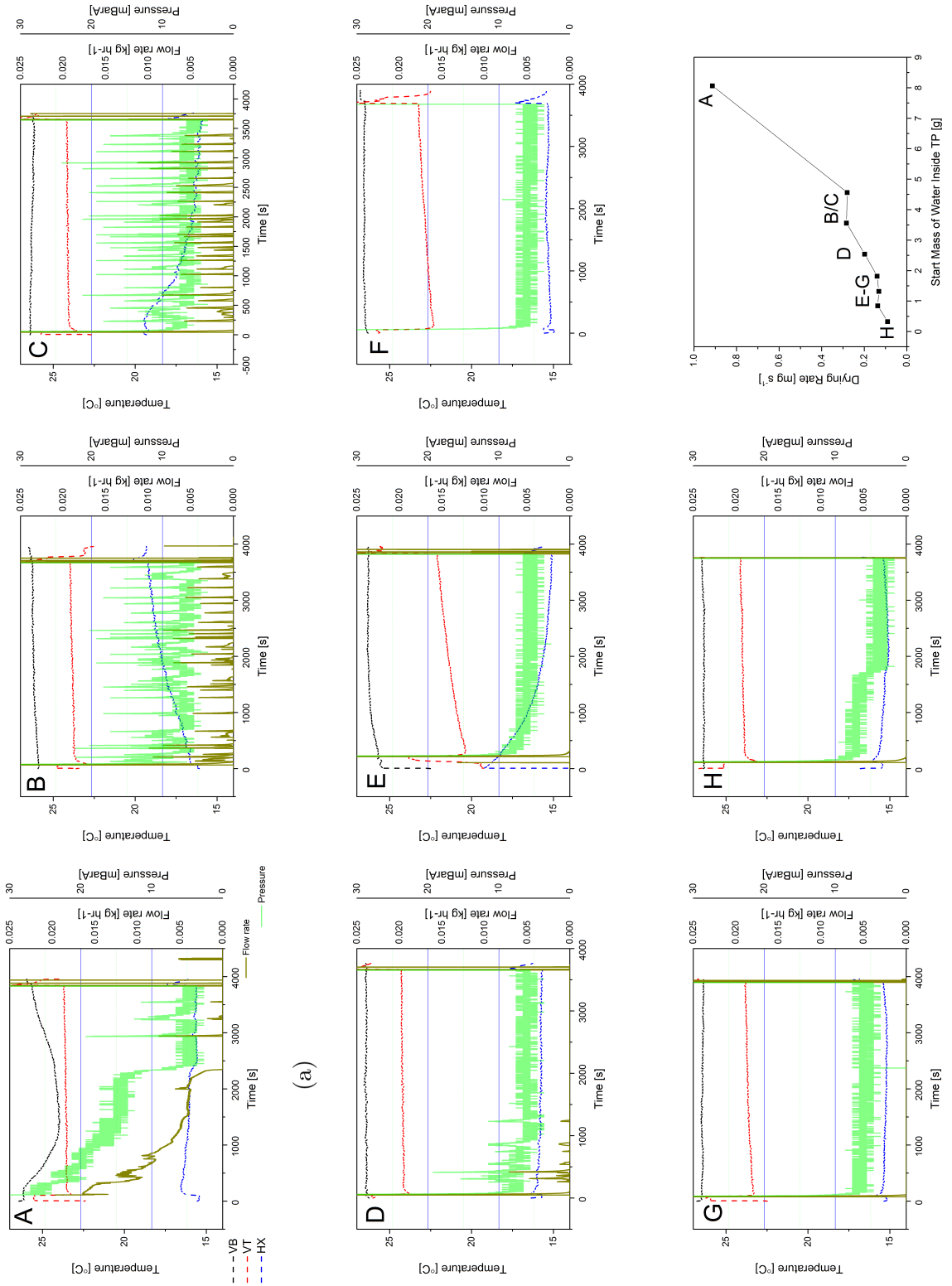

Figure 9.15: Data plots and drying rates for the cracked acrylic test piece.

If the drying rate is calculated from the total length of the test then it is 0.09 mg s^{-1} however if the time to the pressure drop is used it is found to be 0.18 mg s^{-1}.

9.3.2 Proposed Model for the Cracked Acrylic Test Piece

For the cracked test piece the three regimes are broadly similar but with a few key differences.

Regime 1 Regime 1 is once again due to the ejection of water as the air space in the test piece expands. Since the crack runs the full length of the test piece the air space now expands until the pressure within the test piece has equalised with that outside rather than until the pinhole is reached. As a result more water is ejected giving the appearance of a higher drying rate and this regime is longer than previously observed.

Regime 2 Regime 2 is somewhat different to the second regime observed in the pinholed test piece. As the water boils there is a build up of pressure in the test piece. This will continue until the pressure is high enough to push a slug of water through the crack (the plastic is somewhat flexible).

Regime 3 Eventually the water level drops below the level of the Swagelok cap at which point water can not longer be ejected through the crack. The water is now removed by evaporation only.

9.4 Cracked Stainless Steel Test Piece

The cracked stainless steel test piece was manufactured from the length of tube produced in section 3.8. The cracks are of a similar magnitude to those seen in the failed fuel cladding in fig. 2.7 and while some fuel is believed to have smaller defects this test piece is believed to be reasonably representative. This test piece underwent similar testing to the pinholed stainless steel test piece using the same methodology.

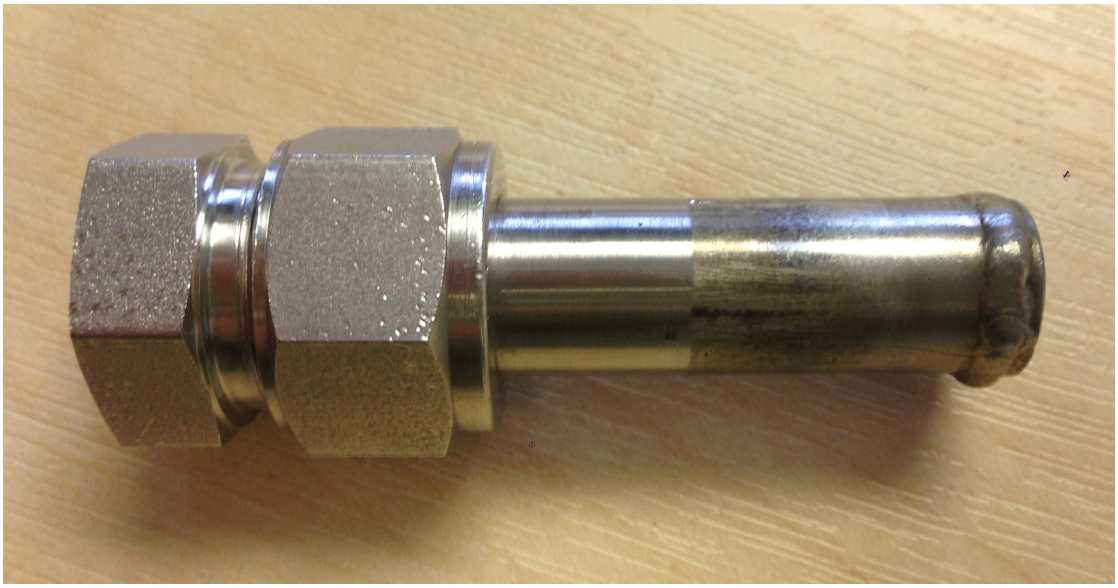

Figure 9.16: Cracked stainless steel test piece.

9.4.1 Cracked Stainless Steel Data Plots

Figure 9.17 shows the first four data plots in a sequence for the cracked stainless steel test piece. The initial behaviour in test A is much the same as observed with the other test pieces with an initially high flow rate and pressure both of which drop away (described as drying regime 1). During this period the vessel base temperature drops suggesting that water has pooled in the base of the vessel. The behaviour then changes somewhat. In previous tests the second regime observed has been described as consisting of erratic spikes in flow and pressure and this is followed by regime 3 where pressure remains constant and the flow rate appears to be zero. For the cracked stainless steel test piece the second drying regime seems to be absent with a transition straight from regime 1 to regime 3. There is however strange behaviour in tests C and D in which spikes in pressure and flow are seen. These are in some ways similar to those observed in regime 2 but rather than being relatively short and frequent there are three spikes (one in test C and two in test D) which are larger and broader[1]. These peaks are accompanied by increases in

[1]Test D is much longer than tests 1-3 but the area of interest is the first 4k s which would be unaffected by this.

condenser temperature which were previously observed alongside spikes pressure and flow.

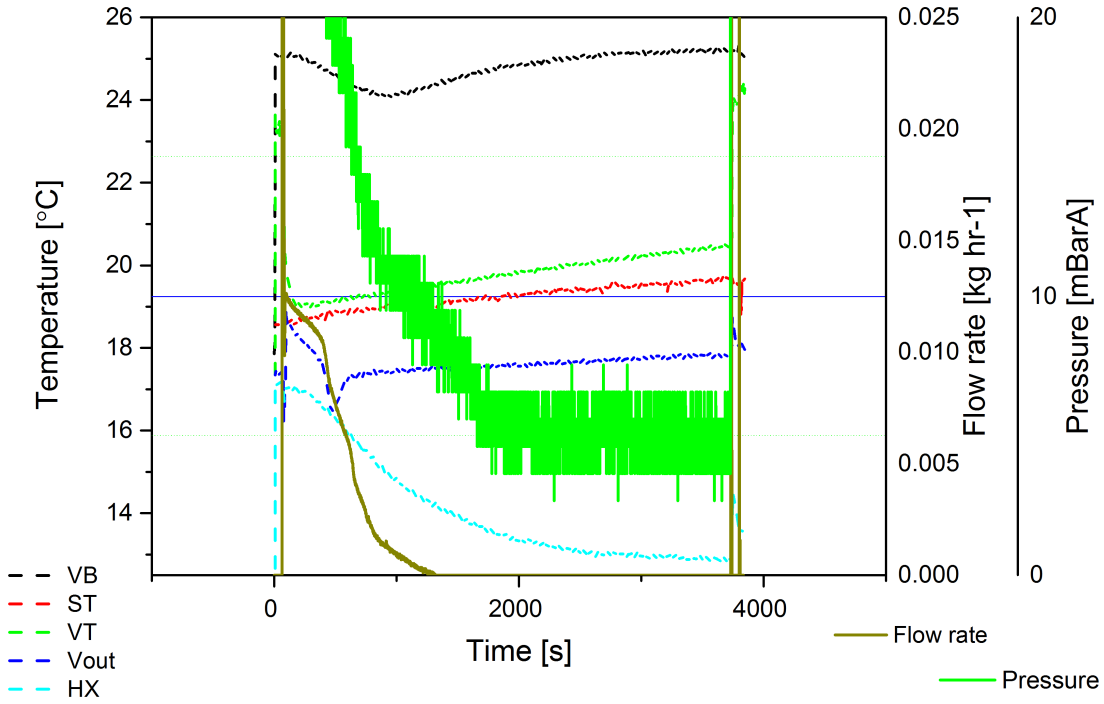

(a) First test of sequence (A).

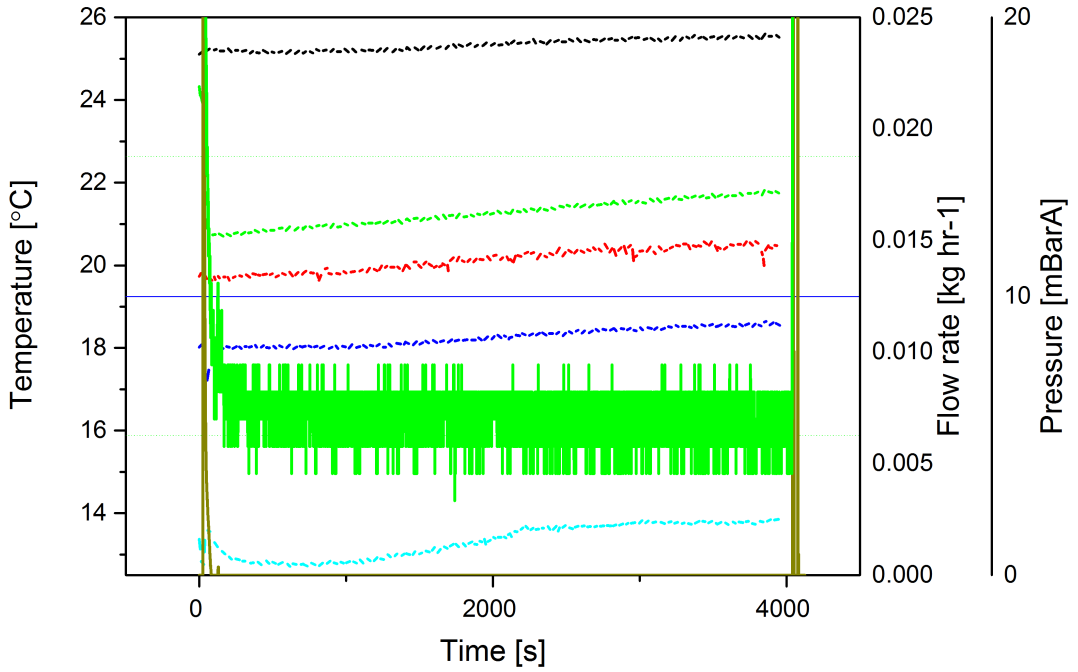

(b) Test B.

[H]

What seems odd with these is that the peaks present themselves in tests C and D beginning after a total drying time of ∼10k s and are completely absent in test B. In order to investigate the possible cause of this a single extended drying test was carried out which is shown in fig. 9.18. This tests once again shows several large spikes in flow and pressure and once again these occur after ∼10k s.

9.4.2 Cracked Stainless Steel Drying Rates

The drying rates for a sequence of cracked stainless steel test piece drying tests are shown in fig. 9.19. The plot would seem to suggest that there are four distinct drying rates. Previously a distinct drying rate has suggested a distinct drying regime (see fig. 9.15) however after the sixth test it was decided to increase the length of each test which is known to reduce the apparent drying rate. In section 9.2.2 the reason for this was discussed in relation to a full test piece. In a mid sequence test water is being removed by evaporation only. At the beginning of the test the water is around 17°C. As the vessel is evacuated the boiling point of the water drops and for a brief time the water is superheated, during which it boils away relatively quickly, however, the water quickly cools and the drying rate drops. This means that as the test time is extended the drying rate appears to drop but does in fact become more accurate. As a result the difference in drying rates for the fifth to seventh tests and the remaining tests is likely to be as a result of test length rather than any change drying behaviour.

For the first test in a sequence (when regime 1 is observed) the drying rate is seen to be broadly similar to the first test observed with other test pieces being around 0.5 mg s^{-1}. Since regime 2 is absent for the cracked stainless steel test piece there is no region for comparison but the rates in regime 3 seem to be around 0.06 mg s^{-1} (for a 60 minute test) compared to 0.2 mg s^{-1} for the pinholed stainless steel test piece.

9.4.3 Discussion

The data plots for the cracked acrylic and pinholed stainless steel test piece show three distinct drying regimes although there are minor differences in the appear-

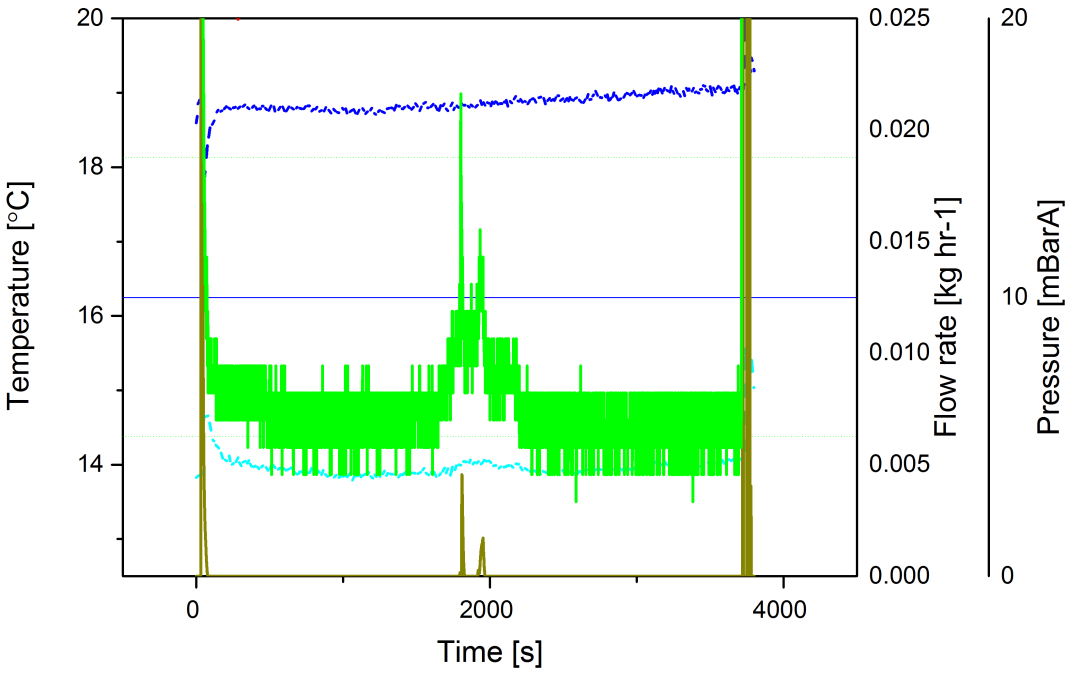

(c) Test C

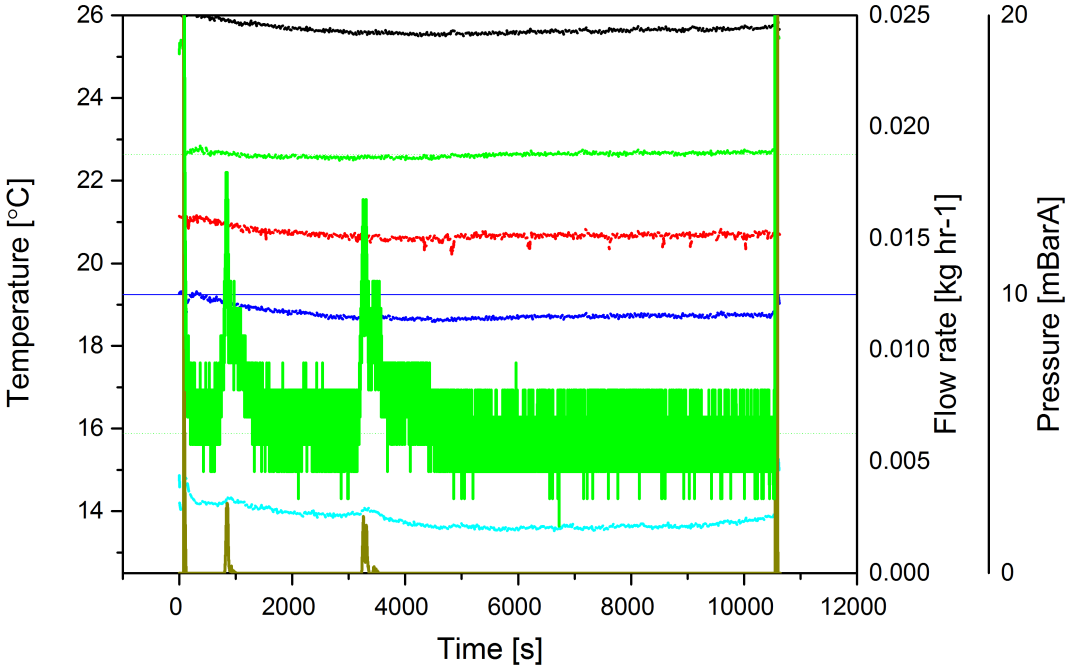

(d) Test D.

Figure 9.17: Data plots for cracked stainless steel test piece.

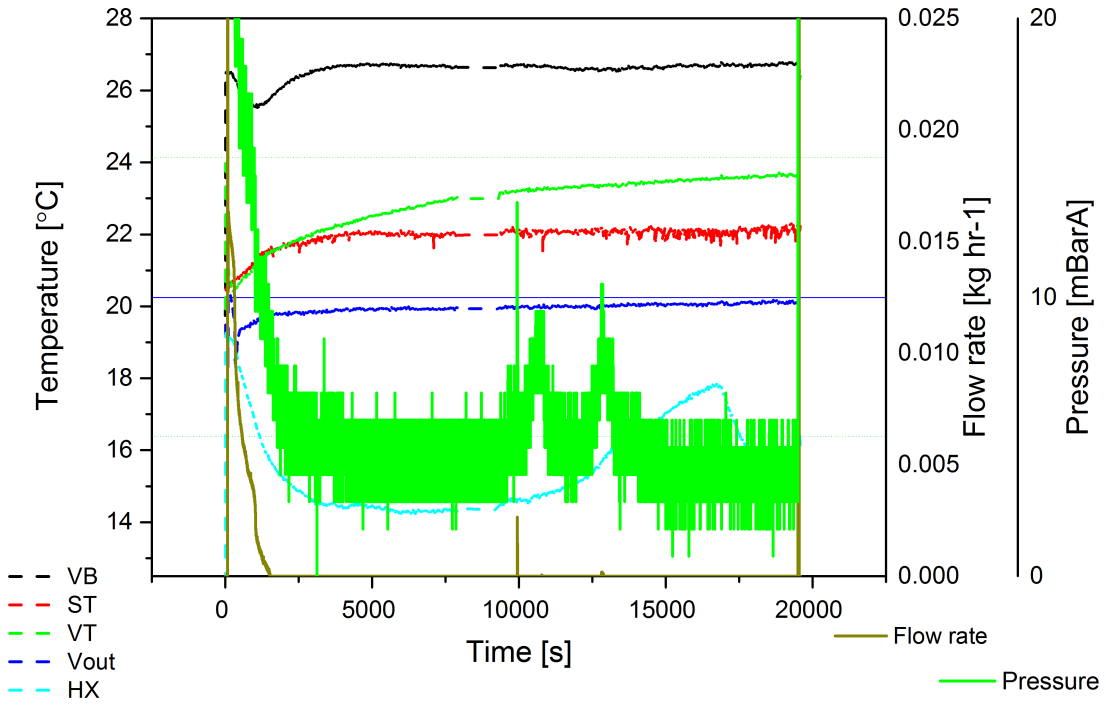

Figure 9.18: Extended test with cracked stainless steel test piece.

ance of regime 2. It could be argued that there are still three regimes for the cracked stainless steel test piece however the second of these is much less distinct consisting of just three peaks. It is interesting to see that these peaks appear after roughly 10k s total drying time whether that is midway through the third of a sequence of tests or after 10k s of a 20k s test. This suggests that these peaks appear as a result of the water reaching a certain level within the test piece rather than being related to temperature or pressure within the system since such factors would not be expected to align at the same time if the test piece had been removed twice from the evacuated vessel. Nevertheless there is no obvious explanation for what is causing this.

The drying rates for regime 1 which is present in all test pieces is somewhat lower for the cracked stainless steel test piece than the others however not substantially so considering the variation observed for drying rates in this regime. In contrast the drying rates during regime 3 are considerably lower for the cracked

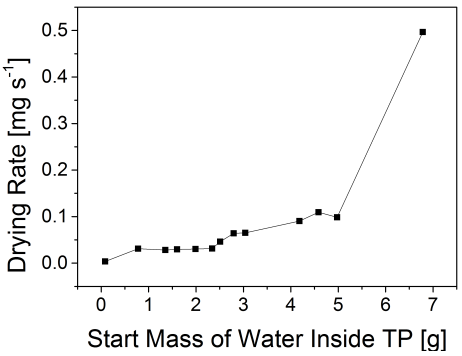

Figure 9.19: Cracked stainless steel test piece drying rates. Each point is a single test.

stainless steel test piece than the others. This indicates that while the cracks are thought to be somewhat larger than the microcracks that are of most concern for the drying of spent nuclear fuel they are small enough to significantly slow the removal of water.

9.4.4 Cracked Stainless Steel Drying Mechanism

The cracked stainless steel test piece appears to behave in a very similar manner to the other test pieces at the beginning and end of a drying sequence with regime 1 and 3 behaviours evident. The regime 2 behaviour, which had previously followed on directly from regime 1 and was characterised by multiple irregular spikes in the flow and pressure as a result of water being ejected from the test piece, was arguably absent or at least significantly modified since it no longer consisted of many different peaks and now appeared as two or three much larger peaks. This would suggest that this regime is now caused by several much larger ejections of water rather than multiple small ones.

9.5 Glass Oven and Drying Videos

While the data plots gave a certain amount of information as to what was happening within the vessel there were some behaviours and events that could not be

fully identified. In order to investigate this the drying vessel was changed to allow behaviour inside the vessel to be observed.

9.5.1 Apparatus

The apparatus used for this work is shown in fig. 9.20a. The standard drying vessel was replaced with a Buchi B585 glass oven. A transparent pinholed acrylic (PA) test piece was also produced to allow the behaviour inside the test piece to be observed (fig. 9.20b).

(a) (b)

Figure 9.20: Glass drying oven and acrylic test piece.

Temperature Measurements Since the glass oven was not designed for this purpose it was not possible to record the vessel gas temperature, the vessel wall or base temperature or the sample surface temperature.

Pressure The system pressure was recorded by relocating the pressure transducer to the pipework closest to the vessel itself since it was not possible to place

it on the vessel as it had been previously.

9.5.2 Results from Drying Videos

The following section shows some data plots collected using the glass drying oven with a description of the events observed at these times. The emphasis is on specific events and how they appear on the data plot rather than the test as a whole.

Cracked Stainless Steel Test Piece At the beginning of the test water is ejected from the test piece and also weeps from a crack in the test piece wall, running down the side. Three key points were then observed (see fig. 9.21).

Point A At point A it is no longer possible to see water weeping through the crack in the test piece.

Point B At point B water is spat from the crack and lands on vessel wall.

Point C At point C water is spat from the crack and landed on the vessel wall and water has wept through the crack and run down the side of the test piece.

Pinholed Acrylic Test Piece 1 (see fig. 9.22a) As the vessel is evacuated, the air space in the test piece top expands and water is ejected until it reaches the level of the pinhole. This water pools in the bottom of the vessel and around the rim of the test piece. This water boils, vigorously at first but less so as it cools. The water in the test piece boils with bubbles forming and rising. Each time this happens a drip of water can been seen to run down the side of the test piece as it comes out of the pinhole. Over time the water level drops with two types of bubbles being seen to form. Small bubbles do not typically lead to ejection of water and rise though the water column or along the the inside of the test piece wall. Large bubbles behave like a wave with a sheet of water rising up from the surface of the water to the pinhole.

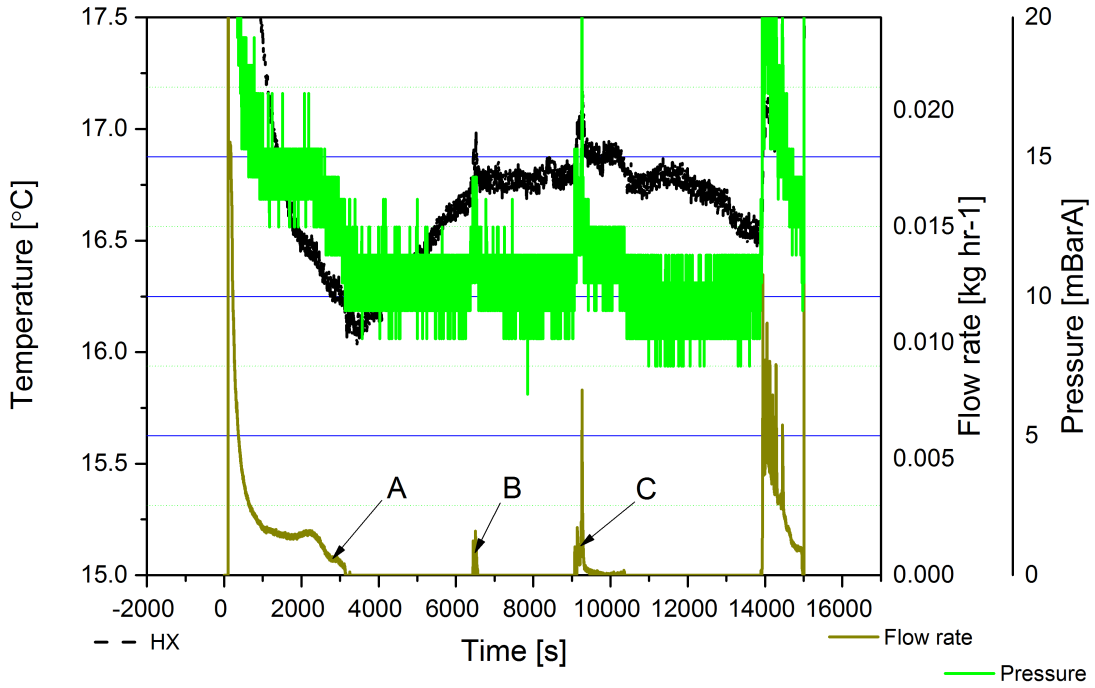

Figure 9.21: Plot of cracked stainless steel test piece in glass oven.

Point A The last of the water pooled in the base of the vessel disappears around 2000 s and the last of the free water visible around around the stainless steel cap disappears around 120 s later. When water runs down the side of the test piece some will go into the gap between the cap nut and tube so is out of site hence the fact that the flow rate continues dropping for several minutes beyond this. There is no boiling within the test piece for a period beyond this.

Point B There is a cluster of small bubbles inside the test piece over a five minute period and one large bubble that leads to a drip of water coming through the hole and running down the side of the test piece.

Point C From this point onwards large bubbles begin to regularly form inside the test piece leading to drips running down the outside of the test piece.

Pinholed Acrylic Test Piece 2 (see fig. 9.22b) The initial behaviour is as described above. Several other points are identified in this test.

Point D In this test there is a noticeable drop in flow as the last of the water in the base of the vessel disappears however the general flow rate does not drop to zero.

Point E The frequency of the spikes in flow from ∼6000 s is roughly that of the observed large bubbles within the test piece.

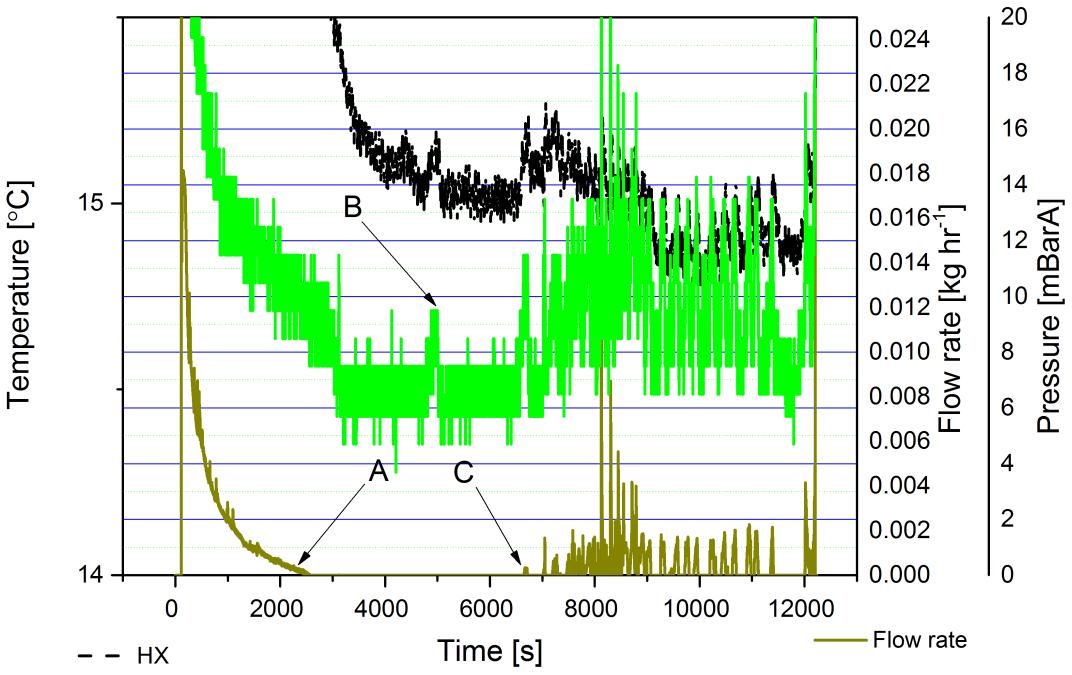

(a) Test 1

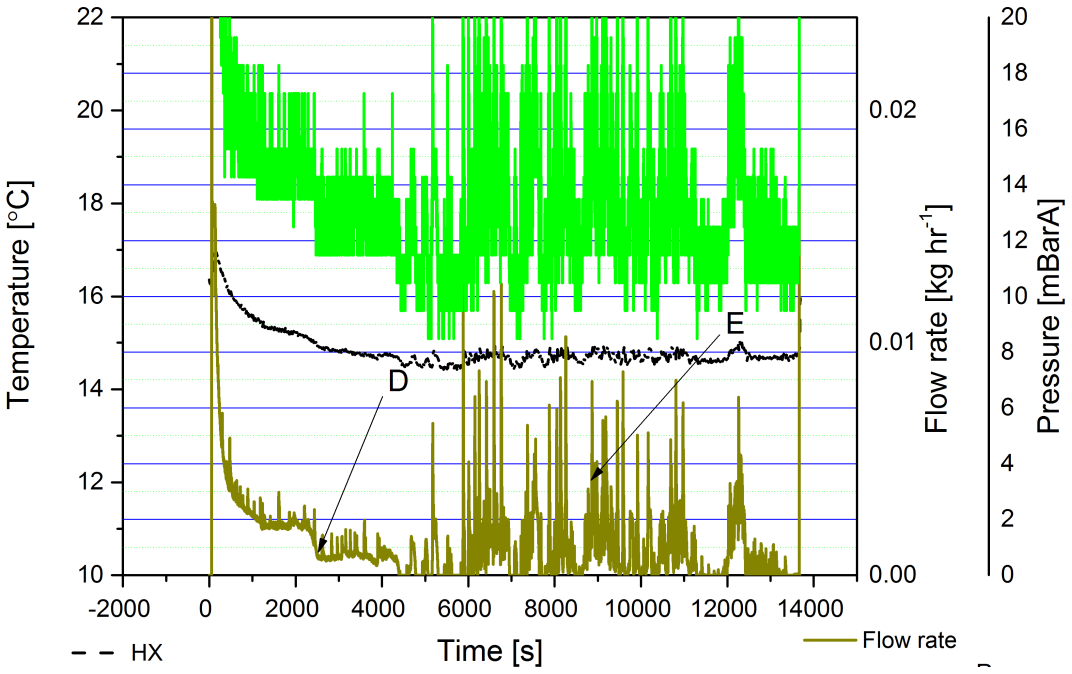

(b) Test 2

Figure 9.22: Plot of pinholed acrylic test piece in glass oven.

9.6 Vacuum Drying Mechanism

In the early part of this section a proposed vacuum drying mechanism was put forward based on what could be deduced from the data plots. With the use of the glass oven and acrylic test piece a couple of minor differences have been observed. A final generalised mechanism is therefore given below and this is once again split into different drying regimes.

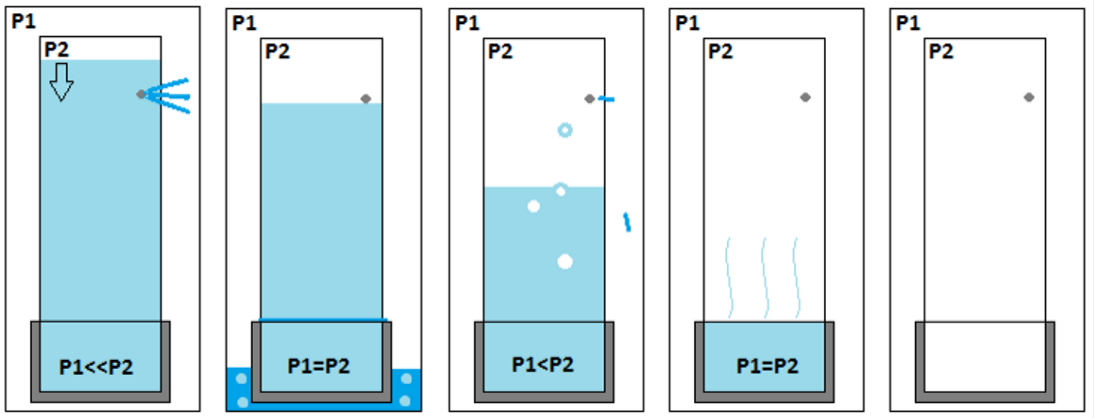

(a) Regime 1 (b) Regime 1 (c) Regime 2 (d) Regime 3 (e) Dry

Figure 9.23: Generalised drying mechanism.

9.6.1 Regime 1 - Forced Ejection and Free Water Drying

This regime has the highest drying rate which is broadly similar for all defects examined. It occurs when the test piece is full of water and is due to liquid water being displaced through the defect. As described, when the vessel is first evacuated the pressure in the vessel (P1) is much less than inside the test piece (P2) so the the air in the headspace expands until the pressure has equalised or the water level is below that of the pinhole or crack[1] (fig. 9.23a). The water ejected is now free water and will run down the side of the test piece pooling in the base of the vessel and around the nut of the test piece cap (fig. 9.23b).

[1] Assuming a starting pressure of 1000 mBarA and a final pressure of 12 mBarA the air space will expand to around 6.4 times its original volume.

The surfaces that the free water comes into contact with are normally in excess of the boiling point and as such the water boils vigorously however as this happens the surfaces cool and the water begins to boil less vigorously and then evaporate with infrequent bubbles forming. This can be seen by a drop in surface temperature and also vessel base temperature during this regime. The flow rate is initially high but as this water boils/evaporates away the flow rate and pressure drop steadily until the flow rate is below the level of detection.

9.6.2 Regime 2 - Erratic Drying

The behaviour of the second regime is due to slugs of water being ejected from the test piece however the behaviour appears differently depending on the defect. In general as the water boils slugs of water are occasionally ejected from the test piece and these lead to spikes in the pressure and flow (fig. 9.23c). The pressure inside the test piece is likely to be slightly higher than in the vessel.

For the cracked acrylic test piece this regime is much longer and the spikes in pressure and flow look at first glance to be almost regular, however this is likely due to the fact that there is a single crack of uniform size which runs the length of the test piece meaning that liquid water can ejected at a similar rate and for longer. As the water boils the pressure builds up inside the test piece causing the crack to open up and eject slugs of water. The suggestion is that these are small slugs of water that vaporise almost instantly when ejected from the test piece and therefore are high in magnitude and of short duration

For the pinholed stainless steel test piece the spikes in pressure and flow are erratic and typically lower magnitude and longer in duration but there is more variation in size. Observation of the test pieces during drying show two types of bubbles form within the test piece; small bubbles which rise slowly in the water column inside the test piece or along the wall and large bubbles which move at a much higher rate and result in a sheet of water moving up the inside of the test piece. As the overall flow rate and pressure is much lower these individual bubbles now lead to spikes in flow rate and pressure as they force water out of the test piece. The glass oven suggested that the size and duration of the peaks on the data plots is related to where the water lands when it is ejected with water that

runs down the side of the test piece typically appearing as longer lower magnitude peaks while water that is spat onto the vessel walls gives shorter higher magnitude peaks as the water boils away more quickly.

For the cracked stainless steel test piece regime 2 consisted of two or three spikes only and these occur a considerable time after the end of the regime 1 but are larger and longer than those for the other test pieces. Since the spikes of regime 2 occur after a similar total time whether part of a sequence of tests or during one extended test it would seem that these peaks are due to the water level.

9.6.3 Regime 3 - Evaporation

This regime has the lowest drying rate and occurs when the water level is too low for water to be able to reach the pinhole or crack and as such water is removed by evaporation only (fig. 9.23d). This is a steady and continuous process so the flow rate is below the level of detection. In all tests it was found that there was a step change in pressure during the final test in a sequence. Interestingly this step change occurred even if there was water held up elsewhere within the system effectively reducing the magnitude of the vacuum. It is also likely that there is a pressure drop across the crack or pinhole and therefore the water inside must be slightly warmer before it will boil.

The final regime is also similar for all defects, being due to removal of water vapour only, however the rate is dependent on the defect size with the cracked stainless steel, which has the smallest defects having a much lower rate. This may be due to a pressure drop across the crack meaning that the pressure inside the test piece is higher leading to a higher boiling point so the drying rate is lower.

9.7 Vacuum Drying Summary

9.7.1 Overall Drying Results

The data collected has unsurprisingly shown that temperature has a clear impact on the drying rate for the pinholed test piece with the 60°C tests having a drying rate roughly twice that of the 30°C tests although with much greater variation.

This is in no way surprising but would indicate that increasing the temperature further would allow further increases in the drying rate and since the temperatures used are low there is significant room for this to be carried out.

The drying rate appeared to be inversely proportional to the test length, however this is likely to be impacted by the fact that these tests were carried out using a full test piece. When a full test piece is used there is an initial ejection of water and then a high drying rate (regime 1) while this is removed. In a shorter test a greater proportion of the test is made up of this regime than the slower regimes 2 and 3 and the overall drying rate is therefore higher.

Several tests were carried out to assess the impact of pressure at 60°C and 30°C. It was found that for the tests at $\geqslant$80 mBarA roughly the same quantity of water was ejected from the test piece however this was later found in the vessel so the drying rate was not a true reflection of what was occurring. This seems to confirm the mechanism which was driving regime 1 since a lower pressure has the potential to eject more water from the test piece and also that the drying of free water outside the test piece is important. There was no obvious correlation between the pressure of the test and the quantity of water that remained in the vessel. This is somewhat surprising as it would be expected that at a lower pressure the free water would be removed more easily however the boiling point of water at 80 mBarA is around 44°C which is warmer than the vessel base reading for both the 30°C and 60°C tests.

The drying rates for both the pinholed and the cracked acrylic test piece show no significant difference in drying rate and in fact for the cracked stainless steel test piece the drying rate when the test piece is full is also comparable. However for the second and further tests in a sequence the drying rate for the cracked stainless steel test piece is significantly less than for the other test pieces. This indicates that the defect dimensions have a clear influence on the drying rate with the smallest defects showing the lowest rate.

Overall the data would seem to suggest that for effective drying the most important factor is to ensure that the pressure is low enough for the boiling point to be reached. As long as this point is reached a relatively high drying rate is found and beyond this the temperature plays a greater role. It may be that it is easier to work at higher temperatures and slightly higher pressures ($\sim$50 mBarA)

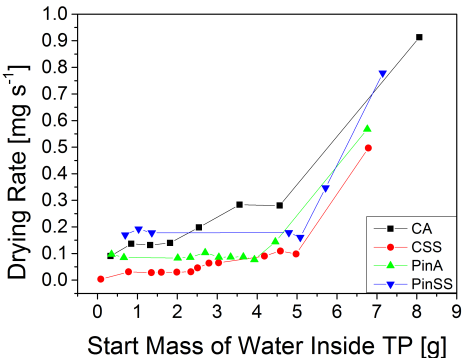

Figure 9.24: Vacuum drying rates for all test pieces used. Each point is a single test.

rather than lower pressures (∼10 mBarA) where the risks of ice formation are increased although since the experiments undertaken in chapter 7 suggested that heat transfer was controlled by conduction rather than convection ice formation may not be a significant issue, particularly for fuel with greater decay heat.

9.7.2 Instrumentation

The data plots collected have shown that a reasonably large amount of information can be detected with the relatively unobtrusive instrumentation used. It had initially been thought that the recording of surface temperature would be one of the more useful temperature measurements but this was actually found not to provide as much data as had been expected which since this would be the most difficult method to use on real fuel is beneficial. The measurement of the vessel base temperature was in fact found to provide relatively good information as to the presence of free water pooled at the base of the vessel. Perhaps the most useful temperature measurement was in fact the temperature recorded at the ice cooled condenser. While the fluctuations at this point were not large it was clear that when slugs of water were ejected from the test piece temperature fluctuations could be detected at the condenser inlet and there is some indication that a temperature fluctuation is apparent when the final drops of trapped water were removed.

The measurement of both flow and pressure have been shown to indicate when

drops of water are ejected from the test piece however when only water vapour is being removed the mass flow of water vapour is below the level of detection. The pressure measurement did however appear to show a drop when the last drops of free water were removed and this appeared to be clear no matter what the system pressure was at the time.

Pressure, flow and downstream temperature (condenser) are all parameters that appear to show some fluctuation as the water level changes and since these do not require instruments that would need to be placed deep within a drying cask they have the potential to be used for real time monitoring when vacuum drying fuel.

Chapter 10

Flowed Gas Drying

In chapter 7 testing was carried out to compare vacuum drying (VD) with flowed gas drying (FGD). Vacuum drying was found to be more effective but there were several parameters relating to flowed gas drying that it was felt could be improved. The following chapter looks at flowed gas drying in more detail to try and establish if the improvements that were identified earlier would improve flowed gas drying sufficiently for it to be comparable with vacuum drying.

10.1 Rig Modifications

The initial testing identified several areas where flowed gas drying could be improved.

Pump Controller The circulation pump was found to regularly trip out and this was due to the design of the pump controller. This was an issue the manufacturers were aware of and they supplied a new controller once it had been developed.

Fitting of Dew Point Meter During the second phase of vacuum drying testing it was felt that enough understanding had been developed for it to be possible to refit a dew point meter (dew point meter) to the system. On this occasion a Michell SF72 dew point meter was fitted which had a range of +60°C to -40°C. The dew point meter was fitted at the outlet of the vessel adjacent to the vessel outlet thermocouple.

Iced Water Cooled Condenser Iced water was used throughout the flowed gas drying testing.

Units of measurement Flow rate is shown in litres per minute corrected to atmospheric pressure and room temperature to allow easy comparison as opposed to mass flow. The data from the dew point meter is shown as parts per million mass since dew point is temperature dependent.

Additional Thermocouples For some of the later flowed gas drying tests thermocouples were fitted to the outside of the molecular sieve housing, one approximately a quarter of the way along the sieve from the inlet (sieve 1-S1) and a second three quarters along from the inlet (sieve 2-S). The original intent for this was to allow monitoring of the sieve condition since absorption of water by molecular sieve is exothermic. The intention was to change the sieve when sieve 2 began to warm however it was found that these temperatures actually provided some information relating to behaviour.

10.2 Methodology

The testing was carried out in a similar manner to the vacuum drying testing with a sequence of tests being carried out beginning with a full test piece, with the test piece being replaced without being refilled until the test piece was empty. Once again the pinholed stainless steel test piece was used for the majority of tests although some were carried out with the cracked stainless steel test piece for comparison.

The test length for flowed gas drying was significantly longer than for vacuum drying. Since it took approximately 2 hours for the system temperature to stabilise so each test was run for 4-6 hours to allow the impact of the different temperatures to be observed.

A number of initial tests were carried out using a set temperature of 60°C and these found that the drying rate was extremely low and further testing at this temperature was abandoned. It was decided that the test temperature would be chosen based on whether a surface temperature of 100°C (the boiling point

of water at atmospheric pressure) could be obtained. Consequently testing was then carried out at a set point of 110°C when a surface temperature of 90°C was achieved and finally a set point of 125°C. The vessel set point was controlled using the thermocouple built into the vessel band heater and the circulation heater was controlled by the vessel inlet thermocouple.

Having fixed upon a temperature the vessel pressure was then increased up to a maximum of 2.1 BarA. One sequence of tests was carried out at 135°C and 1.9 BarA however the temperature recorded at the vessel outlet (adjacent to the dew point meter) was higher than the dew point meter's maximum operating temperature so 125°C was chosen as a limiting temperature. The same is true for pressures in excess of 2.1 BarA so higher pressures were not investigated.

10.3 Typical Pinholed Stainless Steel Flowed Gas Drying Data Plots

As with vacuum drying different behaviours were observed depending on the quantity of water in the test piece and different events could be identified. These are discussed below.

10.3.1 First Test of Sequence

Figure 10.1 shows the first test of sequence using a set point of 125°C and a nominal pressure of 1.5 BarA with various regions highlighted.

The most obvious behaviour is the cyclic nature of most of the data streams. This all stems from the behaviour of the circulation heater. The temperature of the circulation heater (CH) is controlled by the vessel inlet temperature. The system starts cold so the circulation heater warms up until the vessel inlet temperature is at the desired set point. Since the vessel inlet is downstream of the circulation heater it takes some time for the vessel inlet to reach the set point as the pipework must warm first. Once it has been reached the heater is cut off but thermal inertia means that the temperature of both the circulation heater and at the vessel inlet continue to rise before cooling. Once the vessel inlet temperature drops below the set point circulation heater starts to heat up again but the vessel inlet continues

to cool slightly before warming again and the cycle repeats. You can see that the vessel inlet temperature is slightly out of phase with the circulation heater as a result of this behaviour as highlighted by line A. This cycling also causes the system pressure to cycle as the gas density varies. Any change in system pressure is echoed by a similar impact on the flow rate. Water concentration also varies as it is impacted by system temperature and pressure. While it is not clear on this scale surface temperature also cycles. This cyclic behaviour is apparent in all tests.

In all tests the water concentration behaviour typically begins at a high level ($\sim$4000 ppm) and then rises rapidly as atmospheric air is drawn through the system from the drying vessel which had been opened, only to be quickly replaced by dry air that had been sitting inside the circulation heater. Details of highlighted regions B-G are discussed below.

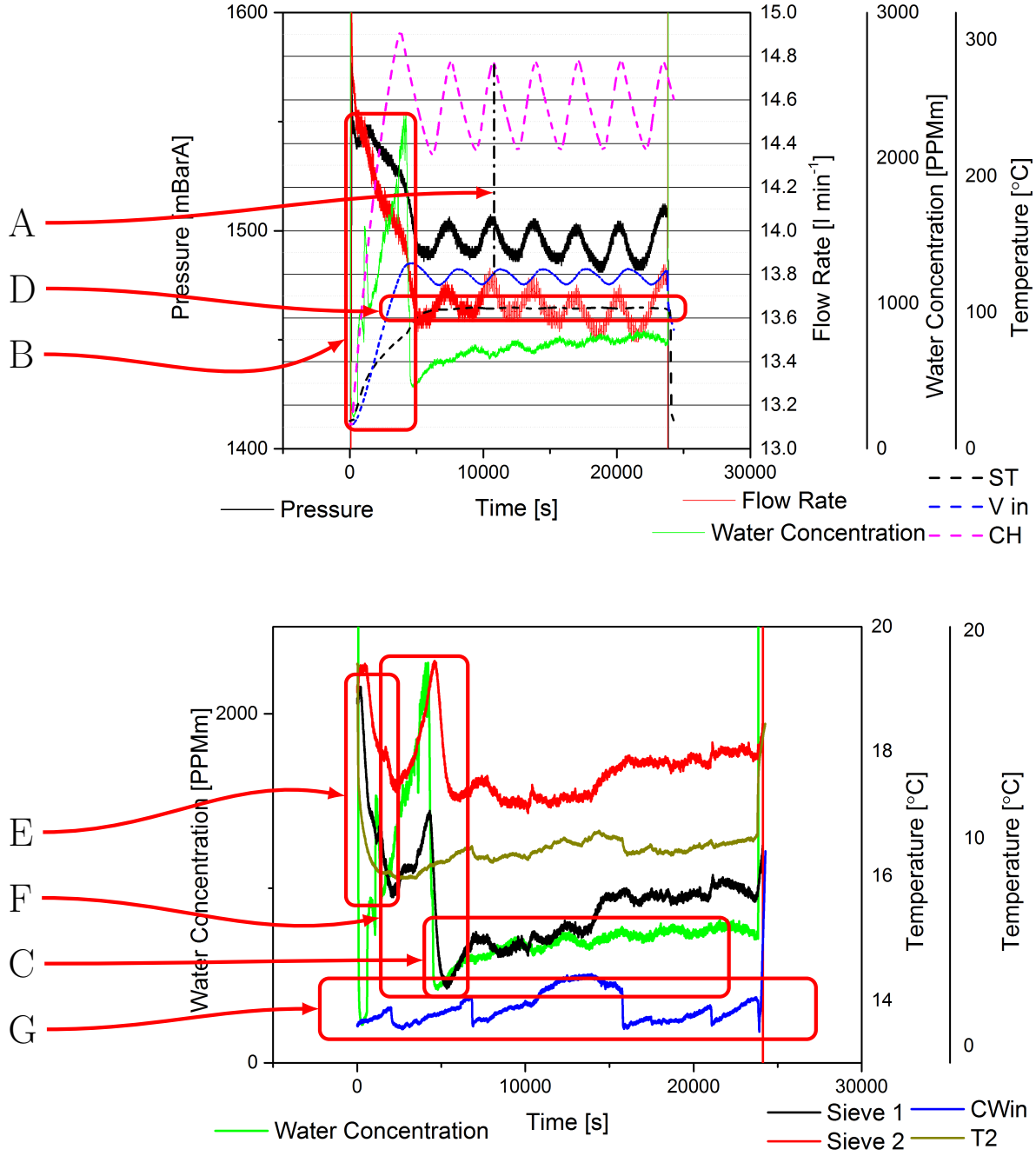

Figure 10.1: Flowed gas drying sequence 1 areas of interest. Expanded scale views are shown below.

Region B In region B (fig. 10.2) the pressure (and flow rate) drops. The water concentration initially drops as the cooling water begins cooling the system and then begins to rise as do the first and second sieve thermocouples. The fact that the pressure drops suggests that something is being removed from the system possibly water since the rise in sieve 1/2 shows that the molecular sieve is functioning. This is surprising behaviour since the regulator should maintain the pressure but it is possible that the pressure drop is too low for the single stage regulator to detect.

The concentration of water spikes during the first ∼5000 s suggesting that water is entering the system. In the test shown this occurs twice, firstly at around 1500 ppm after 1100 s and then at 2300 ppm after 4200s and these spikes are accompanied by shoulders in the pressure plot and also the surface temperature plot.

This would seem to indicate that there is a large initial loss of water from inside the test piece. The belief is that as the test piece and water inside is warmed it is forced out of the pinhole and is then boiled away as it comes into contact with the hot vessel walls.

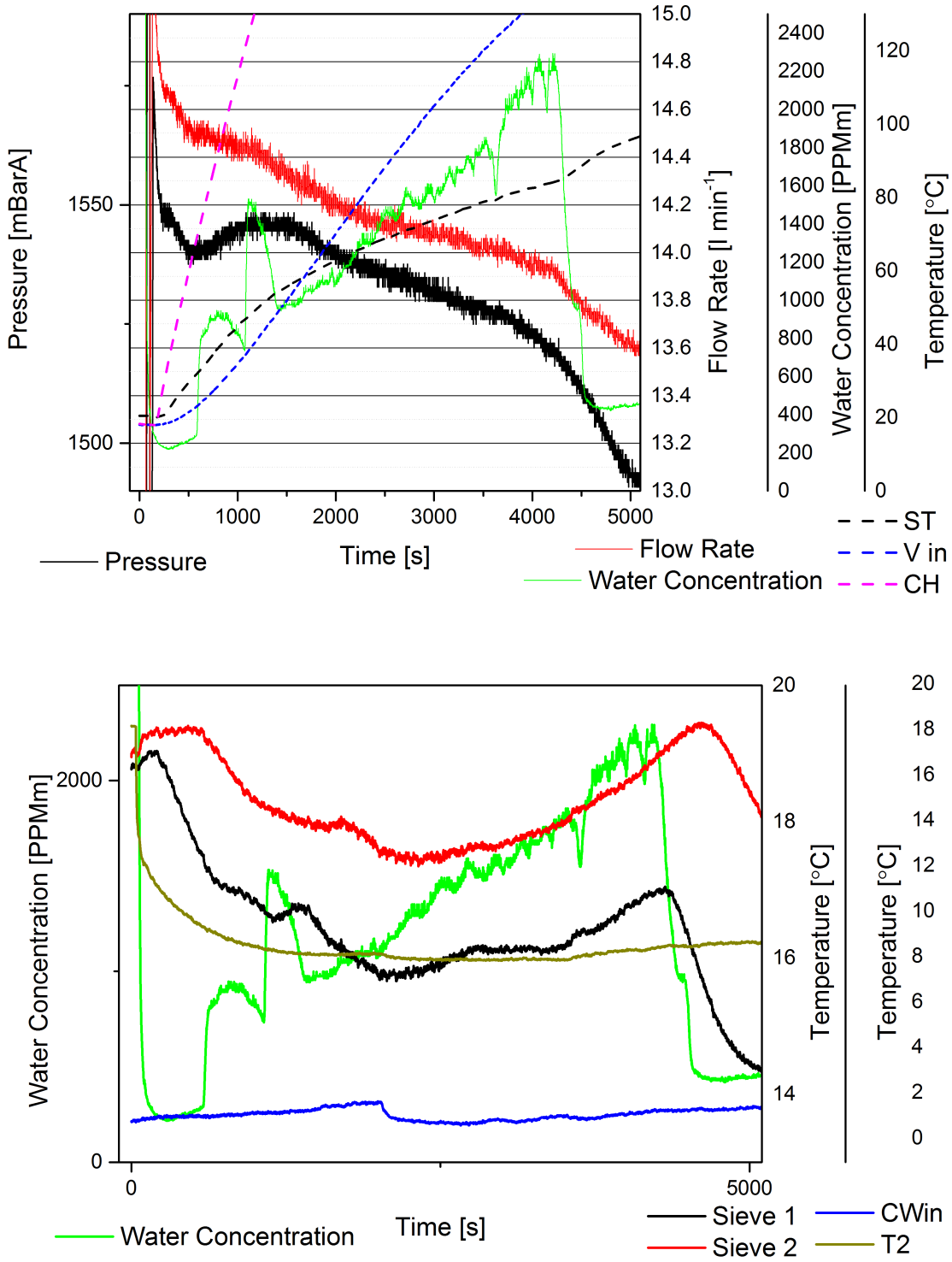

Figure 10.2: Expanded scale view of flowed gas drying region B.

Region C From ∼5000 s (fig. 10.3) the water concentration drops to close to 400 ppm as the last of the water is removed from the test piece and then levels out a little higher at ∼700 ppm.

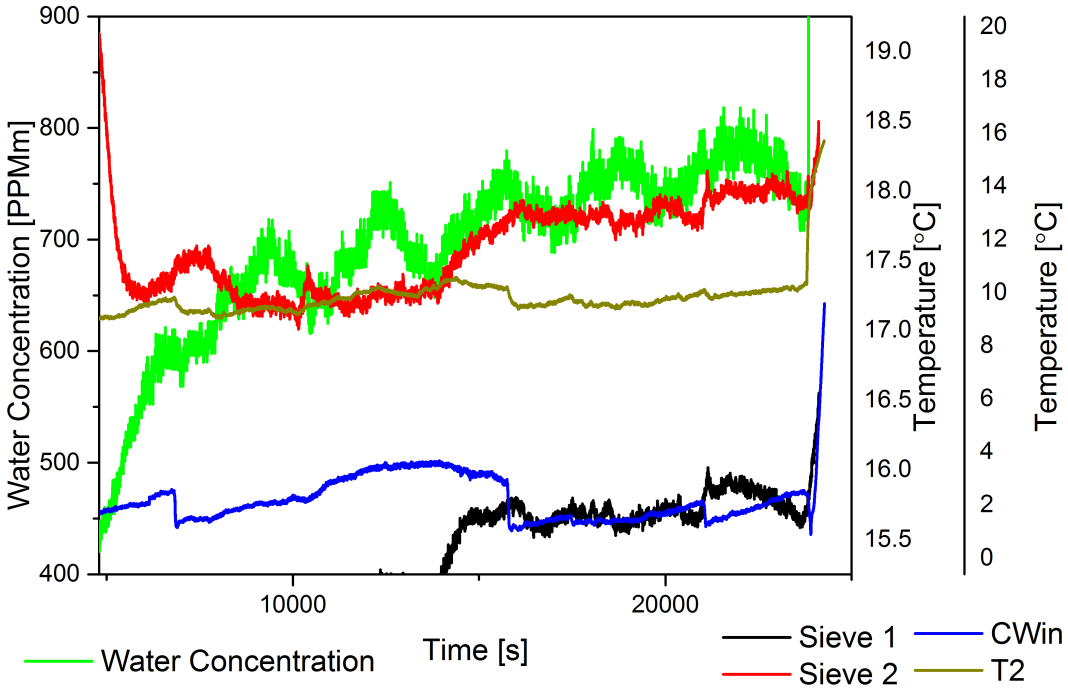

Figure 10.3: Expanded scale view of flowed gas drying region C.

Region D In region D (fig. 10.4) surface temperature levels off at ∼103°C which is cooler than the boiling point at this pressure (∼111°C). This would suggest that the water inside the test piece is unlikely to be boiling so any water loss from inside the test piece is due to evaporation.

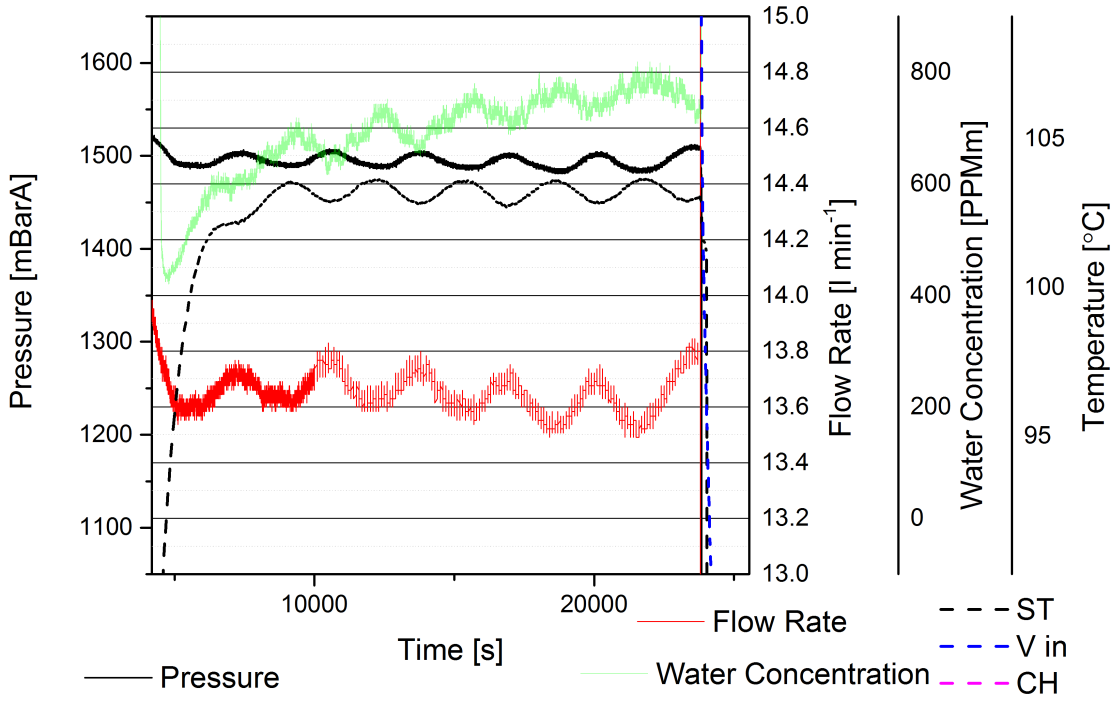

Figure 10.4: Expanded scale view of flowed gas drying region D.

Region E Over the first 2000 s T2 (the temperature midway between the condenser and sieve), sieve 1 and sieve 2 drop as the condenser upstream cools and cooler air is brought through the system.

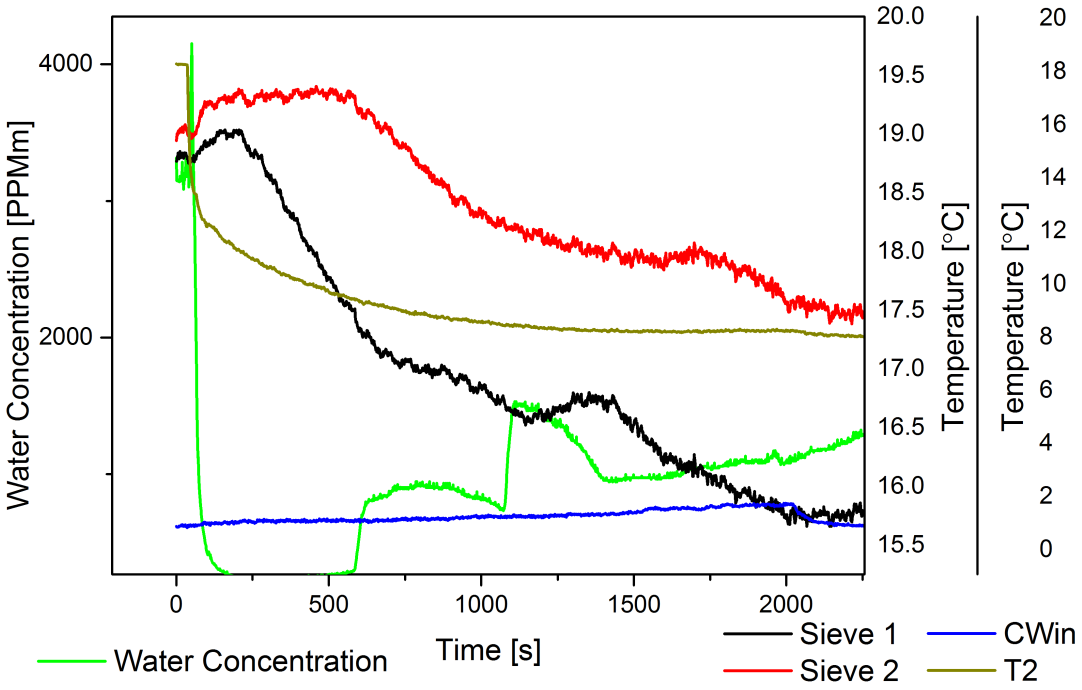

Figure 10.5: Expanded scale view of flowed gas drying region E.

Region F After 2000 s T2 begins to level out however sieve 1 and sieve 2 begin to rise peaking shortly after the water concentration is at its highest before dropping substantially as the water concentration drops. There is a lag in the peaks in sieve 1 and sieve 2 as a the sieve column warms from sieve 1 forward. Also the increase in sieve 1 temperature between its initial trough and peak is ∼1.2°C compared to ∼2°C at sieve 2 presumably because the higher temperature at sieve 1 influences sieve 2 as well as the exothermic adsorption of water.

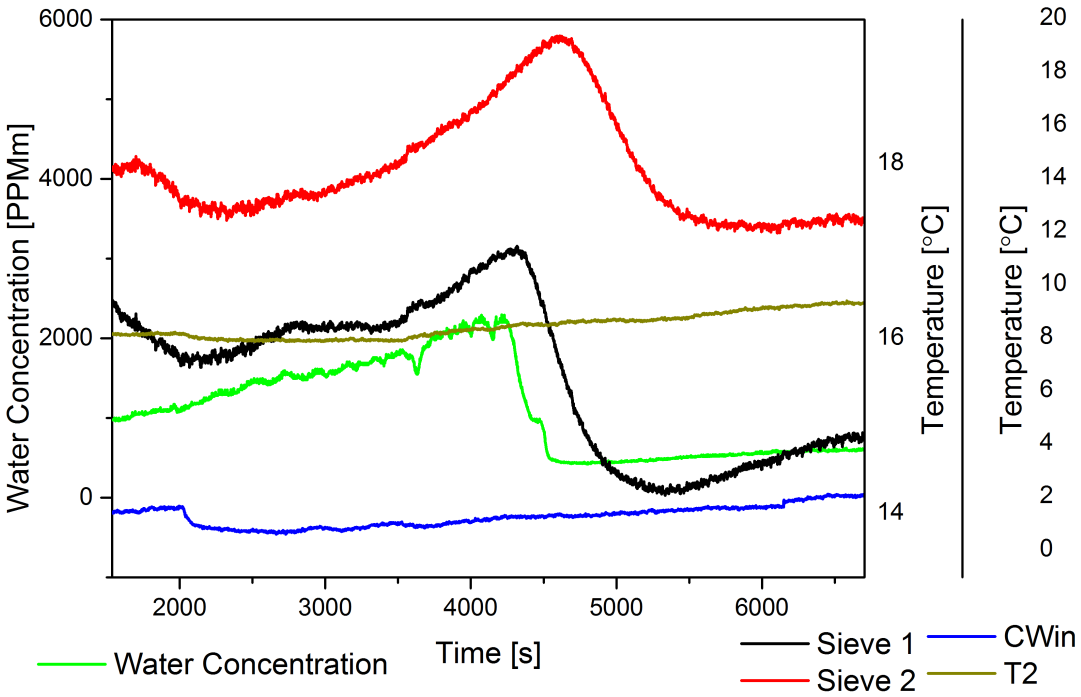

Figure 10.6: Expanded scale view of flowed gas drying region F.

Region G The cooling water plot shows several sharp drops (fig. 10.7). These are the result of the ice being replenished. These drops can be seen to have an impact on T2. Strangely sieve 1/2 appear to rise slightly at these points suggesting that more water vapour is now entering the sieve. Intuitively one would expect cooler water in the condenser to condense out more water thus leading to less water vapour reaching the sieve and cooler air being detected as seen at T2, and also cooler gas to be passing through. The reason for this is not known.

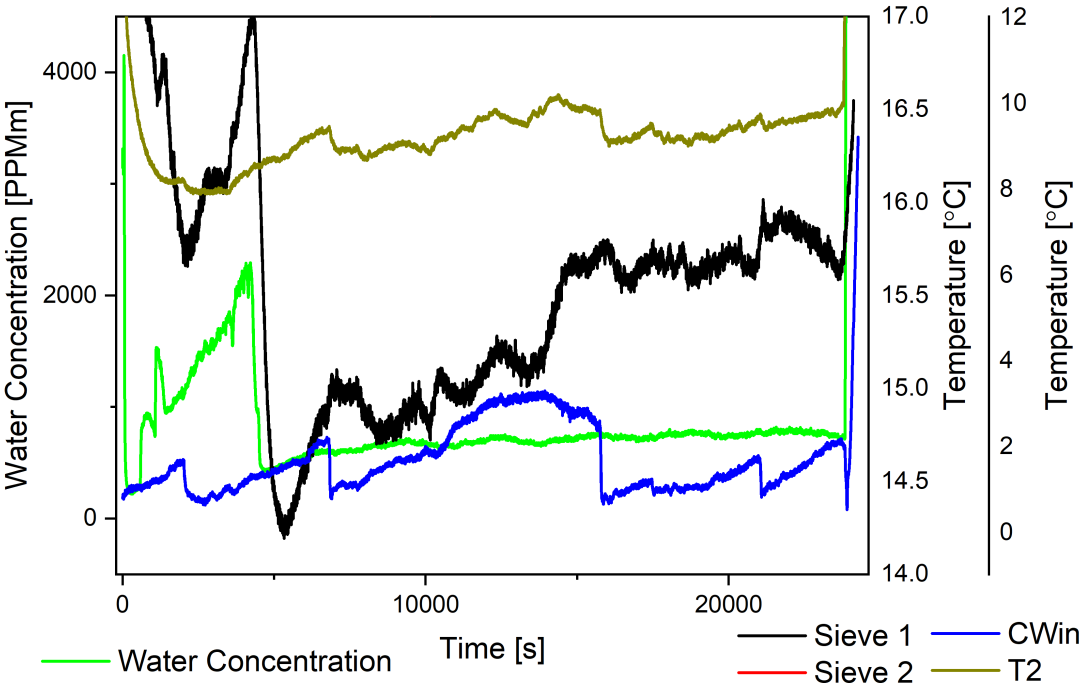

Figure 10.7: Expanded scale view of flowed gas drying region G.

10.3.2 Mid Sequence Tests

The temperature behaviours of the mid sequence tests is generally the same as for the first test of a sequence however there are no obvious shoulders. The pressure behaviour is also generally similar with a cyclic nature following the circulation heater (not shown but can be inferred from the vessel inlet temperature) and with a drop in pressure over the first 5000 s. There are however, seemingly random

jumps in pressure over the following 15,000 s. This occurs for most mid sequence tests and it is not clear what causes this behaviour.

Following the initial crash in water concentration mid sequence tests typically show a steady rise water concentration which levels off around 700 ppm several thousand seconds after surface temperature levels out and remains like this until the end of the test.

There are no apparent shoulders in the surface temperature plot which may be indicative of drying behaviour. The peaks observed in sieve 1/2 which matched the peaks in water concentration in the first test of the sequence are now not observed confirming that sieve 1 and sieve 2 are reacting to water vapour. Once again replenishing the ice in the cooling water appear to lead an increase in sieve 1/2.

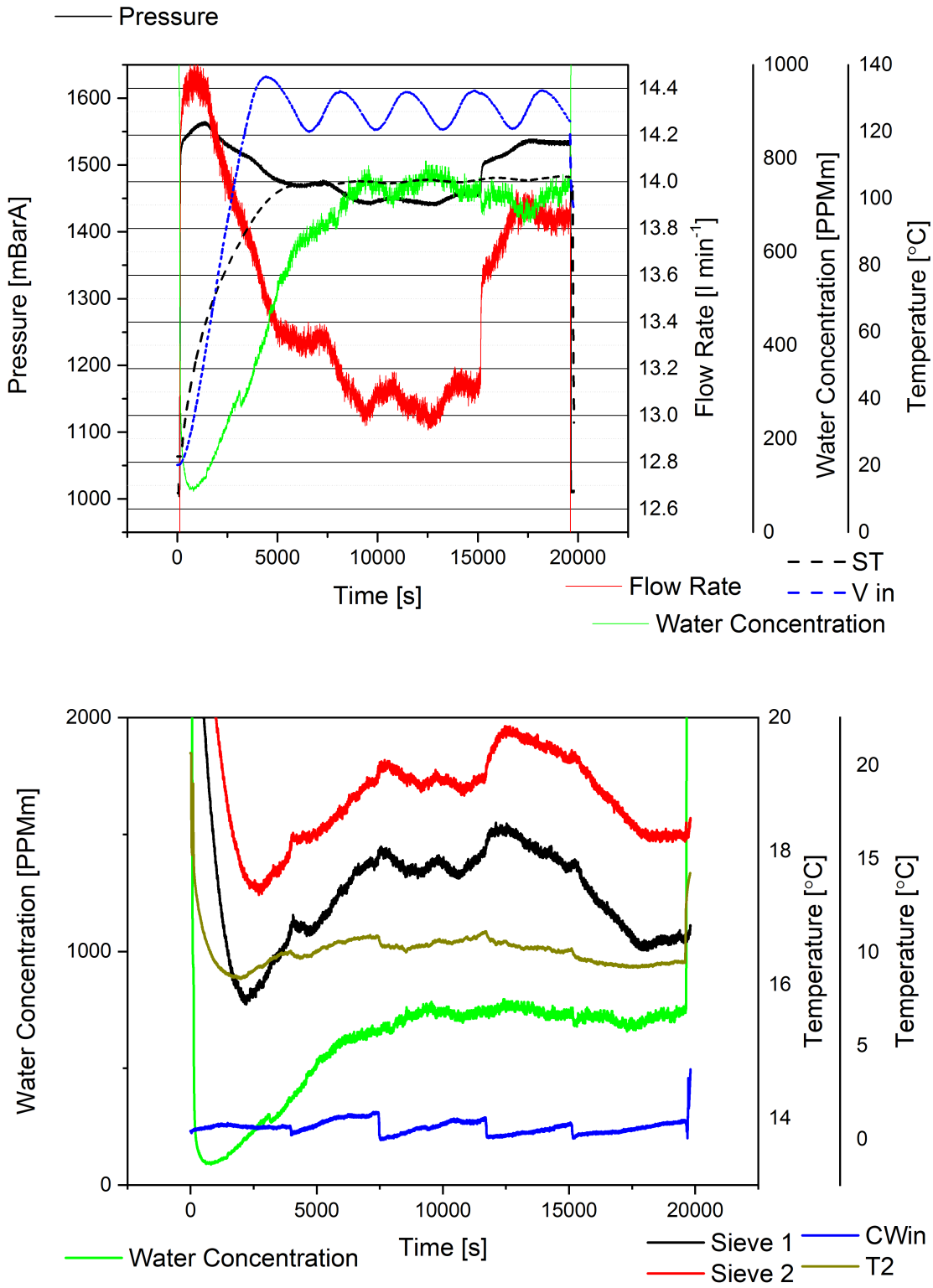

Figure 10.8: Typical data plot for a mid sequence flowed gas drying test.

10.3.3 Final Test of Sequence

The starting behaviour of the final test of a sequence is generally the same as the mid sequence tests. The major difference is a clear drop in water concentration at 18,500 s. This is presumed to be due to the last of the water being evaporated from the test piece. This is also accompanied by a drop in sieve 1/2 although this is partially obscured by the temperature increase as a result of the ice being replenished.

10.3.4 Summary

The data plots above show typical behaviour of the system during flowed gas drying. When vacuum drying it was possible to detect spikes of water vapour with increases in flow and pressure but also fluctuations in temperature at the condenser. In the plots above the flow rate and pressure provided no information as to the drying behaviour of the test piece. It was however possible to pick up changes in the water concentration with the dew point meter and also perhaps more interestingly the temperature changes in the molecular sieve. This could potentially provide another method for measuring the presence of water vapour.

It was interesting to note that when the ice in the cooling water was replenished the temperature of the molecular sieve seemed to spike suggesting an increase in the water content of the gas passing through. This is, as described above, somewhat counter intuitive.

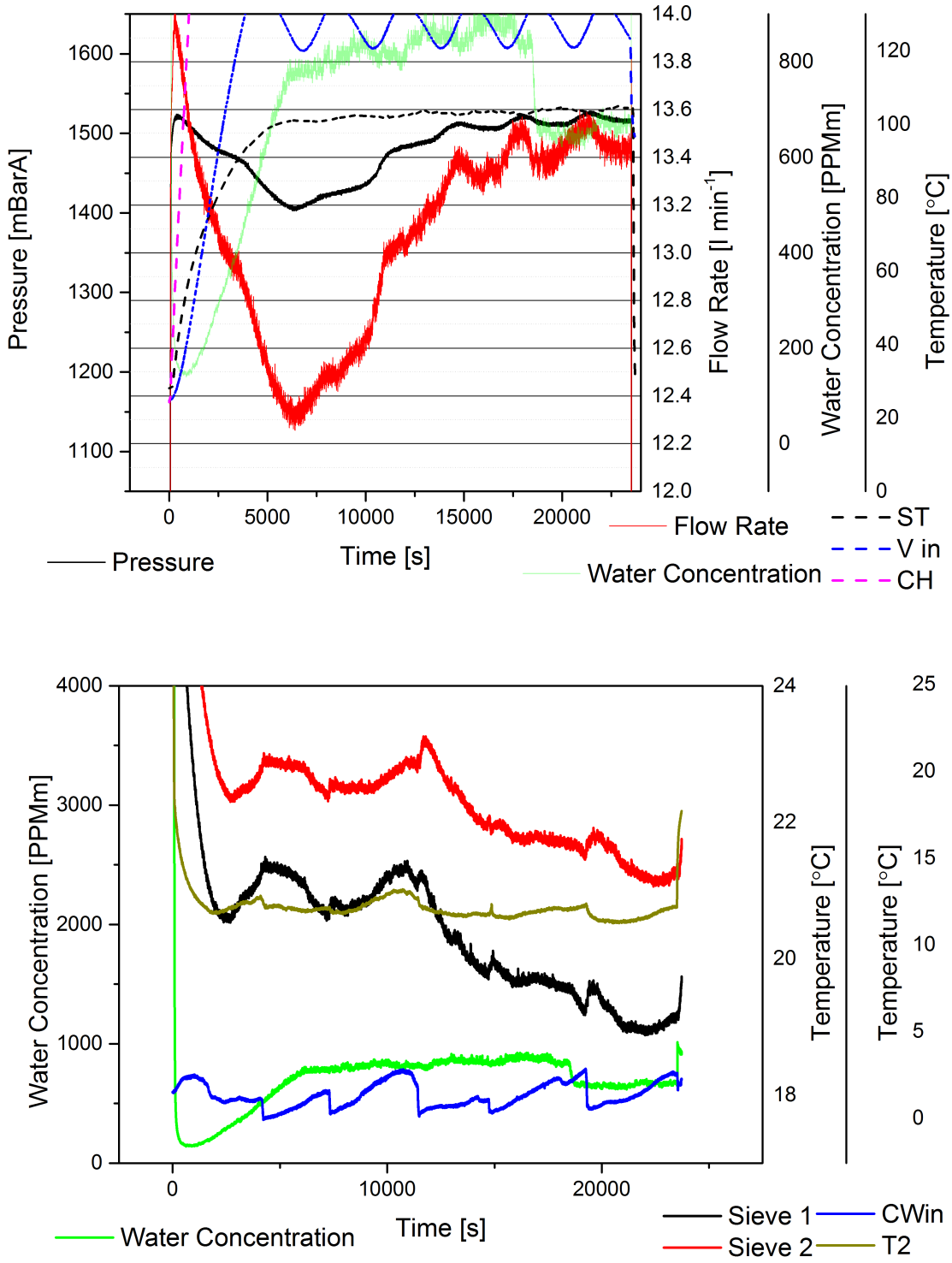

Figure 10.9: Typical data plot for a the final test of a flowed gas drying sequence.

10.4 Overall Pinholed Stainless Steel Flowed Gas Drying Results

For the following figures each data point is a single test. Figure 10.10 shows how the drying rate changes as the mass of water within the test piece changes. The six different pressures used have been roughly grouped into 1-1.2 BarA tests, 1.35-1.5 BarA tests and 1.9-2.1 BarA tests. The set of tests carried out at a higher temperature is also shown. The behaviour is much the same as for the vacuum drying tests with a greater mass of water giving a higher drying rate. For the first test of a sequence the drying rate is typically 0.11-0.19 mg s^{-1} (0.22 mg s^{-1} at 135°C). For tests beginning with 4.4-1.1 g of water the drying rate is between 0.06 and 0.09 mg s^{-1} and at lower masses even lower rates were found but these are the tests in which the test piece dried out so only a portion of the test was active drying time.

In all of these tests there is evidence of a high initial water concentration which drops off suggesting that there is an initial loss of water from within the test piece, however, this does not occur immediately once the test begins but after several thousand seconds. As the test piece is warmed from room temperature at the beginning of the test the water slowly heats up and it is presumed it begins to evaporate leading to a pressure increase inside the test piece which forces a slug of water to be ejected. This then comes into contact with the hot vessel walls and is able to boil away. It would seem unlikely that the water inside the test piece itself is boiling since at the time of these spikes the surface temperature has not yet reached its maximum, and even once the maximum is reached it is below boiling point in the majority of cases. For later tests of the sequence the water level is below the pinhole so slugs of water can not be ejected.

The single sequence carried out at 135°C appears to have the highest rate at all starting masses. For the 125°C tests the 2.1-1.9 BarA tests generally show the highest drying rate while 1-1.2 and 1.35-1.5 BarA tests show a slightly lower rate despite being at a lower pressure and therefore a lower boiling point. This is presumed to be due to the enthalpy of evaporation which reduces as pressure increases. This means that even though it is more difficult to make the water boil it is easier for evaporation to take place.

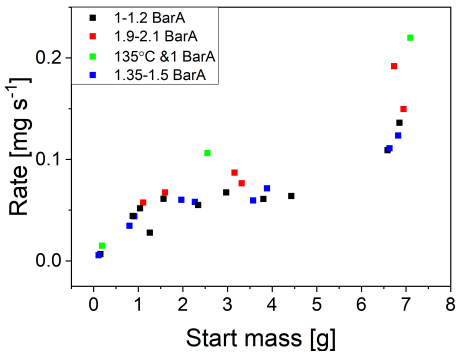

Figure 10.10: Starting mass of water and drying rates for flowed gas drying drying tests at different pressures (and temperatures).

What is interesting to note is the maximum surface temperature observed for the tests conducted. Figure 10.11 shows that only one set of conditions (125°C and 1 BarA), those with the lowest boiling point, led to the surface temperature of the test piece reaching the boiling point of water at the test pressure. This set of conditions did not however yield the highest drying rate seeming to confirm that reaching the boiling point alone is not the critical factor. In fact increasing the pressure and thus allowing higher temperatures to be achieved seemed to lead to higher drying rates.

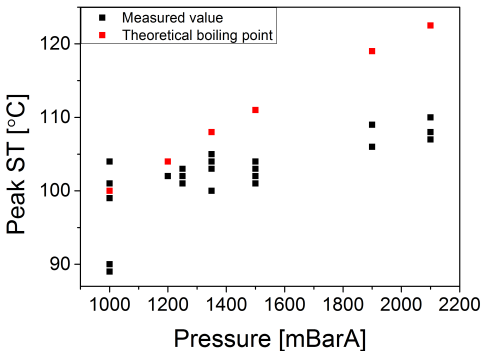

Figure 10.11: Peak surface temperature and pressure.

Not only did the higher pressures lead to higher drying rates but they also lead to much faster heating of the system. Figure 10.12 shows the time taken to reach

the peak surface temperature. The higher pressure tests consistently show that the higher the pressure the sooner the peak surface temperature is reached. This is what one would expect since the denser gas is a more effective heat transfer fluid. This in itself may explain why higher pressures lead to higher drying rates.

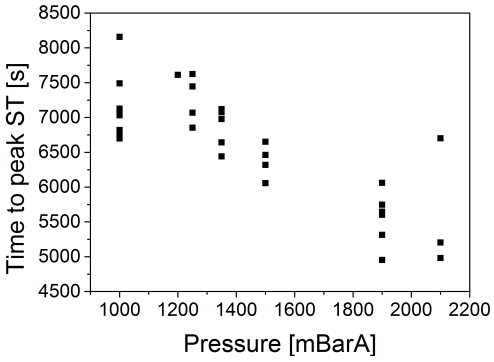

Figure 10.12: Time taken to reach peak surface temperature.

There is single outlying point in fig. 10.12 which is for the first test of the 2.1 BarA sequence. This test shows some unusual behaviour during the initial heating with surface temperature showing clear drops during the ramp phase rather than just shoulders seen in other similar plots which it is thought may play a role in the unusual time to peak surface temperature.

Figure 10.13 shows the approximate water concentration recorded in the final test of a sequence once the last water has been removed. There is no apparent relationship between the test pressure and the final concentration of water detected.

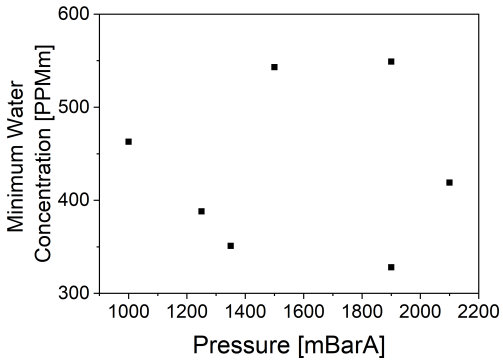

Figure 10.13: Relationship between pressure and final water concentration.

10.5 Typical Cracked Stainless Steel Flowed Gas Drying Data Plots

A small number of flowed gas drying drying tests were carried out using the cracked stainless steel (CSS) test piece at 1 BarA and 125°C. Once again this lead to different regimes throughout the sequence. In all tests the cyclic nature of the heater temperatures, pressure and flow are identical to that seen in the pinholed stainless steel tests.

10.5.1 First Test of Sequence

The first test of a sequence with the cracked stainless steel test piece is shown in fig. 10.17 and is similar to that for the pinholed stainless steel test piece. The water concentration begins high and then drops. There are then multiple peaks in water concentration which are believed to be water being ejected from the test piece. These peaks are accompanied by fluctuations in sieve temperature (sieve 1 and 2) as seen for the pinholed stainless steel test piece. These peaks also seem to impact surface temperature. The major difference is that these peaks seem to continue for longer. This may indicate that the defect was lower down allowing more water to be ejected. This seems to be confirmed from the overall drying rate from this test which was 0.15 mg s^{-1} compared to 0.11 mg s^{-1} for the pinholed

stainless steel test piece at the same conditions suggesting that more water is being ejected.

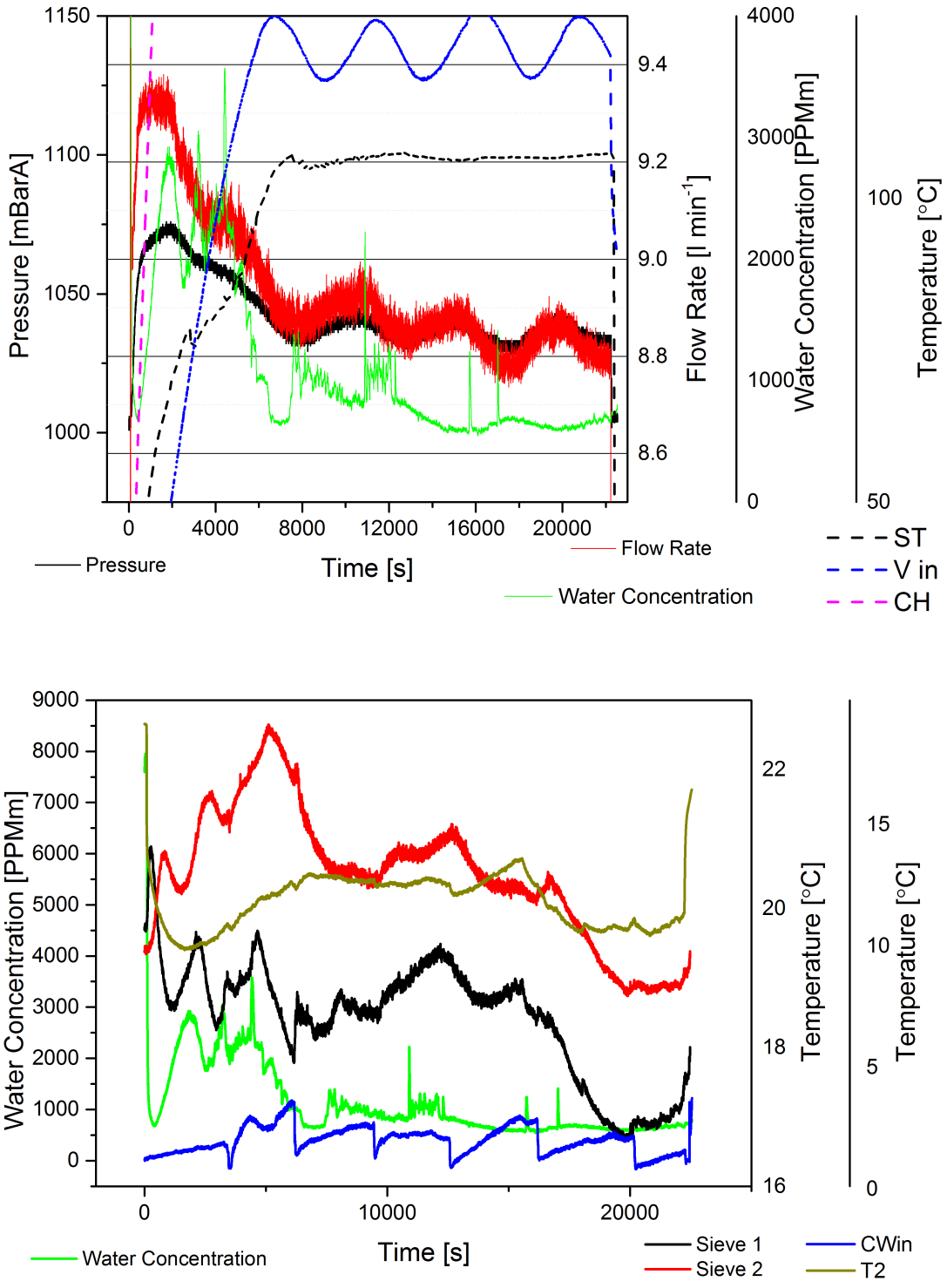

Figure 10.14: Typical data plot for the first test for a cracked stainless steel flowed gas drying Test.

10.5.2 Mid-Sequence Tests

The mid-sequence tests are in general almost identical to those for the pinholed stainless steel test piece in terms of the behaviour of the data plots however the water concentration is in the region of 300 PPMm compared to 600-900 PPMm (parts per million by mass) for the pinholed stainless steel test piece. The overall drying rate was also much lower being around 0.01 mg s^{-1}. There was however a noticeable exception for the seventh test of the sequence which showed clear spikes in water concentration after 14,000 and 23000 s. This is comparable to the vacuum test which showed spikes in pressure and flow indicative of water being ejected from the test piece after a considerable delay.

In some of the later tests (8-11 out of 11) the water concentration drops below the level of detection of the dew point meter (-40°C) and as a result during the first portion of the test (∼4000 s) the water concentration appears to level out at 105 PPMm. The fact that this happens suggests that it is possible to get extremely low water concentration's with this method although they were not observed for the final tests from the cracked stainless steel test piece or indeed the pinholed stainless steel tests. This may however be due to the fact that the test was not run for a sufficient time after the final drops of water were removed or possibly that only completely fresh molecular sieve was capable of achieving these values.

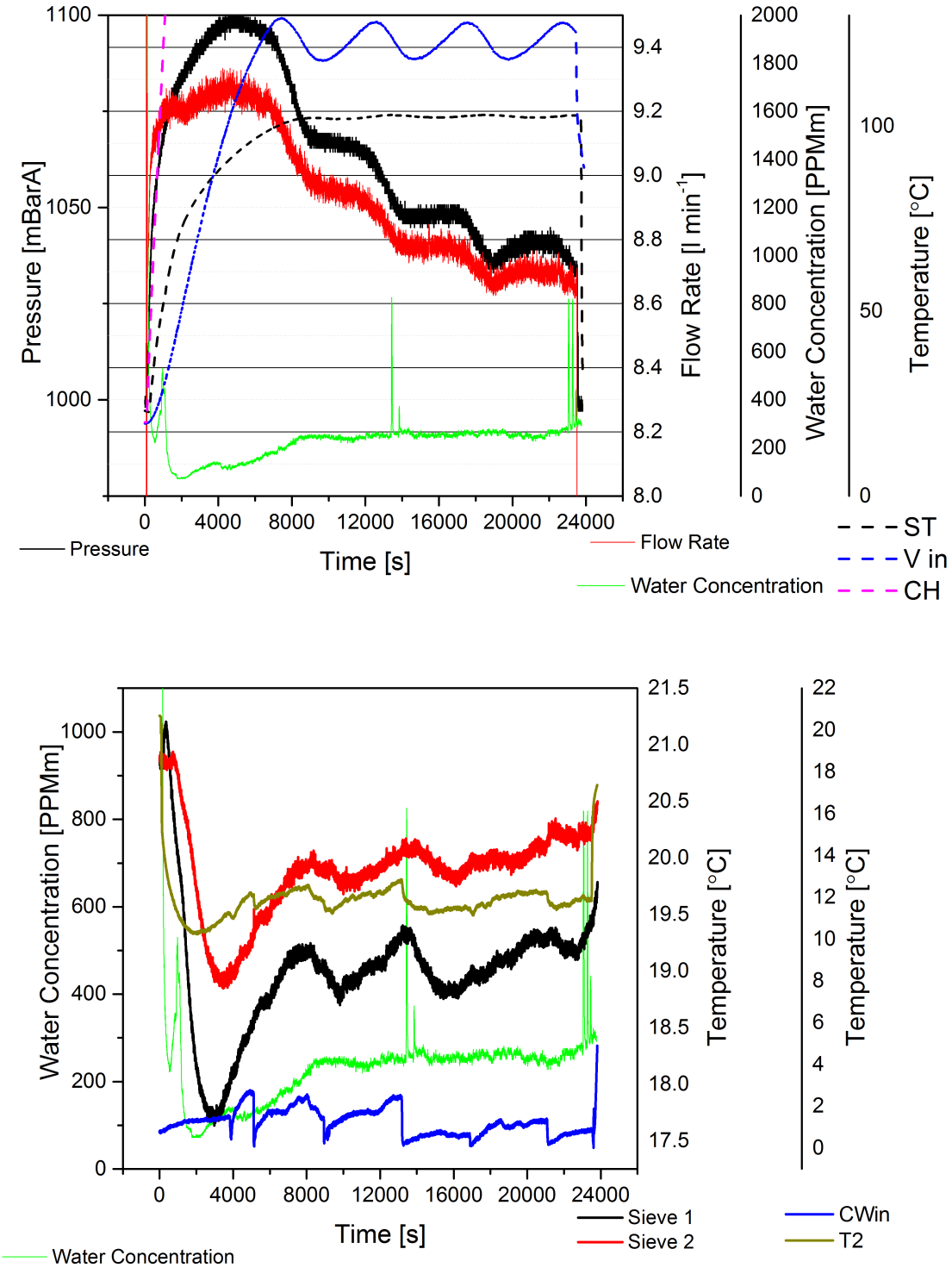

Figure 10.15: Typical data plot for a mid sequence flowed gas drying test for the cracked stainless steel test piece.

10.5.3 Final Test of Sequence

The final test of a cracked stainless steel drying sequence is also almost identical to with the pinholed stainless steel test piece however the water concentration begins below the level of detection as it takes some time for water to begin to be removed. There is a clear drop in water concentration at ∼20k s which is assumed to be the last of the water being removed. There are several spikes in water concentration which are accompanied by increases in sieve 1 and sieve 2 suggesting that water must be coming off at these points at a greater rate but it is by no means clear why.

10.5.4 Overall Cracked Stainless Steel Test Piece Drying

Figure 10.16 shows the drying rates for different starting masses of water with the cracked stainless steel test piece. As with the pinholed stainless steel test piece when less than 4 g of water is in the test piece the drying rate is almost constant. Above this the drying rate seems to reduce as the quantity of water reduces. This is thought to be due to the fact that the position of the defect and the water level within the test piece is critical. Any water above the level of the defect is ejected as liquid and quickly boils away giving a higher drying rate thus a slight increase in the starting mass has a relatively large impact. Once the water is below the defect point water loss is by evaporation only. Since this is primarily controlled by the free surface area which does not change in a cylinder the drying rate remains constant.

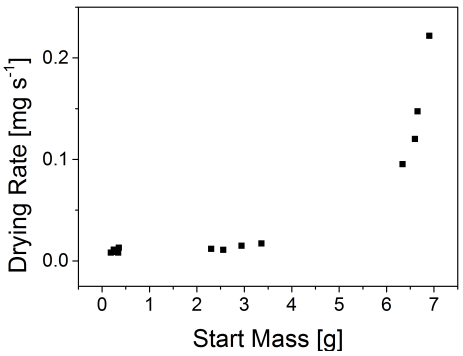

Figure 10.16: Drying rates for the cracked stainless steel test piece. Each data point is a single test.

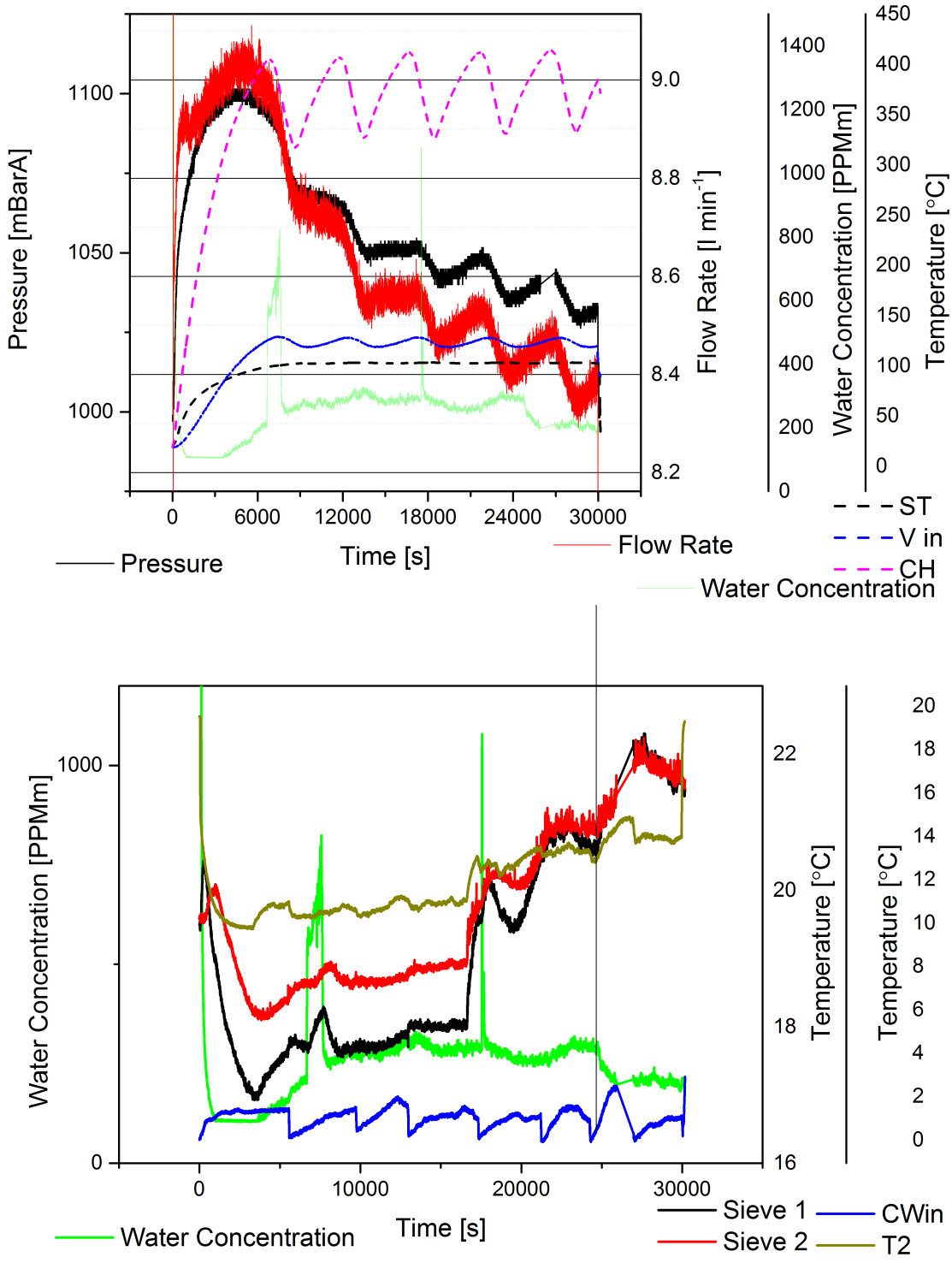

Figure 10.17: Typical data plot for a mid sequence flowed gas drying test for the cracked stainless steel test piece.

10.6 Impact of Drying Gas

An attempt was made to carry out a sequence of tests using argon gas in the system instead of air. Since the tests were begun from room temperature and the tests were considerably longer than those conducted in chapter 7 the gas flushes were not expected to have any detrimental impact on the results obtained. During the course of this test the circulation heater tripped out a number of times. It was established that this was due to the circulation heater's high level trip being reached something that had not occurred when testing with air.

This is thought to have been due to the specific heat capacity of argon gas which is 0.52 kJ Kg^{-1} K^{-1}, roughly half that of air at 1.01 kJ Kg^{-1} K^{-1}[123]. As a result of this the vessel outlet thermocouple heats too slowly for the set point to be obtained before the circulation heater reaches its high level temperature. While it would have been possible to increase the high level trip temperature it was decided that this was not worthwhile and further argon tests were abandoned. Since the purpose of this work was to establish the effectiveness of other gases it was concluded that since the effectiveness of a method seems to be based primarily upon its ability to heat the sample the effectiveness of a gas is likely to be based on its heat capacity. Assuming this to be the case helium (5.19 kJ Kg^{-1} K^{-1}) is likely to be just about the only common non-explosive/combustible gas which will show any improved efficiency.

10.7 Flowed Gas Drying Conclusions

A number of flowed gas drying tests have been carried out using the improved drying rig. The conditions of mid sequence tests for the pinholed stainless steel test piece are broadly comparable to the tests carried out in the initial testing in chapter 7 with roughly the same quantity of starting water but a slightly lower temperature. It was found that the tests with the improved rig gave a drying rate of 0.06-0.09 mg s^{-1} compared to 0.03 mg s^{-1} for the initial tests (at 150°C). Comparison of the data plots shows that the most obvious difference is the surface temperature of the test piece which is considerably higher in the initial testing that the later testing. Since the flow rate from the initial testing was in the region

of $\sim$6 l min^{-1} compared to $\sim$9 l min^{-1} for the later tests the suggestion is that the main driving force for the heating of the test piece is conduction from the vessel walls rather than forced convection since the vessel inlet temperature in the initial tests was considerably lower than that in the second phase testing yet the flow and drying rate were both higher.

For the first test of a sequence there was found to be no significant difference in the drying rates for the two test pieces. The behaviour of the data plots suggests that in this test liquid water is being forced through the defect presumably due to a build up of pressure as the test piece is heated. It would seem that the defect size has little impact on this since the cracks are geometrically much smaller yet appear to give at least equal drying rate. It may however be that since cracks are likely to run the length of the test piece that allows water to be ejected for longer although conversely, one may have thought that this would have allowed any vapour formed to escape rather than build up inside the test piece. Whatever the reason this seems to be short lived.

For the later tests of a sequence the drying rate for the cracked stainless steel test piece was found to be substantially lower than for the pinholed stainless steel test piece. During this period, regime 3 drying is taking place where water vapour is being removed through the defect rather than slugs of liquid water. The low rate suggests that the size of the cracks are such that the rate at at which water is able to pass along them is much less than the rate at which it can pass through the pinhole. This does however raise the question as to why liquid water is able to escape when vapour can not. The most likely explanation is that the pressure increase inside the test piece causes the cracks to widen thus allowing water to escape but there is no evidence to confirm this.

Chapter 11

End Point Determination

The standard test to confirm that a package of spent nuclear has been dried sufficiently for interim dry storage is a pressure rebound test. This normally requires the container to be evacuated and then isolated with a pressure of 4 mBarA being maintained for at least 30 minutes. The drying work in the previous chapters has shown that the instrumentation used was able to provide some information regarding the situation within the drying cask and it was queried whether it would be possible to use the online measurements being recorded to accurately predict whether drying has been completed i.e. the end point. This would be of particular benefit for flowed gas drying drying operations as it may remove the need for a rebound test to be carried out altogether. Since no end point has been established for AGR fuel this section will

11.1 Rig Changes

Two changes were made to the rig before the end point testing was carried out. Firstly a significant part of the pipework was removed to remove the number of joints within the system in an attempt to reduce the ultimate vacuum within the system. This did however have little effect. Secondly the flow meter was re-ranged to allow it detect flow rates as low as 0.003365 l min^{-1} (of air).

11.2 Vacuum Drying End Point

End point determination testing when vacuum drying was carried out for the pinholed stainless steel test piece, cracked stainless steel test piece and also when the vessel contained both the cracked and pinholed stainless steel test piece.

11.2.1 Methodology

Testing was carried out using the pinholed and cracked stainless steel test pieces used previously. In all cases a small amount of water was added to the test piece. The lid was held in place and the test piece was shaken briefly to wet all surfaces before the water was tipped out and the lid replaced and fully tightened. In the majority of tests this resulted in ∼200 mg of water being left within the test piece. The test piece was then placed within the vessel and drying operations were carried out as described previously. When vacuum drying tests were carried out at 60°C and for flowed gas drying tests were carried out at 125°C and atmospheric pressure. These tests are equivalent to the final tests of a sequence seen in chapter 9 and chapter 10.

The primary measurement of dryness was by way of leak rate. A number of rebound tests were carried out for an empty vessel and it was found that the ultimate vacuum was between 2.4 and 3.2 mBarA. The rebound tests carried out after this found that a leak rate of 1.8-6.3 x 10^{-4} mBar s^{-1} was detected after isolation. All of these test also passed the standard test given in ASTM C-1553 discussed in section 2.2. This matches the value of 4.3 x 10^{-4} mBar s^{-1} seen in fig. 8.3. It was decided that a leak rate of less than 10^{-3} mBar s^{-1} would be deemed as a pass and that no water remained i.e. the end point had been reached. The advantage of this is that it allowed rebound tests to be carried out in tests when the system pressure was not below 4 mBarA at the time of isolation. The test piece was also weighed before and after each test and the final mass could be compared to the dry mass of the test piece.

11.2.2 Pinholed Stainless Steel End Point

Data Plots A typical end point test when vacuum drying is shown in fig. 11.1. As the system is evacuated the pressure drops rapidly, the flow rate shoots up and then drops and the dew point drops and then rises as the system stabilises. Once the system has stabilised the pressure is around 21.6 mBarA, the dew point is around 16°C and the flow rate 0.0158 l min^{-1}. Over the next 500 s there is a slight rise in all three of these plots as the water in the test piece begins to boil away with the pressure reaching 22.8 mBarA, the dew point increasing to 20°C and the flow rate peaking at 0.02 l min^{-1}. These values then begin to slowly decay over the next 500 s. After a total elapsed time of ∼1100 s all three values drop rapidly and this is believed to be the point at which the last of the water is removed from the test piece. In the test shown the pressure levels out at around 3.7 mBarA, the flow rate drops below the level of detection. The time at which the vessel is isolated is indicated with a red dot. At the time of isolation the dew point is at -15°C. The dewpoint rises after isolation since it is outside of the isolated vessel.

Following isolation the leak rate is 4.40 x 10^{-4} mBar s^{-1} which is within the pass region. In this test the pressure after 30 minutes was also found to be less than the 4 mBarA limit. The final mass was found to be 0.8 mg greater than the dry mass. This test is classed as a pass as all three of the measurements were in the pass region.

What is interesting to see is the period between 100 and 1100 s when the three values have levelled out. Clearly the dew point reading was not seen in chapter 9 since the dew point meter was not fitted and the flow meter had not yet been re-ranged for lower flow rates so this region was also not observed. What is interesting however is the pressure reading as this would have been observed had it been present. In the earlier tests the pressure typically dropped directly to less than 10 mBarA with another small drop in the region of 1 mBar and this was presumed to be the last of the water being removed. Now however the pressure routinely levelled out at ∼25 mBarA. The most likely explanation for this is that a significant pressure drop is taking place presumably due to an orifice being introduced to the system. While a small section of pipework was changed for these tests which had slightly smaller bore and more acute bends it is still believed to be much to

large for such a pressure drop to be introduced. Consequently the re-ranging of the flow meter is believed to be behind this however the manufacturers can not explain why this would be the case. Whatever the reason for this change the fact that the change of pressure occurs as the flow rate drops is a clear indication in the reduction in the density of a fluid passing through an orifice and this density change is almost certainly due to the end point being reached. It would seem that re-ranging the flow meter has not only allowed a much lower pressure to be recorded but has also allowed amplified the pressure drop thus making an end point more obvious.

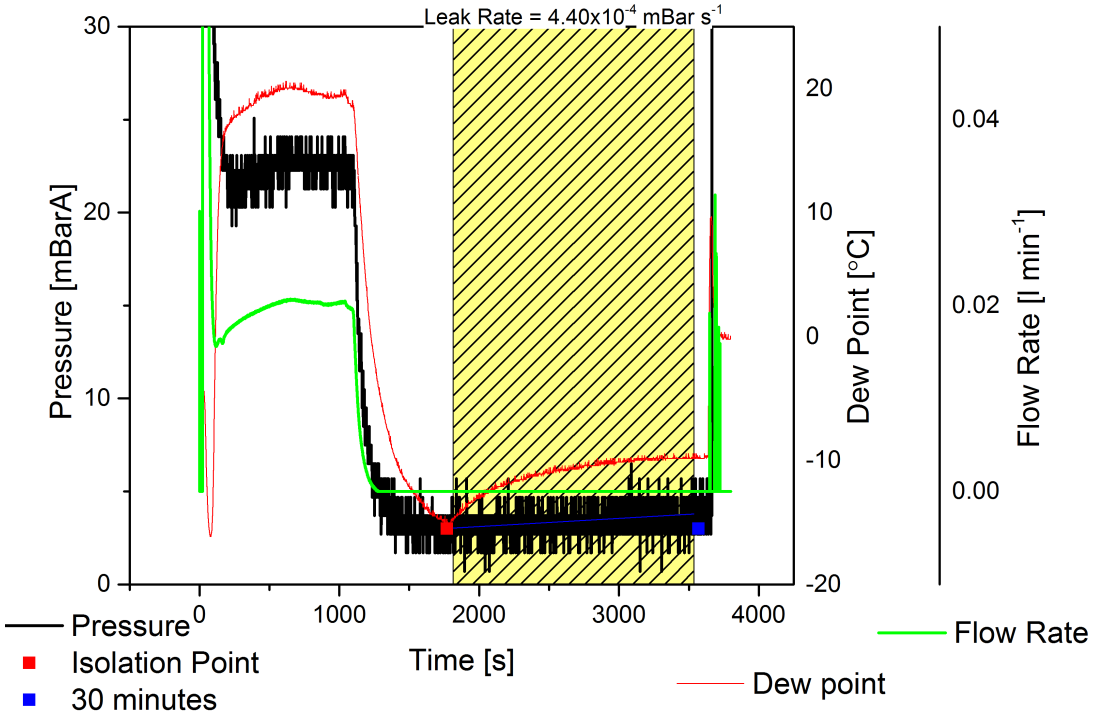

Figure 11.1: Typical end point test.

Having observed that a cliff edge was present a number of tests were carried out to ascertain how close to the cliff edge a test could be isolated and a vacuum rebound test passed. In excess of 30 near identical tests were carried out all of which showed a cliff edge. Of these only four were considered to have failed vacuum rebound tests. Two are shown in fig. 11.2.

One of these shows a test which was cut off when the pressure had reached only 7.2 mBarA (fig. 11.2a) somewhat higher than the ultimate vacuum of the system and at the point of isolation there is still a measurable flow indicating that there is still water being removed. After isolation the pressure rapidly increased to 9.7 mBarA and then levelled out. Based on the correlation between pressure rise and the mass of water introduced to the system seen in fig. 8.4 this pressure rise of 2.5 mBar would equate to less than 2.8 mg of water remaining within vessel. The final mass indicated the test piece to be dry. What this test shows most clearly is that while the cliff edge shows a definite and sudden change taking place there is still some water present within the vessel. This is supported by the non-zero flow rate at the time of isolation.

Figure 11.2b shows another failed test. There is a clear increase in pressure after the vessel was isolated and the test was ended before 30 minutes had elapsed. The final mass of water was found to be ∼8 mg which is considerably higher than in passed tests. What is surprising is the fact that at the time of isolation the pressure had stabilised although this was at 4.6 mBarA somewhat higher than the ultimate vacuum of the system. This was however one of the earlier tests some of which showed an area of stable low pressure before a second reduction in pressure.

The data plots seen in early chapters indicated that the measurement of temperature may give some indications of the end point being reached. This was particularly true of the condenser and sieve 1 thermocouples, however the changes in cooling water temperature sometimes made it difficult to identify a real peak from water vapour from a change in cooling water temperature. Figure 11.3 shows how some of the more interesting thermocouple measurements behave with both room temperature and stirred iced water. The dew point is also shown to indicate the critical parts of a test.

With both room temperature and cool water the sieve 1 value is seen to rise until the cliff edge is reached however when iced cooling water is used it then drops away far more rapidly. The general trend of the condenser plot is not necessarily important but what is apparent is the clear dip that appears when iced water is used as the cliff edge is reached. In both plots there is a similar dip in the vessel outlet reading at this point also.

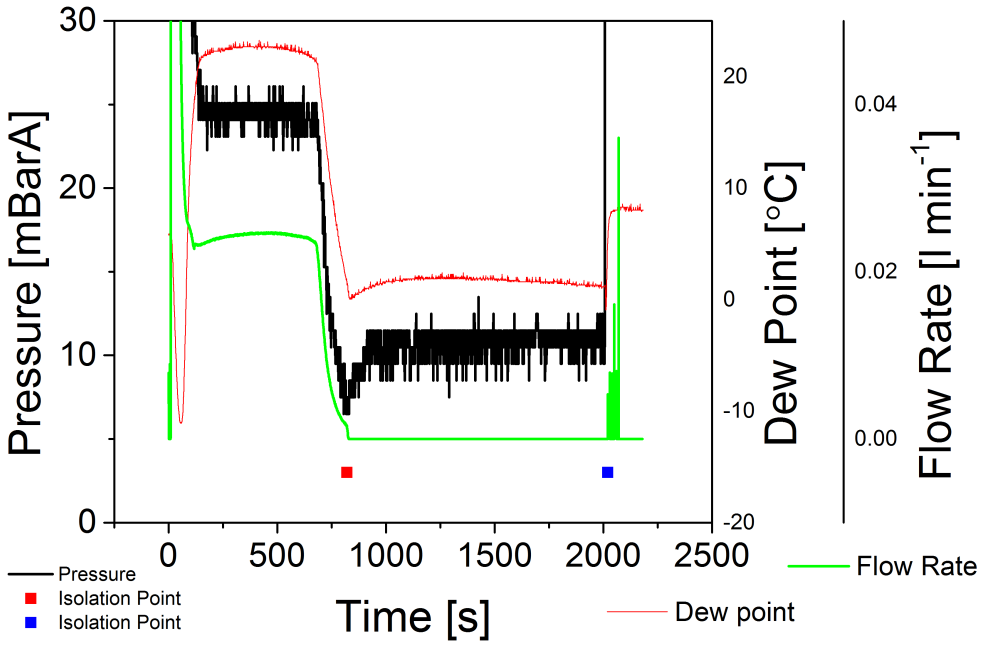

(a)

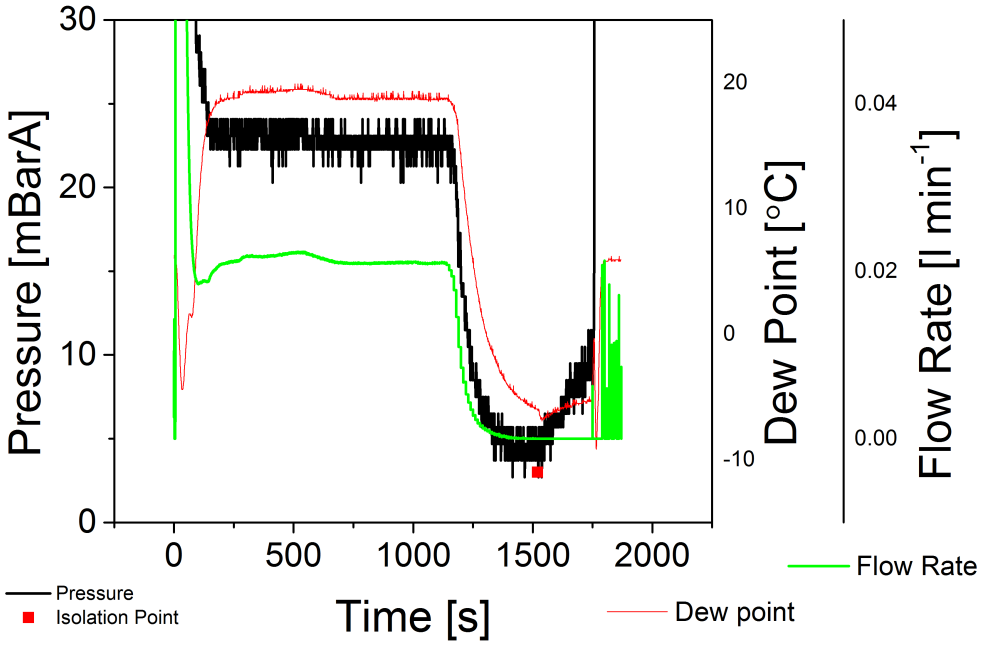

(b)

Figure 11.2: Failed vacuum drying end point tests.

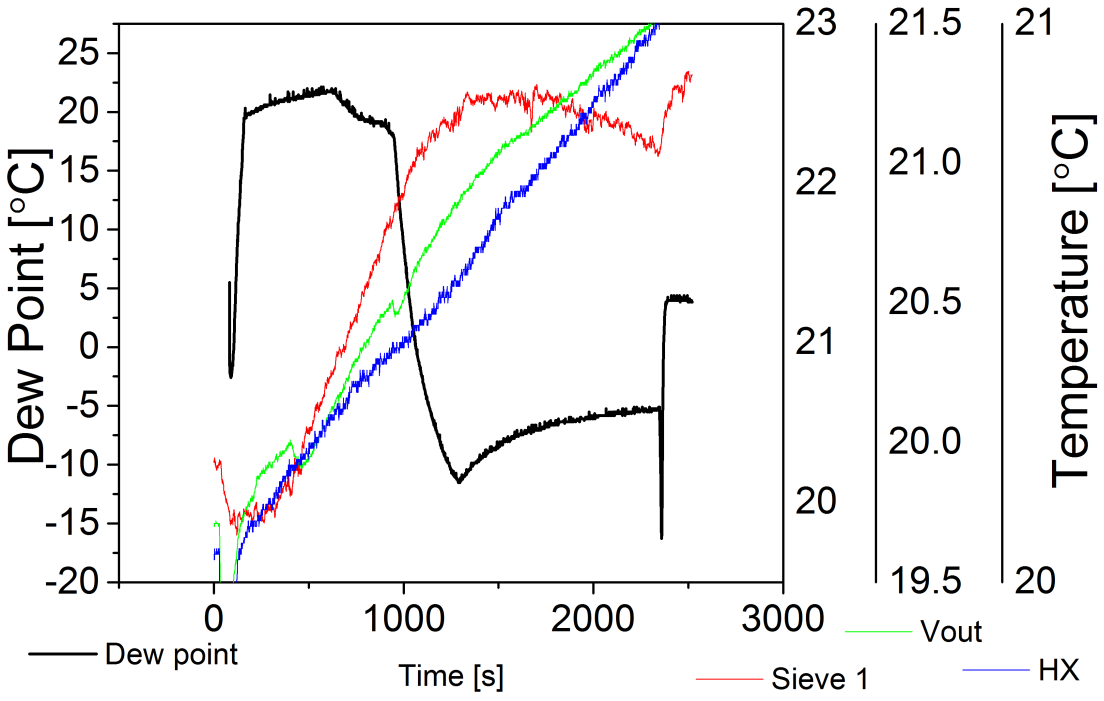

(a) Room temperature cooling water.

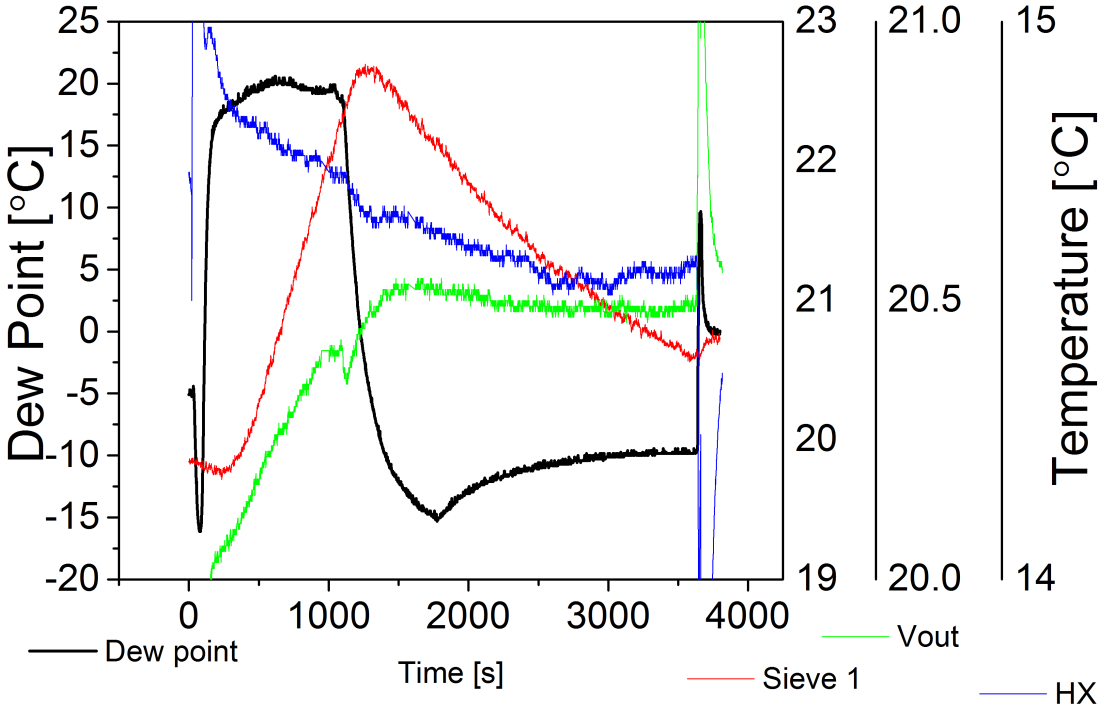

(b) Stirred iced cooling water.

Figure 11.3: Thermocouple behaviour during end point determination tests. Dew point is also shown to indicate the critical parts of a test.

For the majority of tests the system was simply vented at the end however for a small number of tests the vacuum supply to the pipework was turned on and then the vessel isolation valve reopened (fig. 11.4). This leads to a slight rise in pressure since the pipework pressure has increased somewhat but there is also a slight rise in the dew point meter reading indicating that the gas being pulled from the vessel is somewhat wetter than the gas in the pipework suggesting that even for a passed test there is some water vapour within the vessel. The dew point does however remain well below -15°C and there is no detectable flow rate so the quantities of water are minimal. It does however give a clear indication of the sensitivity of the dew point meter.

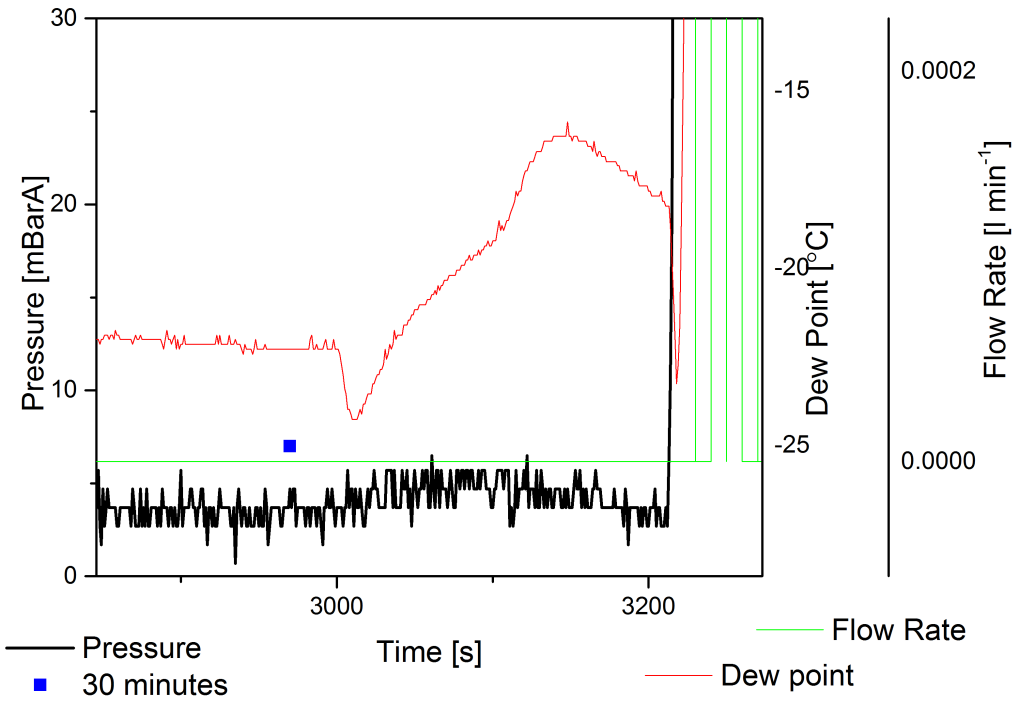

Figure 11.4: Dew point meter behaviour at end of test.

Overall Data and Conclusions The data plots for vacuum drying the pinholed stainless steel test piece all show a clear cliff edge in pressure, flow and dew point which is characteristic of a change in fluid density. In 87% of tests when this

cliff edge was reached the test passed a vacuum rebound test. Figure 11.5 shows graphically the pressure and dew point of all tests at the time of isolation. All tests were isolated at some point after the cliff edge had been reached but necessarily once a stable pressure had been reached. This plot shows that while there is no clear value for either pressure or dew point alone at which a pass is always achieved, in combination a dew point no greater than -10°C and pressure of below 4 mBarA always resulted in a pass being achieved. The cliff edge observed does not in itself guarantee that all water has been removed but it is a very clear early indication that the end point is approaching.

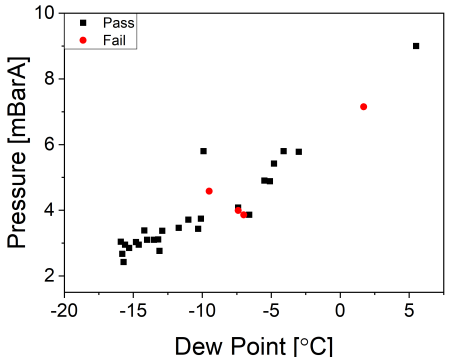

Figure 11.5: Pressure and dew point readings of drying tests. Each data point is a single test.

11.2.3 Cracked Stainless Steel End Point

Data plot A typical data plot for a the end point of a vacuum drying test with the cracked stainless steel test piece is shown in fig. 11.6. In some respects these tests show similarities to the pinholed stainless steel tests with a clear cliff edge in pressure, flow and dew point. The obvious difference is that all values before the cliff edge are significantly lower. This shows that the fluid density is much lower, as the drying rate is much lower, nevertheless the instruments are still able to detect the change. You can see that it takes some time from the start of the test until the flow rate becomes high enough to be detected. The dew point is

consistently lower than with the pinholed stainless steel test piece, being less than 0°C after the vessel has initially been evacuated.

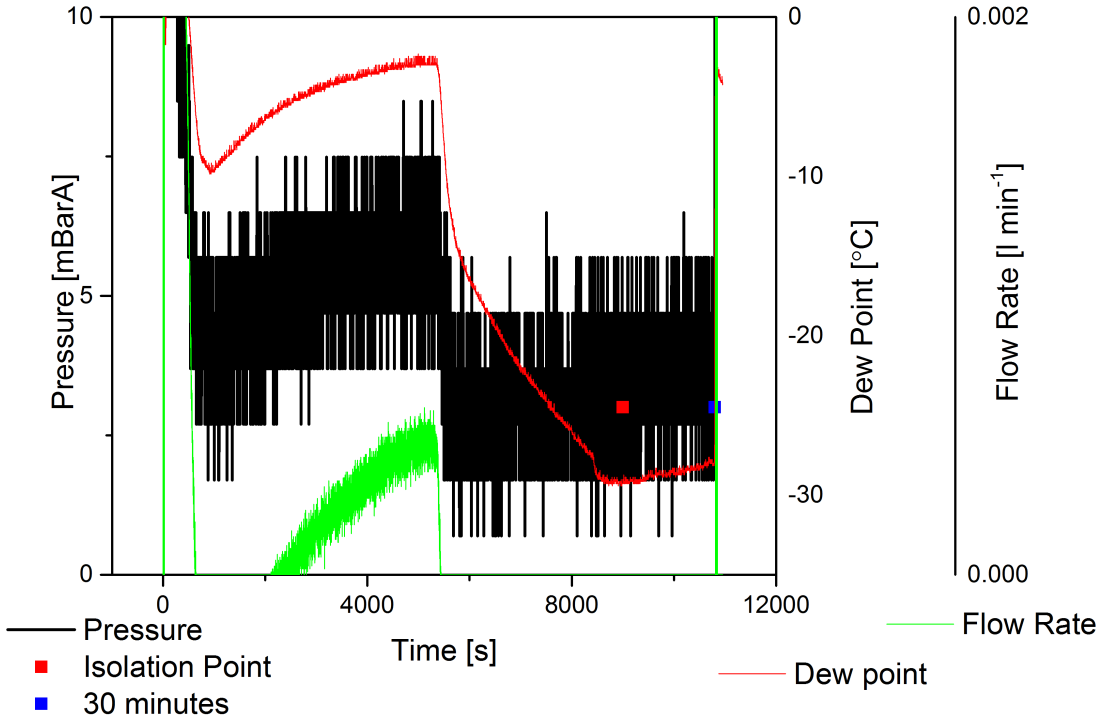

Figure 11.6: Data plot for a cracked stainless steel vacuum drying end point test.

Only five tests were carried out during this phase of testing however of the five the only test to fail was the single test isolated before the cliff edge had been reached.

11.2.4 Multiple Test Pieces

A small number of tests were carried out using both the cracked and pinholed stainless steel test piece in the vessel at the same time and a data plot for one of these is shown in fig. 11.7. The end point behaviours of both the cracked and pinholed stainless steel test piece can be seen with both cliff edges being present. There is however a period after the first cliff edge when the flow rate has briefly reached zero and the pressure is also close to the ultimate vacuum level although

these values all rise as the drying profile of the cracked stainless steel test piece becomes visible.

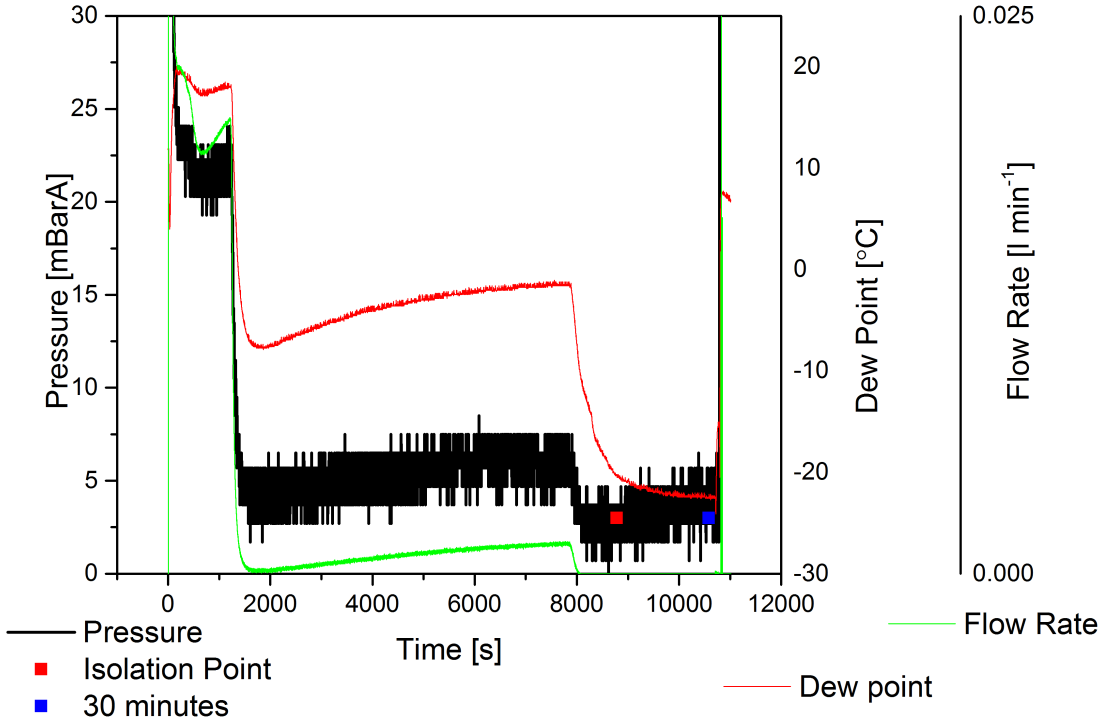

Figure 11.7: Data plot for vacuum drying of a cracked and pinholed stainless steel test piece.

11.2.5 Vacuum Drying Conclusions

The end point tests of both the cracked and pinholed stainless steel test piece have shown clear cliff edge behaviour for the pressure, flow and dew point data. Vacuum rebound tests at the end of these have confirmed that the test piece has been dry on almost all occasions once this cliff has been observed. Detection of a cliff edge alone is not necessarily sufficient and there is however a need to pay attention to the values recorded. The re-ranged flow meter has been shown to detect a flow even when water is being lost at a very low rate through a crack only however the tests have shown that there can be a delay of around 30 minutes from

a test beginning until water loss from such a crack begins. It would seem likely that water loss through the crack is pressure driven and that it takes some time for the pressure to build sufficiently to drive water through the crack. Flow rate alone is not therefore a suitable measure of dryness.

The testing has shown that it is possible to pass a rebound test without reaching the ultimate vacuum of the system, however this has typically been after a cliff edge has been observed and prior knowledge of the system tells one tha this is indicating the end point. Perhaps more importantly it is worth considering that that only two tests have reached a pressure of less than 4 mBar and failed a rebound test, both of which showed a detectable flow rate at the time of isolation which was less than 30 minutes from the start of the test and it would therefore be possible for a flow rate of zero and pressure of below 4 mBarA to be achieved while water is still present. However no test reached 3.8 mBarA or lower and failed a rebound test. What is however unclear is how this behaviour would change if the power of the vacuum pump was increased thus allowing a greater vacuum to be drawn on the vessel despite water being present.

Dew point has been seen to settle at significantly different values depending on the defect size through which drying is being carried out. During pinhole drying tests dew point readings before the end point were typically around 20°C, clearly high enough to indicate that water is present. Following the cliff edge some tests were found to pass a rebound test with a dew point as high as -2°C which is much higher than the minimum value recorded following the first cliff edge when two test pieces were used which was ∼-7°C. However no test appears to have failed once a dew point of less than -10°C has been achieved.

Based on the testing carried out it would seem that an accurate determination of the end point can be indicated by reaching a pressure of less than 3.8 mBarA, however since it is possible for values above this to be passes and that it is possible that a leak in the system could prevent such a level being reached despite dryness being achieved pressure alone can not be recommended as an indicator. Unlike pressure, which will reach an absolute minimum based on the system the testing carried out here has found that dew point will continue to drop as test length is increased (at least to -40°C, the minimum value of the instrument). It would therefore seem likely that dew point alone could be used to determine end point. The

recommendation would however be to use dew point in combination with pressure as pressure seems to be somewhat more indicative of how close to completion a test is and the combination of the two provides an added level of certainty. There would of course be a need to confirm the values required for different systems and defect sizes however it is likely that appropriate values could be found.

All tests isolated when a flow rate was detected resulted in a fail, and none of the passed tests detected a flow rate at the point of isolation. However because of the delay to the start of detection through small defects and the apparent ending of flow when a large and small defect are present flow rate alone can not be used to determine end point. With the system used it would potentially be possible, by allowing a minimum test time, to utilise the flow rate alone but with different systems and with unknown defect sizes this would seem to be all but impossible. Nevertheless the use of a flowmeter would also be recommended in a full scale system since this would provide an extra indicator. This can in some respects be compared to the use of thermocouples which while it is true they provide only limited information what they do provide is delayed somewhat since it typically relies on a slow heat transfer process to impact them. They could therefore be used as a final trigger that the end point has been reached after the other more reliable values have already been achieved.

11.3 Flowed Gas Drying End Point

11.3.1 Methodology

The intention was to be carry out end point testing for flowed gas drying using the cracked and pinholed stainless steel test pieces as was done for vacuum drying end point testing but with the final measurement of dryness limited to a weight test only. The reason for this was that the process of evacuating the vessel would cause any residual water to vaporise and would not therefore give a true representation of the test piece at the end of the drying test. Unfortunately it was found that the circulation pump was faulty and it was not possible to obtain a suitably high flow rate and time constraints meant that it was not practical to get the pump fixed. An attempt was made to use bottled gas however this ran out before an

effective technique could be established. Another attempt was made to use a small compressor but this involved using atmospheric air which was to humid to provide good data. Consequently the end point data for flowed gas drying is limited.

11.3.2 Results

Figure 11.8a shows how the dew point of the system begins very low and does not begin to rise for over 5000 s when bottled gas is used. The obvious explanation for this is that the system begins dry and it takes some time for the test piece to warm enough for water to begin to be detected. The overall dew point does however remain very low. The test had to be ended before an end point could be detected. The condenser temperature appears to stop rising as the dew point begins to rise. This is possibly due to water vapour having some cooling effect. The sieve 1 behaviour is unusual however there is not enough data to be able to asses the reason for this.

Figure 11.8b shows an end point test using the compressor. The dew point throughout the test is significantly higher than recorded previously at around +5°C however this is roughly the same as the dew point within the laboratory during the test. There are however two cliff edge type behaviours which may well be indicators of the end point. The condenser and sieve 1 behaviours seem to show some link to the cliff edge behaviour as well. sieve 1 drops as dew point drops and this also leads to reduced heat transfer and a drop in condenser temperature.

Analysis of the tests from chapter 10, specifically the final tests of a drying sequence show a clear drop in water concentration towards the end of a test and the final masses indicate that the test pieces were dry at the end of all of the tests.

11.3.3 Flowed Gas Drying End Point Conclusions

While there is limited information there are clear changes in online dew point measurements during flowed gas drying testing. Based on a knowledge of what is occurring in the system the rise in dew point seen towards the beginning of flowed gas drying tests is almost certainly water beginning to be removed since there is almost no other logical explanation. Similarly the drop in dew point towards the end of a test is surely the last of the water being removed. Since no testing was

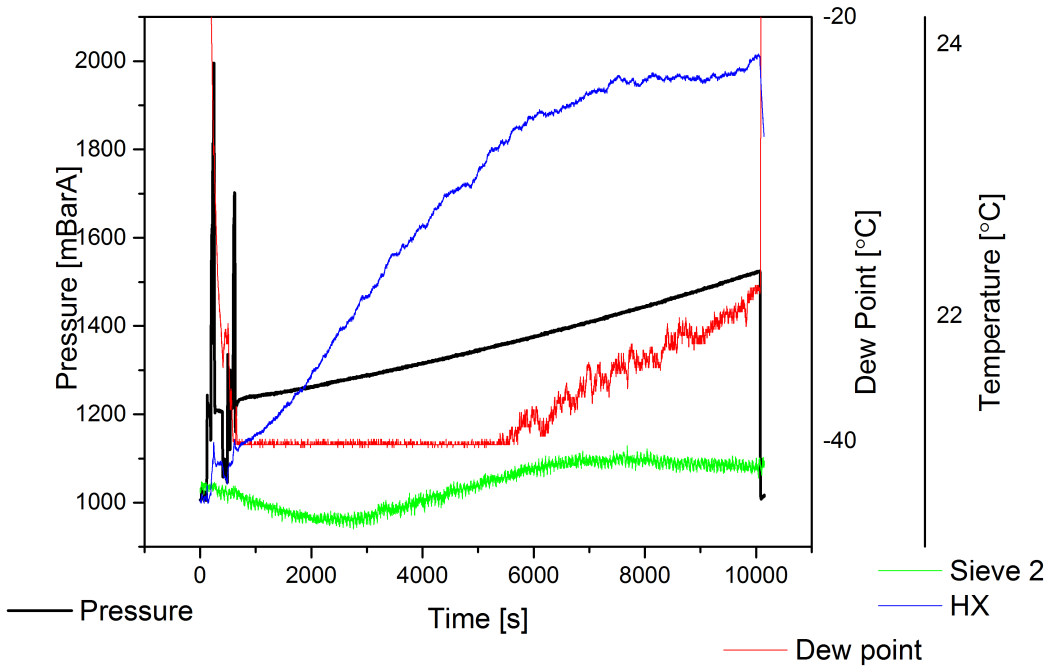

(a) Gas bottle.

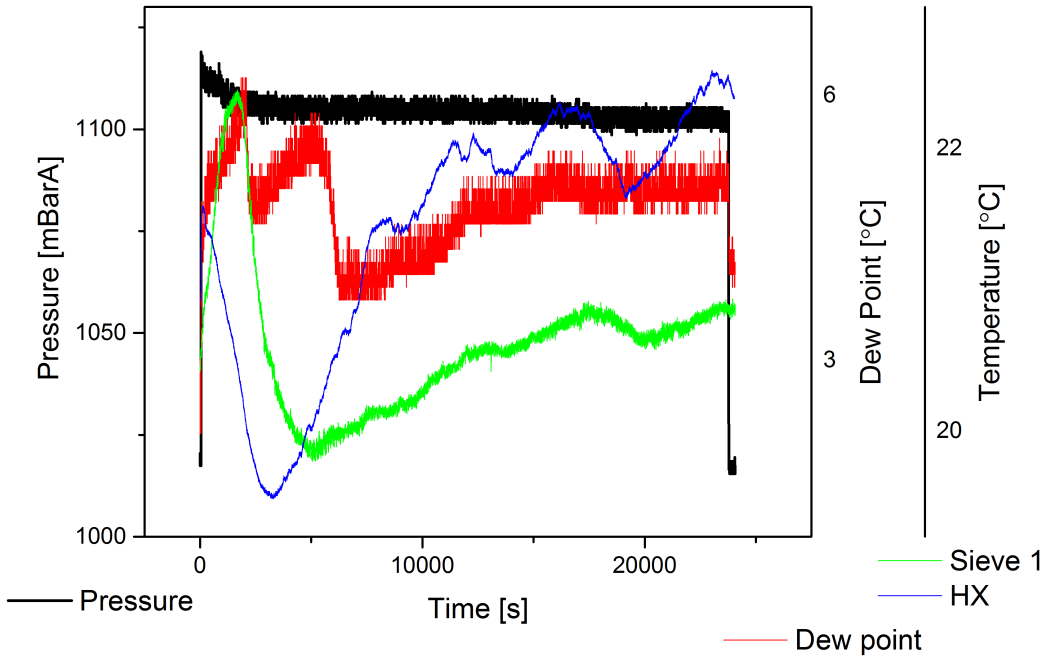

(b) Compressor

Figure 11.8: Flowed gas drying End point tests.

carried out in which a test piece was weighed close to this final drop in can not be said for certain that there is not still a small quantity of water remaining but it would certainly seem likely that such a drop could be used as an indicator of end point.

Neither flow rate nor pressure provide any details as to end point as teh overall values are too large for any water vapour present to influence there level. The condenser and sieve 2 temperature both seem to show some relationship to dew point although in the tests shown it is contradictory. This may well be due to the relative humidities in the system during these tests. Nevertheless it does indicate that the use of temperature as a form of monitoring could have some use.

Chapter 12

Spent Nuclear Fuel Drying Summary and Conclusions

The main purpose of this work was to compare the two recognised methods of drying spent nuclear fuel namely vacuum drying (VD) and flowed gas drying (FGD). The initial testing that was carried out produced preliminary data that suggested that vacuum drying was far more effective than flowed gas drying based on the rate at which water could be removed from inside a sealed simulated fuel pin however this testing resulted in significant variability for hot vacuum drying tests and there was an underlying feeling that issues with the flowed gas drying equipment were limiting the results obtained.

In order to reduce the variability in vacuum drying results the test temperature for vacuum drying was reduced to 30°C with a smaller number at 60°C (compared to 60°C and 150°C previously). To improve flowed gas drying the pipe routing was changed to reduce the length of pipe between the heater and the vessel, the pipe controller was changed and the molecular sieve housing enlarged. There was also a need to reduce the temperature for flowed gas drying from 150°C to 125°C. Following these changes a detailed set of drying tests was carried out for both vacuum and flowed gas drying.

A comparison of the detailed vacuum drying with the flowed gas drying once again shows that vacuum drying is more effective than flowed gas drying. Both types of drying showed a marked difference in behaviour as the mass of water within the test piece was reduced. When the pinholed stainless steel test piece

was full the vacuum drying rate was 0.4-0.5 mg s^{-1} and 0.65-1.00 mg s^{-1} at 30°C and 60°C respectively while the flowed gas drying rate was found to be just 0.1-0.22 mg s^{-1} at a temperature of 125°C. When the test piece contained less water the differences between the two methods was greatly reduced in some cases being almost negligible however this does not take in to account the clear difference in temperatures used. Since the vacuum drying tests were carried out at such low temperatures in comparison to flowed gas drying tests the room for improvement by altering temperature alone is significant. It would of course be possible to increase the flowed gas drying rate by increasing the temperature and pressure further, since these have both been shown to have an impact but the possible gains would likely be somewhat marginal compared to the gains found by increasing the temperature when vacuum drying.

For the testing carried out here the likely reason for vacuum drying being more effective is due to the ease with which the evaporation or boiling of the water within the test piece could be achieved. When vacuum drying the test piece was typically at or close to the boiling point of water throughout the test since the starting temperature was above the boiling point as the vessel was evacuated. As such drying was able to take place for a longer period. Despite the fact that the temperature did tend to drop below the boiling point again reasonably quickly as the system cooled little increase in temperature was required to return to boiling point and this was easy to achieve with conduction.

In contrast flowed gas drying required forced convection to heat the fuel and despite the lower enthalpy of evaporation at higher pressures with the system used it was not possible to heat the as quickly as may be liked. There is also an indication that the flow of cool gas at the beginning may in fact have cooled fuel initially, removing heat supplied by convection from the vessel walls.

12.1 Cost Effectiveness

The primary concern of this work has been to assess the effectiveness of the two methods however one area that should be of equal concern when a full scale system is being considered is the costs. As usual these can be split into capital and ongoing costs.

Even when considering the methods in there simplest form it is clear that the capital costs of a flowed gas drying system are likely to considerably outweigh those of a vacuum drying system. At its simplest a vacuum drying system requires a vessel heater[1] and a vacuum pump. In comparison a simplified flowed gas drying system requires a circulation fans, a gas drying system and a gas heating system, however since the current method of end point determination requires a vacuum rebound test to be completed successfully a flowed gas drying system would also require a vacuum pump. Consequently a flowed gas drying system has sufficiently greater upfront cost.

The operating costs of a flowed gas drying system are also expected to be greater primarily due to the greater energy costs and need for a drying gas which based on current practice is helium. Towards the end of the vacuum drying tests power meters were fitted to the vacuum pump and vessel heater to allow the energy usage to be calculated. For all flowed gas drying tests power meters were in place to record energy usage by the circulation pump, vessel heater and circulation heater. Having recorded the energy usage it is possible to produce a value that represents overall drying efficiency based on the mass of water removed per unit time per watt hour (kWh) of electricity. This gives a true representation of the drying cost and is arguably the most effective way of comparing tests since the energy value accounts for the temperatures used as well as the cost of moving gases at different pressures.

With power meters fitted two extended drying tests were carried out (∼22,000 s duration at 30°C using a full test piece) using the pinholed stainless steel test piece and these produced standard rates of 0.21 and 0.22 mg s^{-1} (this is lower than the values reported earlier which were for shorter tests (∼3600 s) as explained in chapter 9) and this lead to drying efficiencies of 0.129 μg s^{-1} kWh^{-1} and 0.141 μg s^{-1} kWh^{-1}. In comparison the two flowed gas drying tests with the highest drying rate, 125°C and 1.9 Bar with 0.19 mg s^{-1} and 135°C and 1.9 Bar with 0.22 mg s^{-1}) produced efficiencies of 0.71 μg s^{-1} kWh^{-1} and 0.081 μg s^{-1} kWh^{-1} respectively.

[1]Theoretically the vessel heater may not be needed if fuel could be treated after a suitably short cooling time.

12.2 Optioneering

In an attempt to a clear idea as to the most effective method of spent fuel drying an optioneering survey was carried out. The survey considered four areas; time, energy use, capital cost and running cost. All categories were weighted equally. Furthermore the scoring was carried out based on the assumption that the methods are being used to dry long stored, low heat, AGR fuel and as such there is no concern for cladding overheating.

Time and energy use are based purely on the data presented here. No attempt was made to consider the likely impact of scaling up to a commercial since while there is a though that this may change some of the values there is no evidence to support this. Capital cost and consumable cost are ball park estimates.

12.2.1 Optioneering Results

	Time	**Energy Use**	**Capital Cost**	**Consumable cost**	**Total**
Hot Vacuum Drying (>100°C)	4	3	4	4	15
Warm Vacuum Drying (<100°C)	1	4	4	4	13
Flowed Gas Drying (>100°C)	1	1	2	2	6

Table 12.1: Optioneering survey for based on the data presented here.

The results of the optioneering survey suggest that hot vacuum drying is the most effective method followed quite closely by warm vacuum drying and finally with flowed gas drying coming someway behind.

12.3 Drying Conclusion

Based purely on the data obtained in this trial vacuum drying has proven to be significantly more effective than flowed gas drying. It must however be emphasised that this is based purely on the data obtained here and is therefore limited by a number of factors which may influence final selection.

Scale Up It is highly likely that if the two systems were upscaled there may well be a reduction in the effectiveness of vacuum drying and an increase in the effectiveness of flowed gas drying. This is based entirely on heat transfer. In this system the test piece was in direct contact with the vessel wall and as such was able to heat relatively quickly. In an upscaled pins would be in direct contact with the wall and this may reduce the effectiveness of vacuum drying where heat transfer by conduction is key.

In contrast at this scale only low flow rates and small diameter pipes were used. As a result the forced convection results were poor. In an upscaled version heat loses would automatically drop due to the improved surface area to pipe volume ratio and it would also give improved flow rates. As a result this will likely lead to improved heat transfer and therefore improved drying rates.

There is however no evidence to suggest how much of an impact scale up would have.

Fuel Age The impact of fuel age will play a role by impacting the amount of heat that must be supplied. Older fuel is cooler and as such requires more heat to be effectively dried. This is most likely to be beneficial to vacuum drying methods where it may be possible to dry short cooled fuel with significant decay heat without supplying any additional heat, this making vacuum drying even more effective than flowed gas since even relatively hot fuel will not produce enough decay heat for flowed gas drying to be effective.

Cladding Material The conclusions presented here are based on using AGR fuel with stainless steel cladding designed for extended use at temperatures in excess of 800°C. As a result there is little chance of cladding damage occurring during overheating as a result of a drying process. This is a potential danger for short fuelled light water reactor fuel where the typical operating temperature is less than 400°C. In this case short cooled fuel may when undergoing vacuum drying overheat as there is not enough gas flow to remove excess heat.

Drying Cycle Length It is unclear which method would prove most effective if increased to ∼24 hours, a likely cycle time for bulk fuel drying. Since vacuum

drying rates seemed to reduce with time and flowed gas rates tended increase with time it would be interesting to see the impact of much longer tests.

12.4 Pinholed and Cracked Samples

Table 12.2 shows the drying rates for all tests of the pinholed and cracked stainless steel test pieces under the different drying methods. There are both similarities and differences between the cracked and pinholed samples whether dried under vacuum or flowing gas. All test pieces and all drying methods showed a significant difference in the drying rate between when the test piece is full of water and at lower levels. The reason for this seems to be similar in all cases; when the test piece is full, liquid water is ejected from the test piece and then boils away from contact with the hot vessel walls. As the level of water drops the drying regime changes to be dominated by the loss of water vapour through the defects rather than liquid water and mass transfer may become predominantly due to diffusion rather than a pressure gradient.

When the test piece is full the drying rate for the pinholed test piece is slightly higher than for the cracked test piece however the differences are minimal and could easily be accounted for by natural variation. When the test pieces contained <4 g of water the difference between the two test pieces was somewhat increased being 50% lower for the vacuum drying and 10 times lower when flowed gas drying. In a real life drying scenario the most important scenario is the one in which a pin is not entirely full and it has therefore been shown that there is a significant difference in drying rates based on the defect dimensions. This possibly confirms the theory that at low water levels the primary driving force for mass transfer is diffusion which is faster at lower pressures. Since there is a feeling that the cracks in the cracked stainless steel test piece were slightly larger than would be expected in failed fuel a true drying rate is likely to be significantly lower. Nevertheless the work has shown that it is possible to remove water vapour through small cracks.

There would appear to be some indication that the tortuoisty and/or defect length play a significant role in the drying rate. The open area of a 300μm pinhole is 0.07 mm^2. Based on a crack width of 20 μm an equivalent open area would require a crack length of just 3.5 mm, and if the crack width is reduced to just

2 μm this requires a length of 35mm. If the 3 o'clock crack which the CT data shows to have passed fully through the wall is assumed to be a mirror image at 9 o'clock then there is potentially 100 mm of length in which 3.5 mm of crack is required. Based on the assumption that 18% of the length is open as calculated in section 3.8 then for a crack width of 20 μm there should be at least 0.36 mm^2 of open area and even with a 2 μm crack width the open area is likely to be at least 0.036 mm^2, a little over half the area of the pinhole. If the drying rate is assumed to be directly proportional to the open area for a defect of the same length then it is clear that either the tortuoisty of a crack or increased length compared to that of the straight pinhole through 380 μm cladding is playing a role in reducing the drying rate.

	Full test piece		**<4 g**	
	Vacuum	**Flowed gas**	**Vacuum**	**Flowed gas**
	[mg s^{-1}]	[mg s^{-1}]	[mg s^{-1}]	[mg s^{-1}]
Pinholed	0.4-0.5	0.1-0.22	0.15	0.1
Cracked	0.5	0.1	0.1-0.04	0.01

Table 12.2: Drying rates for different drying methods.

12.5 Experimental Error and Accuracy

The use of electronic data logging for most data streams meant that the vast majority of recorded data can be regarded as highly accurate. While a small amount of error may be introduced as a result of the need to start multiple data logging systems this was reduced as testing continued and methods refined. It was also possible to correct for any error in terms of timings on a case by case basis as required. Electronic data logging also meant that a high frequency of data points could be collected to allow trends to be recorded with a high degree of certainty. The accuracy of electronic instruments is also high and table 12.3 shows values for the instruments used. It is worth noting however that since the majority of comparisons are qualitative in nature and that trends are of more importance than

absolute values the repeatability is of more importance than the overall value and for identical tests this was found to be high.

There are known to some areas in which the data collected is not quite ideal. The most obvious example of this is the use of the thermocouple within the vessel heater as a measure of the vessel wall temperature. This is certainly flawed as a higher temperature is recorded since the thermocouple is embedded within the band heaters rather than on the inside of the wall. This is aggravated further by the fact that the band heater is fitted around the sides of the vessel and not the base and most heating is thought to take place at the base of the vessel. This was addressed in later sections with the addition of a further thermocouple on the base of the vessel. Using this thermocouple to control the vessel temperature would complicate matters as it would likely lead to the vessel walls being considerably hotter than the base. This is however of limited concern since it is the relative values that are of more importance and these are unaffected. A similar issue exists with the positioning of the vessel inlet thermocouple which is used to control the circulation heater. Due to the distance between the thermocouple and the vessel it is likely that the gas entering the vessel is somewhat cooler than recorded. Other thermocouples were also added as time passed to address other areas which were considered to be of interest as these areas raised themselves. Despite these additions it is felt that scale up calculations based on the data collected here are not feasible and further testing would be required on a larger scale.

There is likely to be some problems in using the surface temperature of the test piece to judge the temperature of the water within the test piece and assess whether it has reached boiling point or not. This is further complicated by the possibility of a pressure drop occurring across the crack/pinhole within the test piece. During some early unreported testing a noticeable pressure drop was found across the flow meter when a large amount of water was being removed so it is likely that a similar effect is found across the test piece defect. From the data seen in fig. 8.5 in which pressure, bulk water temperature and the vessel base temperature were all found to be closely related (as one would expect) if either the test piece water temperature or test piece pressure could be recorded much useful data could be obtained. As it is the surface temperature value provides an indication of what is taking place inside the test piece when there is a relatively

large amount of water present but as the quantity of water drops this becomes less obvious. Finally the mass of steel is likely to impact temperatures somewhat.

As described earlier the mass flow meter is calibrated for use with air at atmospheric pressure with the software allowing for adjustments to other dry gases and at pressures ranging from 0.8 to 11 BarA. Consequently the actual values recorded for the flow rate are in absolute terms certainly inaccurate when undergoing vacuum drying since the majority of the flowing fluid is water vapour. However once again the important factor is the trend and relative nature of the values between tests and since the calibration remains the same the data provides all the information required since no attempt is being made to explain quantitatively the behaviour on a larger scale.

There is a belief that there are a reasonable degree of error in the temperature readings since in some cases the thermocouples are not in the ideal locations. This is particularly true of the thermocouples controlling the vessel heater since the control thermocouple is built into the heater itself. As such the temperature is more of a nominal set point temperature rather than an accurate temperature of the vessel walls. This is why a thermocouple was added to the base of the vessel after initial testing and the data shows that there is a lag between the vessel temperature reaching set point and the vessel base approaching this temperature. The vessel base thermocouple is however at the coolest point so is a worst case measure and the thermocouple in the vessel head space is giving an accurate reading as it is directly in the vessel gas.

The thermocouple controlling the flowed gas temperature is some distance from the vessel so is likely despite lagging likely to suggesting the gas temperature is somewhat warmer than it is in reality. This was aggravated by the narrow bore of the pipework which allowed considerable heat loss. This issue would be reduced in an upscaled version where the surface area to volume area of the pipework could be reduced and larger mass flows used.

Other thermocouples are however placed directly in the centre of the pipework so are an accurate measure as are pressure measurements. The positioning of the dew point meter is reasonable although it is possible that some liquid is condensing out before reaching it, however for this to be the case dew the dew point upon leaving would have to be above $\sim$19°C which is the temperature of the pipework.

Device	Accuracy	Resolution
Thermocouples	+/- 2.2°C	0.01°C
Flow meter	0.4% rd	0.002655 kg hr^{-1}
Pressure Transducer	+/-0.25% BSL	1 mBarA
Dew Point Meter	+/- 2°C	0.1°C
Flow Meter after re-ranging	0.4%rd	0.0003365 l min^{-1}
Balance 1 (Bulk water)	-	0.05g
Balance 2 (Test piece)	-	0.001g
Balance 3 (Test piece for end point testing)	-	0.0001g

Table 12.3: Accuracy of instruments used.

12.6 End Point Conclusions and Instrumentation

End point testing has shown that dew point appears to provide an indication as to the behaviour within the system for both flowed gas drying and vacuum drying. Pressure and flow data seem to be of use when carrying out vacuum drying but during flowed gas drying the mass of gas present swamps any water vapour present. Some of the temperature data also appears to give some indication as to what is happening. This is particularly true for the temperatures recorded at the inlet to the condenser and also at the molecular sieve, however the condenser reading is only really of any use when iced water is being used. It is also unlikely that molecular sieve would be used to dry gas on a commercial scale, however, since one alternative is to use a freeze drier this may allow data similar to that seen at condenser to be collected. It would also be possible to divert a small stream of the gas through a molecular sieve and observe the behaviour of that assuming it to be representative of the entire gas stream.

The surface temperature of the fuel may be of some interest but in reality this would be difficult to record on a commercial scale. The temperature at the vessel outlet appeared to give some indication of changes within the system and it is possible that using a cooled plate or similar may amplify any data at this

point as it has at the condenser. It would probably also be worthwhile fitting a thermocouple to measure vessel temperature. The cost of a thermocouple would be negligible compared to the cost of drying cask and while in the testing carried out vessel temperature has not provided any particularly useful information it may well be of use when using real fuel and there is greater likelihood of non-normal events taking place.

12.7 Further Improvements

The most significant change that could be made to the rig would be to improve the forced convection characteristics of the vessel for flowed gas drying. This is not however an easy change and may require a new vessel lid with increased bore feed lines which means it may be close to a new system. Being able to place the circulation heater closer to the vessel would also help as would a non pulsing circulation pump this allowing better flow rate measurement.

While the use of iced water in the condenser was an improvement it was hard to tightly control the temperature. A circulating cooler capable of sub zero operation would be a nice improvement for both vacuum and flowed gas drying operations.

Other temperature related improvements would be to improve the vessel temperature control by fitting more thermocouples and potentially by averaging the control vessel temperature around a number of locations. Alternatively a greater number of logged thermocouples around the vessel to give a netter idea of how the vessel temperature.

In terms of instrumentation a second dew point meter for the inlet gas to allow comparison and a lower lower limit (i.e. less than -40°C) may prove advantageous as would a higher upper operating limit. Other instrumentation improvements would include having the ability record the pressure and temperature inside the test piece so that it could be ascertained whether there is any pressure drop across the defect. It is unlcear whether it would be possible to get a flow meter capable of measuring lower flow rates but if possible that may provide useful data.

From an operational standpoint longer tests could prove interesting however that may require different test pieces which would require development. There are also a number of test combinations and scenarios that would be interesting to

assess. There is some suggestion that ice formation may be a potential issue for vacuum drying and while there was no indication that this occurred it would be interesting to see if it could be achieved. It would also be interesting to attempt to fill the test piece underwater this eliminating the air space as this may impact the high initial drying rate observed.

As discussed previously there is also a requirement to use a more representative test piece, in which defects are more similar to thise expected and also took into account complicating factors such as the presence of fuel pellets inside the test piece.

Part III

Summary and Conclusions

Chapter 13

13.1 Summary

The main aim of this thesis was to investigate the drying of stainless steel clad nuclear fuel from the UK's fleet of Advanced gas reactors. The first question posed when the project was conceived related to the condition of the fuel upon removal from the pond. In the early years of pond storage failures were common and post storage examination attributed them to intergranular stress corrosion cracking. However since this was inhibited with caustic dosing of the ponds failures have been stopped and post storage examination has not routinely taken place for around 20 years. Consequently little is known about the fuels condition and as a result the first part of this thesis looked at preparing samples that would be representative.

In general two types of water are regarded as being a concern when drying spent fuel; bound water and trapped water. It was shown in an earlier MSc project that the loss of bound water could be detected from corroded aluminium using TGA and the same technique was used on samples of stainless steel. These were treated to induce intergranular corrosion, pitting and an attempt was made to simulate long term storage in a caustic dosed pond. The TGA results found that there was no detectable mass loss from any of the stainless steel samples used. A number of samples were treated to form carbon deposits on the surface and similar results were obtained. It was therefore concluded that the quantity of bound water on stainless steel is negligible and can be disregarded as far as drying of spent fuel was concerned. While the effect of radiation on corrosion behaviour was not examined it seems unlikely that this will have any significant impact on bound water.

During the course of the sample preparation it was noticed that the corrosion behaviour of the two surfaces of AGR cladding was markedly different. The inner surface was found to be resistant to pitting corrosion yet susceptible to IGC while the opposite was found to be true of the outer surface. One possible outcome of this is that an apparently intact pin may in fact be subject to corrosion from the inside if an unobserved defect has allowed pin flooding.

While this was not felt to be directly relevant the reason for this was investigated by carrying out XPS and electron microscopy of the two surfaces. STEM and EDX found a difference in oxide structure, although little detail was found. XPS analysis was found to be unsuitable due to a significant carbon layer that could not be removed sufficiently for good data to be collected. It should however be mentioned that while differences were found this was in samples of as received material which had not undergone the final anneal during production let alone spent five years in a reactor core so any differences at this stage may be negligible.

Having established that bound water was not an issue of concern, trapped water was considered. Despite the recent prevention of failures microcracks are deemed to be a concern which in turn means that trapped water is a possibility. There was therefore a need to produce a length of stainless steel which contained microcracks in which water could be sealed to be used for the macro scale drying tests. A method was developed with the use of a compression ring to introduce stress and a sample of cracked tubing was produced made from 304 stainless steel. The same treatment was applied to a length of AGR cladding without success. Micro CT of cracks in samples produced in the same manner showed that cracks that were not visible in single cross sections under SEM did pass fully through the tube wall in multiple points.

Having produced samples that are suitable for testing part two the thesis carried out drying tests to compare the effectiveness of vacuum and flowed gas drying. Perhaps most importantly the data has shown that both vacuum and flowed gas drying are capable of removing water through a 300 μm pinhole and a $\sim$20 μm crack. When the test piece (test piece) used was full of water the drying rate was significantly faster than when a lower water level was used and the rate of drying through a crack and a pinhole were broadly similar. At lower water levels, which are likely to be more realistic, the drying rate for the pinholed test piece was found

to be significantly faster than for the cracked test piece despite suggestions that the open area of the two defects could be similar.

When the test piece was full the difference in drying rate between flowed gas drying and vacuum drying was found to be broadly minimal however at lower water levels vacuum drying was significantly faster. The difference in rates depending on water level is attributed to whether liquid water can be ejected through the defect. When vacuum drying it was observed that the pressure change caused the airspace to expand and liquid water to be ejected through the defect from where it would quickly boil away. As the water level dropped this was no longer possible. A similar effect is believed to occur when flowed gas drying with the air space expanding due to the increased temperature. The fact that the difference in drying rate is more pronounced at lower water levels suggests that the driving force for water being removed from the test piece at low water levels is diffusion.

Not only were drying rates found to be higher for vacuum drying but the energy usage of vacuum drying would seem to be significantly lower than for the flowed gas drying test with similar drying rates, thus suggesting that the drying efficiency of vacuum drying is also greater.

13.2 Conclusions and Next Steps

The main conclusions to be drawn from part 1 are that bound water is unlikely to be a concern for stainless steel fuels and that it is possible to produce samples with cracks which are geometrically similar to those found during post storage examination. It is however clear that there is a significant lack of knowledge on the size of defects that may be expected. The images of cracks that are being used for reference are from the days when fuel failures were common and since failures were detected by measurement of pond caesium levels all that is really known is that caesium levels are at an acceptable level. There are three possible reasons for this: Firstly the use of caustic dosing may mean that there is 100% prevention of cracking in which case there will be no trapped water. Another alternative is that crack frequency is reduced significantly and with fewer cracks present the levels of caesium are also reduced to acceptable limits. The final option is that crack size is reduced (possibly in combination with reduced frequency).

It is this third scenario that introduces the greatest risk and uncertainty. The danger is that a crack may have reduced to a size where water is able to slowly penetrate a pin yet caesium is not able to diffuse out at a sufficient rate for detection. In this case the question is whether water can be removed from such cracks at a sufficient rate for drying to be practical. The drying tests carried out in part 2 have clearly shown that water can be removed through a pinhole at a higher rate than through SCC cracks. If the cracks in real fuel are found to be even smaller it is possible that while drying is possible, the drying rate becomes so low that full scale drying of AGR fuel is not feasible, and even if the drying rate is not adversely impacted then the measurement techniques discussed may not prove to be suitable. It is therefore imperative that work is carried out to provide a firm understanding of any defects within fuel, in terms of both size and frequency. However, due to the number of pins involved it seems unlikely that a statistically significant quantity of pins can be assessed. It may however be possible to carry out targeted testing on pins from elements 1 and 2 which have previously been identified as being most susceptible.

Along these lines there is a need to understand how the presence of uranium dioxide pellets within the fuel pins impacts drying. Two possible impacts need to be considered, namely the impact of the pellets on the movement of water within a pin and also whether bound water on the oxide surface is of sufficient quantity to be of concern and if so the ease with which it can be removed.

A further need is for a suitable degree of dryness to be determined for AGR fuel. The use of a vacuum rebound test with pressure of less than 4 mBarA being maintained for 30 minutes is taken directly from the ASTM standard and is based on Zircaloy clad fuels. There is therefore a need to confirm that this value is acceptable for AGR fuel or to produce an alternative measurement in whatever form is deemed appropriate. The drying work carried out has clearly shown that both vacuum drying and flowed gas drying are capable of drying spent fuel, with online instrumentation seeming to show that a certain level of dryness has been reached. If a dryness based on an online reading such as pressure or dew point could be found that would be the ideal scenario.

Based on the data presented here it is the authors belief that vacuum drying is more effective than flowed gas drying. As discussed there are a number of reasons

relating to improved heat flow that would make it possible for flowed gas drying rates to be significantly improved however based on the low temperatures used in this testing it is likely that vacuum drying methods could be improved similarly thus cancelling out any improvements in flowed gas drying.

References

[1] Nuclear Decommissioning Authority. Oxide Fuels - Preferred Option - Publications - GOV.UK. Technical Report SMS/TS/C2-OF/001/Preferred Option, June 2012. URL https://www.gov.uk/government/publications/oxide-fuels-preferred-option. 3

[2] R.L. Sindelar, Caskey Jr, G.R., Peacock Jr, H.B., and Lam, P.S. Evaluation of Degradation During Interim Dry Storage of Al SNF. In *High level Radioactive Waste Management: Proceedings of the Sixth Annual International Conference*, Las Vegas, Nevada, May 1995. American Nuclear Society ; American Society of Civil Engineers. ISBN 0-7844-0082-2 978-0-7844-0082-1. 7

[3] R. L. Sindelar, H. B. Peacock, P. S. Lam, N. C. Iyer, M. R. Louthan, and J. R. Murphy. Scientific Basis for Storage Criteria for Interim Dry Storage of Aluminum-clad Fuels. *MRS Online Proceedings Library*, 412:99–105, 1995. doi: 10.1557/PROC-412-99. 7

[4] ASTM. Guide for Drying Behavior of Spent Nuclear Fuel. Technical Report C-1553, ASTM International, 2008. URL http://www.astm.org/Standards/C1553.htm. 8

[5] J.V. Best, W.J. Stephen, and A.J. Wickham. Radiolytic graphite oxidation. *Progress in Nuclear Energy*, 16(2):127–178, 1985. ISSN 0149-1970. doi: 10.1016/0149-1970(85)90002-2. URL http://www.sciencedirect.com/science/article/pii/0149197085900022. 9, 11

[6] Neale Brittain. EDF Energy - Nuclear Generation The AGR Design, Fukushima and More, February 2012. URL www-diva.eng.cam.ac.uk/mphil-in-nuclear-energy/external-lectures/2011-12-lectures/edf-energy-ng-cambridge-09022012.pdf/at_download/file. 9

[7] J. Winton, M. M. Haberlin, D. Rhodes, R. B. Jones, J. S. Waddington, and A. C. Roberts. 7. The mechanical properties of AGR cladding. In *Nuclear Fuel Performance*, pages 7.1–7.5. Thomas Telford Publishing, January 1973. ISBN 978-0-7277-5160-7. URL http://www.icevirtuallibrary.com/doi/full/10.1680/nfp.48977.0011. DOI: 10.1680/nfp.48977.0011. 9

[8] John Kyffin. Technological Development to Support a Change in the United Kingdom's Strategy for Management of Spent AGR Oxide Fuel. In *Proceedings of the International Conference on Management of Spent Fuel from Nuclear Power Reactors*, Vienna, June 2015. IAEA. 10, 29, 30

[9] J.V. Best, A.J. Wickham, and C.J. Wood. Inhibition of Moderator Graphite Corrosion in CEGB Magnox Reactors 1. Laboratory measurements of the effect of coolant composition on the radiolytic Graphite/CO//2 Reaction. *Journal of the British Nuclear Energy Society*, 135(185):319–324, 1976. URL http://www.scopus.com/inward/record.url?eid=2-s2.0-0016983992&partnerID=40&md5=915c35fbb47bb51abf96e4726b4dc0fe. 11

[10] J.V. Best, A.J. Wickham, and C.J. Wood. Inhibition of Moderator Graphite Corrosion in CEGB Magnox Reactors - 2. Hydrogen Injections into Wylfa Reactor I Coolant Gas. *Journal of the British Nuclear Energy Society*, 135(185):325–331, 1976. URL http://www.scopus.com/inward/record.url?eid=2-s2.0-0016985985&partnerID=40&md5=f4aeea00cb2805b54d15a5cd33f4812b. 11

[11] J.A. Cairns, J.P. Coad, E.W.T. Richards, and I.A. Stenhouse. Carbon deposition on metallic surfaces studied by r.f. plasma discharge. *Nature*, 288(5792):686–687, 1980. URL http://www.scopus.com/inward/record.url?eid=2-s2.0-0042260217&partnerID=40&md5=f4025f10064d6610aec7f2736563fc3b. 11

[12] G.W. Horsley and J.A. Cairns. The inhibition of carbon deposition on stainless steel by prior selective oxidation. *Applied Surface Science*, 18(3):273–286, 1984. URL http://www.scopus.com/inward/record.url?eid=2-s2.0-0021468709&partnerID=40&md5=60bc28d98b47c716a564bb0f71611fb0. 11

[13] M.L. Sykes, I.A.S. Edwards, and K.M. Thomas. Metal carbonyl decomposition and carbon deposition in the advanced gas-cooled nuclear reactor. *Carbon*, 31(3):467–472, 1993. ISSN 0008-6223. doi: 10.1016/0008-6223(93)90135-W. URL http://www.sciencedirect.com/science/article/pii/000862239390135W. 12, 13

[14] Clive Mowforth. Suppression of Carbon Deposition in an AGR. In *Conference on Chemistry in Nuclear Power Generation*, Manchester, November 2014. 12, 13

[15] G.R. Millward, H.E. Evans, M. Aindow, and C.W. Mowforth. The influence of oxide layers on the initiation of carbon deposition on stainless steel. *Oxidation of Metals*, 56(3-4):231–250, 2001. URL http://www.scopus.com/inward/record.url?eid=2-s2.0-0013354192&partnerID=40&md5=14f7e80057f0ecd263b8f337c701c13c. 12

[16] G.R. Millward, H.E. Evans, I.P. Jones, C.D. Eley, and C.W. Mowforth. The influence of carbonyl sulphide on the inhibition of filamentary carbon deposition on stainless steel. *Materials and Corrosion*, 54(11):864–869, 2003. URL http://www.scopus.com/inward/record.url?eid=2-s2.0-0344585500&partnerID=40&md5=609c82c48463f73743e82819b5ebd61f.

[17] G.R. Millward, H.E. Evans, I.P. Jones, and C.D. Eley. Carbon deposition on stainless steel in oxidising environments. *Materials at High Temperatures*, 20(4):535–541, 2003. URL http://www.scopus.com/inward/record.url?eid=2-s2.0-10844227558&partnerID=40&md5=34d871d3680f50df94784719a7d51797.

[18] G.R. Millward, H.E. Evans, I.P. Jones, C.D. Eley, and K.A. Simpson. Burn-off of filamentous carbon and subsequent re-deposition on a 20cr25ni austenitic steel. *Materials at High Temperatures*, 26(1):57–61, 2009. URL http://www.scopus.com/inward/record.url?eid=2-s2.0-72349086337&partnerID=40&md5=10bc279a2d2654434c55872fad462ef6. 12

[19] British Stainless Steel Association. What Is Stainless Steel? URL http://www.bssa.org.uk/faq.php?id=1. 14

[20] Oliver Kuhn. Science Break : Steel. *Recorder-The Official Journal of Canadian Exploarion Geopyhsicists*, 38(08), October 2013. URL http://csegrecorder.com/features/view/science-break-201310. 15

[21] Magmaweld. Stainless Steel Welding. URL http://www.magmaweld.com/stainless_steel_welding.html. 15

[22] Zhiliang Cao and Henry Gu Cao. Cubic Atom and Crystal Structures. *International Journal of Physics, International Journal of Physics*, 2(6): 277–281, January 2014. ISSN 2333-4878. doi: 10.12691/ijp-2-6-11. URL http://pubs.sciepub.com/ijp/2/6/11/abstract.html. 16

[23] James Gordon Parr and Albert Hanson. *An introduction to stainless steel*. American Society for Metals, 1965. 16

[24] Donald Peckner and I. M. Bernstein, editors. *Handbook of stainless steels*. McGraw-Hill, New York, 1977. ISBN 978-0-07-049147-2.

[25] L. Hochmann and J. Colombier. *Stainless and Heat Resisting Steels*. Edward Arnold, second edition edition edition, 1967. 16

[26] W. A. England, M. J. Bennett, D. A. Greenhalgh, S. N. Jenny, and C. F. Knights. The characterization by raman spectroscopy of oxide scales formed on a 20cr\25ni\Nb stabilized stainless steel. *Corrosion Science*, 26(7):537–545, 1986. ISSN 0010-938X. doi: 10.1016/0010-938X(86)90021-1. URL http://www.sciencedirect.com/science/article/pii/0010938X86900211. 16, 18

[27] J. Y. Jeng, B. E. Quayle, P. J. Modern, W. M. Steen, and B. D. Bastow. Laser surface treatments to improve the intergranular corrosion resistance of 18/13/Nb and 304l in nitric acid. *Corrosion Science*, 35(5):1289–1296, 1993. ISSN 0010-938X. doi: 10.1016/0010-938X(93)90350-P. URL http://www.sciencedirect.com/science/article/pii/0010938X9390350P. 17, 26

[28] M. F. Montemor, M. G. S. Ferreira, N. E. Hakiki, and M. Da Cunha Belo. Chemical composition and electronic structure of the oxide films formed on 316l stainless steel and nickel based alloys in high temperature aqueous environments. *Corrosion Science*, 42(9):1635–1650, September 2000. ISSN 0010-938X. doi: 10.1016/S0010-938X(00)00012-3. URL http://www.sciencedirect.com/science/article/pii/S0010938X00000123. 17

[29] S. S. M. Tavares, V. Moura, V. C. da Costa, M. L. R. Ferreira, and J. M. Pardal. Microstructural changes and corrosion resistance of AISI 310s steel exposed to 600-800 C. *Materials Characterization*, 60(6):573578, June 2009. ISSN 1044-5803. doi: 10.1016/j.matchar.2008.12.005. URL http://www.sciencedirect.com/science/article/pii/S1044580308003422. 17, 26

[30] Abdulla Al-Shater, Dirk Engelberg, Stuart Lyon, Cornelius Donohoe, Steve Walters, Guy Whillock, and Andrew Sherry. Characterization of the stress corrosion cracking behavior of thermally sensitized 20cr-25ni stainless steel in a simulated cooling pond environment. *Journal of Nuclear Science and Technology*, 0(0):1–10, April 2017. ISSN 0022-3131. doi: 10.1080/00223131.2017.1309305. URL http://dx.doi.org/10.1080/00223131.2017.1309305. 17

[31] C. Tyzack and H.C. Cowen. The corrosion of reactor materials in carbon dioxide. *Atomic Energy Review*, 14(2):263–324, 1976. URL http://www.scopus.com/inward/record.url?eid=2-s2.0-0016963965&partnerID=40&md5=c3c8ed5610ba613cee9abf20b181440c. 17

[32] J. M. Francis. Structure of Surface Oxides Formed on A 20% Cr/25% Ni/Nb-Stabilised Steel in Carbon Dioxide at High Temperatures. *British Corrosion Journal*, 3(3):113–119, May 1968. ISSN 0007-0599. doi: 10.

1179/000705968798326244. URL http://www.maneyonline.com/doi/abs/10.1179/000705968798326244. 18

[33] J. A. Desport and M. J. Bennett. Investigation by fractography of the high-temperature oxidation of the 20%Cr-25%Ni-Nb stainless steel. *Oxidation of Metals*, 29(3-4):327–346, April 1988. ISSN 0030-770X, 1573-4889. doi: 10.1007/BF00751803. URL http://link.springer.com/article/10.1007/BF00751803. 18, 99

[34] M.J. Bennett, P.C. Blythe, G.H. Chaffey, K. Hand, J.W. McMillan, S.J. Webster, and J.E. Antill. The effect of fission neutron irradiation upon the oxidation of a 20 wt % Cr/25 wt % Ni/Nb stabilised stainless steel by carbon dioxide beween 580 and 840 Â°C. *Journal of Nuclear Materials*, 25(3):260–270, March 1968. ISSN 0022-3115. doi: 10.1016/0022-3115(68)90169-4. URL http://www.sciencedirect.com/science/article/pii/0022311568901694. 18

[35] M.J. Bennett, G.H. Chaffey, and J.E. Antill. Some aspects of the effects of fission fragment irradiation upon the oxidation of austenitic stainless steels by oxygen at 650{Â°} and 800{Â°}C. *Journal of Nuclear Materials*, 32(2):299–309, September 1969. ISSN 0022-3115. doi: 10.1016/0022-3115(69)90079-8. URL http://www.sciencedirect.com/science/article/pii/0022311569900798. 19

[36] William D. Callister. *Materials science and engineering: an introduction*. Wiley international edition. Wiley, New York, NY, 6th international edition, 2003. ISBN 0-471-22471-5 0-471-22471-5 0-555-00205-5 0-471-26456-3. 19

[37] S. M Bruemmer, E. P Simonen, P. M Scott, P. L Andresen, G. S Was, and J. L Nelson. Radiation-induced material changes and susceptibility to intergranular failure of light-water-reactor core internals. *Journal of Nuclear Materials*, 274(3):299–314, September 1999. ISSN 0022-3115. doi: 10.1016/S0022-3115(99)00075-6. URL http://www.sciencedirect.com/science/article/pii/S0022311599000756. 19

[38] E. A. Little. Development of radiation resistant materials for advanced nuclear power plant. *Materials Science and Technology*, 22(5):491–518, May 2006. ISSN 0267-0836. doi: 10.1179/174328406X90998. URL http://0-www.maneyonline.com.wam.leeds.ac.uk/doi/abs/10.1179/174328406X90998. 19, 20

[39] C Taylor. The formation of sensitised microstructures during the irradiation of CAGR fuel pin cladding. In *Symposium on the Radiation-induced Sensitisation of Stainless Steels;*, Berkeley, UK, September 1986. URL https://inis.iaea.org/search/searchsinglerecord.aspx?recordsFor=SingleRecord&RN=18098354. 19

[40] John Kyffin. The technical case for interim Storage of AGR fuel and development of a programme of further work. Manchester, April 2014. IChemE. 19, 29

[41] Kenneth R. Trethewey and John Chamberlain. *Corrosion for science and engineering*. Longman, Harlow, 2. ed., reprint edition, 1998. ISBN 0-582-23869-2 0-582-23869-2. 22

[42] A. V. Byalobzheskii. *Radiation Corrosion*. I.P.S.T., May 1970. ISBN 978-0-7065-1013-3. 22, 23

[43] Robert S. Glass, George E. Overturf, Richard A. Van Konynenburg, and R. Daniel McCright. Gamma radiation effects on corrosion-I. Electrochemical mechanisms for the aqueous corrosion processes of austenitic stainless steels relevant to nuclear waste disposal in tuff. *Corrosion Science*, 26(8):577–590, 1986. ISSN 0010-938X. doi: 10.1016/0010-938X(86)90025-9. URL http://www.sciencedirect.com/science/article/pii/0010938X86900259.

[44] W. G. Burns, W. R. Marsh, and W. S. Walters. The gamma irradiation-enhanced corrosion of stainless and mild steels by water in the presence of air, argon and hydrogen. *Radiation Physics and Chemistry (1977)*, 21(3):259–279, 1983. ISSN 0146-5724. doi: 10.1016/0146-5724(83)

90155-3. URL http://www.sciencedirect.com/science/article/pii/0146572483901553. 22

[45] R. L. Sindelar, P. S. Lam, M. R. Louthan Jr., and N. C. Iyer. Corrosion of Metals and Alloys in High Radiation Fields. *Materials Characterization*, 43 (2-3):147–157, August 1999. ISSN 1044-5803. doi: 10.1016/S1044-5803(99)00042-X. URL http://www.sciencedirect.com/science/article/pii/S104458039900042X. 23

[46] R. J. Guenther, A. B. Johnson Jr, A. L. Lund, and E. R. Gilbert. Initial Evaluation of Dry Storage Issues for Spent Nuclear Fuels in Wet Storage at the Idaho Chemical Processing Plant. Technical Report INEL–96/0140, Idaho National Engineering Lab., Idaho Falls, ID (United States), November 1994. URL http://www.osti.gov/scitech/biblio/285498. 23

[47] R. Winston Revie, Herbert Henry Uhlig, and Herbert Henry Uhlig, editors. *Uhlig's Corrosion Handbook*. Electrochemical Society series. Wiley, New York, 2nd ed edition, 2000. ISBN 978-0-471-15777-9. 24

[48] R. Priya, S. Ningshen, and U. Kamachi Mudali. Influence of Oxidizing Ion Concentration on the Corrosion Resistance of Type 304l Stainless Steel in Nitric Acid Medium. *Corrosion*, 69(4):335–344, April 2013. ISSN 0010-9312. doi: 10.5006/703. URL http://0-corrosionjournal.org.wam.leeds.ac.uk/doi/full/10.5006/703. 24, 25, 27

[49] C. L. Briant. The Effects of Sulfur and Phosphorus on the Intergranular Corrosion of 304 Stainless Steel. *Corrosion*, 36(9):497–509, September 1980. ISSN 0010-9312. doi: 10.5006/0010-9312-36.9.497. URL http://0-corrosionjournal.org.wam.leeds.ac.uk/doi/abs/10.5006/0010-9312-36.9.497. 24, 25, 26

[50] O. V. Kasparova. The effect of boron and carbon on the structure and corrosion-electrochemical behavior of Kh20n20 austenitic stainless steel. *Protection of Metals and Physical Chemistry of Surfaces*, 49(6):734–739, November 2013. ISSN 2070-2051, 2070-206X. doi: 10.1134/

S2070205113060063. URL http://link.springer.com/article/10.1134/S2070205113060063. 25, 27

[51] M. Mayuzumi, J. Ohta, and T. Arai. Effects of Cold Work, Sensitization Treatment, and the Combination on Corrosion Behavior of Stainless Steels in Nitric Acid. *Corrosion*, 54(4):271–280, April 1998. ISSN 0010-9312. doi: 10.5006/1.3284853. URL http://0-corrosionjournal.org.wam.leeds.ac.uk/doi/abs/10.5006/1.3284853. 25, 26, 34

[52] ASTM International. Practices for Detecting Susceptibility to Intergranular Attack in Austenitic Stainless Steels. Technical report, ASTM International, 2014. URL http://www.astm.org/Standards/A262.htm. 25, 26

[53] T. M. Devine, C. L. Briant, and B. J. Drummond. Mechanism of intergranular corrosion of 316l stainless steel in oxidizing acids. *Scripta Metallurgica*, 14(11):1175–1179, November 1980. ISSN 0036-9748. doi: 10.1016/0036-9748(80)90251-3. URL http://www.sciencedirect.com/science/article/pii/0036974880902513. 26

[54] G. H. Aydoğdu and M. K. Aydinol. Determination of susceptibility to intergranular corrosion and electrochemical reactivation behaviour of AISI 316l type stainless steel. *Corrosion Science*, 48(11):3565–3583, November 2006. ISSN 0010-938X. doi: 10.1016/j.corsci.2006.01.003. URL http://www.sciencedirect.com/science/article/pii/S0010938X06000308.

[55] Wenjie Bai, Mengyu Chai, Lichan Li, and Quan Duan. Comparative Study of Acoustic Emission Characteristics for Intergranular Corrosion of 316l Stainless Steel Parent Material and Weldment. In *ASME 2014 Pressure Vessels and Piping Conference Volume 5: High-Pressure Technology; ASME NDE Division; 22nd Scavuzzo Student Paper Symposium and Competition*, Anaheim, California, USA, July 2014. The American Society of Mechanical Engineers. URL http://0-proceedings.asmedigitalcollection.asme.org.wam.leeds.ac.uk/proceeding.aspx?articleid=1938090. 26

[56] P. Fauvet, F. Balbaud, R. Robin, Q. T. Tran, A. Mugnier, and D. Espinoux. Corrosion mechanisms of austenitic stainless steels in nitric media used in

reprocessing plants. *Journal of Nuclear Materials*, 375(1):52–64, March 2008. ISSN 0022-3115. doi: 10.1016/j.jnucmat.2007.10.017. URL http://www.sciencedirect.com/science/article/pii/S002231150701046X. 26

[57] Fanny Balbaud, Gérard Sanchez, Gérard Santarini, and Gérard Picard. Cathodic Reactions Involved in Corrosion Processes Occurring in Concentrated Nitric Acid at 100 Â°C. *European Journal of Inorganic Chemistry*, 2000(4):665–674, 2000. ISSN 1099-0682. doi: 10.1002/(SICI)1099-0682(200004)2000:4⟨665::AID-EJIC665⟩3.0.CO;2-N. URL http://onlinelibrary.wiley.com/doi/10.1002/(SICI)1099-0682(200004)2000:4<665::AID-EJIC665>3.0.CO;2-N/abstract. 26

[58] K. Fukuya, S. Shima, H. Kayano, and M. Narui. Stress corrosion cracking and intergranular corrosion of neutron irradiated austenitic stainless steels. *Journal of Nuclear Materials*, 191-194, Part B:1007–1011, September 1992. ISSN 0022-3115. doi: 10.1016/0022-3115(92)90626-V. URL http://www.sciencedirect.com/science/article/pii/002231159290626V. 27

[59] NACE International. Stress Corrosion Cracking (SCC). URL https://www.nace.org/Corrosion-Central/Corrosion-101/Stress-Corrosion-Cracking-(SCC)/. 28

[60] Philippe Marcus. *Corrosion Mechanisms in Theory and Practice*. CRC Press, July 2002. ISBN 978-0-203-90918-8. Google-Books-ID: 69bImhlRCdcC. 28

[61] ASTM International. ASTM G38 - 01(2013) Standard Practice for Making and Using C-Ring Stress-Corrosion Test Specimens. Technical report, 2007. URL https://www.astm.org/Standards/G38.htm. 28, 29

[62] ASTM International. ASTM G36 - 94(2013) Standard Practice for Evaluating Stress-Corrosion-Cracking Resistance of Metals and Alloys in a Boiling Magnesium Chloride Solution. Technical report, 2007. URL https://www.astm.org/Standards/G36.htm. 28

[63] Heinz Kohl. A Contribution to the Examination of Stress Corrosion Cracking of Austenitic Stainless Steels in Magnesium Chloride Solutions. *CORROSION*, 23(2):39–49, February 1967. ISSN 0010-9312. doi: 10.5006/0010-9312-23.2.39. URL http://www.corrosionjournal.org/doi/abs/10.5006/0010-9312-23.2.39. 28

[64] Osama M. Alyousif and Rokuro Nishimura. The stress corrosion cracking behavior of austenitic stainless steels in boiling magnesium chloride solutions. *Corrosion Science*, 49(7):3040–3051, July 2007. ISSN 0010-938X. doi: 10.1016/j.corsci.2006.12.023. URL http://www.sciencedirect.com/science/article/pii/S0010938X07000248. 28

[65] Osama M. Alyousif and Rokuro Nishimura. The effect of test temperature on SCC behavior of austenitic stainless steels in boiling saturated magnesium chloride solution. *Corrosion Science*, 48(12):4283–4293, December 2006. ISSN 0010-938X. doi: 10.1016/j.corsci.2006.01.014. URL http://www.sciencedirect.com/science/article/pii/S0010938X06000643.

[66] C. Garcia, F. Martin, P. De Tiedra, J. A. Heredero, and M. L. Aparicio. Effects of prior cold work and sensitization heat treatment on chloride stress corrosion cracking in type 304 stainless steels. *Corrosion science*, 43(8): 1519–1539, 2001. ISSN 0010-938X. URL http://cat.inist.fr/?aModele=afficheN&cpsidt=14117343. 28

[67] David Hambley. Technical Basis for Extending Storage of AGR Fuel. Salt Lake City, September 2013. URL https://www.researchgate.net/profile/David_Hambley/publication/279058579_Technical_Basis_for_Extending_Storage_of_the_UK's_Advanced_Gas-Cooled_Reactor_Fuel/links/5589322308aed6bff80b421d.pdf. 29

[68] Craig W. Jones. Environmental Application of Hydrogen Peroxide. In *Applications of Hydrogen Peroxide and Derivatives*, pages 213–217. Royal Society of Chemistry, Cambridge, 1999. ISBN 978-0-85404-536-5. Google-Books-ID: QLePlhTsE0oC. 30

[69] Mark C. Biesinger, Brad P. Payne, Andrew P. Grosvenor, Leo W. M. Lau, Andrea R. Gerson, and Roger St. C. Smart. Resolving surface chemical states in XPS analysis of first row transition metals, oxides and hydroxides: Cr, Mn, Fe, Co and Ni. *Applied Surface Science*, 257(7):2717–2730, January 2011. ISSN 0169-4332. doi: 10.1016/j.apsusc.2010.10.051. URL http://www.sciencedirect.com/science/article/pii/S0169433210014170. 31, 75, 77, 79

[70] Thermo Scientific. XPS Interpretation of Calcium. URL https://xpssimplified.com/elements/calcium.php. 32

[71] P. Stefanov, D. Stoychev, M. Stoycheva, A. R. Gonzalez-Elipe, and Ts. Marinova. XPS, SEM and TEM characterization of stainless-steel 316l surfaces after electrochemical etching and oxidizing. *Surface and Interface Analysis*, 28(1):106–110, August 1999. ISSN 1096-9918. doi: 10.1002/(SICI)1096-9918(199908)28:1⟨106::AID-SIA628⟩3.0.CO;2-J. URL http://onlinelibrary.wiley.com/doi/10.1002/(SICI)1096-9918(199908)28:1<106::AID-SIA628>3.0.CO;2-J/abstract. 32, 33

[72] S. Jin and A. Atrens. ESCA-studies of the structure and composition of the passive film formed on stainless steels by various immersion times in 0.1 M NaCl solution. *Applied Physics A*, 42(2):149–165, January 1987. ISSN 0947-8396, 1432-0630. doi: 10.1007/BF00616726. URL http://link.springer.com/article/10.1007/BF00616726. 32

[73] P Stefanov, D Stoychev, M Stoycheva, and Ts Marinova. XPS and SEM studies of chromium oxide films chemically formed on stainless steel 316 L. *Materials Chemistry and Physics*, 65(2):212–215, July 2000. ISSN 0254-0584. doi: 10.1016/S0254-0584(00)00249-2. URL http://www.sciencedirect.com/science/article/pii/S0254058400002492. 33

[74] V. Maurice, W. P. Yang, and P. Marcus. XPS and STM Study of Passive Films Formed on Fe-22cr(110) Single-Crystal Surfaces. *Journal of The Electrochemical Society*, 143(4):1182–1200, April 1996. ISSN 0013-4651, 1945-

7111. doi: 10.1149/1.1836616. URL http://0-jes.ecsdl.org.wam.leeds.ac.uk/content/143/4/1182. 34

[75] R. Li, M. G. S. Ferreira, M. A. Anjos, and R. Vilar. Localized corrosion of laser surface cladded UNS S31254 superaustenitic stainless steel on mild steel. *Surface and Coatings Technology*, 88(1-3):90–95, January 1997. ISSN 0257-8972. doi: 10.1016/S0257-8972(96)02865-4. URL http://www.sciencedirect.com/science/article/pii/S0257897296028654. 34

[76] M. A. Ashworth, D. I. R. Norris, and I. P. Jones. Radiation-induced segregation in Fe-20cr-25ni-Nb based austenitic stainless steels. *Journal of Nuclear Materials*, 189(3):289–302, August 1992. ISSN 0022-3115. doi: 10.1016/0022-3115(92)90383-V. URL http://www.sciencedirect.com/science/article/pii/002231159290383V. 34

[77] Jiang Hsieh. *Computed Tomography: Principles, Design, Artifacts, and Recent Advances*. SPIE PRESS, 2015. ISBN 978-1-62841-825-5. URL http://ebooks.spiedigitallibrary.org/book.aspx?doi=10.1117/3.2197756. DOI: 10.1117/3.2197756. 35

[78] D. A. Horner, B. J. Connolly, S. Zhou, L. Crocker, and A. Turnbull. Novel images of the evolution of stress corrosion cracks from corrosion pits. *Corrosion Science*, 53(11):3466–3485, November 2011. ISSN 0010-938X. doi: 10.1016/j.corsci.2011.05.050. URL http://www.sciencedirect.com/science/article/pii/S0010938X11002721. 35

[79] L. Babout, T. J. Marrow, D. Engelberg, and P. J. Withers. X-ray microtomographic observation of intergranular stress corrosion cracking in sensitised austenitic stainless steel. *Materials Science and Technology*, 22(9):1068–1075, September 2006. ISSN 0267-0836. doi: 10.1179/174328406X114090. URL https://doi.org/10.1179/174328406X114090. 35

[80] A. King, G. Johnson, D. Engelberg, W. Ludwig, and J. Marrow. Observations of Intergranular Stress Corrosion Cracking in a Grain-Mapped

Polycrystal. *Science*, 321(5887):382–385, July 2008. ISSN 0036-8075, 1095-9203. doi: 10.1126/science.1156211. URL http://science.sciencemag.org/content/321/5887/382. 35

[81] W. Stephen Walters, Peter Durham, and Nicholas A. Hodge. The adsorption and desorption of water from a carbonaceous deposit layer on the surface of stainless steel representing spent AGR nuclear fuel cladding. *Journal of Nuclear Science and Technology*, 0(0):1–12, December 2017. ISSN 0022-3131. doi: 10.1080/00223131.2017.1403384. URL https://doi.org/10.1080/00223131.2017.1403384. 51

[82] Yunus A. Çengel and Michael A. Boles. 2.1 Pure Substance. In *Thermodynamics: an engineering approach*, page 48. McGraw Hill, Boston, 3rd ed edition, 1998. ISBN 978-0-07-011927-7. 119

[83] The Engineering Toolbox. Water Saturation Pressure. URL http://www.engineeringtoolbox.com/water-vapor-saturation-pressure-d_599.html. 121

[84] Yunus A. Çengel and Michael A. Boles. 2.3 Phase-change Processes of Pure Substances. In *Thermodynamics: an engineering approach*, pages 49–55. McGraw Hill, Boston, 3rd ed edition, 1998. ISBN 978-0-07-011927-7. 121

[85] Yunus A. Çengel and Michael A. Boles. 2.4 Property Diagrams for Phase-change Processes. In *Thermodynamics: an engineering approach*, pages 55–62. McGraw Hill, Boston, 3rd ed edition, 1998. ISBN 978-0-07-011927-7. 122, 123, 124, 125

[86] J.M.Sullivan Jr. ES 3001 Thermodynamics. URL http://users.wpi.edu/~sullivan/ES3001/Lectures/Lecture-A/Lecture-2-2011.htm. 123

[87] Wikipedia, The Online Encyclopedia. *Phase diagram*. November 2015. URL https://en.wikipedia.org/w/index.php?title=Phase_diagram&oldid=692814655. Page Version ID: 692814655. 126

[88] Yunus A. Çengel and Michael A. Boles. 2.5 Vapour Pressure and Phase Equlibrium. In *Thermodynamics: an engineering approach*, pages 62–66. McGraw Hill, Boston, 3rd ed edition, 1998. ISBN 978-0-07-011927-7. 127, 129

[89] Robert J. Hunter. Thermodynamics of Surfaces. In *Foundations of colloid science*, pages 87–93. Oxford University Press, Oxford ; New York, 2nd ed edition, 2001. ISBN 978-0-19-850502-0. 129

[90] Fèlix Casanova, Casey E Chiang, Chang-Peng Li, Igor V Roshchin, Anne M Ruminski, Michael J Sailor, and Ivan K Schuller. Gas adsorption and capillary condensation in nanoporous alumina films. *Nanotechnology*, 19(31): 315709, 2008. ISSN 0957-4484. URL http://stacks.iop.org/0957-4484/19/i=31/a=315709. 129

[91] Yunus A Çengel. 1-3 Heat Transfer. In *Introduction to thermodynamics and heat transfer*, pages 5–6. McGraw-Hill, Dubuque, IA, 2008. ISBN 978-0-07-128773-9. 131, 133

[92] 1.1 What and How. In Frank P. Incropera, David P. DeWitt, Theodore L. Bergman, and Adrienne S. Lavine, editors, *Principles of heat and mass transfer*, pages 3–5. Wiley, Singapore, 7. ed., international student version edition, 2013. ISBN 978-0-470-64615-1 978-0-470-50197-9. 131

[93] Yunus A Çengel. 9-2 Conduction. In *Introduction to thermodynamics and heat transfer*, pages 374–381. McGraw-Hill, Dubuque, IA, 2008. ISBN 978-0-07-128773-9. 132

[94] J. P. Holman. 1-2 Thermal Conductivity. In *Heat transfer*, McGraw-Hill series in mechanical engineering, pages 5–9. McGraw-Hill, New York, 9th ed edition, 2002. ISBN 978-0-07-240655-9 978-0-07-112230-6. 133

[95] Thermal Conductivity of common Materials and Gases. URL https://www.engineeringtoolbox.com/thermal-conductivity-d_429.html. 133

[96] Yunus A Çengel. 9-3 Convection. In *Introduction to thermodynamics and heat transfer*, pages 382–383. McGraw-Hill, Dubuque, IA, 2008. ISBN 978-0-07-128773-9. 133

[97] J. P. Holman. 1-3 Convection Heat Transfer. In *Heat transfer*, McGraw-Hill series in mechanical engineering, pages 9–12. McGraw-Hill, New York, 9th ed edition, 2002. ISBN 978-0-07-240655-9 978-0-07-112230-6.

[98] 1.2.2 Convection. In Frank P. Incropera, David P. DeWitt, Theodore L. Bergman, and Adrienne S. Lavine, editors, *Principles of heat and mass transfer*, pages 6–8. Wiley, Singapore, 7. ed., international student version edition, 2013. ISBN 978-0-470-64615-1 978-0-470-50197-9. 133, 135

[99] 14.1 Physical Origins and Rate Equations [Diffusion Mass Transfer]. In Frank P. Incropera, David P. DeWitt, Theodore L. Bergman, and Adrienne S. Lavine, editors, *Principles of heat and mass transfer*, pages 934–939. Wiley, Singapore, 7. ed., international student version edition, 2013. ISBN 978-0-470-64615-1 978-0-470-50197-9. 135, 136

[100] Jaime Benítez. 1.2 Molecular Mass Transfer. In *Principles and modern applications of mass transfer operations*, pages 3–15. Wiley-Interscience, New York, 2002. ISBN 978-0-471-20344-5. 135

[101] A. H. P. Skelland. 2 Molecular Diffusion. In *Diffusional Mass Transfer*, pages 6–48. John Wiley & Sons Inc, New York, 1st edition edition edition, April 1974. ISBN 978-0-471-79374-8. 136

[102] Jaime Benítez. 1.3 The Diffusion Coefficient. In *Principles and modern applications of mass transfer operations*, pages 15–34. Wiley-Interscience, New York, 2002. ISBN 978-0-471-20344-5. 137

[103] E. L. Cussler. 5.1 Diffusion Coefficients in Gas. In *Diffusion: mass transfer in fluid systems*, pages 101–111. Cambridge University Press, New York, 2nd ed edition, 1997. ISBN 978-0-521-45078-2 978-0-521-56477-9. 137

[104] E. L. Cussler. 6.5-Solute Boundary Interactions. In *Diffusion: mass transfer in fluid systems*. Cambridge University Press, New York, 2nd ed edition, 1997. ISBN 978-0-521-45078-2 978-0-521-56477-9. 137

[105] Diffusion of Fluids in Porous Solids. In Robert H. Perry and Don W. Green, editors, *Perry's chemical engineers' handbook*, pages 5.48–5.49. McGraw-Hill, New York, 8th ed edition, 2008. ISBN 978-0-07-142294-9. 137

[106] NRC: Glossary – Crud. URL http://www.nrc.gov/reading-rm/basic-ref/glossary/crud.html. 139

[107] W. S. Large. Review of Drying Methods for Spent Nuclear Fuel. Technical Report WSRC-TR-97-0075, Savannah River Site (US), Aiken, SC 29808, October 1999. URL http://www.osti.gov/scitech/biblio/14490. 139, 141

[108] G. E. Culley. Hanford's Progress Toward Dry Interim Storage of K Basin's Spent Fuel. Technical Report WHC-SA–3107-FP; CONF-960804–, Westinghouse Hanford Co., Richland, WA (United States), May 1996. URL http://www.osti.gov/scitech/biblio/330736. 139

[109] A. L. Pajunen. Cold Vacuum Drying Residual Free Water Test Description. Technical Report HNF–1851, Fluor Daniel Hanford Inc., Richland, WA (United States), December 1997. URL http://www.osti.gov/scitech/biblio/10148296. 139

[110] P. G. Loscoe. Transitioning Metallic Uranium Spent Nuclear Fuel from Wet to Dry Storage. In *WM 2000 Proceedings*, Tucson, Az, March 2000. URL https://www.wmsym.org/archives/2000/pdf/54/54-9.pdf. 140

[111] L Rodrigo, L Therrien, and B. Surette. Low-Temperature, Vacuum-Assisted Drying of Degraded Spent Nuclear Fuel. In *Waste Management, Decommissioning and Environmental Restoration for Canada's Nuclear Activities Current Practices and Future Needs*. Canadian Nuclear Society, Toronto, 2005. ISBN 978-0-919784-81-9. 140, 141

[112] W.C.H Kupferschmidt and M.E. Stephens. AECL's Waste Management and Decommissioning Program. page 685. Australian Nuclear Association, 2006.

[113] DS Cox, IB Bainbridge, and KR Greenfield. Management of Legacy Spent Nuclear Fuel Wastes at the Chalk River Laboratories: Operating Experience and Progress Towards Waste Remediation. In *Proceedings of WM'05 Conference*, Tucson, Az, March 2005. 140

[114] J.C. Crepeau, S. Reese, H.M. Mcllroy Jr., and R.E. Lords. Drying of Mock Spent Nuclear Fuel Elements. *Drying Technology*, 16(3-5):545–560, 1998. ISSN 07373937. 141, 142

[115] R. E. Lords, W. E. Windes, J. C. Crepeau, and R. W. Sidwell. Drying Studies of Simulated Doe Aluminum Plate Fuels. Technical Report INEL–95/00437; CONF-9606116–44, Idaho National Engineering Lab., Idaho Falls, ID (United States), May 1996. URL http://www.osti.gov/scitech/biblio/236247. 142

[116] R. E. Lords, W. E. Windes, J. C. Crepeau, and R. W. Sidwell. Drying Studies for Corroded Doe Aluminum Plate Fuels. Technical Report INEL–96/00134; CONF-960804–29, Idaho National Engineering Lab., Idaho Falls, ID (United States), May 1996. URL http://www.osti.gov/scitech/biblio/260992. 141, 142

[117] D. Caramelle, A. Bastianelli, F. Boussard, A. Milesi, G. Polydor, and G. Christin. CEA Spent Fuel: Reprocessing and Storage Management. In *Proceedings of WM'97*, Tucson, Az, March 1997. URL http://www.wmsym.org/archives/1997/sess12/12-04.htm. 143

[118] P Michaille. Retrieval of Degraded Irradiated Fuel and Conditioning for a Safe Storage: the CEA Experience, October 2003. URL http://www.iaea.org/OurWork/ST/NE/NEFW/CEG/documents/ws102003_michaille3-e.pdf. 143

[119] Krishna Pal Singh. Forced gas flow canister dehydration, June 2004. URL http://www.google.com/patents/EP1429344A2. International Classification G21C17/06, G21F5/14, G21C19/32, G21F5/00, G21F5/06, G21F9/36, F26B3/00, G21C19/06; Cooperative Classification G21F5/06, G21Y2004/40, G21Y2002/207, G21F9/34, G21Y2002/501, G21Y2002/201, G21Y2002/202; European Classification G21F5/06, G21F9/34. 143

[120] J Morris, S Wickham, P Richardson, C Rhodes, and M Newland. Contingency Options for the Dry Storage of Magnox Spent Fuel in the UK. In *Proceedings of the 12th International Conference on Radioactive Waste Management and Environmental Remediation, ICEM*, volume 1, pages 817–823, Liverpool, October 2009. ISBN 978-0-7918-4407-6. doi: 10.1115/ICEM2009-16331. 143, 144

[121] R. Sindelar, D. Vinson, N. Iyer, and D. Fisher. Overview of Criteria for Interim Wet and Dry Storage of Research Reactor Spent Nuclear Fuel. Technical report, SRS, 2010. URL http://sti.srs.gov/fulltext/SRNL-STI-2010-00688.pdf. 144

[122] Rick Springman. Forced Gas Dehydration (FGD) System for Drying Nuclear Fuel and Waste Packages. 17th Packaging and Transportation of Radioactive Materials Symposium (PATRAM 13). San Francisco, August 2013. 169

[123] Engineering Toolbox. Specific Heat and Individual Gas Constant of Gases. URL http://www.engineeringtoolbox.com/specific-heat-capacity-gases-d_159.html. 264